Sequence-controlled surface modification *via* thiol-ene/yne "click" chemistry

Zur Erlangung des akademischen Grades eines

Doktors der Naturwissenschaften

(Dr. rer. nat.)

von der KIT-Fakultät für Chemie und Biowissenschaften

des Karlsruher Instituts für Technologie (KIT)

genehmigte

Dissertation

von

M. Sc. Benjamin Bitterer

Dekan: Professor Dr. M. Wilhelm

1. Referent: Professor Dr. M. A. R. Meier

2. Referent: Professor Dr. P. Théato

Tag der mündlichen Prüfung: 21.04.2020

„Ich bin noch immer verwirrt, aber auf einem höheren Niveau"

Enrico Fermi, Kernphysiker

Die vorliegende Arbeit wurde von November 2016 bis März 2020 unter Anleitung von Prof. Dr. Michael A. R. Meier am Institut für Organische Chemie (IOC) des Karlsruher Instituts für Technologie (KIT) durchgeführt.

Hiermit versichere ich, dass ich die Arbeit selbstständig angefertigt, nur die angegebenen Quellen und Hilfsmittel benutzt und mich keiner unzulässigen Hilfe Dritter bedient habe. Insbesondere habe ich wörtlich oder sinngemäß aus anderen Werken übernommene Inhalte als solche kenntlich gemacht. Die Satzung des Karlsruher Instituts für Technologie (KIT) zur Sicherung wissenschaftlicher Praxis habe ich beachtet. Des Weiteren erkläre ich, dass ich mich derzeit in keinem laufenden Promotionsverfahren befinde, und auch keine vorausgegangenen Promotionsversuche unternommen habe. Die elektronische Version der Arbeit stimmt mit der schriftlichen Version überein und die Primärdaten sind gemäß der Satzung zur Sicherung guter wissenschaftlicher Praxis des KIT beim Institut abgegeben und archiviert.

Karlsruhe, 10.03.2020

I. Kurzzusammenfassung

In Folge des industriellen Fortschritts und der Globalisierung steigt die Nachfrage nach portablen Energiespeichern rasant an. Einhergehend, wird es in den nächsten Jahren zu einem exponentiellen Anstieg des Bedarfs an Lithiumkarbonat (Li_2CO_3) kommen (*1, 2*). Um diese endliche Ressource möglichst effizient einzusetzen, müssen die Produktionsprozesse und Anwendungen optimiert werden. Dies wird vor allem beim hohen Verlust an Lithium-Ionen beim ersten Lade-/Entladezyklus und der Zersetzung des Elektrolyten in Lithium-Ionen Batterien deutlich. Obwohl der Mechanismus zur Bildung der Feststoff-Elektrolyt Grenzfläche (SEI) noch nicht vollständig geklärt ist, passiviert dies die Graphitelektrode und verlangsamt die weitere Zersetzung des Elektrolyten enorm. Um diesem Vorgang zuvorzukommen, ist das Ziel dieser Arbeit, einen grundlegenden Prozess zur kontrollierten Beschichtung von Silizium Oberflächen durch multifunktionelle Bausteine zu entwickeln. Darüber hinaus soll ein Gradient (Elektronegativität, Porengröße, usw.) in das aufgebaute Netzwerk eingebracht werden. Die daraus resultierenden Ergebnisse sollen innerhalb des Sonderforschungsbereichs 1176 auf reale Elektroden übertragen werden.

Der erste Teil der Arbeit konzentriert sich auf die Optimierung bereits bekannter Syntheserouten für die Darstellung von Tetrakis(*p*-mercaptophenyl)methan (TPM-SH) und Tetrakis(*p*-acetylphenyl)methan (TPM-Acetylen) und darüber hinaus auf die Synthese von neuen funktionalisierten Tetraphenylmethan-Bausteinen, die sekundäre Amine in *para*-Position besitzen. Des Weiteren werden poröse, organische Gerüststrukturen aus diesen sekundären Aminen *via* Amino-In „Click" Chemie realisiert und mittels dynamischer Differenzkalorimetrie (DSC) und Brunauer-Emmet-Teller-Messung (BET) analysiert.

Der zweite Teil behandelt die Auftragung der zuvor dargestellten TPM-Bausteine mittels molekularer Schichtabscheidung (MLD) auf Siliziumoberflächen. Zuerst werden die Bausteine mittels Röntgenphotoelektronenspektroskopie (XPS) und Flugzeit-Sekundärionen-Massenspektrometrie (ToF-SIMS) detailliert untersucht. Nach der Optimierung des Silanisierungsprozesses mit Hilfe verschiedener Silane, wurden abwechselnd Schichten aus TPM-SH/TPM-Acetylen (drei Lagen) und TPM-SH/TPM-Acetylen (vier Lagen) dargestellt. Bei den Beschichtungen, die durch Amino-In „Click" Chemie erhalten wurden, konnte aufgrund von Nebenreaktionen und zu kurzen Reaktionszeiten nur eine Schicht realisiert werden.

Der letzte Teil dieser Arbeit beschäftigt sich mit Kraftfeldberechnungen tetraedrischer Bausteine und den daraus gebildeten idealisierten Netzwerken. Dadurch konnten die maximale Oberfläche (7444 m^2/g), das freie Volumen (4.09 cm^3/g), der Durchmesser der Kanäle (11.3 Å) und der Porendurchmesser (13.1 Å) berechnet werden. Zusätzlich werden quantenchemische Berechnungen zur Wechselwirkung zwischen Lithium und den TPM-Bausteinen unter Ausschluss externer Einflüsse durchgeführt. Aus diesen errechneten Energiedifferenzen können erste Hinweise zu einer optimalen Anordnung eines Elektronegativitätsgradienten durch Einsatz ausgewählter TPM-Bausteine gewonnen werden.

II. Abstract

Due to the industrial progress and the globalisation, the demand on portable energy storage systems and thereby also the demand on natural resources like lithium carbonate (Li_2CO_3) will exponentially increase in the next decade (*1, 2*). Thus, the need for considerate handling of given feedstocks is high. The high loss of lithium ions in the first charge/discharge step in lithium ion batteries (LIBs) *via* degradation of the electrolyte and the resulting formation of a solid electrolyte interface (SEI) are two of many issues to be addressed in the near future (*3*). To anticipate the degradation this thesis investigates the modification of surfaces with multifunctional building blocks, introducing a gradient (electronegativity, pore-size, etc.) along the *z*-axes. Based on the upcoming results, modification of real graphite electrodes and their electrochemical behaviour are part of studies within the collaborative research centre 1176.

In the first part of this thesis, the reaction procedure for the synthesis of substituted tetraphenylmethane building blocks is improved in regard to purity and yield. Besides the formerly known tetrakis(*p*-mercaptophenyl)methane (TPM-SH) and tetrakis(*p*-acetylphenyl)methane (TPM-acetylene), various *para* substituted secondary amines based on the TPM-core with yields up to 43% are obtained. Furthermore, first studies of the crosslinking reaction of activated acetylenes and the aforementioned tetrafunctional secondary amines *via* amino-yne "click" reaction are performed and characterised by differential scanning calorimetry (DSC) and Brunauer-Emmett-Teller analysis.

In the second part, silicon surfaces are modified *via* molecular layer deposition. In a first step, the necessary building blocks for the modification of functionalised silicon surfaces *via* thiol-ene "click" chemistry are thoroughly characterised by (X-ray photoelectron spectroscopy (XPS)- and time-of-flight secondary ion mass spectrometry (ToF-SIMS) measurements. Secondly, the silanisation process with a variety of silanes is investigated. Those functionalised surfaces are further coated up to the third layer applying alternating layers of TPM-SH and TPM-acetylene. TPM-SH and tetrkis(*p*-acetylphenyl)germanium (TPGe-acetylene) are applied up to the fourth layer and both fully characterised by XPS and ToF-SIMS. In regard to surface modification *via* amino-yne "click" chemistry, only one layer is obtained, and more investigations are necessary to establish a successful procedure.

In the third part, force field calculations of the tetrahedral building blocks and the corresponding thiol-yne derived idealised network are performed. Accordingly, the maximum calculated surface area is 7,444 m^2/g and the free accessible volume is calculated to be 4.09 cm^3/g. Additionally, it is shown that the approximated window size in the channel straight direction (space diagonal) is about 11.3 Å. Based on the van-der Waals radius of the atom species in the channel and inside the pores, the calculated pore diameter is 13.1 Å. Furthermore, quantum chemical calculations of Li-building block interactions were executed, giving a brief insight into a possible arrangement for an electronic gradient along the *z*-axes.

III. Table of Contents

IV. Danksagung

1. Introduction

In the past decade, the commercial use of Li-ion batteries (LIBs) was concentrated on portable electronic devices like cell phones, laptops etc. Due to the advantageous density of LIBs (0.534 g/cm^3) and the electrochemical potential of $-$ 3.045 V of the lithium metal itself and LIBs' unique energy density between 100 and 265 W h/kg and specific power of up to 340 W/kg, LIBs can be employed for numerous applications besides portable electronic devices (*4, 5*). The increasing importance of lithium ion-based batteries as energy storage systems will presumably lead to a higher demand of natural resources. Chobey *et al.* predicted a (worldwide) demand increase of Li$_2$CO$_3$ from 265 kilotons in 2015 to 498 kilotons in 2025, which equals to an increase of nearly 188% (*1, 2*). Additionally, Tesla's latest plans for a "Giga factory" would consume the entire supply of globally produced LIBs per year (*6*) Although LIBs have become important for many applications in everyday life, they display some major disadvantages compared to other accumulator cells, such as the expensive manufacturing and low abundance of lithium. One of the most important problems is aging due to reductive electrolyte decomposition accompanied by irreversible consumption of lithium forming a passivation layer, a solid electrolyte interphase (SEI). At the first charging / discharging step, this is most pronounced and leads to capacity loss and power fading (SEI) (*3, 7*) On the other hand, this interphase acts as a "protective layer" and enhances the lifespan of the graphite electrode (*8–10*).

A possible solution for inhibiting the problematic ageing effects of LIBs can be, for instance, tailored surface coatings on graphite electrodes. Since the coating of macroscopic surfaces has become a well-established method to influence the properties of materials in industry and for technical applications, the utilisation of coatings for electrical devices could be a possible solution for preventing SEI formation. Nowadays, there are basically three methods for homogeneously coating activated surfaces:

(i)   the grafting-to approach (using an anchor-group on the surface to attach a polymer chain),

(ii)   the grafting-from approach (*i.e.* initialising a polymerisation on an anchor-group of the surface) and

(iii)   the layer-by-layer method (*i.e.* the alternating deposition of thin films or connection of several monolayers on the surface) (*11*).

1. Introduction

Concerning the layer-by-layer method, on a charged surface alternatingly charged polymers are applied, whereby the different layers adhere to each other by electrostatic interactions. On the one hand, this method does not carry the disadvantage of requiring special building blocks, but on the other hand the layers are not precisely defined on the molecular level (*12, 13*). Furthermore, it is possible to use commercially available small building blocks to selectively introduce monomolecular layers, which makes the characterisation a challenging task (*14–16*). A lot of examples combining the controlled surface modifications with electrochemical applications exist. Vilan and Cahen for instance showed how semiconductor surfaces can be manipulated by introducing organic dipole monolayers *via* radical- (H terminated silicon) or nucleophilic-substitution (OH terminated silicon), serving as *e.g.* tunnelling barrier, thus influencing their performance in applications like LEDs, solar cells and other electronic devices (*17*).

In this thesis, multifunctional monomers were synthesised and were introduced in a controlled manner by covalent molecular layer deposition on a silicon surface. Tetrathiols and tetraalkynes were therefore employed, as thiol-ene/yne "click" chemistry was selected for the surface functionalisation. Additionally, new secondary amine building blocks were investigated on silicon surfaces *via* hydroamination reaction (amino-yne click) reactions.

2. Theoretical background

2.1 "Click" reactions

Sharpless, Kolb and Finn established the term "click chemistry" (CC) in the beginning of the 20th century. Nature's strategy of achieving astonishing biological diversity in high yields from a rather limited feedstock of monomers (amino acids, etc.) served as model for this group of reactions. The authors described it as "the reinvigoration of an old style of organic synthesis", which was set out to fulfil the demands of modern chemistry regarding the high amount of carbon-heteroatom bonds and to improve yields and reaction control (*18, 19*).

The criteria for molecular processes that must fully or mostly be fulfilled to be considered as "click" chemistry are:

- modular setup
- high yields with no or easily removable, inoffensive by-products (non-chromatographic methods, such as distillation or crystallisation)
- stereospecific (but not necessarily enantioselective)
- insensitivity to oxygen / water
- mild reaction conditions, solventless or in water
- orthogonality to other common organic reactions
- accessibility for high variety of commercially available components
- avoidance of protection steps

Until today, the need for this kind of reactions especially in pharmaceutical science, where researchers are constantly seeking for new molecules and constructs, is still increasing. For instance, Guida and co-workers have estimated the pool of "reasonable" drug candidates with $\leq$ 30 non-hydrogen atoms, $\leq$ 500 Da, a restricted composition of atoms (H, C, N, O, P, S, F, Cl, Br), stable at room temperature and in presence of water and oxygen to be in a range of 10^{62} to 10^{63} discrete molecules (*20*).

2. Theoretical background
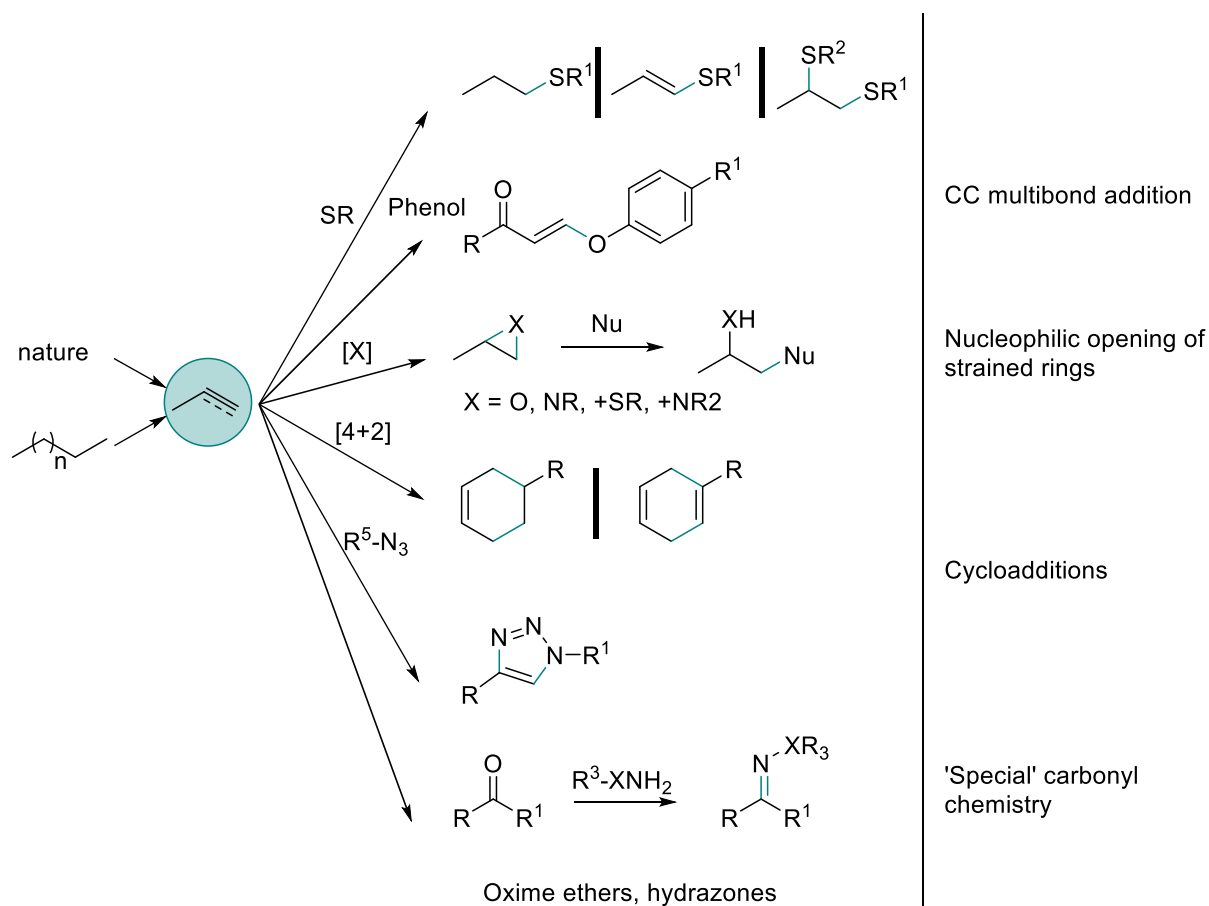
Scheme 1: General classification of "click chemistry" reactions in CC multibond addition reactions, nucleophilic opening of strained rings, cycloadditions and "special" carbonyl chemistry (21).

Thus, some very effective and popular conjugation techniques (shown in Scheme 1) are used not only in drug discovery, but also in polymer science, nanoscience, bioconjugation and sensor development. To date, "click" reactions fall in one of four major classes (22):

- Cycloadditions: primarily 1,3-dipolar cycloadditions (Huisgen 1,3-dipolar cycloaddition of azides and terminal alkynes), but also hetero Diels-Alder cycloadditions (21)
- Nucleophilic ring-opening reactions: opening of strained heterocyclic electrophiles (aziridines, aziridinium ions, epoxides, cyclic sulfates, episulfonium ions) (21)
- Non-aldol type carbonyl chemistry: formation of ureas, thioureas, hydrazones, oxime ether, amides, aromatic heterocycles, etc. (18)
- Additions to C-C multiple bonds: epoxidations, aziridinations, dihydroxylations, sulfenyl halide additions, nitrosyl halide additions, and certain Michael additions (18, 21)

An exception are aldol type reactions, even if they partially fulfil the criteria listed above. The reasons why they cannot be defined as "click chemistry" relate to their low thermodynamic driving forces and the corresponding longer reaction times as well as the high possibility of side product formation. Based on a literature research, since the first definition, over 25,000 articles have been published to date on "click" chemistry, with more than 2,000 articles per year since 2011 (SciFinder® 18.01.2020, research topic "click" chemistry). At the end of 2009, the Cu(I)-catalysed Huisgen 1,3-dipolar cycloaddition (HDC) of azides and terminal alkynes to form 1,2,3-triazoles was the most employed "click" reaction, but over the last decade the popularity of other "click" reactions surpassed the HDC. This thesis focuses on the alkyne-based click reactions, the HDC being the most famous example, but also employing thiol-ene/yne and amino-yne reactions.
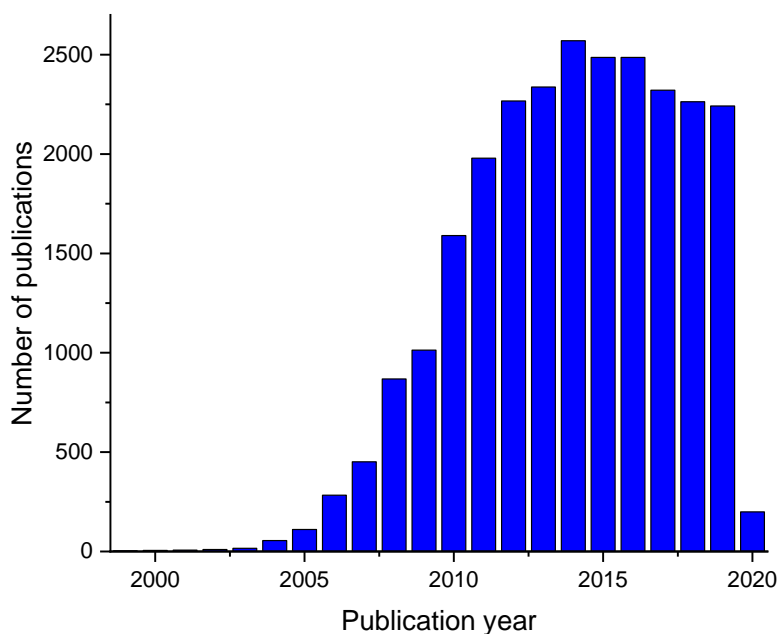

Figure 1: Number of publications about "click chemistry". Information was gathered from SciFinder ®
(accessed on 18.01.2020).

2. Theoretical background

2.1.1 Huisgen 1,3-dipolar cycloaddition

The Huisgen 1,3-dipolar cycloaddition (Scheme 2) is one of the most discussed click reactions. Under physiological conditions, both alkynes and azides are not inclined to undergo cycloaddition. Only at high temperatures, the 1,4- and 1,5-products can be achieved (*23–25*). The product mixture typically contains both molecules in an almost 1:1 ratio. The reason behind this behaviour lies in the small difference between the highest occupied molecular orbital and lowest unoccupied molecular orbital (HOMO/LUMO) energy levels of alkynes and azides, thus enabling both HOMO and LUMO dipoles to operate (and *vice versa*). On metallic substrates however, both starting materials can easily be introduced and react without catalysis because of its highly exothermic nature (ΔH_0 = -50 – -65 kcal/mol). The use of electron deficient terminal alkynes can, however, to some extent, favour a 1,4-regioselectivity. These features make the uncatalysed Huisgen 1,3-dipolar cycloaddition an inefficient conjugation technique.
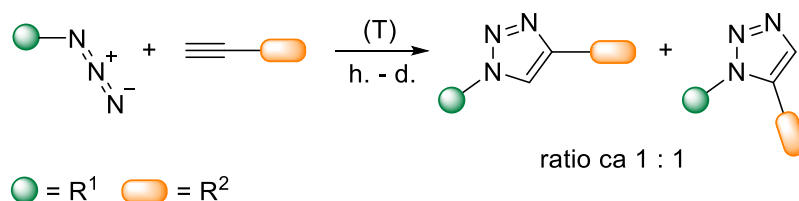
Scheme 2: Uncatalysed Huisgen 1,3-dipolar cycloaddition at elevated temperatures resulting in a 1,4- and 1,5-product mixture.

By using Cu(I), the HDC evolved to a very reliable and regioselective reaction, now fulfilling all criteria of click chemistry (CuAAC). Even at room temperature, the cycloaddition is accelerated by a factor of 10^7 compared to the uncatalyzed version and yields only the 1,4-substituted product. Additionally, the reactions can be performed in a variety of solvents including water, the linkage is stable up to 160 °C and resistant over a wide range of pH values. Although the decomposition of aliphatic azides is thermodynamically favoured, there is a kinetic hindrance (*26*). Independently, Sharpless (*25*) and Meldal (*27*) introduced the Cu(I) catalyst for this reaction. Sharpless reported the *in situ* generation of the active catalyst species by reducing copper sulfate pentahydrate ($CuSO_4 \cdot 5H_2O$) with ascorbic acid in an ethanol/water mixture as solvent

(*25*), whereas Meldal catalysed the cycloaddition for the conjugation of peptides in solid phase with cuprous iodide (*27*).

Most electrocyclic cycloadditions proceed through a concerted mechanism. The Cu(I) catalysed Huisgen 1,3-dipolar cycloaddition, on the contrary, seems to favour a stepwise reaction path. The energy for activation barriers of the concerted and stepwise pathway were calculated for both the uncatalyzed and catalysed HDC. The barrier of the concerted pathway is 1.8 kcal/mole lower (27.8 kcal/mol without cat. *vs.* 26 kcal/mol with cat) and the barrier of the stepwise catalysed pathway is 11 kcal/mol lower (*28*). As shown in Scheme 3, the first step of the reaction is the π-complexation of a CuI dimer to the alkyne followed by a deprotonation of its terminal hydrogen, forming a Cu-acetylide by displacing one of the ligands of the Cu. The formed π-complex (equilibrium of mono and dimer) entails a decrease of the pKa-value by as much as 9.7 pH units, enabling a deprotonation in aqueous media without need of a base. If a solvent other than water is employed, a base such as *N,N'*-diisopropylethylamine (DIPEA) or 2,6-lutidine is necessary.
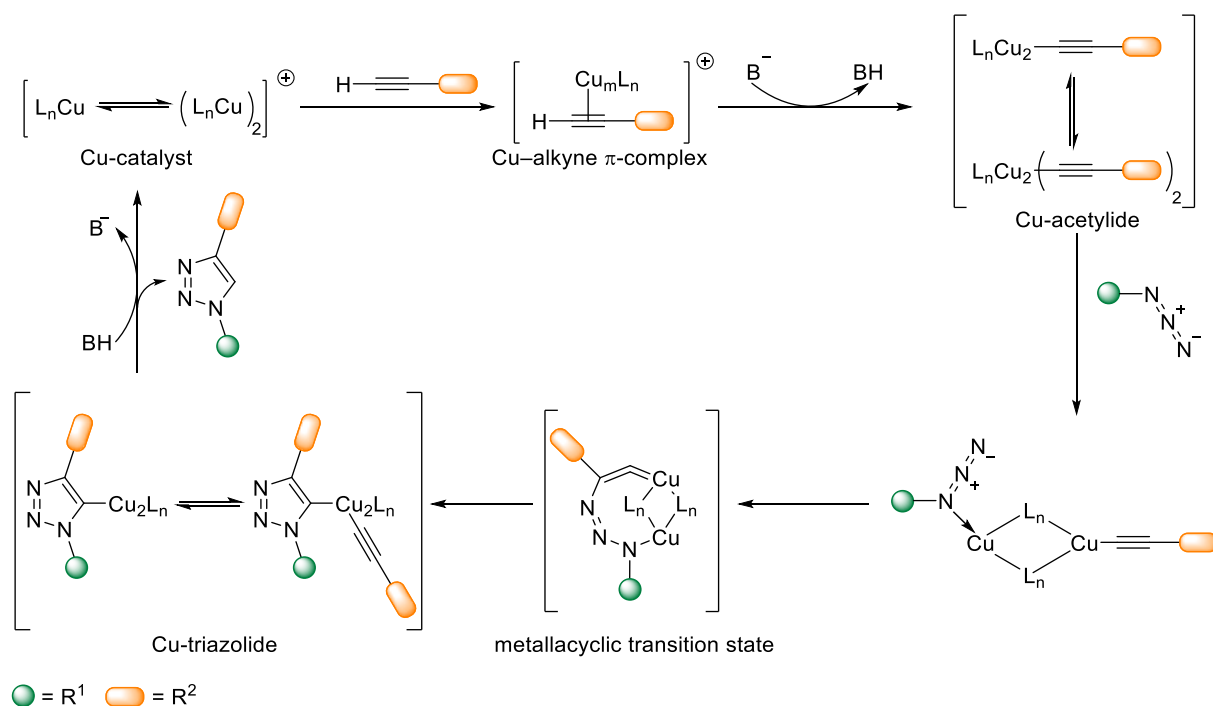
Scheme 3: Reaction mechanism of the Cu(I) catalysed Huisgen 1,3-dipolar cycloaddition (CuAAC) (26).

The Cu-acetylide complex activates the terminal nitrogen of the azide for a nucleophilic attack on the internal carbon of the alkyne to give a metallacycle. The lone electron pair on the substituted nitrogen of the azide subsequently attacks the carbon-copper double-bond through a transannular interaction forcing a ring contraction of the

2. Theoretical background

metallacycle. The formed Cu-triazolide releases the 1,4-disubstitued triazole after protonation and regenerates the Cu(I)-catalyst.

As already mentioned, the active Cu(I)-catalyst can be generated *in situ* or provided as salt. Furthermore, ligands which are capable of forming heterocyclic chelates with Cu^{1+} ions are found to increase the reaction rate and stability of the catalyst. One very efficient ligand is the tetradentate ligand tris-(benzyltriazolylmethyl)amine (TBTA), restraining the copper ions from interactions, normally leading to degradation. Additionally, the tertiary amine group acts as base. Not only nitrogen-based ligands can be used, but also phosphorous (*29*), carbon (*30*), and sulfur (*31*) containing donor atoms. Moreover, other catalysts are able to enhance the reactivity of the Huisgen 1,3-dipolar cycloaddition. Amongst those, Ru(II) catalysts were found to be the most promising (RuAAC). In 2005, Zhang *et al. (32)* used cyclopentadienyl ruthenium (II) complexes (Cp*Ru) such as Cp*RuCl(PPh₃)₂, Cp*RuCl, Cp*RuCl(COD) and Cp*RuCl(NBD) to form, contrary to all other catalysts, only 1,5-substituted 1,2,3-triazoles.
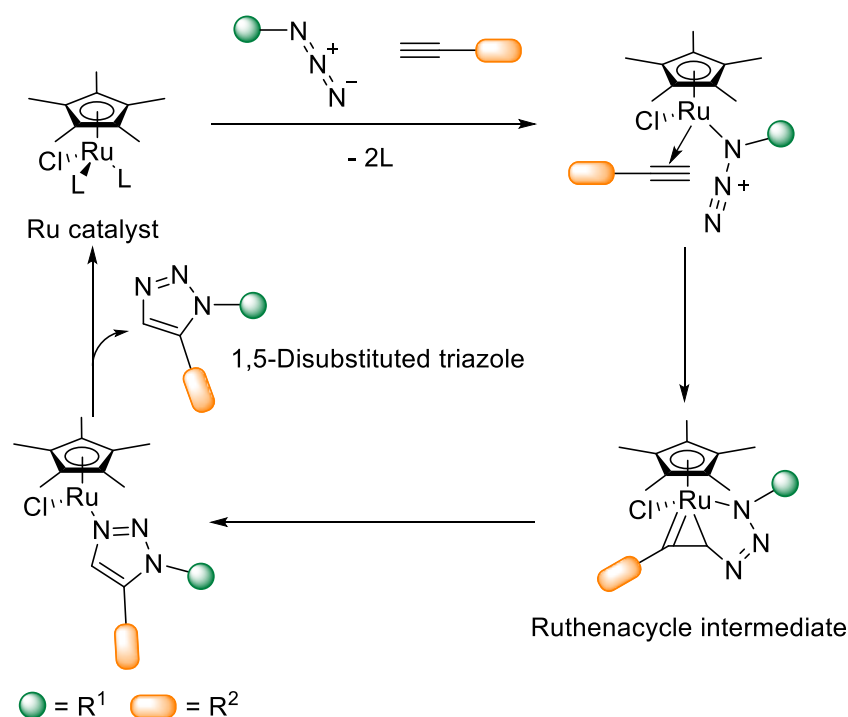
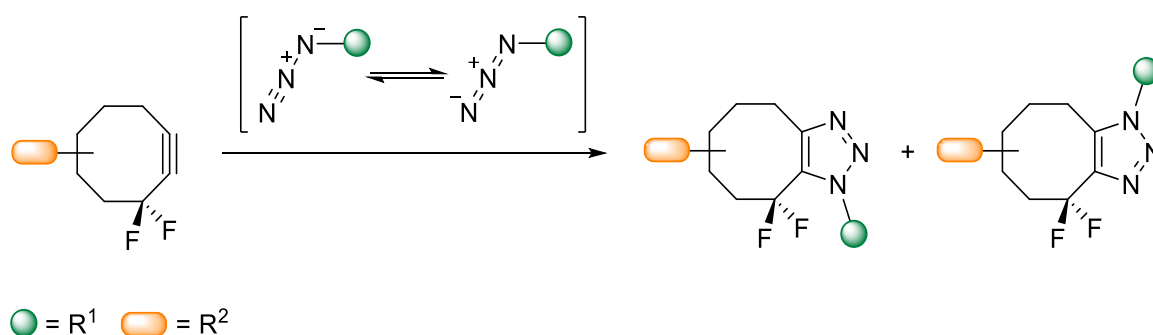*Scheme 4: Reaction mechanism of the Ru(II) catalysed Huisgen 1,3-dipolar cycloaddition (RuAAC) (33).*

On the other hand, the Ru-catalyzed HDC reaction is more dependent on the steric demand of the azides. Primary and secondary azides are quite reactive with a wide range of terminal alkynes, while tertiary azides are not. The reaction mechanism is

based on density functional theory DFT calculations of Fokin and co-workers in 2008 (*34*) (Scheme 4).). First, the azide and the alkyne coordinate to the ruthenium metal centre, followed by an oxidative coupling forming a six-membered ruthenacycle intermediate caused by a nucleophilic attack of the electronegative carbon on the terminal electrophilic nitrogen. Then, the rate-determining reductive elimination to a triazolyl complex takes place liberating a 1,5-disubstituted triazole product in the next step through ligand exchange.

For many biological applications, like site specific protein/virus modifications and usage in *in-vivo* or *in-vitro* experiments, the use of transition metal-catalysed reactions can be detrimental for living cells. Copper salts, for example, are known to degrade oligonucleotide strands and are highly cytotoxic in higher concentrations. Therefore, apart from drug synthesis, this method is not recommended, and alternatives are required for such applications. One possibility to overcome this hindrance, is the use of electron-deficient alkynes, but due to their high reactivity side products are formed in considerable amounts. Another alternative is the incorporation of the alkyne into an eight-membered ring, forming a cyclooctyne. This results in enhanced reactivity by ring tension (Scheme 5). In 1961, Wittig and co-workers first reported the reaction of the smallest stable cyclic alkyne, cyclooctyne, and phenylazide (*35*). The driving force was the release of ring strain of almost 18 kcal/mol. This strain-promoted azide-alkyne click reaction (SPAAC) was later used for bioconjugation by Bertozzi and co-workers (*36, 37*). To increase the reactivity of the ring, mono- and difluorinated cyclooctyne derivatives were synthesised, which possess lower LUMO energy (*22, 38*).

$\bigcirc$ = R^1 $\oslash$ = R^2

Scheme 5: Reaction mechanism of the uncatalysed strain-promoted Huisgen 1,3-dipolar cycloaddition (SPAAC) (39).

2. Theoretical background

Getting more efficient and popular over the last decades, click chemistry reactions receive more attention from other fields of chemistry, *e.g.* polymer synthesis and multi-component reactions (MCRs). Due to their well-defined structures, high efficiency by using three or more components, polymer scientists increased the effort to incorporate the benefits of multi-component reactions into multi-component polymerisations (*40*). The CuAAC-polymerisation stands out because of the mild reaction conditions, highly active intermediates and well-defined structures. Scheme 6 (top) shows the Cu(I)-catalysed reaction of a sulfonyl azide and various alkynes producing a *N*-sulfonyl triazolyl copper intermediate.


ketenimine intermediate

ketenimine intermediate

● = R¹   ▭ = R²   ◆ = R³   ⬭ = R⁴
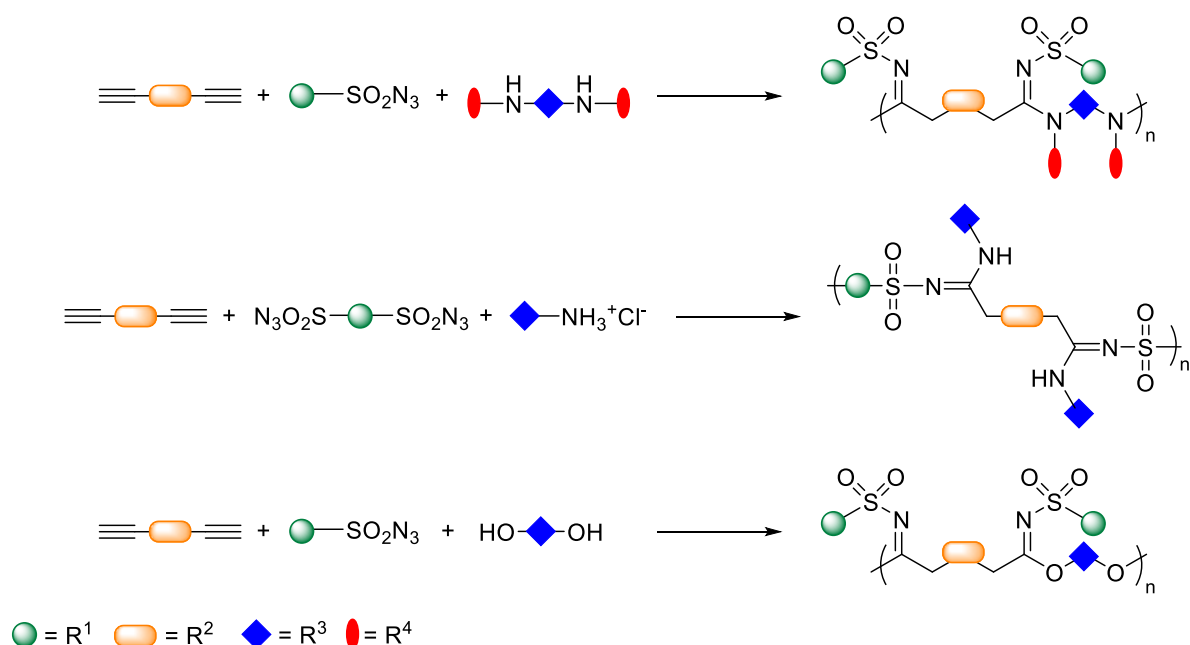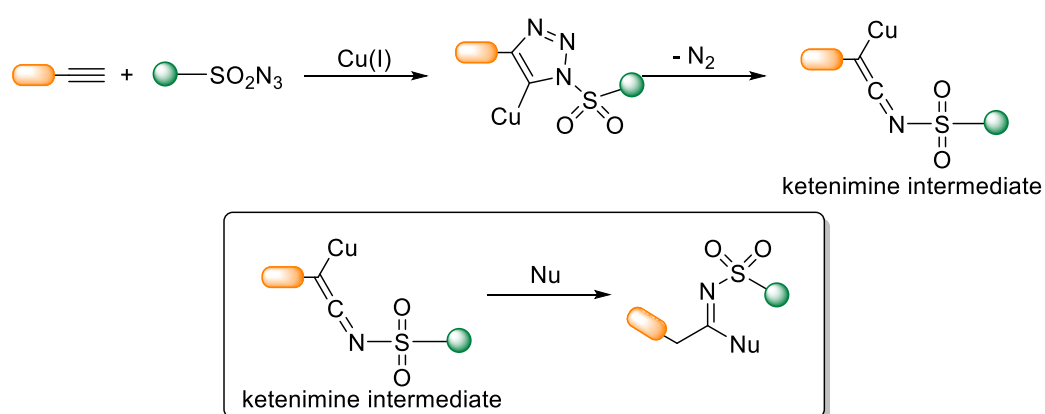
Scheme 6: General reaction of various sulfonyl-azides and alkynes with different nucleophiles (41–44).

This can be converted into the more active keteneimine intermediate *via* a ring-opening rearrangement and *in-situ* react with a vast number of nucleophiles (H_2O, alcohols, amines, etc.). Thus, many different properties like photo-patterning, refractivity, helical chirality and topological structures (linear, hyperbranched, dendronised, etc.) (*41–45*) can be introduced to polymers. Their synthesis via this route is schematically depicted in Scheme 6 (bottom).

Even in the field of organic dyads, the Cu(I) catalysed Huisgen 1,3-dipolar cycloaddition is a versatile and easily accessible method to build up benzodithiophene-based push-pull linkages to a fullerene derivative. Blanchard and Cabanetos achieved modest efficiencies with 0.4 % (TPA-T-C_{60}) and 0.6 % (TAT-T-C_{60}). Based on these results, they expanded their efforts and used benzo[1,2-*b*:4,5-*b*']dithiophene (BDT) coupled to a C_{60} fullerene and reached an efficiency of 0.5 %(*46–48*).
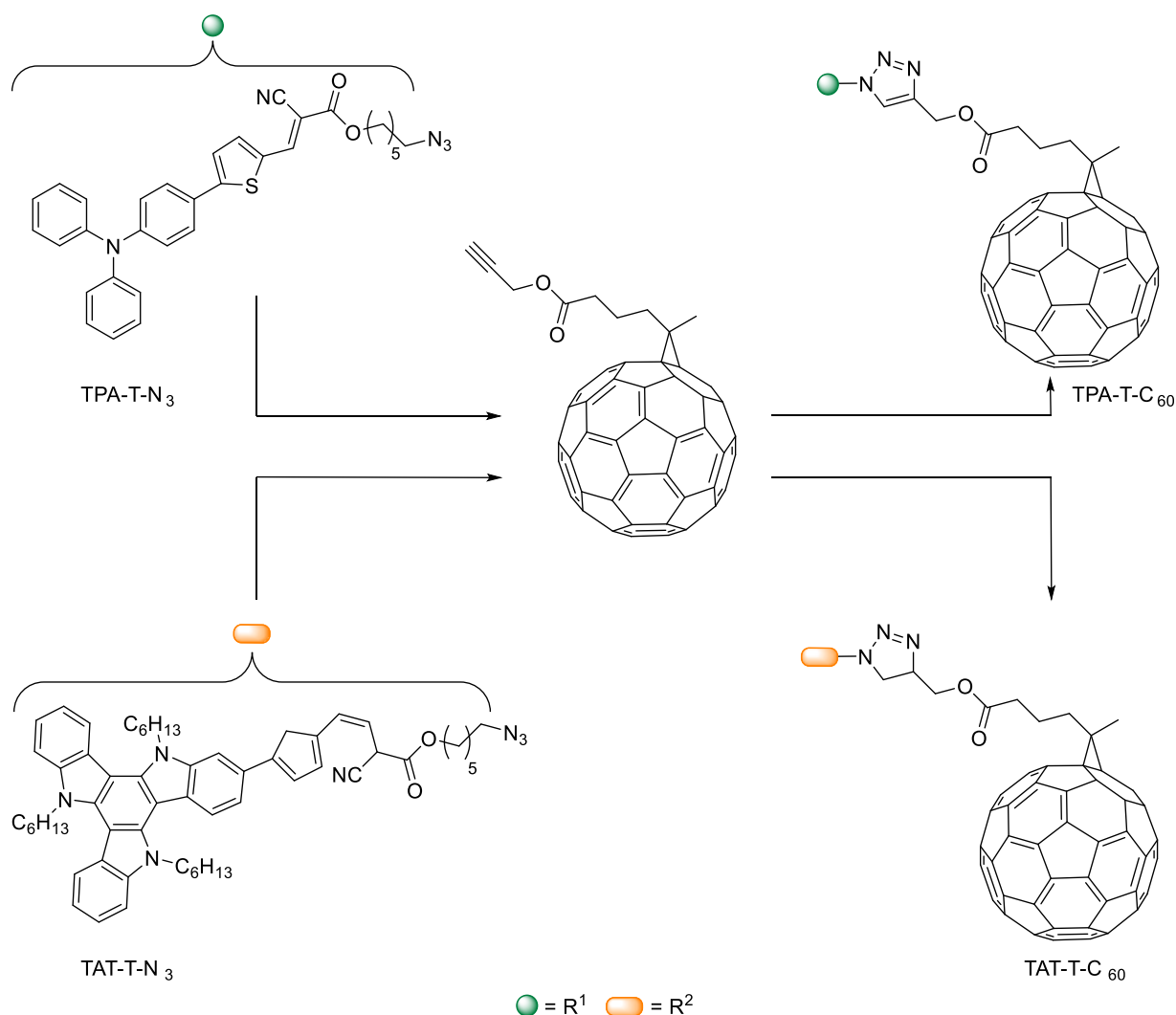
Scheme 7: Modification of C_{60} fullerenes via CuAAC reaction (46–48).

2. Theoretical background

In conclusion, as the most known so called "click" chemistry reaction, the Huisgen 1,3-dipolar cycloaddition offers a broad variety of applications due to the diverse process control. This experience serves to improve the knowledge about other relevant candidates.

2.1.2 Thiol-ene/yne click chemistry

The thiol-ene/yne click reaction is part of the CC multibond addition reactions. The beginning of the classical radical addition of thiols with a wide variety of unsaturated functional groups was the vulcanisation process of natural rubber (poly(*cis*-isoprene)) with elemental sulfur, patented by Charles Goodyear in the mid-19th century (*49*). By the mid 20th century, this reaction was extensively applied for the production of crosslinked networks (*50, 51*)Over the past decades, the effort in expanding the area of applications of the thiol-ene/yne coupling increased due to its various benefits, such as tolerance to many reaction conditions and solvents, clearly defined reaction pathways and products, a variety of commercially available starting materials and high efficiency (*52, 53*). This method has thus been utilised for routine organic syntheses, polymerisations and surface functionalisation reactions leading to –hundreds of publications per year (Figure 2).
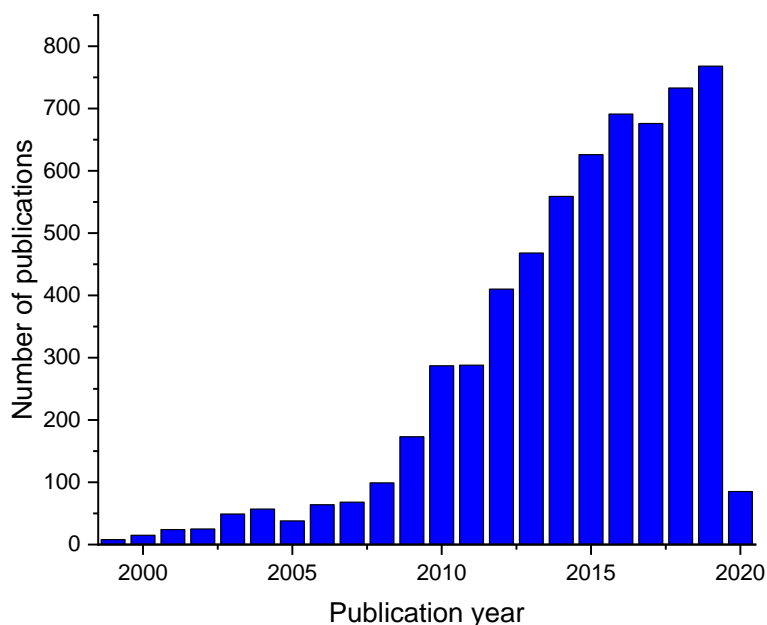
Figure 2: Number of publications with thiol-ene chemistry content. Information was gathered from SciFinder⍉ (accessed on 18.01.2020).

The initiation of a thiol-ene/yne reaction (or hydrothioalation of alkenes) proceeds by abstracting a hydrogen radical from the thiol in the presence of UV-light and/or a radical initiator. The mechanism for the thiol-ene reaction then involves two steps: the thiyl radical addition across the ene functional group and the chain transfer reaction where

2. Theoretical background

a hydrogen is abstracted from another thiol by the carbon-centred radical, thus regenerating a thiyl radical. The addition is reversible for non-terminal double bonds until the free radical intermediate abstracts a hydrogen atom from another thiol. Termination takes place *via* one of three pathways, as shown in Scheme 8. For thiol-ene polymerisations *via* step-growth, full conversion is often limited by mass-transfer at the end of the reaction, which is a process analogous to other step-growth polymerisations.
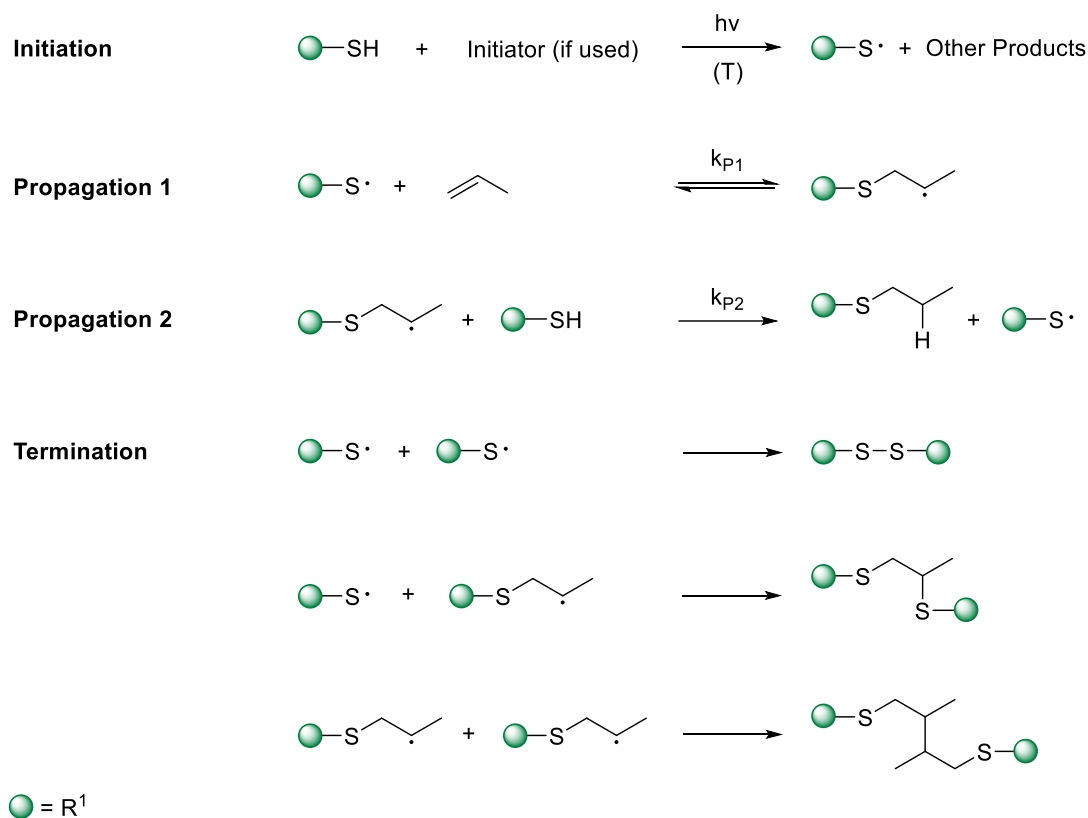
Scheme 8: Mechanism of the radical thiol-ene addition: initiation, propagation 1, propagation 2 and termination *(54)*.

Considering the ideal thiol-ene reaction, homopolymerisation does not occur (no propagation of the carbon centred radical through the ene moiety), and full conversions are obtained. Therefore, the net reaction is simply the addition of the thiol functional group to the ene moiety and thus the molecular weight growth and structure is identical to other step-growth polymerisation reactions, if difunctional enes and thiols are applied. The range of reaction-enthalpy varies between -10.5 kcal/mol for vinyl-ether double bonds and -22.6 kcal/mol for *N*-alkyl maleimides *(55)*.

14

The nature of the alkene functional group, *i.e.* its position and degree of substitution as well as the presence of other functional groups, influences its reactivity. For many years the characterisation of the rate determining step and the exact kinetics was a great challenge. The reaction can be separated into a two-step sequence: the chain-transfer and the propagation (Scheme 9).
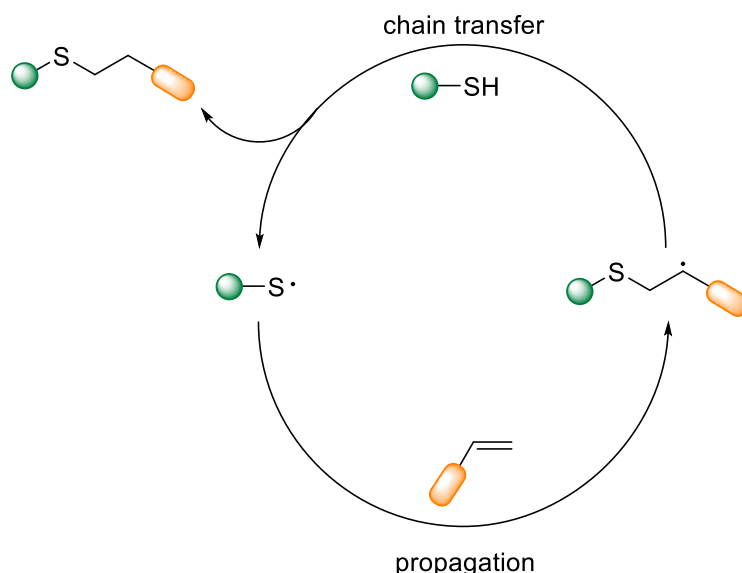
Scheme 9: Simplified reaction mechanism of the thiol-ene "click chemistry" reaction (55).

Presuming the overall rates are equal and the cyclic nature of the reaction mechanism shown above, the influence of an inherently slower reaction step and a lower kinetic constant has been analysed. In the following equations, three possible cases are displayed (*56*):

1) the kinetic constants of the two reactions are approximately equal (Equation 1)
2) chain transfer is the slower reaction step (Equation 2)
3) the thiyl radical propagation is the rate determining step (Equation 3)

$$k_{CT} \cong k_P$$

$$\frac{[R-S*]}{[R-S-C-C*-R']} \approx 1 \; and \; R_P \propto [R-SH]^{\frac{1}{2}} [R'-C=C]^{\frac{1}{2}} \quad \textbf{(1)}$$

$$k_{CT} \ll k_P$$

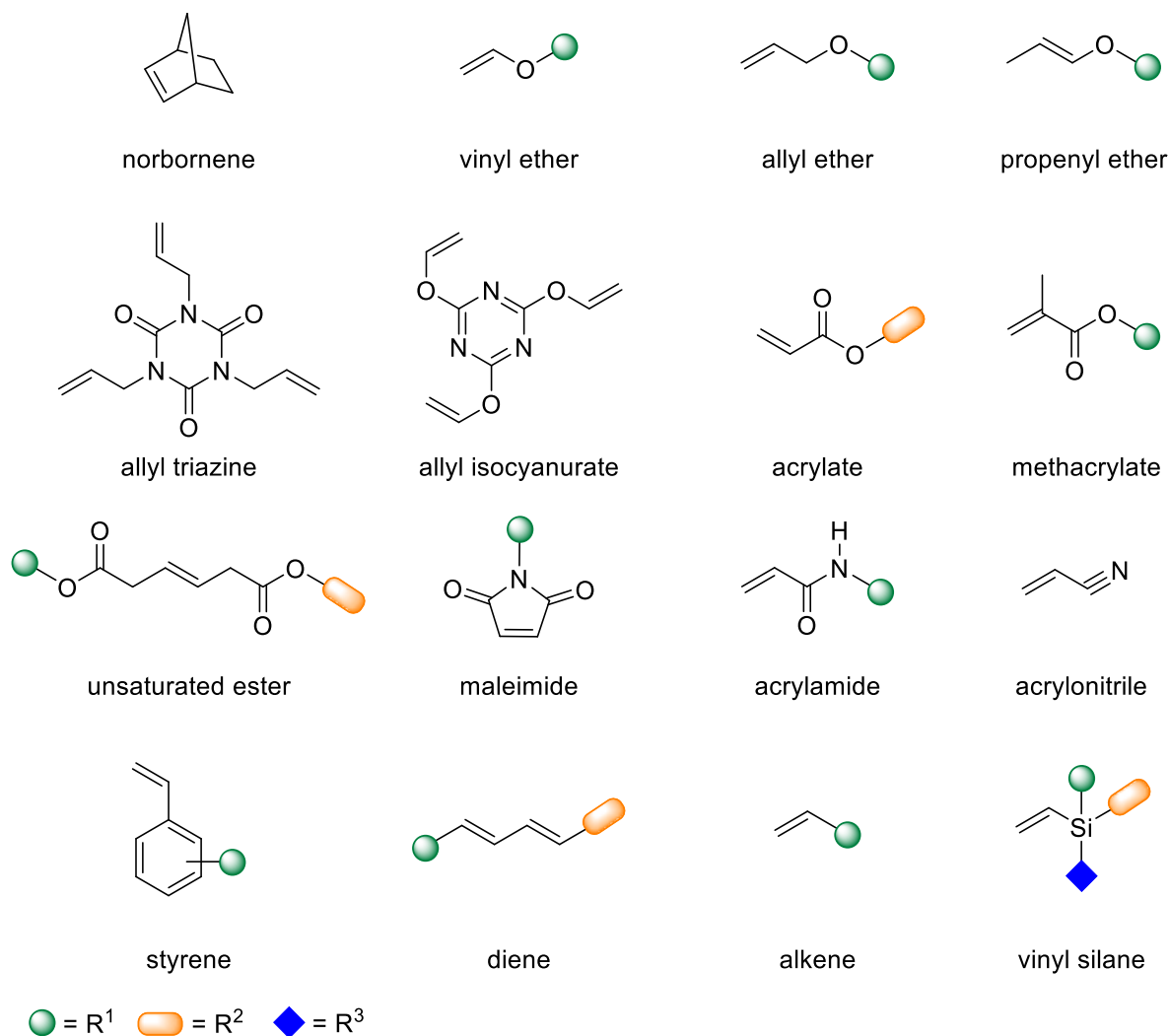$$\frac{[R-S*]}{[R-S-C-C*-R']} \ll 1 \; and \; R_P \propto [R-SH]^1 \quad \textbf{(2)}$$

$$k_{CT} \gg k_P$$

2. Theoretical background

$$\frac{[R-S*]}{[R-S-C-C*-R']} \gg 1 \; and \; R_P \propto [R'-C=C]^1 \qquad \textbf{(3)}$$

K_{CT} is the chain transfer rate constant, k_P is the propagation rate constant, [R-SH] is the thiol concentration, [R`-C=C] is the alkene concentration, [R-S*] is the thiyl radical concentration, [R-S-C-C*-R´] is the carbon-centred radical concentration and R_P the overall reaction rate. In each case, the overall reaction rate is first order in the monomer concentration. Depending on the nature and reactivity of both thiols and alkenes, the reaction rate differs. Less acidic thiols, such as alkyl thiols, have a lower k_{CT}, while more unreactive alkenes cause a reduction of k_P. Northrop and Coffey (*57*) evaluated this effect in a computational study and obtained the following relative order of reactivity for alkenes: (norbornene > vinyl silane > methyl allyl ether > methyl vinyl ether > dimethyl fumarate > propene > maleimide > methyl acrylate > methyl crotonate > styrene > acrylonitrile > butadiene). This was in agreement with the studies of Hoyle, Lee and Roper (*54*). An overview of the mentioned alkenes is given in Scheme 10. The reason behind the exceptionally fast addition of thiols to norbornene is a combination of release of ring strain and the fast, subsequent hydrogen-abstraction from a thiol after the addition of the thiyl radical to the double bond. In the case of methacrylates, styrenes, or conjugated dienes, the lower reactivity can be explained by the formation of stable carbon-centred radicals with inherently low hydrogen-abstraction rate constants. Non-conjugated dienes are more reactive than conjugated dienes because of the absence of resonance stabilisation and thus the delocalisation of electrons at the double bond.

norbornene	vinyl ether	allyl ether	propenyl ether
allyl triazine	allyl isocyanurate	acrylate	methacrylate
unsaturated ester	maleimide	acrylamide	acrylonitrile
styrene	diene	alkene	vinyl silane

⬤ = R^1 ▢ = R^2 ◆ = R^3

*Scheme 10: Possible alkenes for Thiol-Ene click chemistry (54, 57).*

Another important aspect considering the reactivity is the position of the double bond. Model studies concerning the reaction of a 1:1 ratio of three different hexenes with a monofunctional thiol (*58*) showed that 1-hexene is 8 times more reactive than *trans*-2-hexene and 18 times more reactive than *trans*-3-hexene, leading to the conclusion that the thiol-ene-reaction of internal double bonds with thiols is less favoured.

1-hexene	*trans*-2-hexene	*trans*-3-hexene
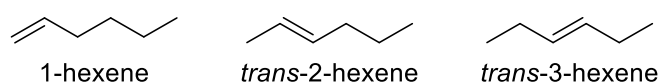
*Scheme 11: Possible position of the double bond in hexene.*

2. Theoretical background

Concerning the thiol structure, three types of multifunctional thiols are mainly used in photoinitiated polymerisations: alkyl thiols, thiol glycolate esters, and thiol propionate esters (Scheme 12). Cole (*59*) reported that thiols based on propionate and glycolate esters show higher reaction rates because of the weakening of the thiol-hydrogen bond by hydrogen-oxygen interaction with the ester carbonyl.

Alkyl 3-mercaptopropionate   Alkylthioglycolate   Alkyl thiol

$\bigcirc = R^1$
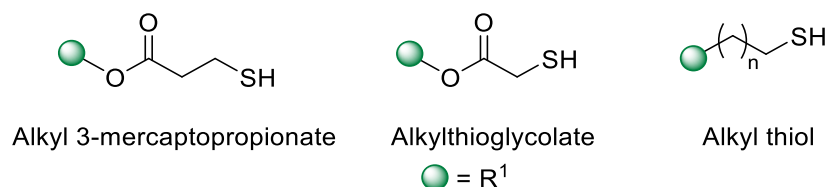
Scheme 12: Examples of multifunctional thiol types (54).

In principle, the thiol-yne radical reaction follows the same first steps of initiation and propagation like the thiol-ene reaction. The first addition to the alkyne is not stereoselective and leads to a mixture of *cis* and *trans* isomers of the anti-Markovnikov product. After that, the vinyl radical with a β-thioether functionality abstracts a hydrogen atom from another thiol molecule.
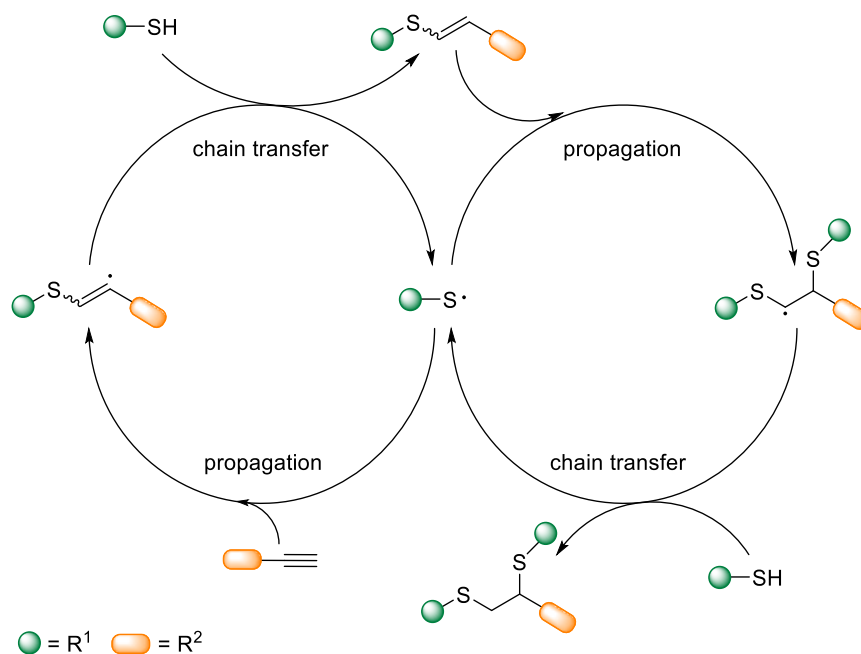


Scheme 13: Reaction mechanism of thiol-yne reaction (38).

The 1,2-dithioether is then formed by addition of the thiol radical to the remaining double bond. In this case, the rate limiting step is the first addition of the thiol to the

alkyne group, whereas the second addition is approximately three times faster but sterically more hindered (*60*). Analogously to the thiol-ene reaction, it has been found that the thiol-yne reaction is slower for internal alkynes than terminal alkynes. Moreover, these reactions are very sensitive to steric crowding.

Encouraged by the easy reaction procedure and high tolerance to other functional groups, the thiol-yne click reaction provides outstanding features for a variety of applications. Rojas *et al.* published the modification of ligno-cellulose *via* photoinduced thiol-yne coupling. The cellulose surface was functionalised with 4-pentynoic acid to introduce the alkyne moiety, followed by investigations on a procedure for the thiol-yne reaction. After that, this procedure was transferred onto nanocellulose films to form spatially resolved micropatterned surfaces with hydrophilic channels and hydrophobic boundaries (*61*). These patterned structures could easily be further functionalised with tin or zinc by evaporation, sputtering, or airbrushing to be used as e.g. paper-based electronics (*62, 63*).

= H, 4-pentynoic acid   = ethylamin, ethanol, acetic acid, $C_9H_4F_{17}$
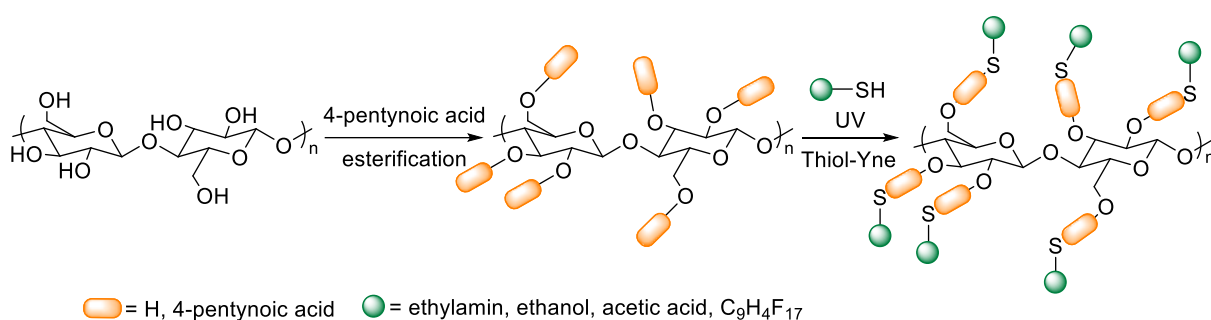
Scheme 14: Thiol-yne modification of ligno-cellulose for spatially resolved micropatterned surfaces (61).

Furthermore, post-modified microporous organic networks (MONs) have been used as separation materials of chiral product mixtures. Yang and co-workers modified the internal triple-bonds of MONs with either 1-thioglycerol, mercaptosuccinic acid or *N*-acetylcysteine. After packing, they compared the performance of their coated capillary columns and commercial columns in a gas chromatograph (GC) with different chiral alcohols, achieving better separations(*64*).
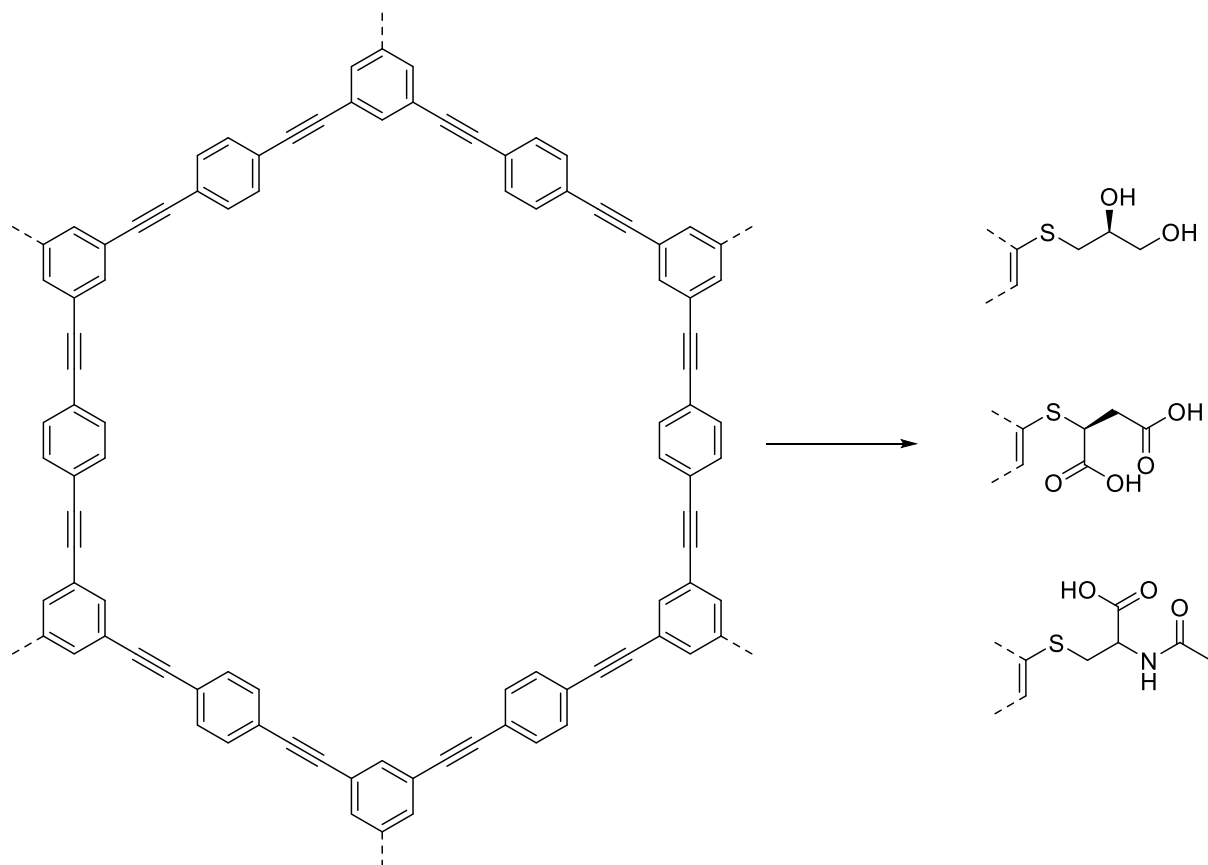
Scheme 15: Modification of MONs with chiral thiols for usage in chiral GC-columns (64).

In conclusion, thiol-ene/yne "click chemistry" is a versatile reaction type adoptable to lots of applications such as in biomedicine, electrochemistry *etc.* due to its easy processability.

2.1.3 Amino-yne click chemistry

The hydroamination of primary or secondary amines to form carbon-nitrogen multibonds is well known since the beginning of the 20th century (*65, 66*). In Scheme 16 the hydroamination products of alkenes, alkynes, dienes and allenes are shown. A variety of different metal catalysts have been investigated for an efficient and selective transformation. Those approaches include alkali metals, acid catalysts, early transition metals (group IV), late transition metals and organo-f-element metal complexes (actinides and lanthanides) (*67*).
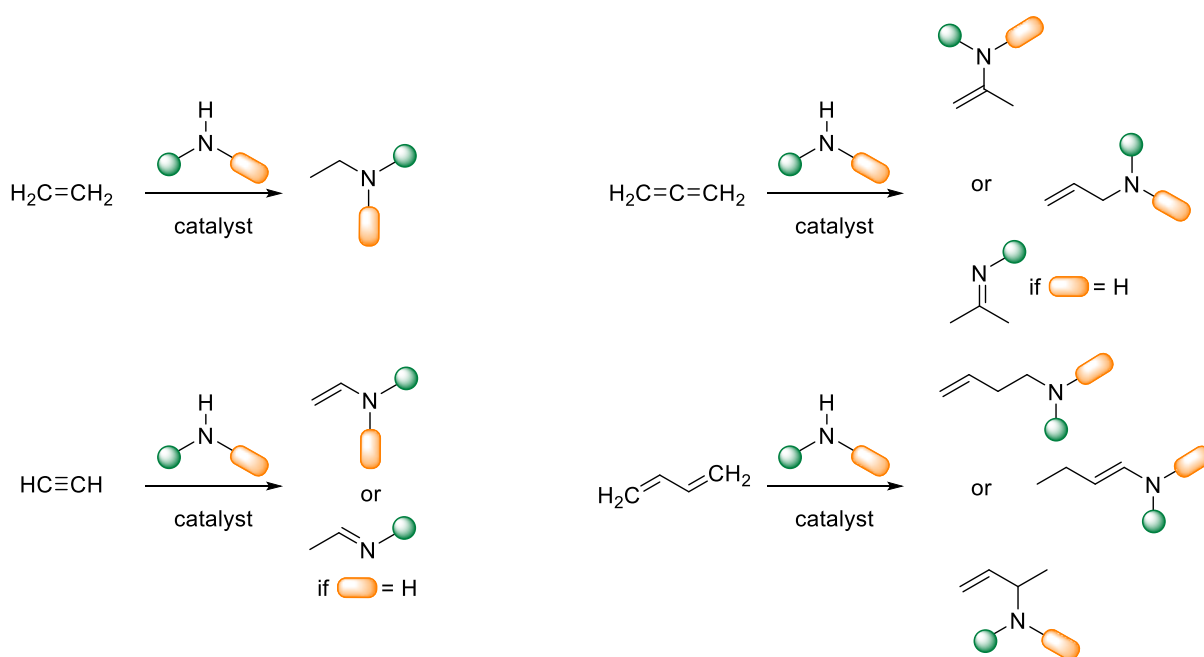

Scheme 16: General overview of the hydroamination of carbon-carbon multibonds by primary or secondary amines (68).

In the middle of the 20th century, Truce and Brady analysed the stereochemistry of the hydroamination reaction. Therefore, various amines and activated alkynes (sulfone- and carboxylic esters) were used *(69)*. In principle, the addition follows the same mechanism as the Thia-Michael reaction and results in four different products: *Z*-Markovnikov and *E*-Markovnikov as well as anti-Markovnikov products. Yet, only anti-Markovnikov products were observed (Scheme 17). Additionally, depending on the activation, *trans*- or *cis*-addition is favoured. For sulfones, most of the products are cis conformers but convert to trans conformers over time, being the thermodynamically more stable configuration.(*65*). Furthermore, Tang and co-workers employed density

2. Theoretical background

functional theory (DFT) calculations to analyse the reaction mechanism for the model system of methyl propiolate and diethylamine in detail (Scheme 18) (*70*).

1,3 proton shift
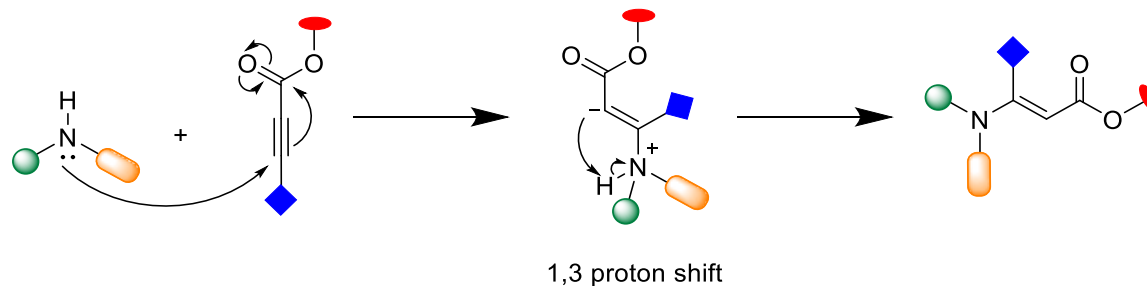
Scheme 17: General reaction mechanism of the amino-yne click reaction (65).

As shown, the two elementary reaction steps are the nucleophilic addition and the proton transfer, enabling two transformation pathways between zwitterionic and stable intermediates. The nucleophilic attack forms the transition states (TS) for *E* (E-TS-1) and *Z* (Z-TS-1) conformation of the zwitterionic precursors (TS1) exhibiting weak selectivity of low differences in Gibbs free energy barrier and the intermediates. After the attack of the nucleophile, the proton transfer takes place including the inter- and intramolecular pathway. As for the *E* intermediate, a four membered ring with a Gibbs energy barrier of 26.1 kcal/mol is calculated, whereas the intramolecular proton transfer of the *Z*-intermediate is sterically hindered because of the ester group. Considering the Gibbs energy of the *E* and *Z* products, the *E* configuration should be the dominant isomeric product (thermodynamically more stable). In fact, both configurations were observed, but transformed over a few hours fully to the *E* product by nitrogen-activated double bond rotation (TS2) although the Gibbs energy barrier of 34.3 kcal/mol exceeds the energy barrier of the additions.

ΔG (Kcal/mol)
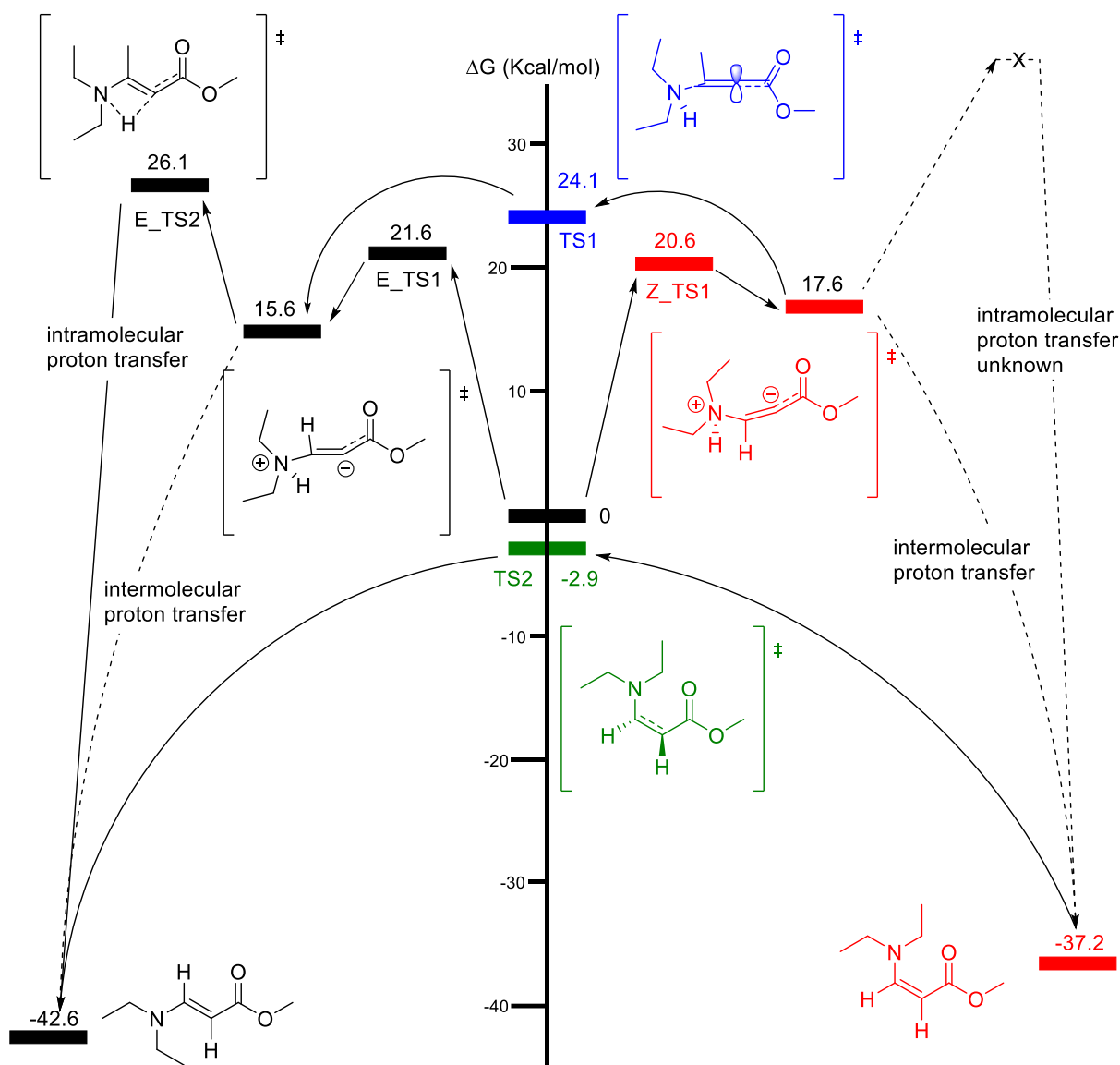
Scheme 18: Density functional theory calculation on the reaction of diethylamine and methyl propiolate (70).

With the growing application of click chemistry as an easy approach for defined polymers, Hong *et al.,* for example, combined the Thia-Michael and amino-yne click reaction resulting in a broad variety of multifunctional polymers (*71*). Moreover, amino-yne click reactions can be used to synthesise injectable hydrogels providing a non-catalytic pathway. Therefore, Jiang and Huang modified commercially available and water soluble carboxymethyl chitosan (CMC) with polyethylene glycol dipropiolate esters. The resulting gels were non-toxic, showed favourable gel formation with promising biomedical applications (*72*).
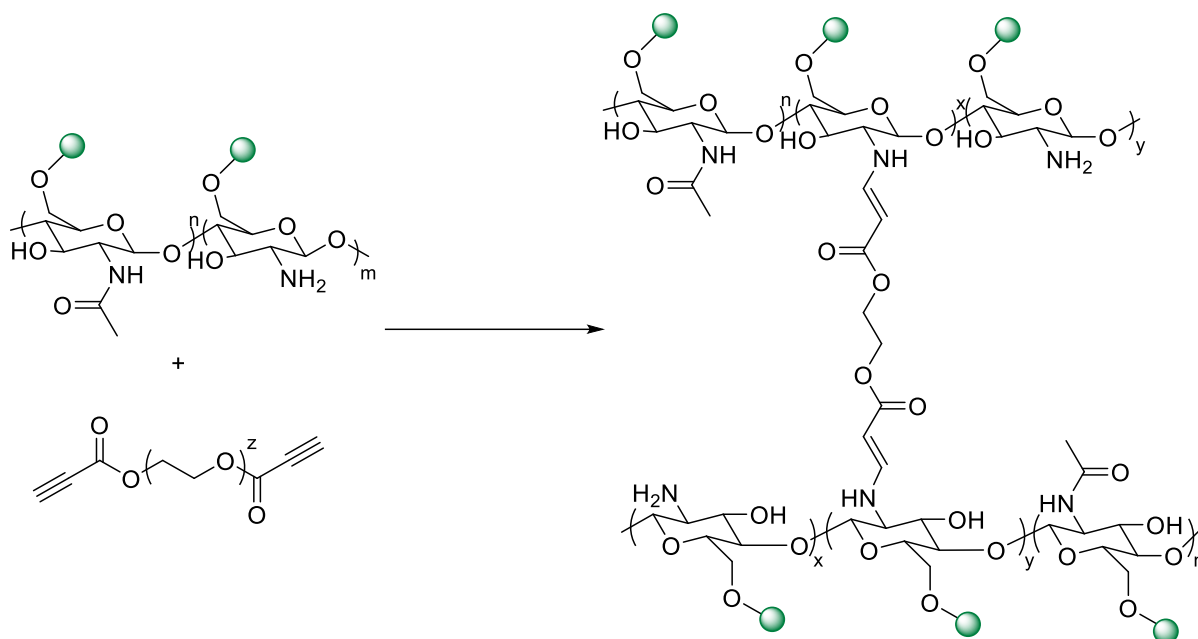
Scheme 19: Crosslinking of carboxymethyl chitosan by hydroamination with polyethyleneglycol dipropiolate esters (72).

As shown in this chapter, the uncatalysed hydroamination reaction (or amino-yne "click" reaction) offers favourable characteristics, such as high atom efficiency and high conversion combined with selective product formation. This defines it as worthy member of the "click chemistry" family, usable in a variety of application such as polymerisation, gel formation or selective functionalisation.

2.2 Reticular Chemistry

The study of discrete chemical entities, such as molecules and clusters, linked by strong bonds generating extended structures like metal organic frameworks (MOF), covalent-organic frameworks (COF), and porous-organic polymers (POP) is referred to as reticular chemistry. Moreover, many highly porous 3D inorganic materials, such as zeolites (Greek for "boiling stone") consisting of hydrated aluminosilicates have instigated the research into organic/inorganic hybrid materials with similar properties. Modern metal-organic chemistry originates from coordination chemistry discovered centuries ago: Prussian blue ($Fe_4^{3+}[Fe^{2+}(CN)_6]\cdot6H_2O$) is a pigment, which is the first reported coordination compound and was discovered by accident by the German colour maker Johann J. Diesbach in 1704 (*73*). A conceptional foundation of modern coordination chemistry was laid by Alfred Werner, disproving August F. Kekulé's assumption of one fixed coordination number for one specific element (*74, 75*). Thus, the coordination of ammonia in $CoCl_3\cdot nNH_3$ is not a linear chain and a fixed coordination number of three of the metal centre, but spatially distributed around the Co^{3+} metal ion in an octahedral manner (*76*). Werner's work served as inspiration to expand the coordination chemistry from 1D to higher, more demanding dimensions. An early example was the synthesis of $Ni(CN)_3(\eta^6\text{-}C_6H_6)$ published by Karl A. Hofmann in 1897 (*77*). The first structural recommendation was a molecular assembly. However, X-ray diffraction analysis revealed a structure built from alternating layers of octahedral and square planar Ni^{2+} ions linked by CN-ions and being separated by benzene guests.

2.2.1 Metal organic frameworks (MOF)

Modern metal-organic frameworks consist of so-called secondary building units (SBU) and stiff organic linker molecules. Originally used to classify and describe the structural chemistry of Zeolites in a simple manner, MOF chemistry adopted this principle. SBUs are formed by chelation of multiple metal ions to polynuclear clusters, envisioned as nodes, to replace the single metal-ion nodes. Its main advantage is the higher rigidity accompanied by directionality (Figure 3).
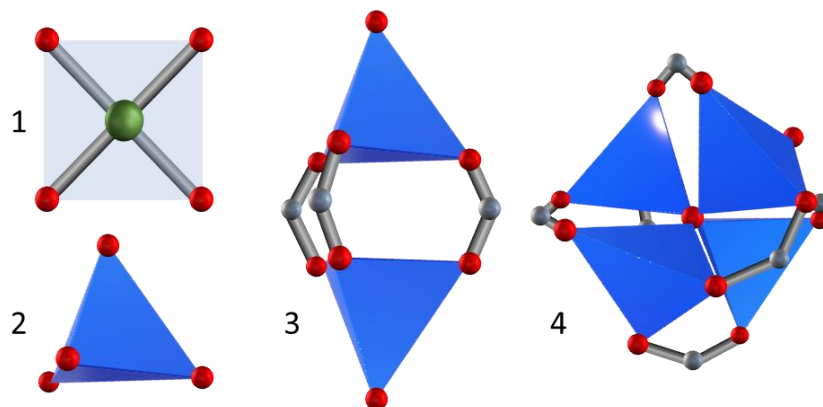
2. Theoretical background

Figure 3: Tetratopic metal-centres (quadratic planar 1, tetrahedral 2) and two possible secondary building units.

Until 1990, neutral linkers such as bipyridines and nitriles were used. Unfortunately, these MOFs were unstable in the presence of water and difficult to process. To further enhance the stability of metal organic frameworks, linkers with charged functional groups, such as carboxylates, phosphates, pyrazolates, tetrazolates, catecholates, and imidazolates, are used today. Since carboxylates are the most prominent ones, this thesis focuses on explaining them. Generally, increasing bond energy between two molecules or metals and organic linkers enhances the stability of the formed network, but may also reduce the crystallinity (reversibility of bonds). In the following, interactions/bonds are listed by increasing bond energy: van der Waals forces < hydrogen bond < M-donor bonds < M-charged linker bonds < covalent bonds (*78*). Carboxylate linkers, in particular, offer various positive features:

- charged linkers neutralise positive charges at the metal nodes, leading to neutral frameworks without interfering counter-ions
- more rigidity and directionality
- formation of secondary building units with a fixed overall coordination geometry and connectivity is favoured
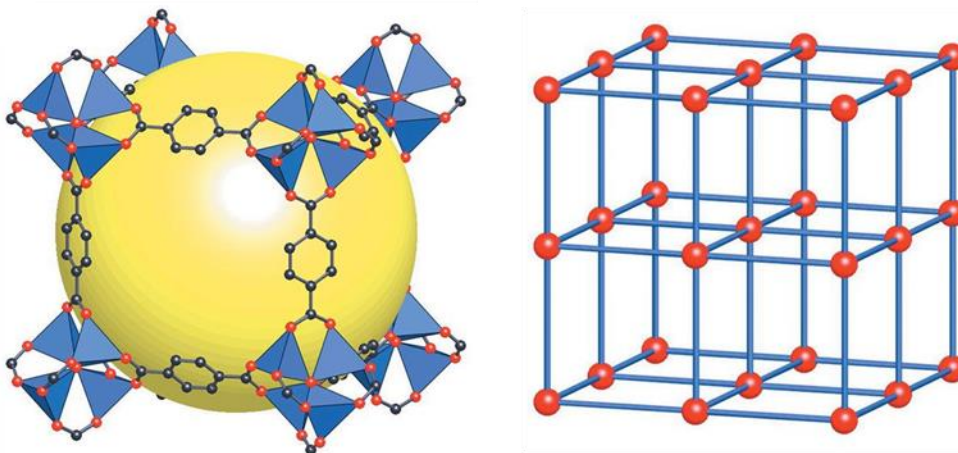- high thermal, mechanical, and chemical stability

Figure 4:: General structure of MOF-5 with Zn_4O nodes and terephthalic acid linker and simplified cubic structure. Reprinted with permission from Springer Nature (78).

One well known example of a MOF combining all these features is MOF-5 (Figure 4) (*78, 79*). The general formula is $Zn_4O(BDC)_3$, whereby the SBU is formed by four Zn^{2+} ions surrounding one oxygen in a tetrahedral manner, leading to an octahedral node connected by terephthalic acid as linker. To further ensure the stability, linkers are in general highly symmetric and consist of rigid, unsaturated hydrocarbon fragments. Additionally, many possible combinations of multifunctional linkers and SBUs are possible, leading to virtually limitless frameworks. Since organic chemistry is based on carbon, basic geometries include two, three, four, six, eight or twelve points of extension, which are also described by the term topicity (ditopic, tritopic, etc.). Nonetheless, there are many possible arrangements for e.g. tetratopic linkers: classical cubic, rectangular and tetrahedral geometry, but also linear geometries with two functional groups at each side. These linkers are commonly accessible through carbon-carbon, carbon-heteroatom and heteroatom-heteroatom couplings, such as the well-known cross-coupling reactions (Suzuki, Sonogashira, Heck, etc.). Therefore, the linkers are divided into the following:

- core unit defining the geometry of the backbone
- functional groups also called "binding groups" for the SBUs
- extending units responsible for the size of the linker

Figure 5 shows an excerpt of possible core units, extending units and the aforementioned functional groups.
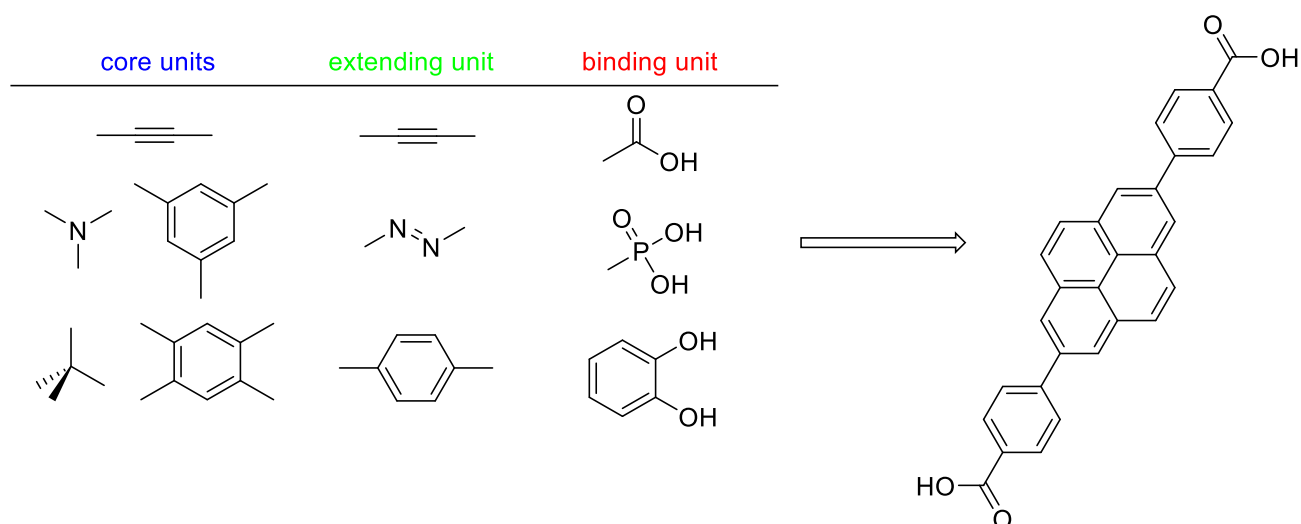
2. Theoretical background

Figure 5: Typical building units of a linker: the core, extending, and binding unit (80, 78).

In general, core units mostly determine the geometrical information (e.g. tetraphenylmethane imparts a tetrahedral symmetry). If linear extending units, such as alkynes or 1,4-substituted phenyls, are used, the geometry and connectivity are not influenced. By using angled or offset extending units, only the geometry is changed, whereas branched units alter both geometry and connectivity. Therefore, it is important to define the number of extension points and their shapes. As previously mentioned, ditopic linkers may be perfectly linear (1,4-substituted phenyls e.g. terephthalic acid H_2BDC), bent (1,3-substituted phenyls e.g. *m*-H_2BDC) or have an offset (double bonds e.g. (*E*) 4,4'-(ethene-1,2-diyl)dibenzoic acid, H_2EDBA). Tritopic linkers can either be equilateral or unsymmetric. The smallest core unit with 3 expansion points is 1,3,5-benzenetricarboxylic acid (trimesic acid, H_3BTC) and is often modified with additional aryl extending units, forming longer linkers such as H_3BBC, 4,4',4''-(benzene-1,3,5-triyltris(benzene-4,1-diyl))tribenzoate. Tetratopic linkers can be grouped in three shapes: tetrahedral, square/rectangular, and irregular (offset, bent). Often, planar tetratopic linkers are based on porphyrin units, tetrahedral on sp³ hybridized carbon or silicon and rectangular structures on biphenyl or pyrene cores. Higher topicities share the same cores as tri- or tetratopic structures but use isophtalic - instead of benzoic - acid groups. All these parameters (SBU, linker and the corresponding geometry) influence the porosity of these 3D networks and lead to the desired "permanent porosity" (stable under pressure, elevated temperatures, humidity, etc.). Porosity is defined as the ratio of the total pore volume compared to the occupied volume of the MOF and include following parameters; the specific pore volume (eq. 4), specific surface area (eq. 5), porosity (eq. 6) and pore size as well as their size distribution.

$$Specific\ pore\ volume\ \left[\frac{cm^3}{g}\right] = \frac{total\ pore\ volume\ (cm^3)}{mass\ of\ the\ porous\ solid\ (g)} \qquad (4)$$

$$Specific\ surface\ area\ \left[\frac{m^2}{g}\right] = \frac{total\ surface\ area\ (m^2)}{mass\ of\ the\ porous\ solid\ (g)} \qquad (5)$$

$$Porosity\ (\%) = \frac{volume\ of\ the\ pores}{volume\ of\ the\ solid} \cdot 100\% \quad (6)$$

According to the International Union of Pure and Applied Chemistry (IUPAC), pore sizes are grouped into micropores (< 2 nm: MOFs, COFs, ZIFs, Zeolites, activated carbon), mesopores (2 – 50 nm: MOFs, COFs, ZIFs, mesoporous silica, activated carbon) and macropores (> 50 nm: MOFs, COFs, ZIFs, sintered metals and ceramics) (*81*). The porosity can be influenced directly by the pore size and geometry. Enhancing the pore size by altering the metrics and functionality without changing its underlying topology leads to isoreticular metal organic frameworks (IRMOFs). This can be achieved by simple elongation and/or functionalisation of the linkers because of *a priori* knowledge of the synthetic conditions.
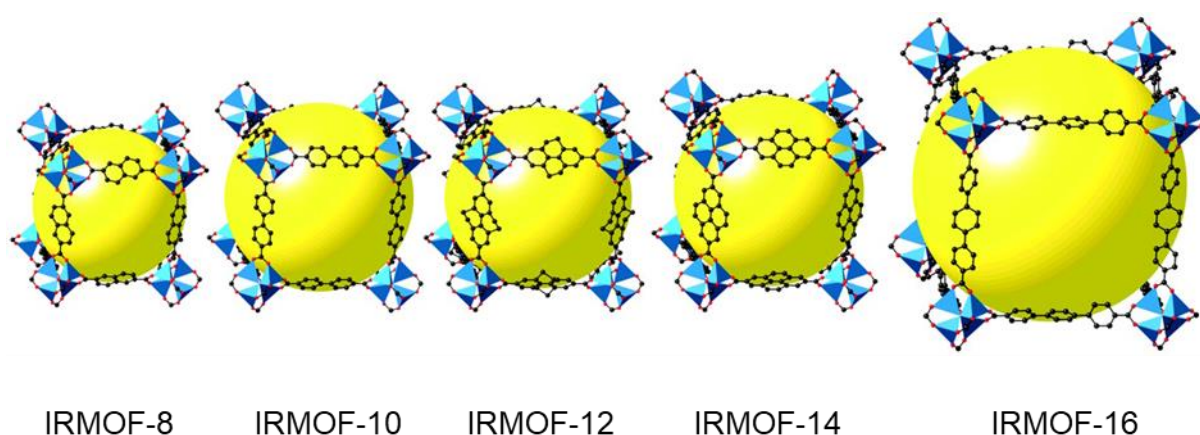

| IRMOF-8 | IRMOF-10 | IRMOF-12 | IRMOF-14 | IRMOF-16 |

Figure 6: Influence of the linker on the pore size of the MOF displayed by the isoreticular metal organic frameworks IRMOF-8, IRMOF-10, IRMOF-12, IRMOF-14 and IRMOF-16 (79). Permitted by The American Association for the Advancement of Science (Licence Nr.: 4762500844169)

MOF-5 is herein chosen as an example to illustrate the IRMOF strategy. It is also defined as IRMOF-1 because many isoreticular MOFs have been synthesized based on this topology (**pcu** = primitive cubic) by replacing the linker with a variety of other ditopic carboxylate linkers (Figure 6) (*79*). This way, pore sizes up to 28.8 Å in IRMOF-16 have been achieved. One drawback accompanying the isoreticular pore size growth is the increasing possibility of interpenetrations, like in IRMOF-9,

2. Theoretical background

IRMOF-11, IRMOF-13, IRMOF-15 (*79, 82*). Changing the topology of the networks, higher dilution in synthetic procedures and spatially more demanding linkers suppress the formation of interpenetrated systems (*83*) These few examples represent only a glimpse on the possible geometries and topologies of networks and the already achieved surface areas of over 10,000 m^2/g (*84–86*).

To better define these structures, a nomenclature of three letters was introduced by Yaghi and O'Keeffe, which are compiled in the reticular chemistry structure resource (RCSR) database http://rcsr.anu.edu.au/ (*87*). These letters often represent naturally occurring minerals (**dia** = diamond, **qtc** = quartz, **pcu** = primitive cubic, etc.) (*88*).

Solvent exchanged sample:
- same solvent as in synthesis
- starting material and side products removed from solvent but still in pores

As synthesized sample:
starting material and side products in solvent and pores

synthesis of metal organic framework

first solvent exchange

multiple cycles of solvent exchange

activation by dynamic vacuum and CO_2

solvent exchange (low boiling point)

Preactivated sample:-
- solvent with lower boiling point
- no starting materials and side products

Fully solvent exchanged sample:
- same solvent as in synthesis
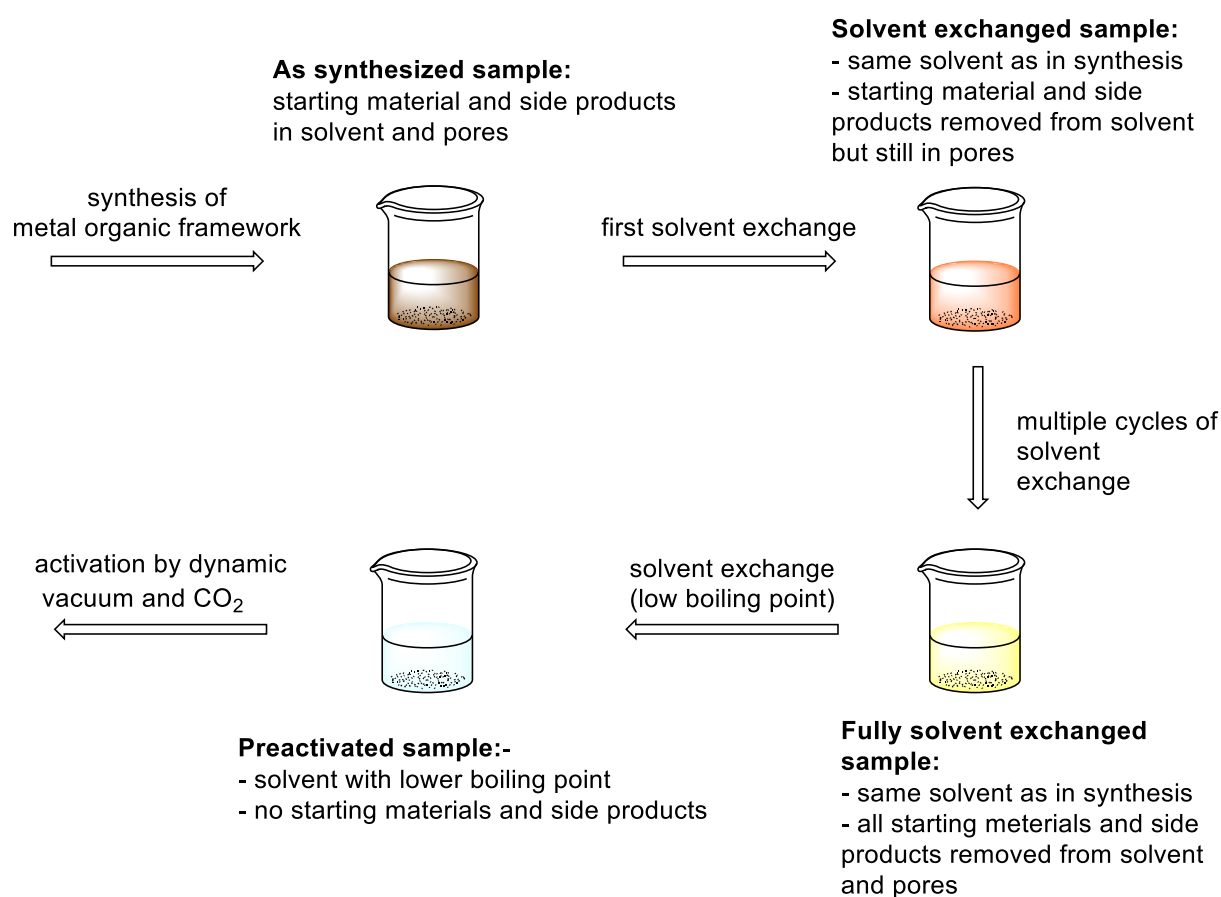- all starting meterials and side products removed from solvent and pores

Figure 7: General work-up of MOFs (79, 89).

To release the full potential of a synthesized MOF, it has to be activated. Therefore, multiple cycles of solvent exchange steps and subsequent application of dynamic vacuum are performed to remove guest molecules, such as unreacted or decomposed starting materials (Figure 7) (*89*). Initially, the solvent with the remaining starting materials and side products of the freshly synthesized metal organic framework are

removed (Figure 7 ,first solvent exchange). Then, multiple washing cycles with the same solvent as the one used in the synthesis are performed to get rid of all contamination inside the pores. To allow a better processing of the clean MOF in the vacuum, the solvent is exchanged to one with lower boiling point. To further reduce the stress by the capillary effects on the framework itself, supercritical CO_2 is used to fully eliminate remaining solvent and activate it (*89*).

Accompanied by this high flexibility in synthesis and the resulting tremendous surface areas, MOFs are well suited for many applications such as gas storage, catalysis, or electron conductivity. Through thoroughly planned synthesis of manufactured linkers, the properties can be fine-tuned for each application (*90, 91*). This topic will further be discussed in chapter **2.3.3**.

2.2.2 Porous organic frameworks (POF)

In general, organic networks are referred to as porous organic frameworks (POFs). This field can be divided into amorphous organic frameworks and crystalline organic frameworks. Examples for amorphous organic frameworks are covalent triazine networks (CTFs) and porous aromatic frameworks (PAFs). Crystalline organic frameworks (COFs) consist of periodic networks, making them the non-metal containing analogues of metal organic frameworks. Other than ion-metal or donor-metal interactions, covalent organic frameworks are based on reversible covalent bonds, such as boron-oxygen or carbon-nitrogen bonds.

One of the first representatives of porous organic frameworks (POFs) were the hyper crosslinked polymers (HCPs, (*92, 93*)), first published over 40 years ago. 20 years ago, chemists and material scientists still believed that porous organic frameworks should be amorphous (POPs) and not crystalline. In parallel, McKeown and Budd explored another type of the POF family, the polymers of intrinsic microporosity (PIM) (*94–96*). Modern COF synthesis highly depends on reversible, covalent bond forming reactions referred to as dynamic covalent chemistry. These reactions are commonly thermodynamically and not kinetically controlled. Therefore, dynamic covalent chemistry implicates "error checking" or "proof-reading" to finally lead to the more stable and more defined product. Scheme 20 shows examples of the dynamic chemical reactions such as boroxine (B_3O_3) ring formations, boronate-ester ring formations, $ZnCl_2$ mediated nitrile cyclotrimerization, imine reaction and hydrazone reaction.
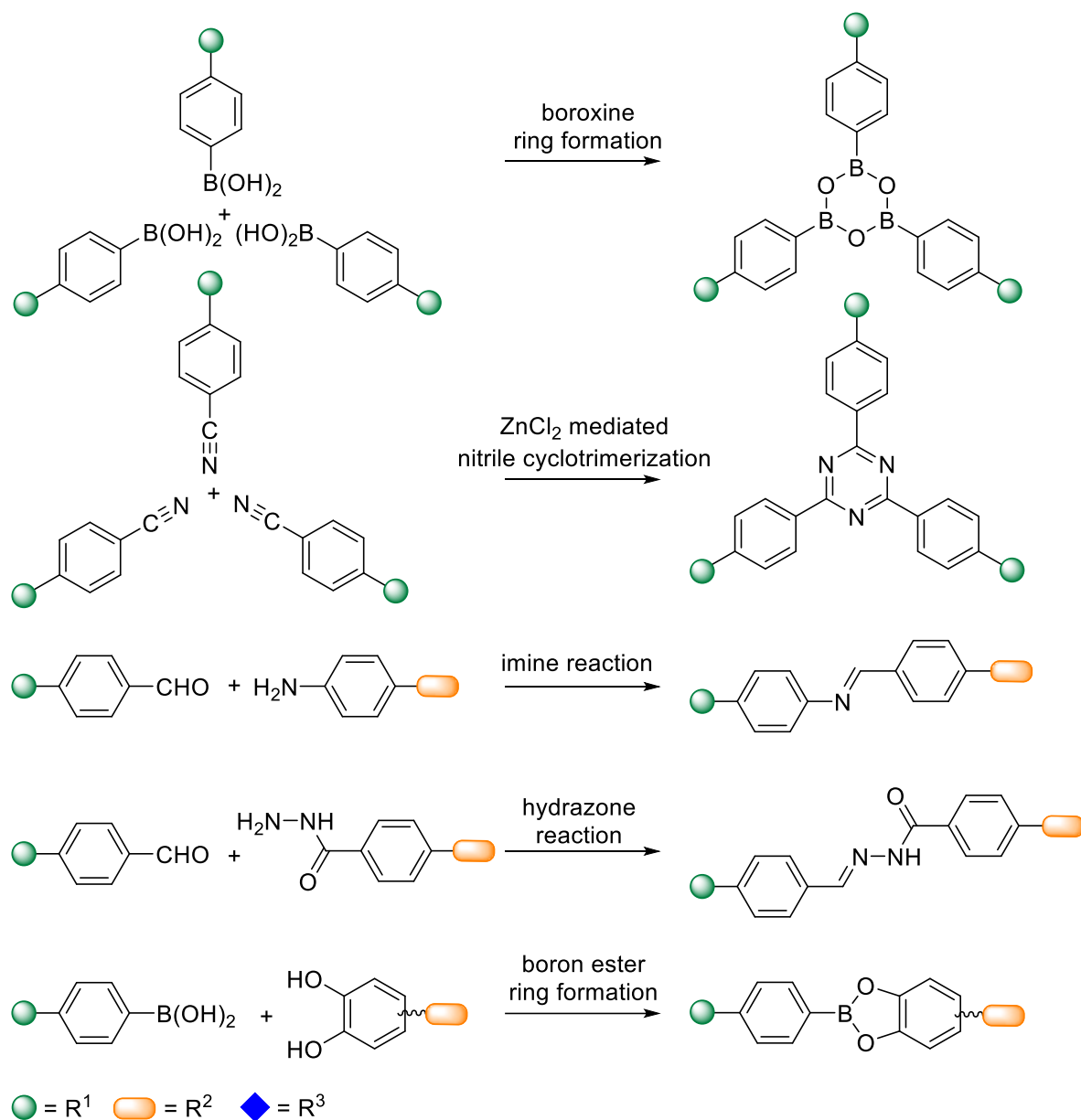
Scheme 20: Possible reversible reaction pathways for the synthesis of covalent organic frameworks (97, 98).

COF-1 and COF-5 were the first synthesized COFs by Yaghi and co-workers in 2005 (*99*). The topology is adopted from MOF synthesis of secondary building units and linkers, but replacing the metal complexes by organic pendants of the same geometry (Scheme 21) (*100*).

2. Theoretical background
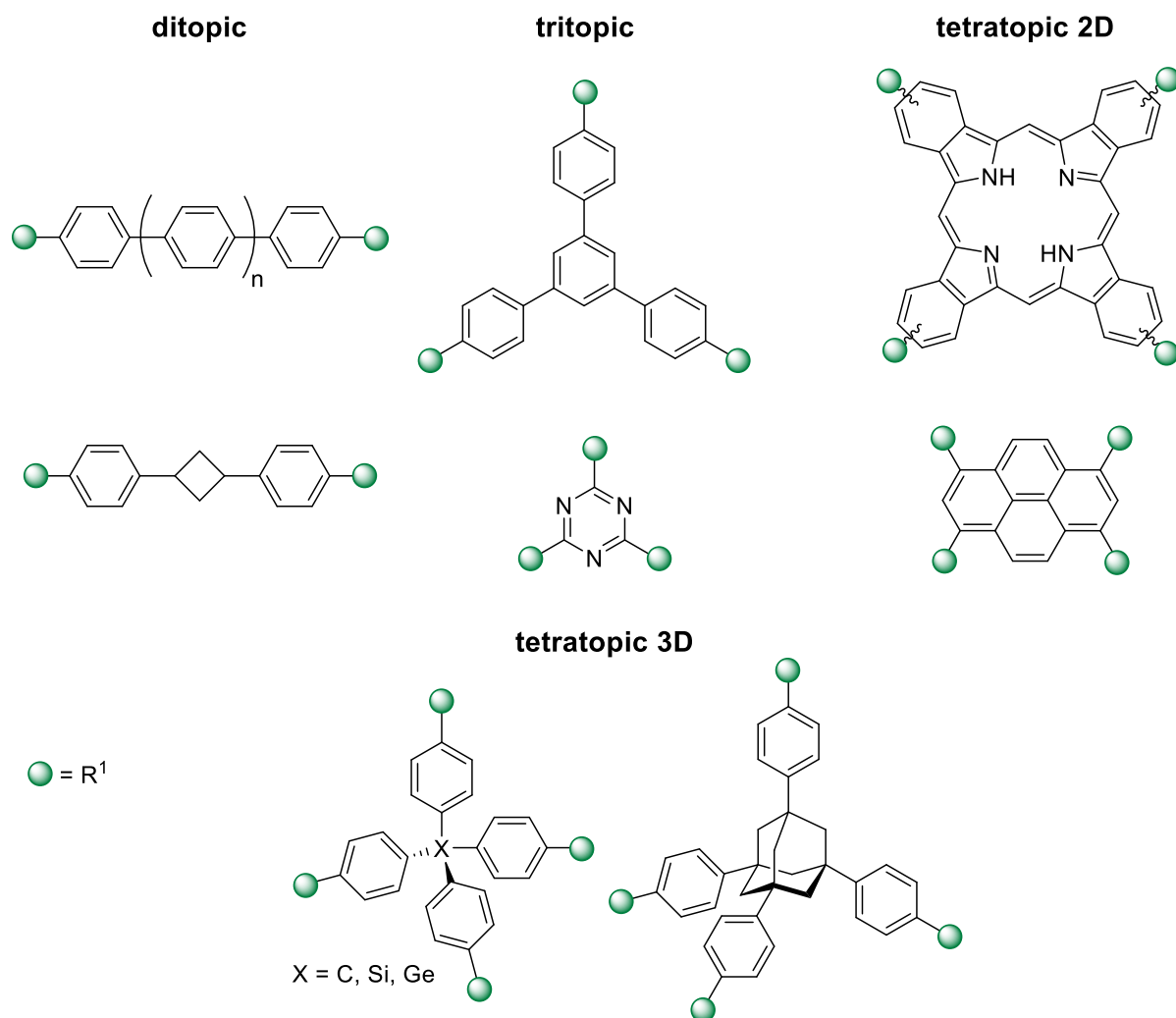
Scheme 21: Overview of various di-, tri- and tetratopic building blocks for POF synthesis (100).

In the beginning of COF synthesis, the intended design was not reported. To reduce the resulting high error rate in synthesis, a facile and rational strategy was necessary. In principle, two pathways exist: the bottom-up and the top-down approach. COF-105 is used as example to explain both (Figure 8). In the case of the bottom-up method, a suitable building block is first chosen for a tetrahedral node and with computational help, the geometry (here: **ctn**) can be predicted. The top-down pathway starts from the opposite perspective. By computational studies and consulting the database of Yaghi and O'Keeffe (http://rcsr.anu.edu.au/ (*87*)), the underlying topologies (here: **ctn**) can be determined and subsequently the suitable monomers be chosen (tetrahedron).
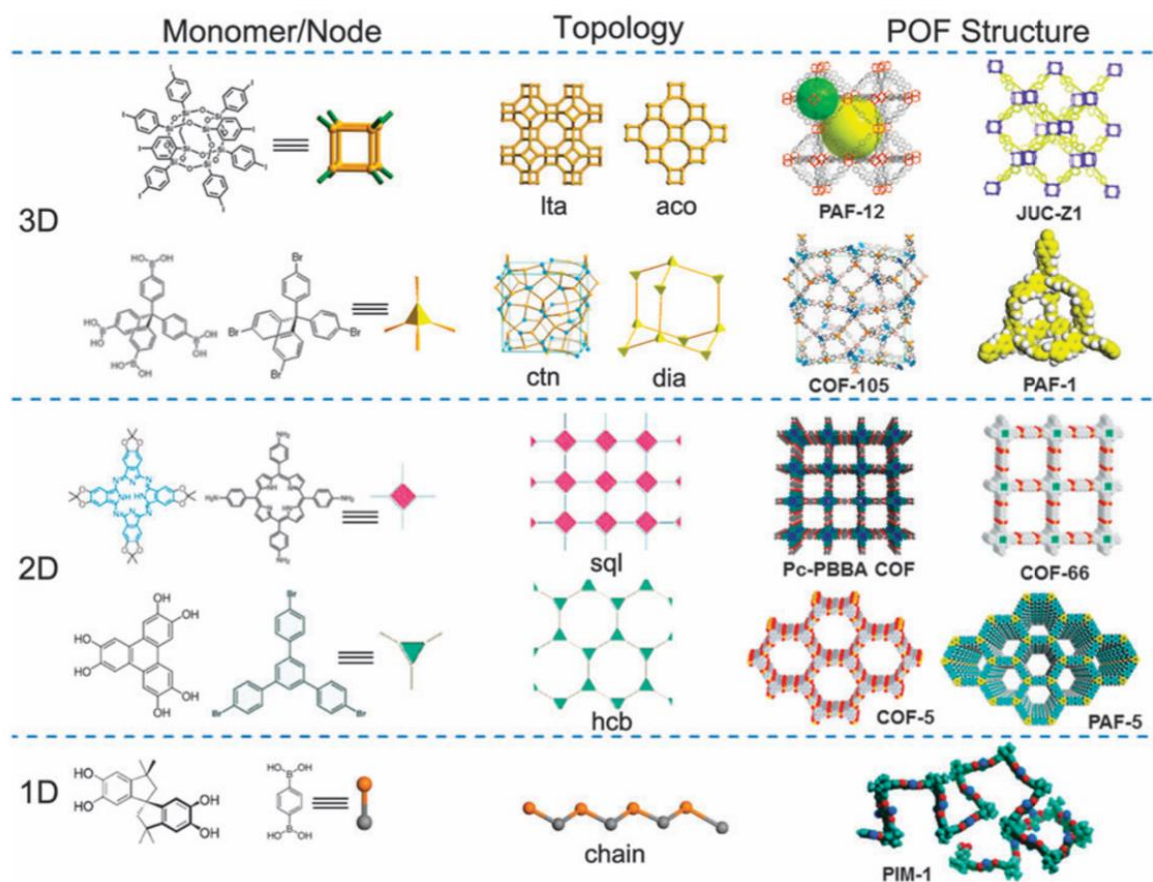
Figure 8: Overview of monomers/nodes and the corresponding topology and POF structure. Reproduced from reference (101) with permission from The Royal Society of Chemistry

Furthermore, it is important that the building blocks are rigid, and the bond formation direction is discrete to obtain ordered and porous POFs. Generally, to afford 2D COFs, 2D block are fundamental and are mostly formed by combination of 2D-ditopic + 2D-tritopic, 2D-tritopic + 2D-tritopic and 2D-ditopic + 2D-tetratopic building blocks. To obtain 3D-COFs, combinations of 3D-tetratopic + 3D-tetratopic, 3D-tetratopic + 2D-ditopic or 3D-tetratopic + 2D-tritopic are possible (Scheme 21). Like in MOFs, the surface area and the pore size can be influenced by the geometry and length of linkers and nodes. If the linkers are not sufficiently rigid, the pores will collapse reducing the total pore volume and lead in most cases to amorphous networks (*102, 103*). In principle, there is almost no restriction to the type of chemistry and geometrical structures used and the active groups can be easily varied. To date, many different reactions have been performed synthesizing amorphous POFs, including cross-coupling reactions like Sonogashira (*104*) and Suzuki (*105*), trimerisation reactions of aromatic nitrile compounds (*106*), Friedel-Crafts reactions (*107*), Cu(I)-

catalysed Huisgen azide-alkyne click reaction (*108*), etc.. As previously mentioned, amorphous porous organic frameworks can be divided in different categories such as PIMs (*94–96*), HCPs (*92, 93*), POPs (*109*), etc. Unfortunately, when changing to new coupling reactions, most of the previously achieved knowledge for the best conditions is invalid. An example about the extent of variables is given by the copolymerisation of 1,3,5-triethynylbenzene with 2,5-dibromobenzene via Sonogashira cross-coupling. When changing the solvent from THF to either DMF, 1,4-dioxane or toluene, the respective surface areas obtained vary from 847 m^2/g to 1043 m^2/g, 778 m^2/g, and 761 m^2/g, respectively (*110*). Similarly, by increasing the temperature from 400 to 500, 600 and 700 °C in the cyclisation reaction of 1,4-dicyanobenzene, the respective surface areas increased from 920 m^2/g to 1600 m^2/g, 1750 m^2/g, and 2530 m^2/g (*111*). Furthermore, the catalyst loading is very important for the performance of a reaction. Zhu and co-workers evaluated the influence of $ZnCl_2$ as catalyst for the nitrile cyclomerisation reaction of tetrakis(4-cyanophenyl)silica (TCPSi) with 1, 5, and, 10 mol equivalents. The resulting POPs were analysed by N_2 sorption and showed an immense increase of surface area from 190 m^2/g (1 eq.) to 979 m^2/g (5 eq.) and even 1166 m^2/g (10 eq.) (*112*).

2.2.3 Post-modification of metal/porous organic frameworks

To further optimize the networks for their intended applications, organic linkers/monomers have been rationally designed and prepared to satisfy the proposed requirements owing to synthetic features of organic chemistry. Therefore, special functional groups, which do not interfere with the framework building reaction, are introduced. As a result, porous networks with reactive sites are obtained enabling the change of porosity and functionality by synthetic post-modification (*113, 114*).

One of the most basic principles of altering the properties of a charged network like zeolites is also applicable for MOFs and POFs. For example, the pore size of zeolite A can be changed from 3 to 5 Å by replacing K^+ (3 Å) with Na^+ (4 Å) or Ca^{2+} (5 Å). Li and co-workers synthesised the first charged POF in 2012 (*115*) through a Yamamoto cross-coupling reaction of a quaternary phosphonium and tertiary phosphorus. By exchanging the bromine with fluorine, an increase of surface area from 650 cm^2/g to 980 cm^2/g was achieved.
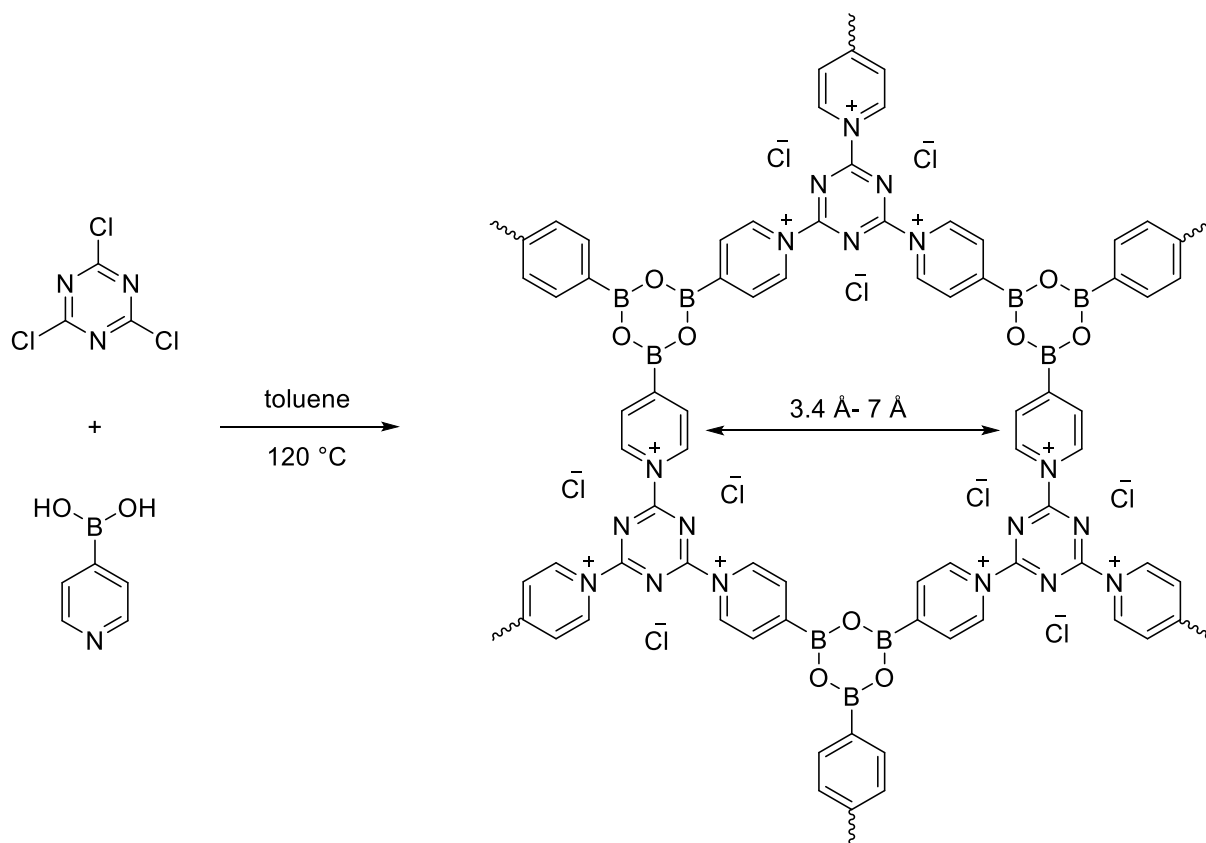
Scheme 22: First synthesised charged POF by Yamamoto and co-workers (116, 117).

2. Theoretical background

Inspired by the similarity of pore size distribution of PAF-50 compared to zeolite A, Yuan *et al.* exchanged the chlorine ions with fluorine (F-PAF-50), bromine (Br-PAF-50) and iodine (I-PAF-50), expanding the pore size volumes to a maximum of 7 Å for the smallest ion (Scheme 22).

To activate POFs or MOFs for catalytic applications, two principal pathways have been reported. Either the catalyst is already implemented into one of the linkers (i) or the linker holds active binding sites for a convenient post-modification tethering (ii). Hupp and co-workers introduced a hydrogen-bond-donating catalyst in form of 5,5′-(carbonylbis(azenediyl))diisophthalic acid linker combined with the non-functional linker 4,4′-bipyridine. The resulting MOF NU-601 was shown to catalyse numerous reactions, such as Diels-Alder or Friedel-Crafts reactions (Scheme 23). After activating the network by solvent exchange with MeNO$_2$, a Friedel-Crafts reaction between *N*-methylpyrrole and *(E)*-1-nitroprop-1-ene showed full conversion after 36 h at 60 °C with 10 mol% catalyst loading compared to approximately 23% conversion without catalysis (*118*).
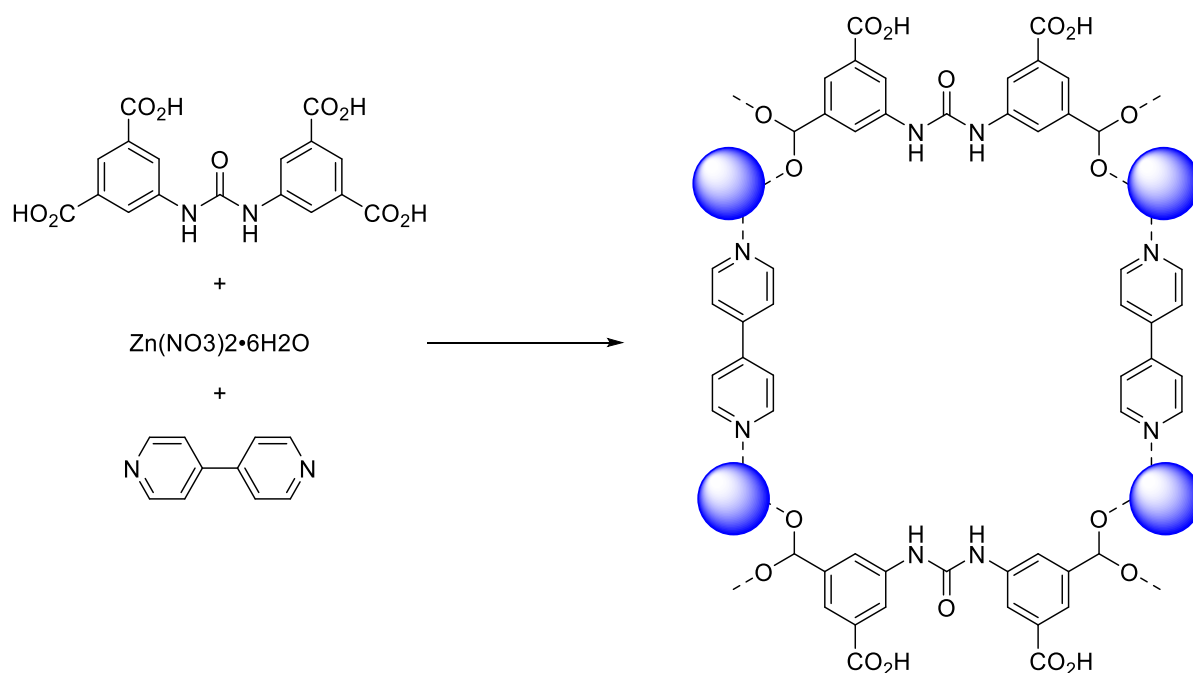
Scheme 23: Synthesis of the hydrogen-bond donating catalyst MOF NU-601 (118).

Furthermore, not only catalytically active organic molecules can be introduced, but also metal containing linkers such as porphyrin derivatives (Por-MOFs) (*119*). Based on the results of the catalytic NU-601 MOF, the same group reported the synthesis of numerous metalloporphyrin MOFs combining 1,2,4,5-tetrakis(4-carboxyphenyl)-

benzene (tcpb) and various porphyrin linkers containing different side groups and metal centres (M = Zn, Mn, Al, Co, Pd, Fe, Ru) (*120–122*).
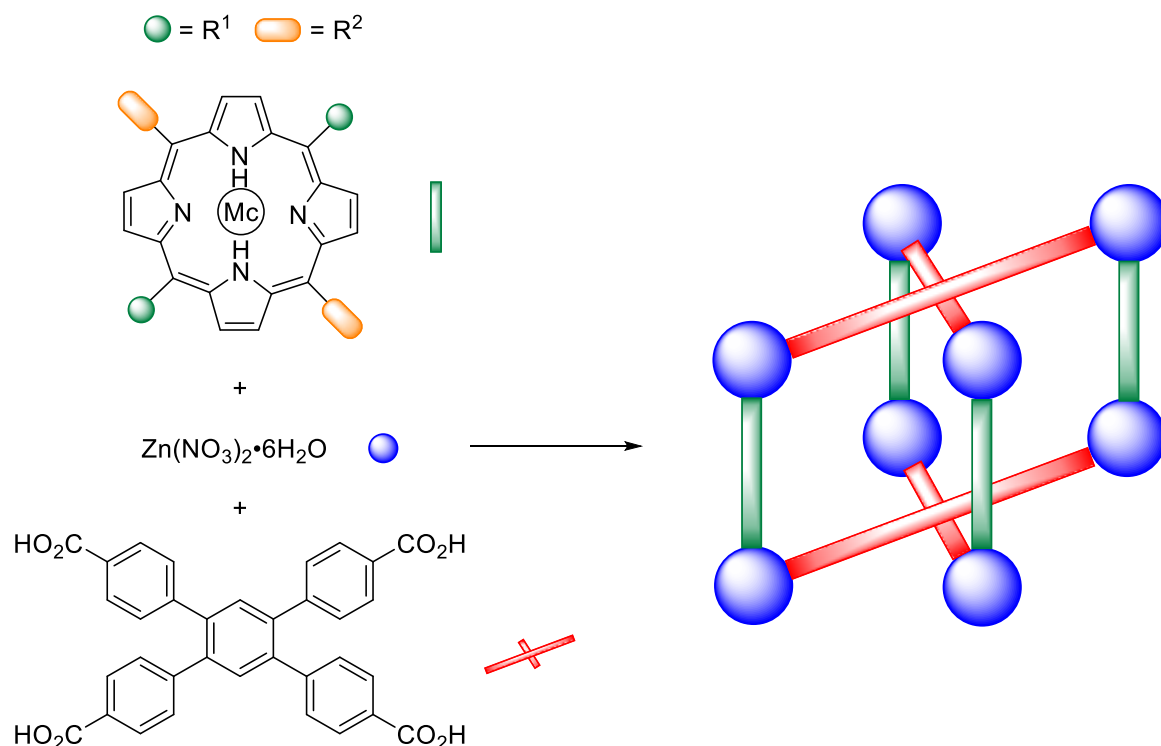
Scheme 24: Synthesis of NU-601 MOF, containing a variety of catalytically active metals other than the SBUs (120–122).

The post-modification of metal organic frameworks with metal ions on free binding sites inside the network is quite limited due to competitive interactions between metal centres and reactant. Li and co-workers modified MOF-253 (Al(OH)(bpydc), bpydc = 2,2′-bipyridine-5,5′-dicarboxylate) through soaking of a solution of CuI in acetonitrile. Cohan *et al.* studied the tandem post-synthetic modification of MOFs. As first step, a covalent modification to introduce coordinating sites took place followed by the coordination of a metal salt to obtain immobilized organometallic complexes (*123–125*). For COFs, the post-modification through soaking of metal-containing solutions proceeded in the same way. Another way for the metallisation process, which is however only possible in COFs, involves frameworks containing free -OH groups (e.g. PAF-18-OH) or the more reactive carboxyl-group (e.g. PAF-26-COOH), which were subsequently transformed into Li-alkoxy or Li-carboxy PAFs, respectively (*126, 127*).

The synthetic benefits of "click" reactions, *i.e.* full conversion, ease, etc., led to their implementation in the modification of MOFs and COFs. Jiang *et al.* synthesised a

variety of azide-containing COF-5 networks (5 – 100 % of azide-functionalised linkers) (*128*) The azide groups provided the opportunity to post-modify COFs *via* click reactions with alkynes. As a result, introducing triazole-linked moieties into the channels of the COFs tuned the pore size. Furthermore, the same group modified H$_2$P-COF through Cu(I)-catalysed azide-alkyne click chemistry to introduce pyrrolidine as an organo-catalytic compound (*129*).
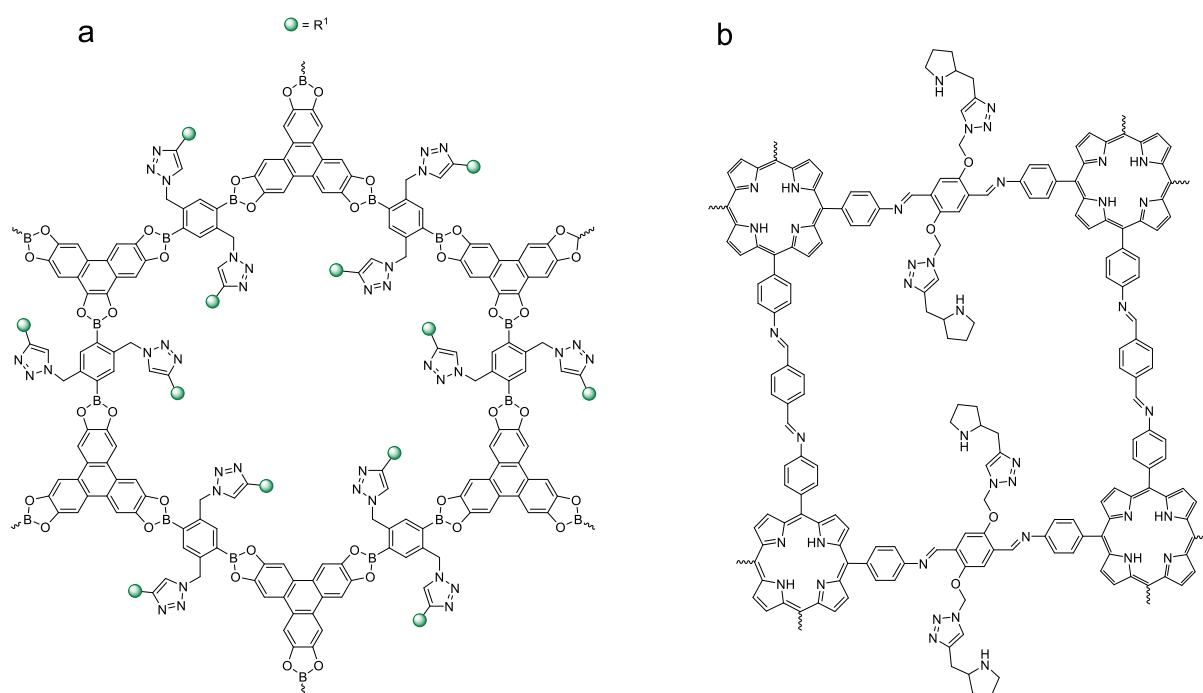
Figure 9: Post-modified of COF-5 (a) and H$_2$P-COF (b) via CuAAC click chemistry (128, 129).

In conclusion, porous materials like MOFs or POFs are thoroughly studied and have many applications due to their high porosity and tunability of properties. They can be found in applications like gas storage (*130–132*), catalysis (*133, 134*), filter agents (*135*), etc.

2.3 Surface Modification

Silicon is one of the most common semi-conductor materials for microelectronic devices. The chemical modification of silicon surfaces is of interest for various applications. Appropriate pathways include the utilisation of organosilanes, which are capable to anchor onto the surface in a self-limiting self-assembly process (*136, 137*). Due to the wide range of functional groups that can be attached to the surface by silanisation, further organic molecules can be introduced onto the interfacial silane film, endowing new surface properties.

2.3.1 Surface chemistry of silicon

This chapter only focuses on the silicon (100) planes due to the high relevance with this work and further information is presented by Waltenburg and Yates (*138*). These planes have a square unit cell with sp^3-hybridisation of each silicon atom. Each silicon atom is bonded to two others in the plane below and two in the plane above thus leading to a diamond structure (Figure 10) (*139*). A more detailed insight is given by the side-view of the first three layers, representing the boat like conformation. The silicon bond lengths are 2.35 Å with a bond strength of 226 kJ/mol (*140*) For nominally flat silicon (100) surfaces, the dimer-model proposed by Schlier and Farnsworth is the conventionally accepted one (*141*) and expanded to the model of buckled dimers by Hanemann *et al (139).*
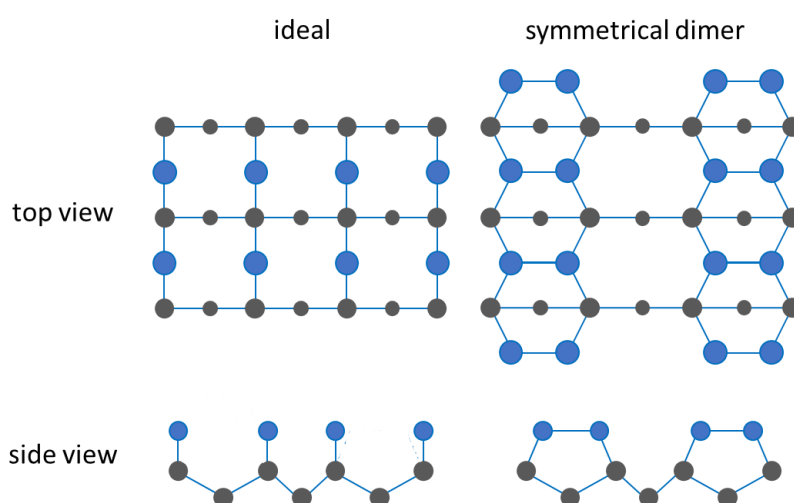
Figure 10: Structure of silicon atoms on the surface in ideal manner or as symmetrical dimer from top and side view. Blue circles represent the surface atoms which form two bonds (immobilized free radical) each, grey circles represent the bulk atoms. The size of the circles decreases as their distance from the surface increases (139).

2. Theoretical background

On closer inspection of the tetrahedral bonding structure of the silicon lattice, the direction of the dangling bonds in a (100) surface will rotate by 90° by crossing a step of single-layer height, thus being found on consecutive terraces perpendicular to each other. Since macroscopic crystals are not perfect, the low-energy electron diffraction (LEED) pattern is a superposition of two identical patterns rotated by 90° (2×1 pattern rotated by 90° → 1×2 patterns perpendicular to each other), leading to several possibilities of energy transfer to stabilise the surface (*142*).

Si-H surfaces

For hydrogen bonds having a prominent role in organic chemistry, where C-H bonds are predominant, the same importance applies as to the chemistry of silicon with its Si-H bonds. As a result of the reaction of the reactive dangling bonds with hydrogen, the Si-H bond formation provides a high degree of passivation of a crystalline silicon surface. Comparison of the bond strengths of Si-Si in bulk, Si-Si in the dimer and Si-H, in this order, increases from 226 kJ/mol to 318 kJ/mol to 366 kJ/mol. The standard procedure for preparing hydrogen terminated silicon surfaces involves the selective etching of silicon oxide layers with HF solutions (*143*) since the reactivity of molecular hydrogen towards silicon surfaces is very low, and requires high temperatures (appr. 2000 K) (*144*).

Si (100)-(1x1)
dihydride

Si (100)-(2x1)
monohydride

Si (100)-(3x1)
mono- and dihydride
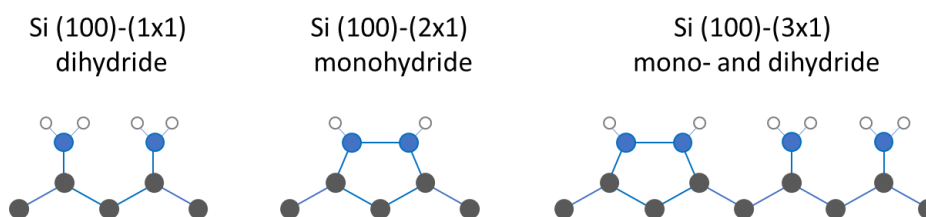
Figure 11: Hydrogenated silicon surface and the dihydride, monohydride and combined structure (138).

In principle, for silicon (100) surfaces, two different ideal hydrogen terminations were proposed. On the one hand there is the monohydride phase preserving the Si-dimers on the surface by capping one dangling bond on each surface atom (Figure 11, 2×1 monohydride), on the other hand is the dihydride phase (Figure 11, 1×1 dihydride), in which the dimer bonds were broken by capping both dangling bonds. The trihydride species can only be produced by breaking the back-bonds of the silicon network and is not displayed.

Si-O$_x$ surfaces

Being the only representative of a group VI element in the periodic table for which the interaction with silicon has been excessively studied, Si-O chemistry is very important for protective coatings or insulator films. The interaction of oxygen gas and silicon can lead to two different oxidation processes, depending on the processing. At high temperatures or ambient pressures, active oxidation takes place (edging of the surface), while passive oxidation dominates at high oxygen pressures or low temperatures (*138, 145*).

passive oxidation: $Si_{(solid)} + O_2 \rightarrow SiO_{2\ (solid)}$

active oxidation: $Si_{(solid)} + 0.5\ O_2 \rightarrow SiO_{(gas)}$

Freshly cleaned silicon surfaces are relatively rapidly oxidized by atmospheric oxygen (passive oxidation), building a native oxide layer of approximately 3 nm. A variation of thicknesses can be produced by wet oxidation in a chemical etching environment or by exposing silicon surfaces to oxygen at elevated temperatures (active oxidation). The latter involves two different preparation methods: the so-called dry oxidation or the steam oxidation utilizing water vapour. However, both methods are less reproducible and less homogeneous than the passive oxidation. In crystalline SiO_2, oxygen has a bridging position between the silicon atoms in a tetrahedral configuration. For the SiO_2 modifications, *α*- and *β*-cristobalite and *α*- and *β*-quartz exists, while the silicon-oxygen bond is 1.6 Å (*146*).
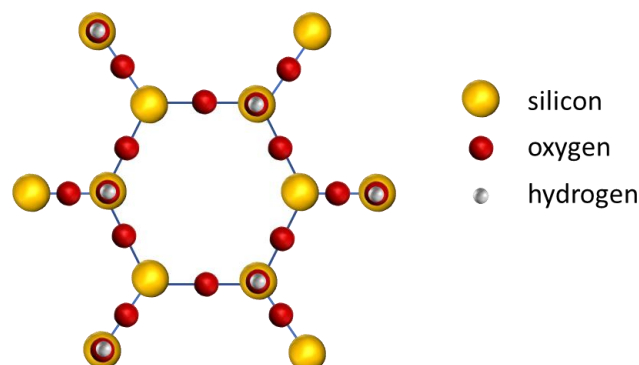
Figure 12: Top view of one silicon oxide hexagon with three OH groups perpendicular to the surface (147).

Figure 12 shows an exemplary SiO_2 surface in a top view, in which the Si-O bonds in the surface are saturated with hydrogen atoms resulting in three OH-groups perpendicular to the surface due to the tetrahedral configuration of the silicon atom. The yellow dots represent silicon, the red ones oxygen and the grey ones hydrogen. Additionally, Stevens *et al.* calculated the density of OH-groups to be 1/22 $Å^2$ (*147*).

2.3.2 Self-assembled monolayers

Self-assembled monolayers (SAMs) are organic assemblies, formed by the adsorption or covalent bonding of molecular constituents from a solution or gas phase onto the surface of solids. They provide a simple, convenient, and flexible pathway to tailor the properties of metal surfaces. The used molecules typically consist of a specific headgroup for each metal (*148, 149*). Generally, modified surfaces can be used to influence the adhesion capabilities or patterning during the process of micro- and nanofabrication. For silicon oxide surfaces, organosilanes are particularly well-suited to introduce a variety of functional groups enabling different applications. The general structure of these silanes is $XSiR_3$, X_2SiR_2 or X_3SiR with X being either a chloride or an alkoxy group and R a combination of at least one organic spacer bearing a functional group and methyl/ethyl groups. Perfluorinated alkyl chains as R groups have been used as release agents in soft lithography or to avoid soil adhesion to surfaces, while amine groups have enabled the immobilisation of biomolecules, such as enzymes or DNA. Thiol- and vinyl groups have been applied for the synthesis defined multilayers due to the properties shown in chapter **2.1.3** (*150–154*).
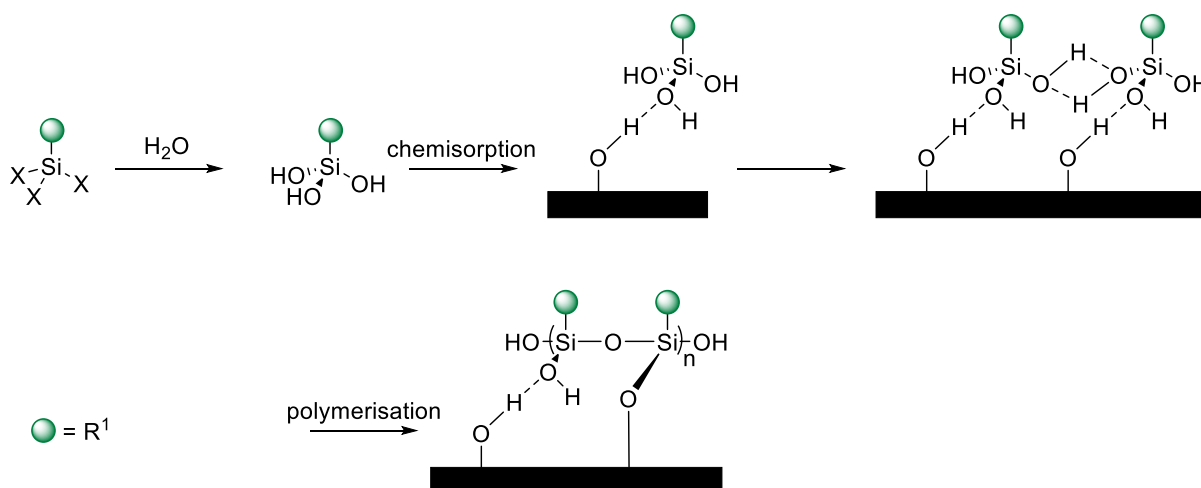
Scheme 25: Proposed mechanism of silanisation reaction (155).

The silanisation mechanism was first proposed by Lee and further remodelled by Zisman (*155*). They suggested that the formed silanol is hydrolysed in a first step followed by a polymerisation reaction of the silanes (Scheme 25) without being covalently bound to the surface. As later studies showed, the surface interacts with the

silanols, not only *via* hydrogen bridge bonds, but also with covalent Si-O bonds. Furthermore, it was found to be more likely that a chemisorption process first occurs with an ultrathin water layer on the substrate making direct alkoxy groups on the substrate not a necessary element to form SAMs (*156, 157*).
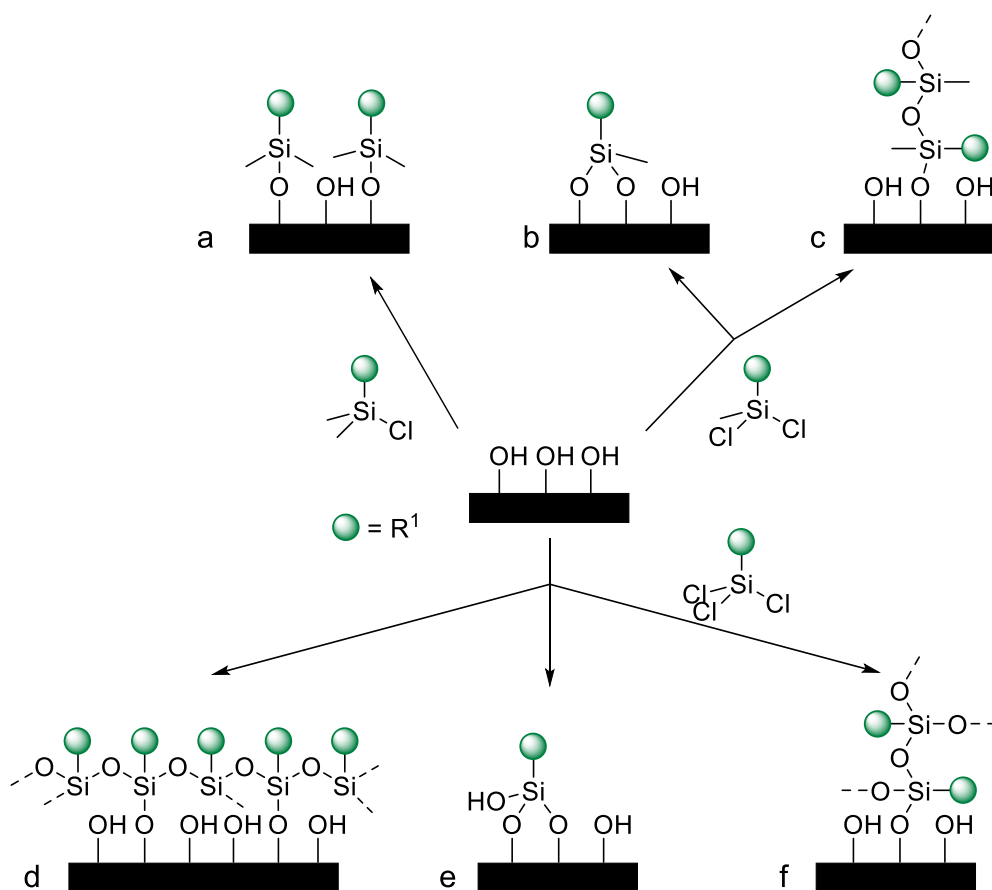
Scheme 26: Theoretical reactions possible for mono-, di- and tetrachlorosilanes on hydroxy functionalised silicon surfaces (148).

Scheme 26 shows the theoretically possible reactions between mono-, di- and trichlorosilanes with the hydroxy groups on a surface. Due to their mono functionality, monochlorosilanes are very attractive for reproducibility, since there is only one possible siloxane species formed as product (Scheme 26, (a)). However, the more hydrolysable groups are present in a silane, the more reactive it becomes thus the monochlorsilanes show slow reaction rates compared to di- or trichlorsilanes (*148*). On the other hand, silanes with more than one hydrolysable group polymerise in the presence of water leading to several kinds of silanol-species on the surface (Scheme 26, (b)). Octadecyltrichlorosilane (OTS) is one of the most often applied silanes, leading to surface densities up to 4.5 − 5 groups/nm^2 (*158–160*). At full coverage,

cross-polymerisation is unlikely to occur. Stevens showed in a theoretical study that the siloxane cross-link is too short, leading to an overlap of the alkyl chains and to twice as dense surfaces as feasible (Scheme 27) (*147*). These results were further confirmed by White and co-workers, who modified a piranha treated (hydroxylated) surface with OTS under strict anhydrous conditions and additionally in the presence of moisture. In the first case, uniform and densely packed monolayers were prepared, whereas in the second case non-uniform topologies were observed (*161, 162*).
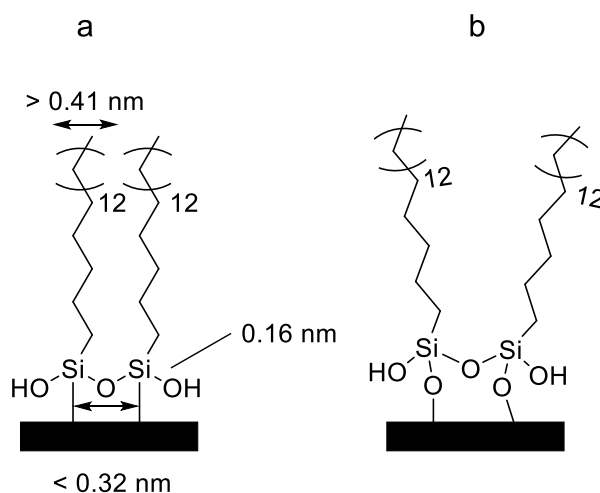
Scheme 27: Densely packed octadecylsilane surface and the corresponding theoretical distances of Si-O-Si and C-C diameter of the alkyl chain (a) and the resulting more likely twisted structure (147).

Zannoni and co-workers programmed an atomic model of molecular dynamics simulations (MD simulations) of self-assembled monolayers. They calculated standard physical observables, such as density of packing, thickness of the monolayer, tilt angle of the molecules and crystal structure of octadecyltrichlorosilane and 1H,1H,2H,2H-perfluorodecyltrichlorosilane (FDTS) with good agreement to experimental data available in the literature (*163*). Both compounds were chosen because of their relevance and use in organic electronic applications. Figure 13 shows the orientation of OTS (grey) and FDTS (green) at various densities without bonds being explicitly considered for the alkylsilane derivatives and the amorphous silica substrate. It was concluded that the order of the molecules is highly dependent on the coverage with high disordered phases below 3.2 molecules/nm^2 (FDTS) and 3.6 molecules/nm^2 (OTS) and ordered phases above these values. Additionally, the nature of the alkyl chain influences the angle of the silanes: the higher electronegativity of the fluorines weakens the bending of the chains compared to the OTS SAM.
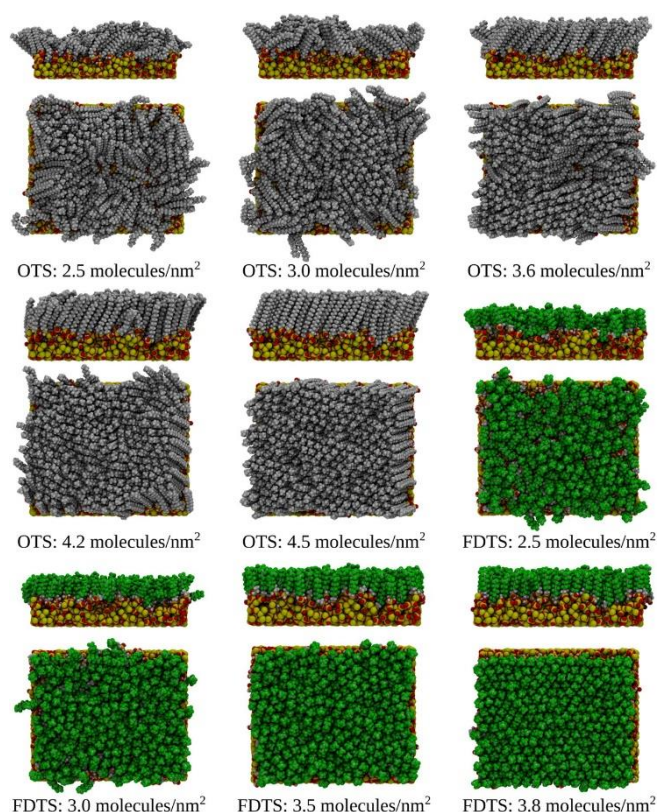
Figure 13: Calculated structure of OTS and FDTS modified silicon surfaces depending on its density. With permission of the American Chemical Society (163).

Water is not the only parameter influencing the quality of the silanisation process. The effects of temperature, solvent, concentration, pressure, deposition-time and silane-age are also of great importance. Furthermore, catalysts, such as trimethylamine, are typically used in the formation of amino-terminated SAMs (*161*). There are two prominent established procedures employed for creating SAMs on surfaces: liquid phase deposition (LPD) or vapor phase deposition (VPD). The first method uses dissolved silanes: the substrate can be dipped into, covered or sprayed with the solution, however long reactions times are often necessary. In VPD, the substrate is placed in a sealed box at ambient/elevated temperatures and/or reduced pressure, while the silane is evaporated and subsequently transported into the vessel by inert-gas. Due to the higher possibility of contamination, LPD tends to lead to clustered multilayers whereas VPD produces high quality monolayered SAMs (*164*).

2.3.3 Controlled surface modifications

Three practical modification methods are available, which allow controlled modification of a silicone surface. Due to its relevance to this work, all types are explained in the following with an example using thiol-ene "click" chemistry. The first method, the "grafting from" approach, uses molecules bearing a thiol or double bond moiety to induce the grafting by radical photoinitiation or catalytically activated Michael addition (Scheme 28, b & d). In contrast, the "grafting to" approach utilises pre-formed macromolecules (photoinduced: a & c left, Michael addition: a & c right) that mostly utilises photo-induced coupling reactions or Michael addition reactions. The third method is the "layer-by-layer" (LBL) approach, in which alternating layers of different molecules connected stepwise, achieving high control. The monomers are applied *via*, for instance, spray- or dip-coating.
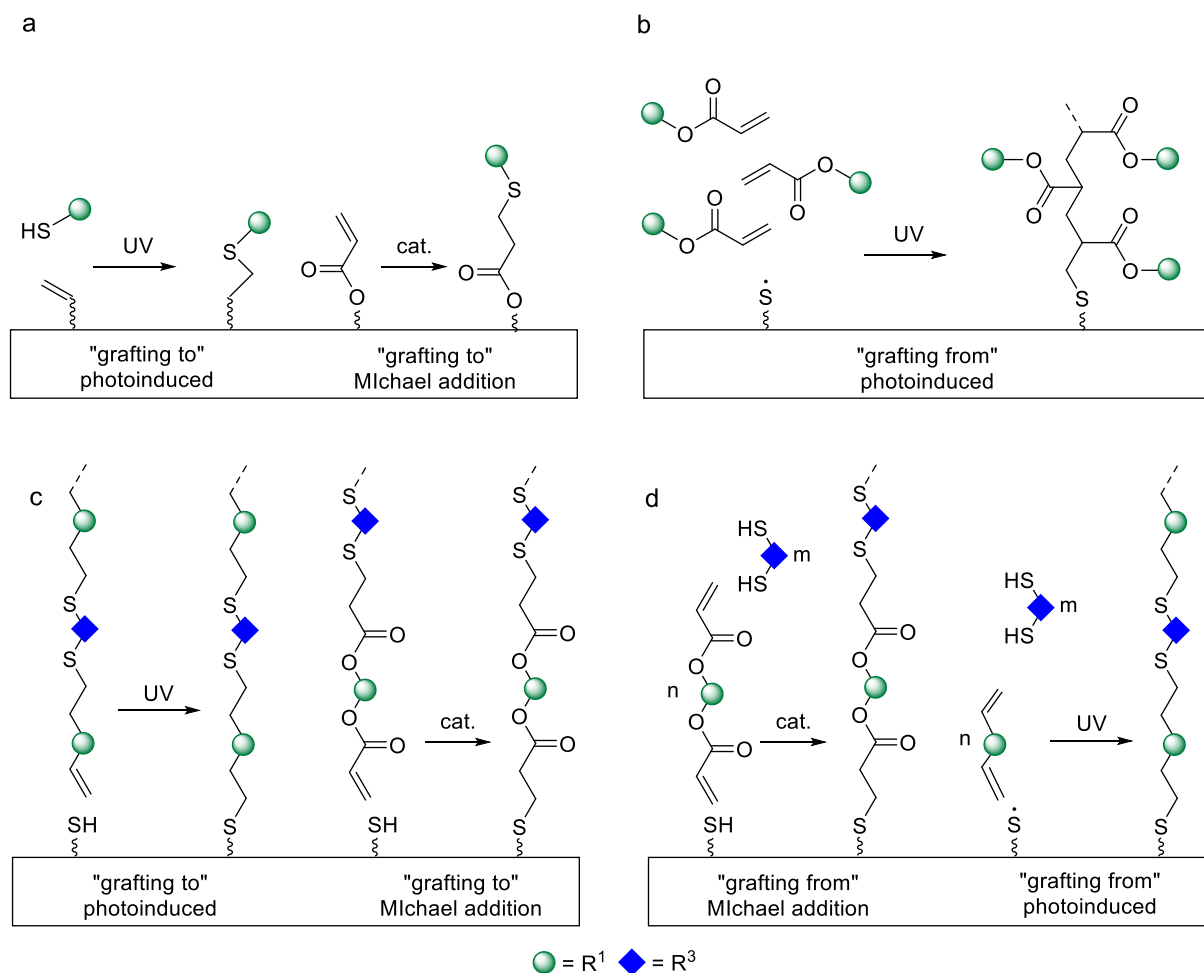
Scheme 28: Schematic representation of the "grafting to" and "grafting from" mechanism employing thiol-ene chemistry (165, 166).

2. Theoretical background

Sometimes a fourth way occurs that combines the "grafting from" and the "grafting to" approach, the "grafting through" approach. The initiator is attached to the surface rather than contributed from solution and monomers are supplied *via* a dialysis membrane. This promotes the growth of short chains while avoiding the growth of very long chains (*165, 166*).

Depending on the application of the modified surface, each process is considered based on advantages and disadvantages, as outlined in Table 1. For example, the "grafting to" approach uses defined pre-synthesised building blocks but, due to the highly sterically demanding molecules, the grafting density is often reduced. On the other hand, the "grafting from" procedure overcomes this issue as the macromolecules increase in size *in situ* and simultaneously.

Table 1: Advantages and disadvantages of "grafting to", "grafting from" and layer by layer synthesis.

"grafting to"	"grafting from"	"layer-by-layer"
molar mass well characterised	higher grafting density	higher grafting density
low grafting density	difficult to characterise chain length	defined chain length and molecular structure
formation of brush-like and mushroom-like structures		no complicated instruments needed
		multiple steps
		possible bridges *via* crosslinking

Due to the higher relevance, this thesis focuses on the LBL method, which offers the highest control over the formed films. First introduced by Iler in 1966 by depositing alternately charged colloid particles, the utilisation was expanded to polyvalent ions, surfactants, water soluble polymers, and proteins by Decher and co-workers (*167, 168*). Besides the classical electrostatic interaction, other complementary interactions have been used, such as hydrogen-bonded layers of poly(acrylic acid) (PAA, hydrogen bond donor) and poly(4-vinylpyridine) (PVP, hydrogen bond acceptor), metal-oxide gel

films formed from a surface sol-gel process (various alkoxides of titanium, zirconium, etc.), charge-transfer interactions of e.g. electron-accepting groups (3,5-dinitrobenzoyl group) and electron-donating groups (carbazolyl group) (*169*). Most of the aforementioned layer-by-layer methods have some drawbacks or features, depending on the application. The weak interactions of hydrogen bonds or electrostatically formed layers can easily be reversed by changing the pH of the environment, thus making the layers less stable. If high stability is of importance, these methods are not preferred. However, their dynamic binding properties render them well suited for binding and release applications, such as drug delivery (*170*). Covalent assembly is an alternative to graft multilayers on diverse surfaces. The similarities of the LBL procedure to atomic layer deposition (ALD) mainly used in chemical vapor deposition (CVD) led to a new nomenclature for self-limiting covalent LBL reactions, the so-called molecular layer deposition (MLD) process (*171*). The earliest examples of this reaction type were amide, ester, urea, urethane, oxime and imine bond forming reactions, while amides have been the most published ones to date (*172–175*). Potential compounds for LBL are α,ω-substituted molecules of the A-A and B-B type forming covalent bonds *in situ*, under mild reaction conditions and ambient atmosphere, whereas none or easily removable side-products are obtained. Therefore, "click"-chemistry, e.g. thiol-ene chemistry, shows great promise for this procedure.

Buriak *et al*. investigated the reactivity of different α,ω-dithiols and α,ω-dienes. First, they prepared a hydride-terminated silicon surface by simple etching of silicon shards with diluted hydrofluoric acid. After that, the desired α,ω-dienes were introduced by simple irradiation with a small UV lamp. By subsequent irradiation of alternating layers of α,ω-dithiols and α,ω-dienes, up to nine layers were achieved. One problem concerning the surface modification *via* thiol-ene/yne chemistry (and other chemistries using A-A building blocks) observed is shown in Figure 14. On a surface, dithiols can be deposed like brushes with only one thiol group bound to the surface (a = ideal, b = realistic), or both functional groups bound to the surface with short chains (c = flat) and longer chains (d = buckled) because of their high interaction leading to lower experimental heights per building block (*154*) Furthermore, disulfide formation of the

applied thiols can occur as a side reaction in a thiol-ene/yne process and consequently further decrease the average heights.
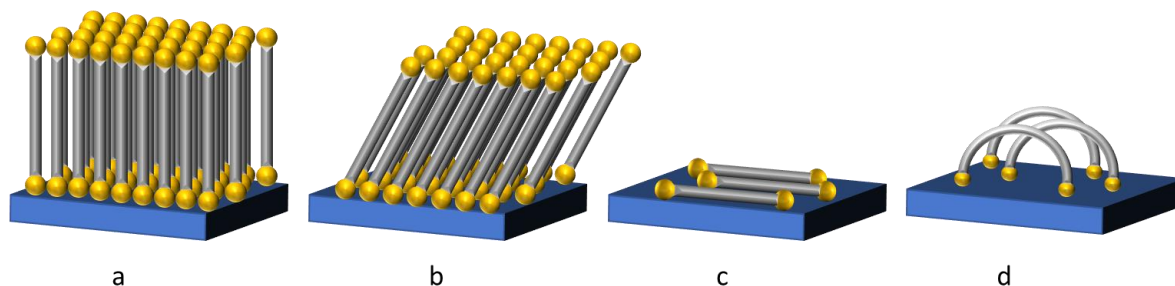
Figure 14: Spatial deposition of dithiols on surfaces (a) idealised brush like, (b)bent brush-like, (c) flat and (d) buckled (154).

To further investigate the possibility of sequence-controlled surfaces and the resulting structure-property relationship, Meier and co-workers combined the synthesis of several functional building blocks and independent analytics, such as X-ray induced photoelectron-spectroscopy (XPS), time-of-flight secondary ion mass spectrometry (ToF-SIMS) and atomic force microscopy (AFM). They obtained six individual layers *via* thiol-ene "click" chemistry with molecular precision while every layer could be fully characterised (Scheme 29) (*16*).
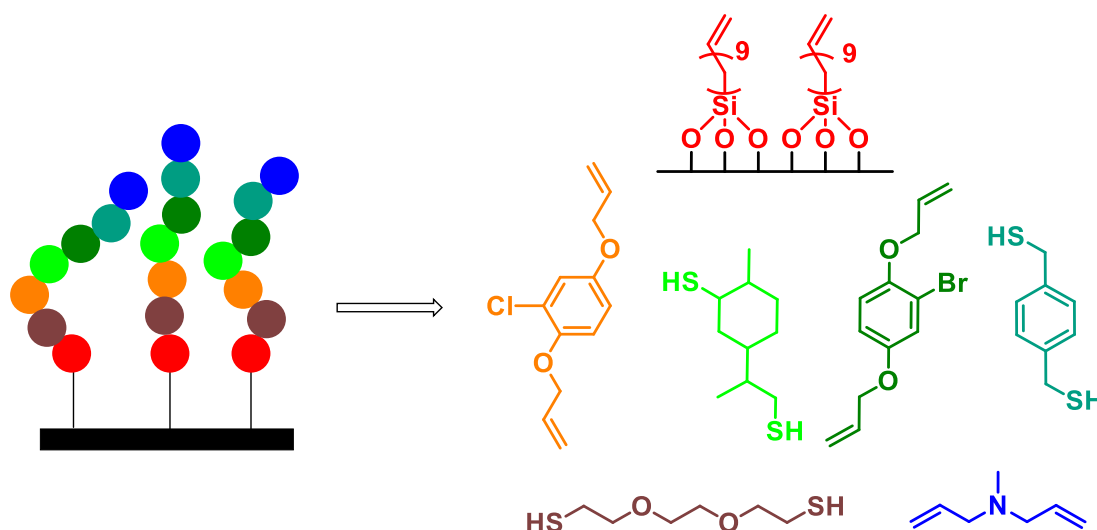
Scheme 29: Modified silicon surface via molecular layer deposition with labelled building blocks in a brush like manner (16).

Based on these results, Ehrenberg and co-workers adapted the procedure of preparing controlled layers to modify graphite electrodes. As such, electrografting of diazonium salts with protected alkyne groups was used to functionalise the surface. After deprotection, 2,2′-(ethylenedioxy)diethanethiol was introduced as α,ω-dithiol. Those modified electrodes were tested in cyclovoltammetry and galvanostatic measurements revealing higher stability compared to unfunctionalised graphite electrodes while reducing the permeability of the lithium ions (Figure 15) (*176*).
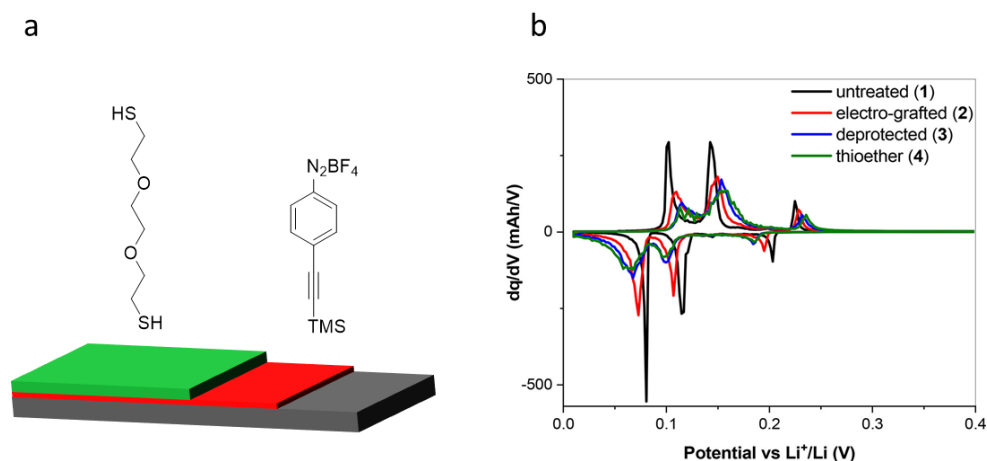
Figure 15: Modification of graphite electrodes by electrografting of diazonium salts, subsequent thiol-ene reaction and cyclovoltammetric and galvanostatic measurements. With permission of the American Chemical Society (176).

2.3.4 Characterisation of surfaces

This chapter gives a short overview on three of the most common and relevant surface analytical methods: X-ray induced photoelectron-spectroscopy, time-of-flight secondary ion mass spectroscopy and atomic force microscopy.

X-ray induced photoelectron-spectroscopy (XPS)

One of the most applied and versatile spectroscopic methods for analysing surfaces is X-ray induced photoelectron-spectroscopy (XPS) or electron spectroscopy for chemical analysis (ESCA). The advantage of XPS is the possibility to detect the elemental composition of surfaces (except hydrogen and helium). In general, XPS analyses are routinely used to determine the composition of the surface qualitatively and quantitatively in order to find contaminations on surfaces (mapping) or in depth (depth profiling, angle resolved XPS), as well as the chemical state and binding energies of certain atoms (*177, 178*).
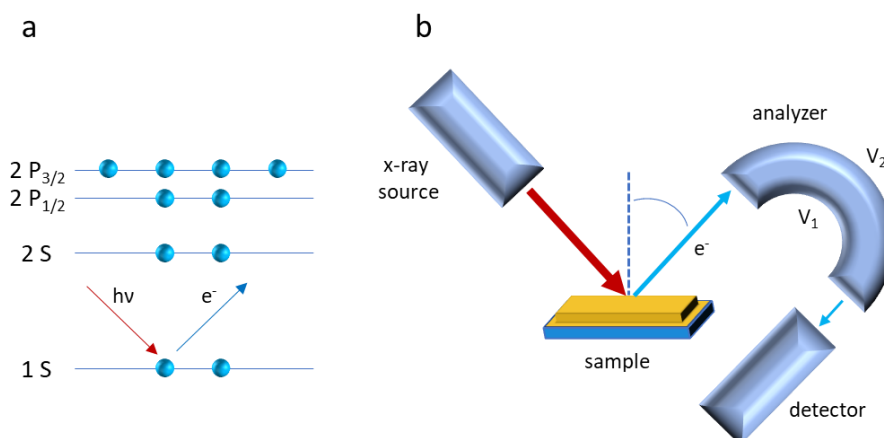
Figure 16: General mechanism (a) and setup (b) of an X-ray induced photoinduced spectroscope (177, 178).

The basic setup is shown in Figure 16. A focused X-ray beam with defined wavelength (around 1.5 kV) is shot at the sample. This X-ray beam excites an electron in an atomic shell (e.g. 1s electron shell) of the substrate and creates a shell specific photo-emitted electron with an energy < 1.5 kV. The photoelectron is then separated by an electron energy analyser and then, depending on its kinetic energy, analysed in a detector which calculates the electron energy. The whole XPS system has to stay under ultra-high vacuum to eliminate signals from gas molecules. The area of this analysis method

ranges from mm to cm scale and depends on the composition of the sample (*179*). The binding energies of core-electrons are affected by valence electrons and therefore by the chemical environment of the atom. For example, the shifts of the photoelectrons in an ESCA reflect the diminished amount of shielding energy with higher oxidation state of the detected atom (*53*).

Time of flight secondary ion mass spectroscopy

Time of flight secondary ion mass spectroscopy (ToF-SIMS) is used as an analysis technique for the identification of the chemical composition of the surface of materials. First, a primary ion beam of ionic clusters (0.1 – 20 keV) is shot from a primary ion gun (e.g. Bi liquid metal ion gun (Bi-LIMG)) at the sample surface to sputter a variety of secondary ions from the sample surface. Then, the mono- and polyatomic particles with negative and positive charges are separated in the ToF chamber by the ion mirror, based on electrostatic repulsion, and reach the ion detector (*180*). Additionally, a second ion beam can be installed, known as the sputter gun, for controlled erosion of the sample (sputter depth profiling or removal of unwanted material) (Figure 17) (*181*).
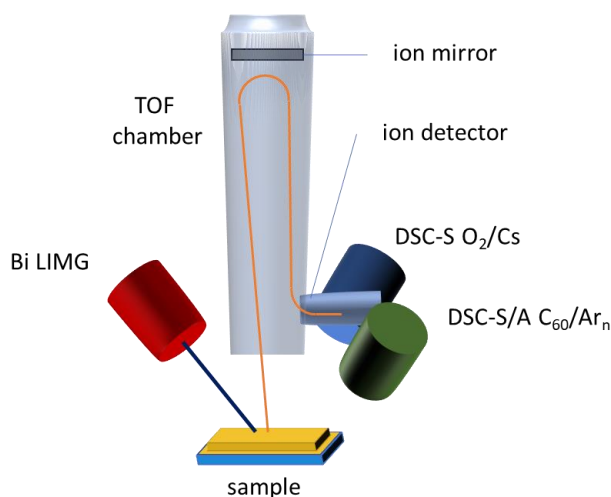
Figure 17: Schematic setup of a time-of-flight secondary ion mass spectrometer (181).

This technique can be very surface sensitive, depending on the primary ion dose and the resulting sputtered fragments. Basically, there are two different modes for ToF-SIMS analysis: (i) static SIMS with a low primary ion dose (>10^{13} cm^{-2}) and a low

flux (10 pA – 5 nA), which only sputters up to 0.1 % of the top monolayer and (ii) dynamic SIMS with a high flux (µA), which generates a rapid erosion of the surface yielding elemental distribution and depth profiling (*182*) . A schematic description of the bombardment of the surface by the primary ion gun is shown in Figure 18. By utilizing different types of commonly used primary ion sources for ToF-SIMS different experimental setups can be obtained.
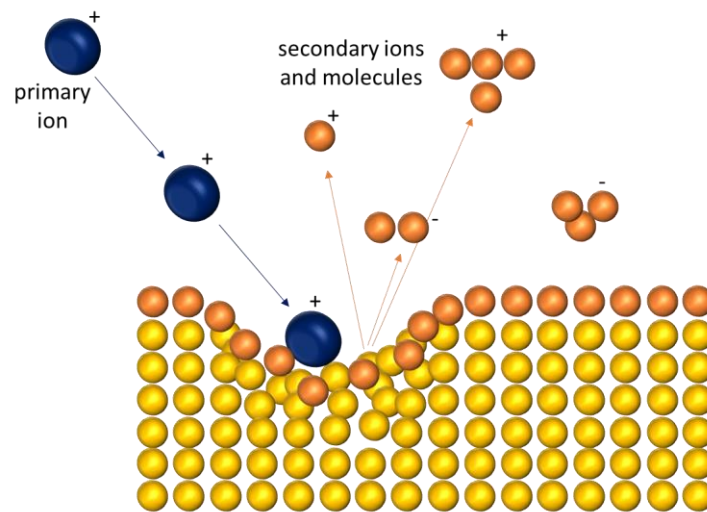
Figure 18: Effects of the primary ion beam when hitting a surface (181).

Atomic force microscopy

Atomic force microscopy was introduced in 1985 as a member of the scanning probe microscopy family by Binnig, Quate and Gerber (*183*). In principle, a sharp tip (typically less than 5 mm tall and often less than 10 nm in diameter at the apex) mounted on a cantilever (100 – 500 nm) is used to scan the sample. A piezo scanner precisely controls the probe-sample position and is combined with a laser as feedback-control system. The feedback control system is applied to receive and adjust the precise probe-sample position (*184*) (Figure 19).
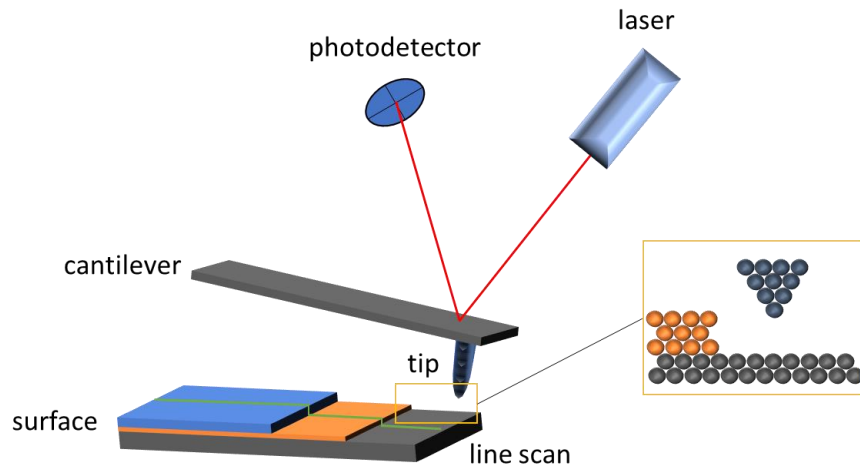
Figure 19: General setup of an atomic force microscope (184).

Due to the attractive and repulsive forces between the tip and the surface of the sample and/or surface topology, the cantilever is moving and this movement is detected by a laser. If the cantilever is bent, the laser projected onto a 2D position sensitive detector shifts and the force is calculated depending on the deviation from the centre.

Depending on the way of application or analysis, there are in principle three different modes: contact (constant force and constant height), tapping and non-contact mode. In the first case (constant force mode), the tip is in contact with the surface and the deflection of the cantilever is constant, therefore representing the topography. The second (constant height mode), uses the spatial variation of the cantilever deflection to generate the topographic data set. One drawback of both is the high abrasion of the tip and the destruction of the surface, especially in very soft specimen. Nevertheless, this method can also be used as force mode dip-pen lithography (*185*) or to determine the elastic-modulus, as has been showcased for spider silk (*186*). The tapping mode (intermittent contact mode) uses a constant stimulation to vibrate the cantilever near its resonance frequency and scans the surface at a distance of 1 – 100 nm with intermittent touching of the surface. When the tip encounters a height-difference, the oscillation amplitude is diminished and thus the height can be calculated without any surface modification. The non-contact mode is a variation of the tapping mode with equivalent operation parameters but without any surface contact (*187, 188*).

3. Aim of the present thesis

This PhD thesis is part of the Cooperative Research Centre 1176 "Molecular Structuring of Soft Matter" and in particular project A2: "Sequence-Controlled Growth of Cross-Linked Polymer Layers for Artificial Solid Electrolyte Interfaces". Preliminary studies on this project were conducted by A. Llevot, S. Steinmüller, and the author of this thesis during his Masters studies, synthesising markers bearing bifunctional monomers and, as proof of principle, up to six defined layers were deposited on functionalised silicon surfaces *via* thiol-ene "click"-chemistry (*19, 16*) Based on the results of the preliminary studies, the methods in this thesis and knowledge generated therein should be transferred to building blocks with more than two functional groups in order to gain control over the pore size or introduce a gradient in electronegativity within the stepwise built and surface anchored network. Initially, thiol-ene/yne, and later amino-yne chemistry are selected for the formation of the individual layers in order to demonstrate different synthetic approaches, further taking advantage of the characteristics of "click" chemistry (discussed in chapter **2.1.2** and **2.1.3**). In particular, tetraphenylmethane-based monomers are advantageous because of their defined and rigid structure, while they are readily accessible. First, the monomer synthesis has to be investigated with a focus on the determination and optimisation of the experimental conditions. Thiol, acetylene, secondary amine, and activated alkyne groups are introduced, while further modifications on the *ortho* and *meta* position should be carried out (Scheme 30).

Scheme 30: Structures of targeted building blocks suitable for network formation via thiol-yne or amino-yne "click" reaction.

After synthesis of the aforementioned building blocks, this thesis further aims at the sequence-controlled modification of silicon surfaces utilising a variation of the step-by-

step polymerisation of microporous nanomembranes *via* thiol-yne chemistry shown by Bräse and co-workers (*189*). However, the published nanomembranes were not analysed after each layer, thus a detailed knowledge of the composition could not be given then. Subsequently, procedures for a homogeneous modification of each layer are investigated, which should yield controlled porous networks (Figure 20 (a)). Furthermore, post-modification of the unreacted functional groups inside the previously prepared porous network will be evaluated (Figure 20 (b)).
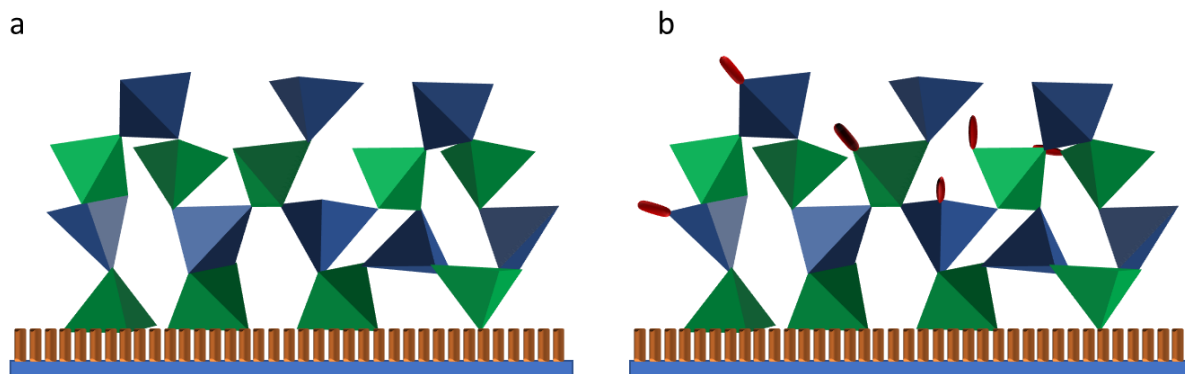
Figure 20: Schematic structure of surface anchored network, with controlled [AB]$_n$-sequence (a) and the postmodified remaining active sites.

Regarding the characterisation of the modified surfaces, several complementary analytical techniques such as XPS (x-ray photoelectron spectroscopy), ToF-SIMS (time of flight secondary ion mass spectrometry) and AFM (atomic force microscopy) should be used.

4. Results

4.1 Monomer synthesis

4.1.1 Building blocks for thiol-yne/ene chemistry

The first step towards molecularly tailored surfaces was the synthesis of the therefore required multifunctional building blocks. Thus, the core unit tetraphenylmethane (TPM) was synthesised starting with trityl chloride (1 eq.) and aniline (2.6 eq.) at 220 °C. Recrystallisation in a mixture of ethanol and hydrochloric acid and additional suspension in cold chloroform led to (*p*-aminophenyl)triphenylmethane, which was further reduced in a mixture of isoamyl nitrite (1.7 eq.), sulfuric acid and hypophosphorous acid to yield TPM (Scheme 31). TPM was obtained as a white powder with yields up to 79% over three steps (literature: 86%) (*190, 191*).
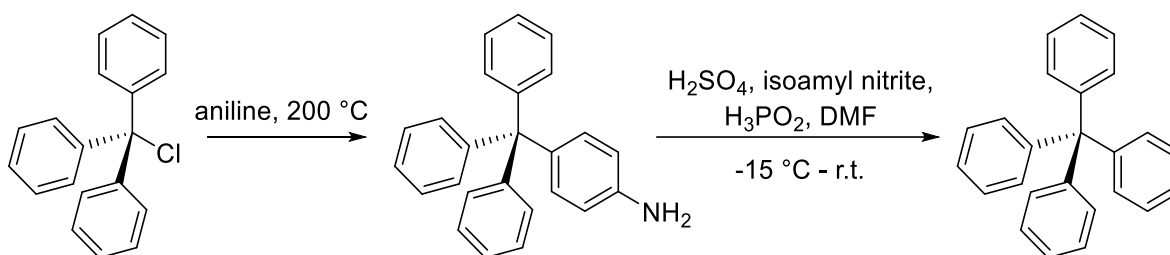
Scheme 31: Synthesis procedure for TPM starting from tritylchloride in two steps (190, 191).

Afterwards, the white solid was slowly added to bromine (20 eq.) and stirred for 30 minutes to obtain the product tetrakis(*p*-bromophenyl)methane (TPM-Br) bearing four bromine functionalities (Scheme 32). Quenching with cold ethanol and sodium thiosulfate yielded a beige solid at 72% yield (*190*). However, the applied reaction conditions led to a fifth bromine addition as could be concluded from the ^{1}H and ^{13}C NMR spectra, where additional peaks in the aromatic region were observed (Figure 21, Figure 22 Additionally, atmospheric pressure chemical ionization (APCI) measurements proved the additional bromination. Separation of the four and the five times brominated product *via* column chromatography was not possible, because of their indistinguishable R_f value (0.88).
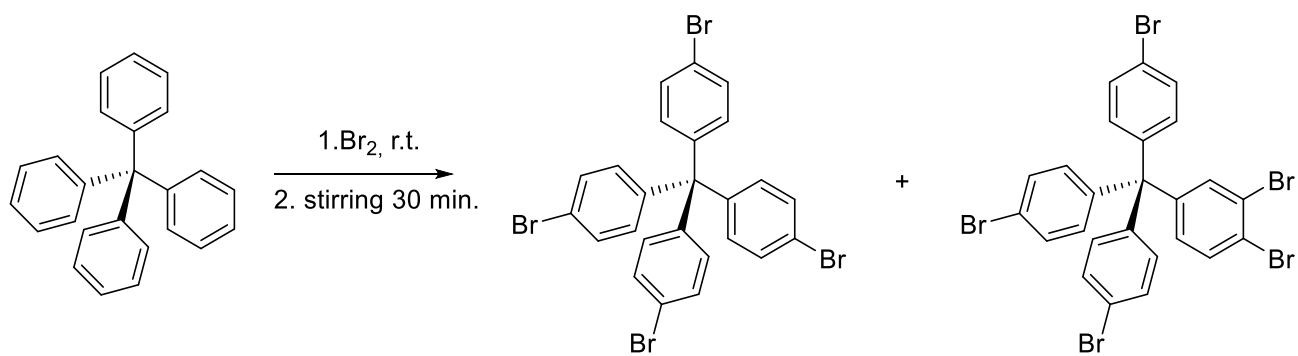
Scheme 32: Bromination of TPM and the fourfold and fivefold substituted product (190).
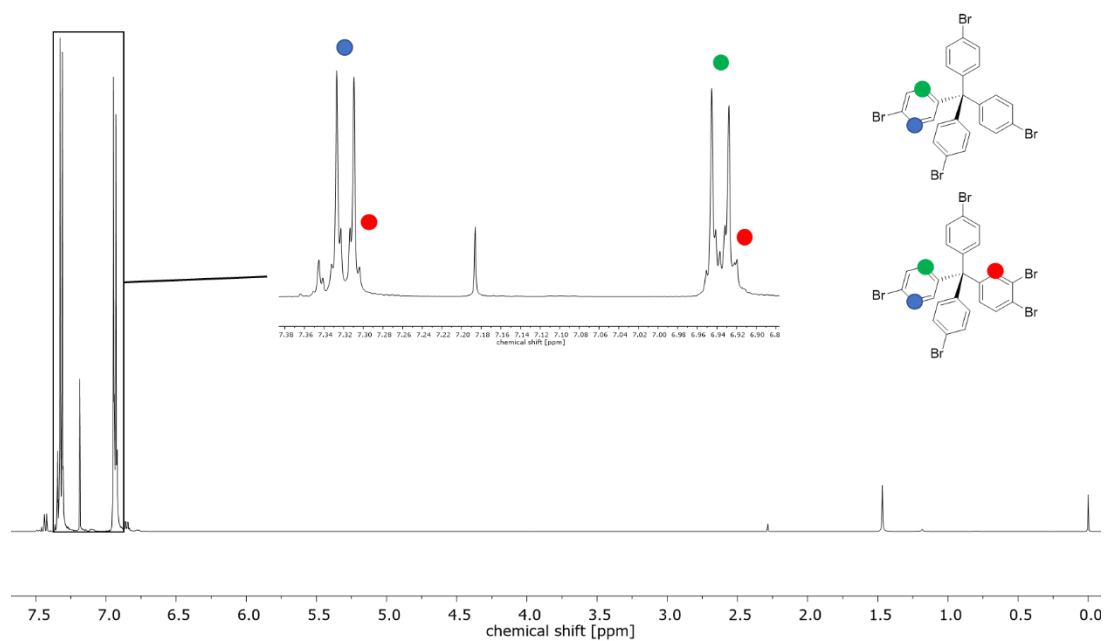
Figure 21: ^{1}H-spectrum of a mixture of fourfold and fivefold substituted TPM-Br.
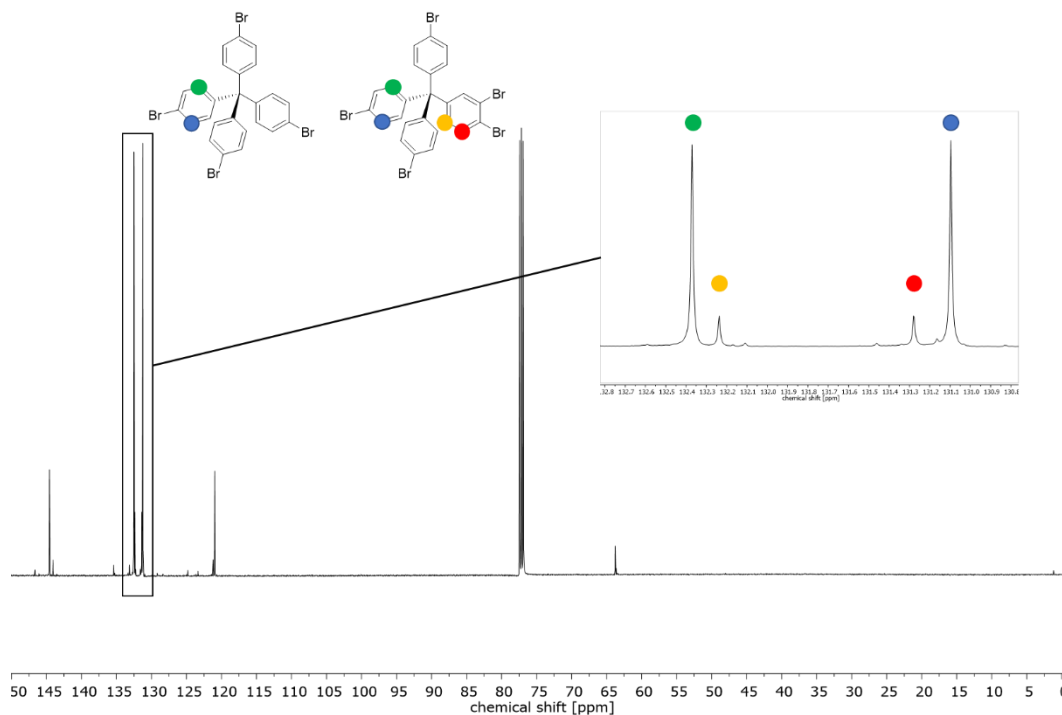
Figure 22: ^{13}C-spectrum of a mixture of fourfold and fivefold substituted TPM-Br.

To prevent the formation of the by-product bearing five bromine functionalities, the reaction conditions were adjusted. Table 2 shows the variation of the equivalents, the solvent and the reaction temperature. The best results were achieved using 16 eq. of bromine, which were added to a pre-cooled suspension of TPM and chloroform (1.5 mL/g) at 0 °C. The solution was then stirred at room temperature for 24 h. The workup was performed as mentioned before, obtaining the only fourfold functional product as a beige powder with an improved yield of 90%.

Table 2: Overview of different entries for the bromination of TPM.

Entry	Solvent	Equivalents (bromine)	Temperature	Yield [%]
1	-	10	r.t.	0%
2	CHCl₃	12	0 °C → r.t.	23%
3	CHCl₃	16	0 °C → r.t.	90%

By comparison of the ^{1}H and ^{13}C NMR spectra resulting from the reaction using the harsh reaction conditions with the ones obtained after optimisation of the reaction conditions, it was observed that the additional peaks corresponding to the fivefold brominated product are not present in the latter (Figure 24).). Additionally, the signals of the aromatic peaks in the ^{1}H NMR spectrum (Figure 23)) are more symmetrical and the "roof effect" is clearly visible. Furthermore, fast atom bombardment (FAB) measurements showed to existing fivefold functionalised species.
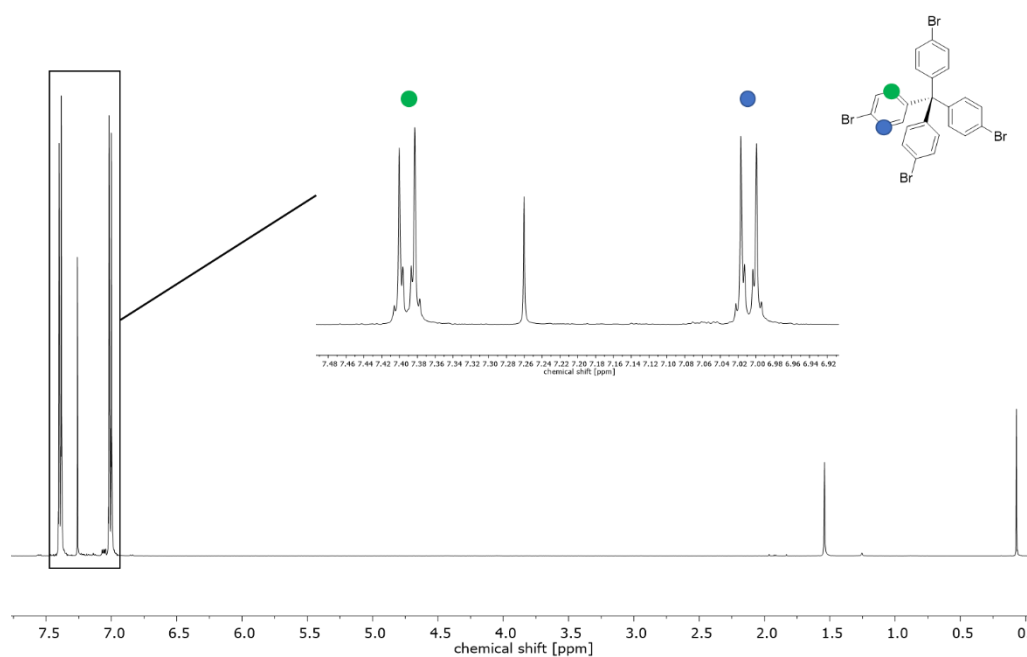
Figure 23: [1]H-spectrum of purely fourfold substituted TPM-Br.
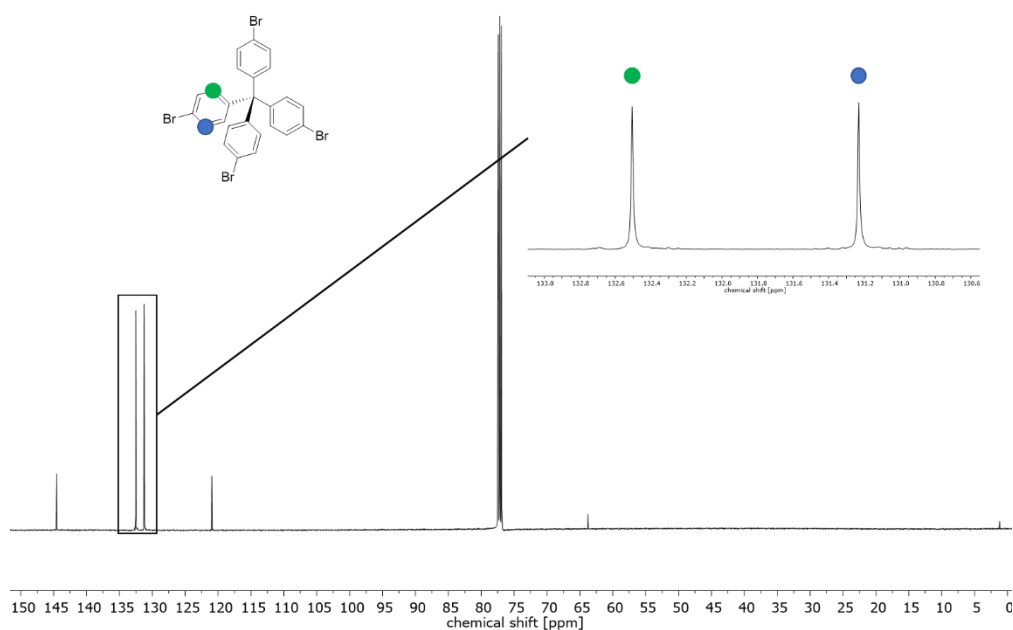
Figure 24: ^{13}C-spectrum of purely fourfold substituted TPM-Br.

Referring to previous studies of the Meier working group, marker groups in *ortho* or *meta* position were introduced as well (*16*) First, sulfonation of the previously synthesised tetrakis(4-bromophenyl)methane (TPM-Br) was tested using concentrated chlorosulfonic acid (10 eq.) in chloroform. However, no conversion to the desired tetra-substituted product was detected (Scheme 33). Furthermore, longer reaction times (2 days instead of 18 hours) and gentle heating (40 °C) did not lead to product formation.
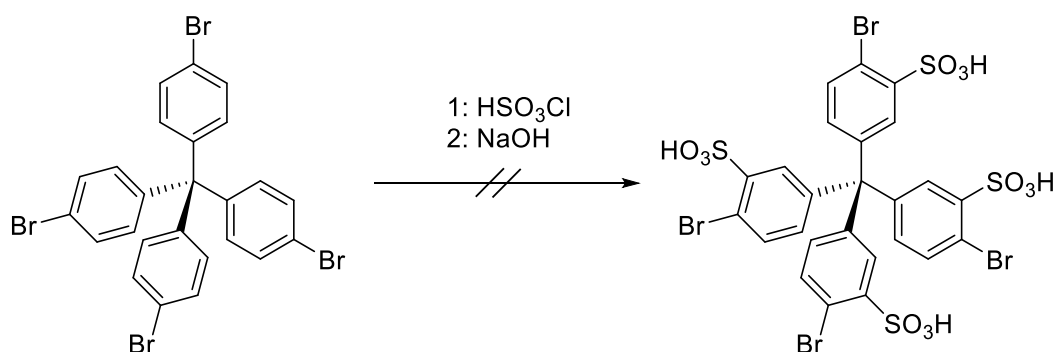
Scheme 33: Reaction conditions for the sulfonation of TPM-Br.

To find another way for introducing marker groups, the nitration of the TPM-Br building block was tested. Therefore, different procedures were performed. Initially, TPM-Br

was added to a freshly prepared solution of concentrated nitric acid (10 eq.) and concentrated acetic acid and stirred for 24 hours. Due to the lack of conversion, the procedure was changed according to a procedure described by Becker *et al.* (*192*). Following this procedure, TPM-Br was added to a solution of concentrated nitric acid (10 eq.) and concentrated sulfuric acid and stirred overnight (Scheme 34). Again, no conversion was detected *via* TLC. It was hypothesised that these modifications did not work due to the high steric hindrance and other methods were thus evaluated to verify the monomolecular deposition (see chapter **4.3.3.5**).
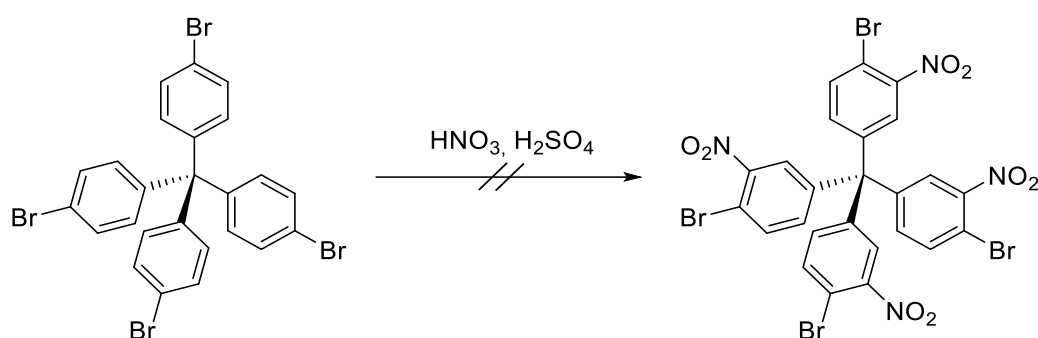
Scheme 34: Reaction conditions for the nitration of TPM-Br.

One of the key building blocks for this study is tetrakis(*p*-thiyphenyl)methane (TPM-SH). It is one of the two foreseen tetrahedral molecules to modify silicon surfaces by MLD. First, TPM-Br was modified through nucleophilic addition of sodium 2-propanethiolate in dry dimethylacetamide under Schlenk-conditions at 100 °C for 16 hours, as described by Bräse and co-workers (*193*). Precipitation in water led to the colourless solid (tetrakis(*p*-isopropylthiolphenylether)methane at 99% yield (Scheme 35). The modification was confirmed *via* ^{1}H-, ^{13}C-NMR, IR and FAB-mass analysis. Further reduction using elemental sodium in dimethylacetamide led to a maximum yield of 60%, compared to 90% reported in the literature, confirmed by the non-existence of the characteristic isopropyl peaks (3.38 ppm (heptet), 1.30 ppm (duplet)) in ^{1}H-NMR plus previous mentioned analytics.

4. Results
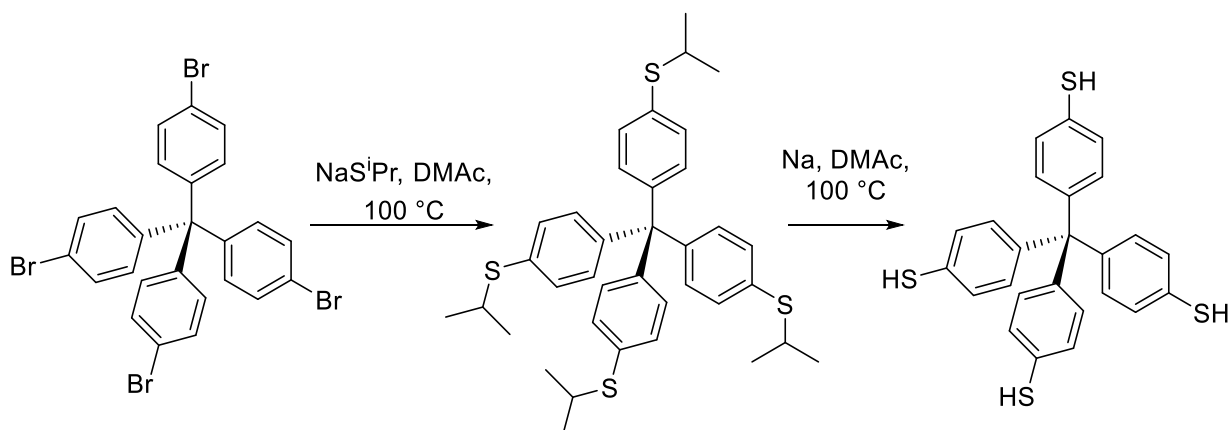
Scheme 35: Reaction conditions of the thiolation of TPM-Br to TPM-SH (193).

The second building block, which is of equally high importance for the realisation of the aims included in this thesis, is tetrakis(*p*-phenylacetylene)methane (TPM-acetylene). For the synthesis of TPM-acetylene, as reported by Nguyen and co-workers (*194*), TPM-Br, *bis*(triphenylphosphine)palladium(II) dichloride (Pd(PPh$_3$)$_2$Cl$_2$) (0.1 eq.) and CuI (0.09 eq.) were dissolved in dry and degassed diisopropylamine. Then, trimethylsilylacetylene was slowly added to the solution and stirred for 24 hours at 80 °C. Simple silica filtration and washing with ethanol led to a colourless powder (tetrakis(*p*-TMS-phenylacetylenel)methane, TPM-TMS-acetylene) at 84% yield (literature 67% yield) (Scheme 36), confirmed, for example, by the arising trimethylsilyl peak at 0.23 ppm (singlet).
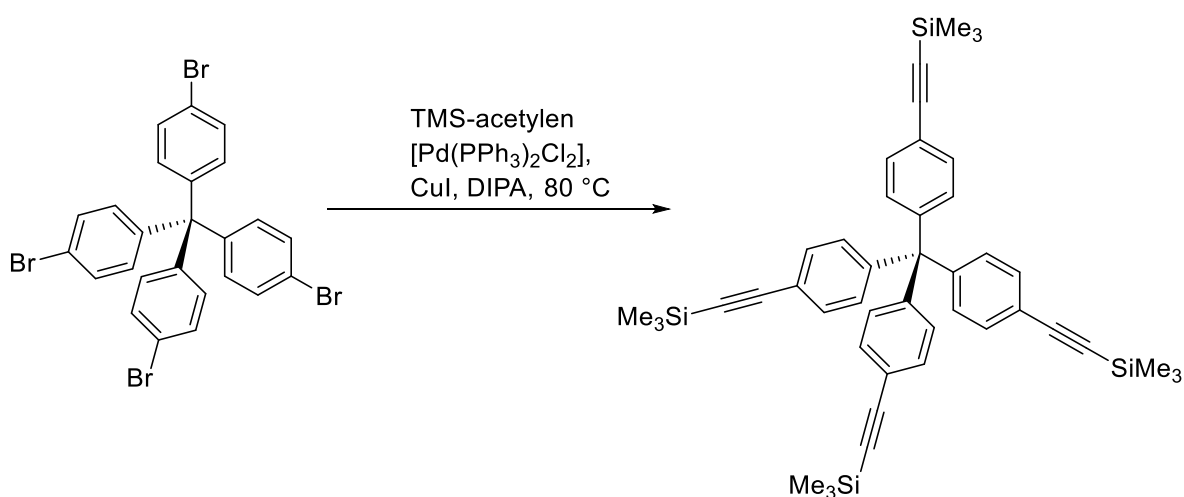
Scheme 36: Reaction conditions for the synthesis of TPM-TMS acetylene (194).

To deprotect TPM-TMS-acetylene, the product from the aforementioned reaction, was dissolved in dichloromethane and a solution of methanol and 30 eq. of K_2CO_3 were added and stirred overnight. After column chromatography, tetrakis(*p*-phenylacetylene)methane was obtained at a yield of 98% (Scheme 37) (*194*) and confirmed by the disappearing TMS-signal and appearance of the acetylene signal at 3.06 ppm (^{1}H-NMR).
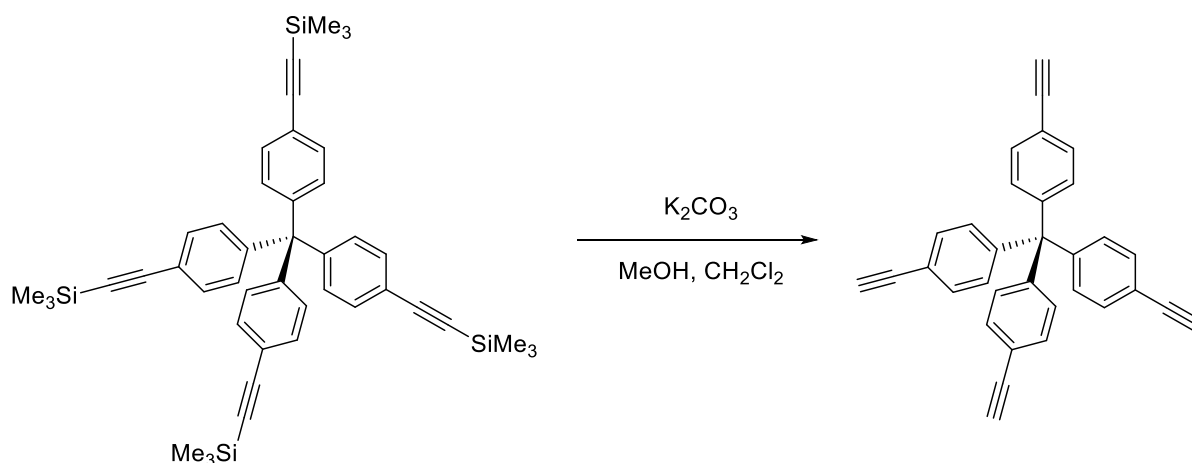
Scheme 37: Reaction conditions for the deprotection of TPM-TMS acetylene to TPM-acetylene (194).

Similar tetrahedral building blocks can be synthesised with a silicon or germanium centre instead of a carbon centre. In this study, silicon centred building blocks are not suitable because of the planned modification of silicon surfaces and the resulting problems in analytical detection. For the synthesis of germanium-centred tetraphenyl monomers (TPGe), dibromobenzene was lithiated with *n*-butyllithium in hexane at -30 °C. Afterwards, a solution of diethyl ether and $GeCl_4$ was slowly added *via* a dropping funnel and stirred for at least 8 hours. The resulting colourless solid was recrystallised in toluene and the product tetrakis(*p*-bromophenyl)germane was received at a rather low yield of 40% (Scheme 38). In comparison to TPM-Br, FAB-mass analysis of TPGe-Br shows the same fragmentation patterns shifted to higher masses. ^{1}H-NMR results show a slight shift to higher ppm-values. Compared to literature, the lower obtained yield was either a result of using desactivated *n*-butyllithium or insufficient Schlenk-conditions (*195*). Even after using fresh *n*-butyllithium, no improvement was observed.
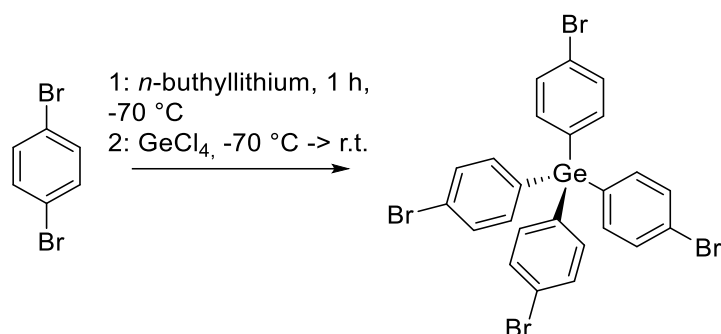
Scheme 38: Reaction conditions synthesis of TPGe-Br (195).

The subsequent modification steps to synthesise tetrakis(*p*-phenylacetylene)germane from Bräse and co-workers proceeded in the same way as already described for the synthesis of TPM-acetylene with yields of 90% (coupling) and 99% (deprotection) (Scheme 39) (*196*). By comparison of the ^{1}H-NMR results of TPGe-acetylene and TPM-acetylene, a shift to higher ppm-values is detected as well (Figure 25).
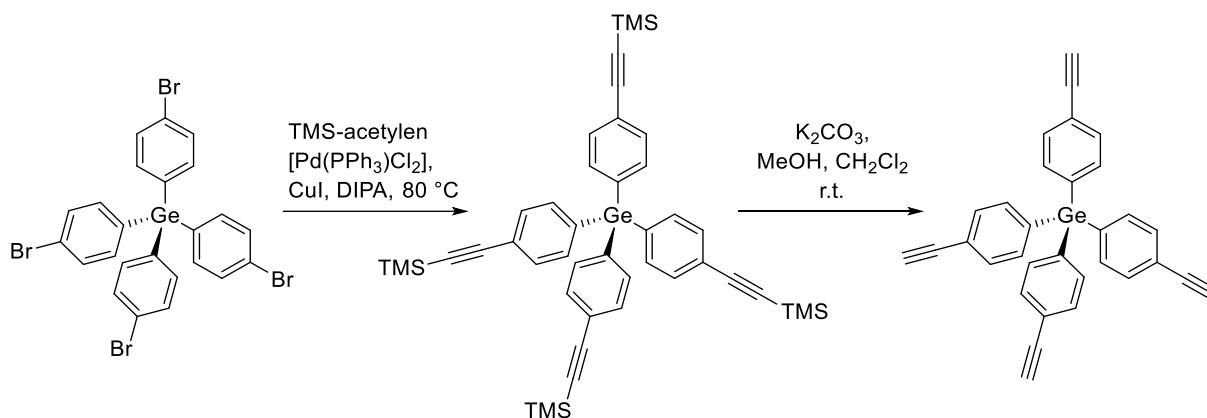
Scheme 39: Reaction conditions for the synthesis of TPGe-acetylene starting from TPM-Br (196).
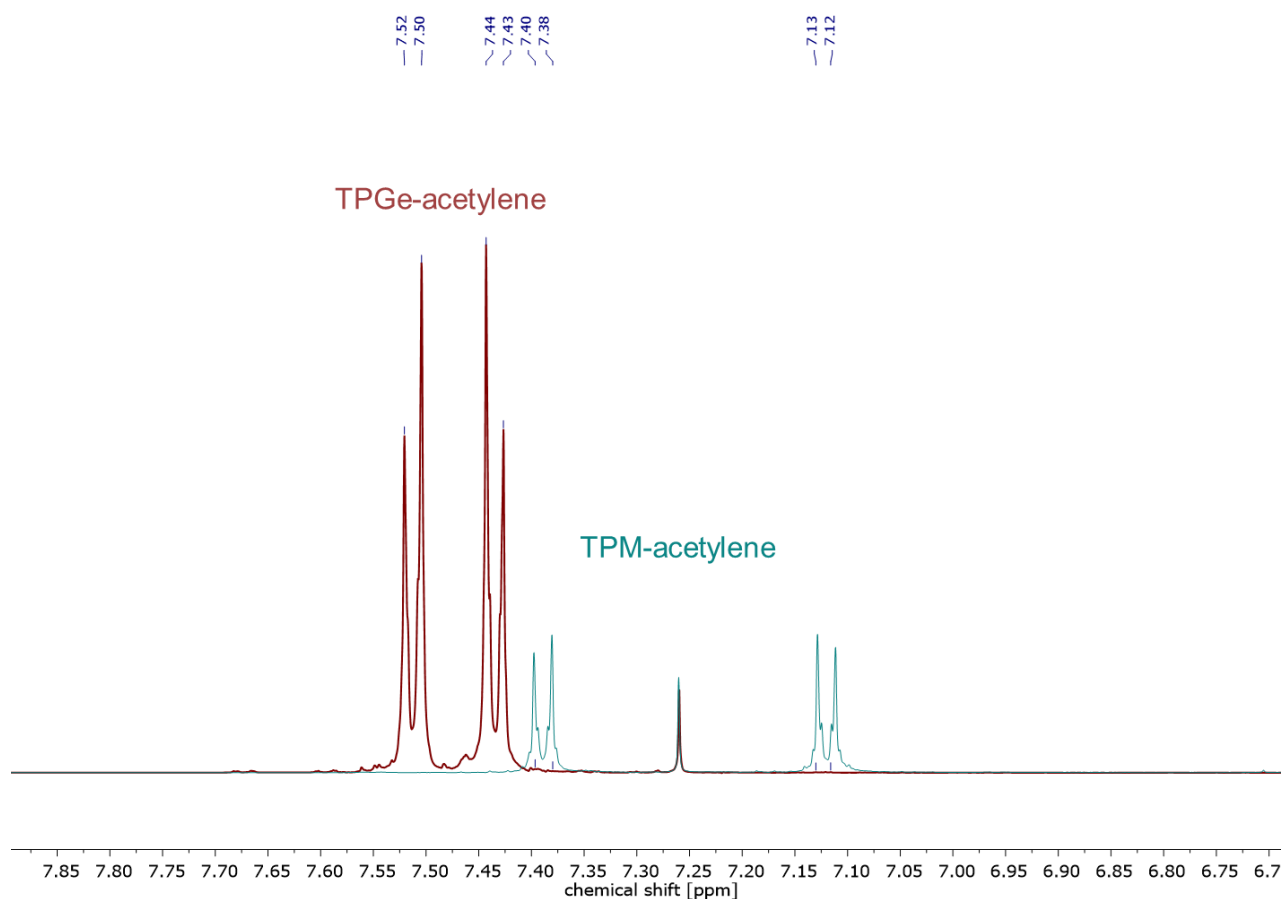
Figure 25: Combined ^1H spectrum of the two aromatic duplets of TPGe-acetylene (red) and TPM-acetylene measured in CDCl$_3$.

To enhance the pore size, but maintain the tetrahedral structure, adamantane was also used as the core unit. Therefore, adamantyl bromide was modified *via* Friedel-Crafts alkylation using aluminium chloride as the catalyst, benzene as the solvent and reactant, and *t*-butyl bromide under reflux conditions for 24 hours. After washing the resulting precipitate, tetraphenyladamantane (TPA) was obtained as a colourless powder at a yield of 74% (Scheme 40) (*197*). Due to insolubility, no NMR-spectra could be obtained but the product was confirmed by FAB- and high resolution mass electron ionisation measurements.

4. Results
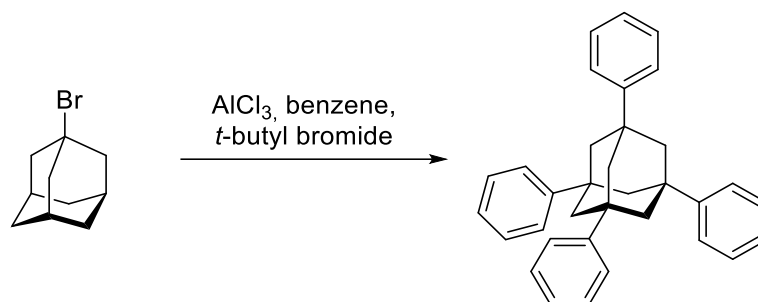
Scheme 40: Reaction conditions for the synthesis of TPA (197).

To introduce accessible functional groups for further modifications in the *para* position, bromination was performed. Due to the lower steric hindrance, compared to the TPM as core unit, a higher number of *meta* substituted product is obtained by following the procedure of Bräse and co-workers (*198*). Subsequently, the process for the bromination of TPM was adapted for the adamantane product. Due to the poor solubility of tetraphenyladamantane in chloroform, high yields were found to require more equivalents (18 eq.) of bromine. After recrystallisation, tetrakis(*p*-bromophenyl)adamantane (TPA-Br) was obtained as a colourless solid at a yield of 74% and confirmed *via* NMR-spectroscopy, mass analysis and IR-spectroscopy. Further modifications of TPA-Br were not performed due to prioritising the establishment of surface modifications by TPM-core building blocks.
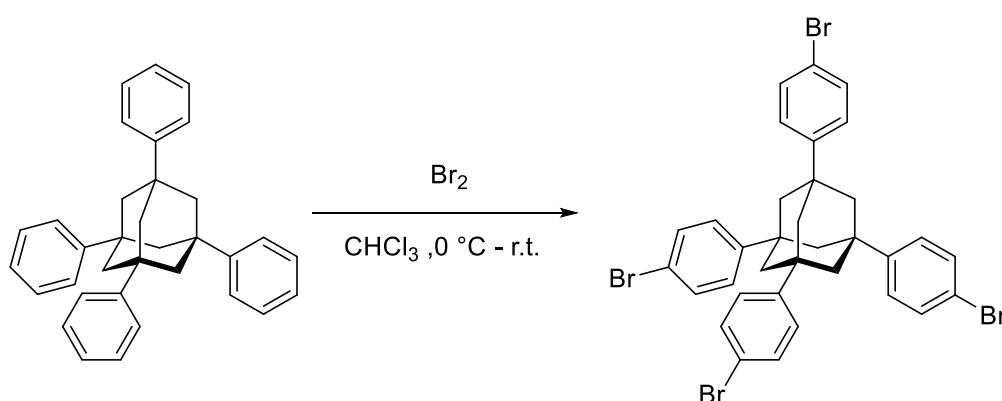
Scheme 41: Reaction conditions for the synthesis of TPA-Br starting from TPA.

4.1.2 Building blocks for amino-yne chemistry

In order to synthesise suitable building blocks for amino-yne "click" reactions, various reactions to obtain secondary amines were evaluated in the Bachelor thesis "Bausteinsynthese für Amino-In Synthesen auf Oberflächen" by David Geiß under the supervision of Prof. Dr. Michael Meier and under my practical co-supervision (*199*). Those included, imine-condensation of 1,4-phenylenediamine with isobutyraldehyd and terephtalaldeyde with butylamine and subsequent hydrogenation (*192, 200*) nucleophilic substitutions of bromobenzene and TPM-Br with butylamine, and preliminary Hartwig-Buchwald cross-coupling reactions of TPM-Br with buylamine (*201–203*) The latter was chosen due to incomplete conversions when employing the other procedures. Scheme 42 shows the general synthesis procedure for tetrakis-(*p-n*-butylaminophenyl)methane (TPM-*sec* butylamine) *via* a Hartwig-Buchwald cross-coupling reaction. Tris(dibenzylideneacetone)dipalladium(0) (Pd$_2$dba$_3$) (0.08 eq.) as catalyst, 2-dicyclohexylphosphino-2′,6′-dimethoxybiphenyl (SPhos) (0.24 eq.) as ligand, potassium *tert*-butanolate (KOtBu) (5.6 eq.) as base, and *n*-butylamine (6.0 eq.) were dissolved in 7 mL dry toluene and heated to 100 °C for 20 hours under argon atmosphere (HB1).
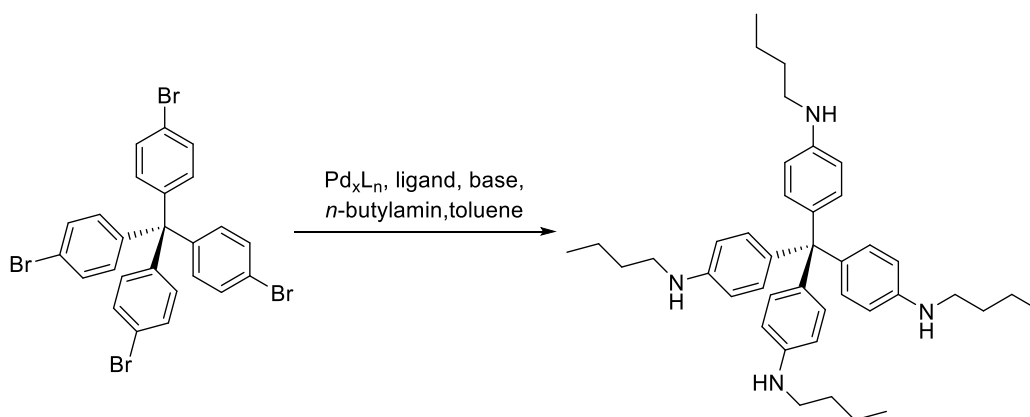
Scheme 42: General synthesis of TPM sec. butylamine.

To evaluate the best reaction conditions, various parameters were changed, and the crude reaction mixture was analysed *via* gel permeation chromatography (Figure 26). First, the equivalents of KO^{t}Bu used as a base were varied from 5.6 to 6 (Figure 26 (a This change increased the conversion to the desired product (retention time ca. 19 minutes). Moreover, the influence of using caesium carbonate (Cs$_2$CO$_3$) as a base instead of KO^{t}Bu was evaluated. As can be seen from Figure 26 (b) this resulted

4. Results

in a higher amount of product, even with lower catalyst loadings (16 mol% instead of 20 mol%).
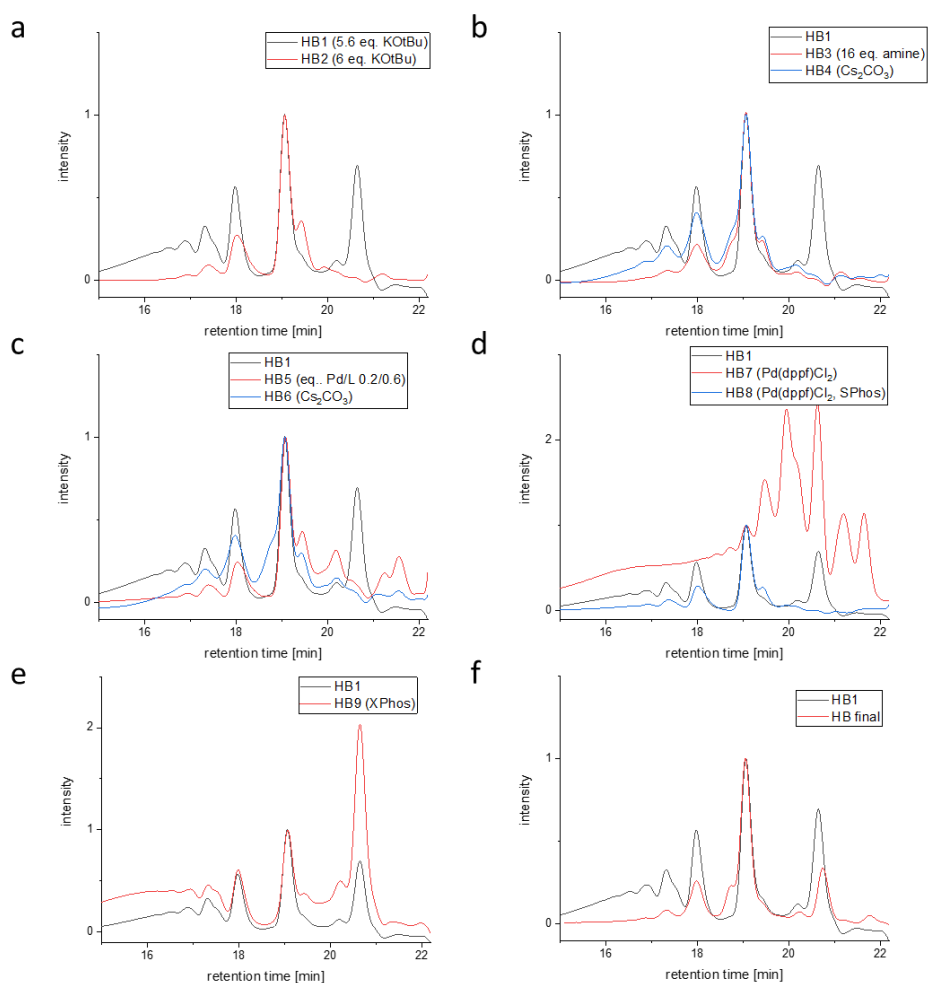
Figure 26: SEC-data of the Hartwig-Buchwald reaction using several reaction conditions compared to the standard 0 (0.08 eq. Pd_2dba_3, 0.24 eq. SPhos, 5.6 eq. KOtBu, 6 eq. butylamine, 7 mL toluene)(HB1): (a) 6 eq. of KOtBu instead of 5.6 eq (HB2). (b) variation of the base: 8 eq. Cs_2CO_3, 6 eq. butylamine (black) (HB4) followed by higher equivalent of amine: 8 eq. Cs_2CO_3 and 16 eq. butylamine (HB3) (c) higher equivalent of catalyst/ligand and variation of the base: (0.2 eq. Pd_2dba_3 and 0.6 eq. SPhos (black) (HB5), X 0.2 eq. Pd_2dba_3, 0.6 eq. SPhos and 8 eq. Cs_2CO_3 (red) (HB6), (d) variation of the catalyst and additional ligand: 0.08 eq. Pd(dppf)Cl_2 (green) (HB7), 0.08 eq. Pd(dppf)Cl_2 and 0.24 eq. SPhos (red) (HB8) (e) variation of the additional ligand: 0.24 eq. XPhos (black) (HB9) instead of 0.24 eq. SPhos (HB1) (f) comparison of initial reaction conditions and the optimised ones: 10 eq. Cs_2CO_3, 12 eq. butylamine, 0.16 eq. Pd_2DBA_3, and 0.48 eq. SPhos (HB final).

Additionally, increasing the equivalents of the amine had a positive effect as well. In case of higher catalyst loadings (Figure 26 (c)), the influence of the base was insignificant. Also, the separation of the products *via* column chromatography was facilitated. By using Pd(dppf)Cl_2 as palladium catalyst instead of Pd_2dba_3, as described by Jørgensen, no improvement was detected, but in addition with SPhos, the conversion and selectivity towards the product increased (Figure 26 (d))(*204*). Furthermore, XPhos was evaluated as additional ligand instead of SPhos using

72

Pd$_2$dba$_3$ as catalyst. However, the selectivity towards the desired product decreased (Figure 26 (e)). In conclusion, the best result was achieved using 0.16 eq. Pd$_2$dba$_3$ as catalyst, 0.48 eq. SPhos as additional ligand, 10 eq. Cs$_2$CO$_3$ as base, 12 eq. butylamine, 0.16 eq. Pd$_2$DBA$_3$, and 0.48 eq. SPhos.
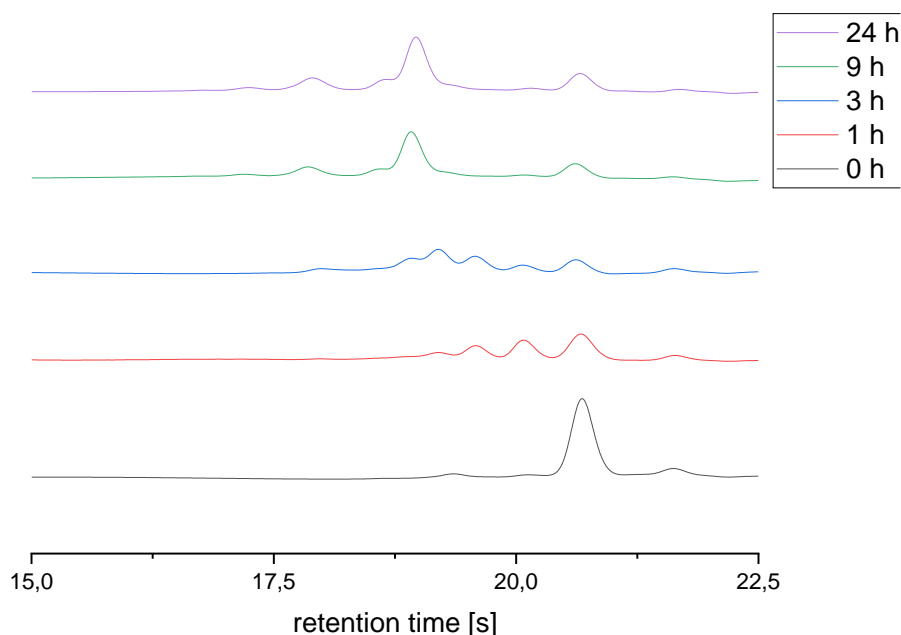
Figure 27: SEC curves of the Hartwig-Buchwald reaction at the beginning (black), after one hour (red), three hours (blue), nine hours (green) and 24 hours (violet)

After determining the optimised reaction conditions, the optimum reaction time was investigated. Therefore, every hour a sample was taken, quenched with water, filtered through a syringe filter and analysed *via* size exclusion chromatography (SEC). As can be seen from Figure 27 after 9 hours, no further change in the product composition was observed. Therefore, the subsequent reactions were run for at least 9 hours. Applying this procedure, the following building blocks were synthesised (Scheme 43). Exemplarily, Figure 28 shows the ^{1}H-NMR of TPM-*sec.* butylamine and the distinct labels for each type of hydrogen atom.

4. Results
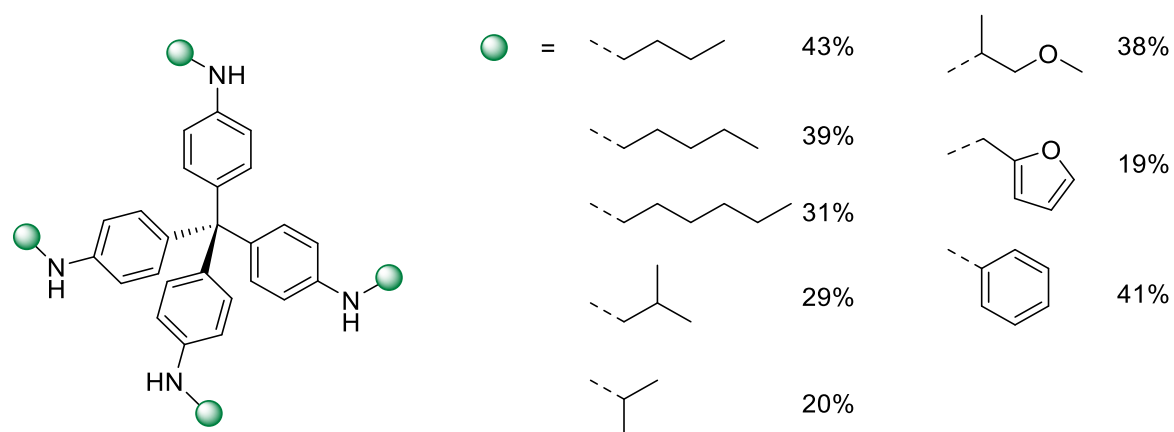
Scheme 43: Synthesised secondary amine building blocks based on a TPM core. The green dot represents different rests bound to the amine with the corresponding yield derived after column chromatography.
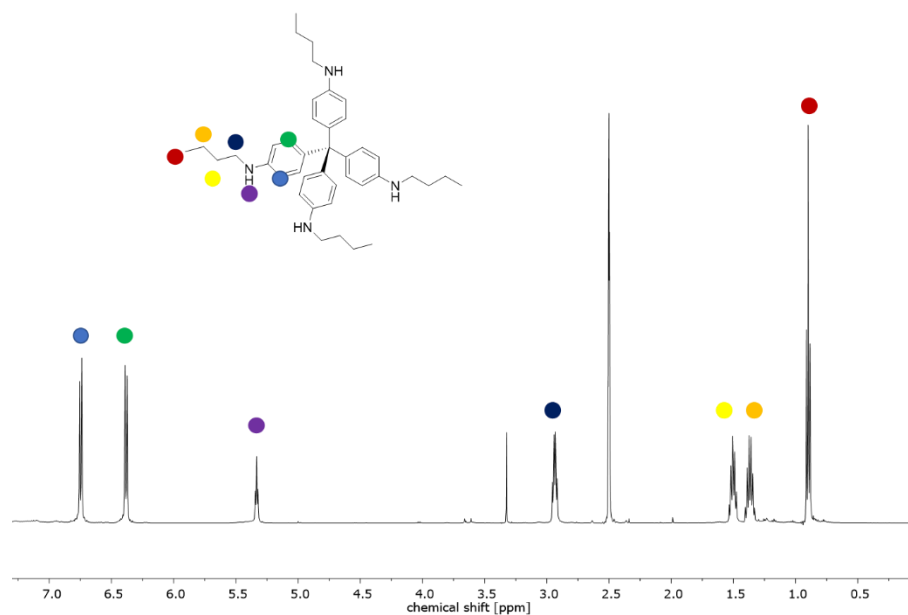
Figure 28: ^{1}H-NMR of TPM-sec. butylamine in DMSO-d$_6$ as solvent.

The synthesis of tetrakis-(*p*-allylaminophenyl)methane starting from TPM-Br was performed the same way: 10 eq. Cs$_2$CO$_3$, 12 eq. allylamine, 0.16 eq. Pd$_2$DBA$_3$, and 0.48 eq. SPhos, and heated overnight in a crimp vial. Nevertheless, the desired product could not be isolated. Thin layer chromatography showed a large number of inseparable spots. To suppress side reactions, such as the potential polymerisation of allylamine, different reaction conditions were evaluated. First, tetrakis(*p*-aminophenyl)methane (TPM-NH$_2$) was added to allylbromide dissolved in toluene and coupled *via* nucleophilic addition under elevated temperatures. Due to the higher equivalents of the allylbromide (TPM-NH$_2$: allylbromide = 1:12), double substitution on

the amine was observed resulting in tetrakis(*p-N,N'*-dallylaminophenyl)methane (TPM-diallylamine) at a yield of 86%. Even after reducing the molar ratio of the reactants to 1/4 (TPM-NH$_2$/allylbromide), no monofunctionalisation was observed; instead a variation of non, mono- and di-substituted amines was obtained. This mixture might be due to the higher reactivity of the secondary amine compared to the primary amine (*205*). Another approach to synthesise tetrakis-(*p*-allylaminophenyl)methane was performed: a Tsuji-Trost allylation in water using allylcarbonate, catalysed by Pd nanoparticles, as described by Meier and co-workers (*206*). In an additional reaction, applying the aforementioned reaction conditions, DMSO was used as co-solvent. However, the reaction without co-solvent, as well as the reaction using DMSO as co-solvent, led to the fully substituted amine at a yield of 28% and 72%, respectively (Scheme 44).
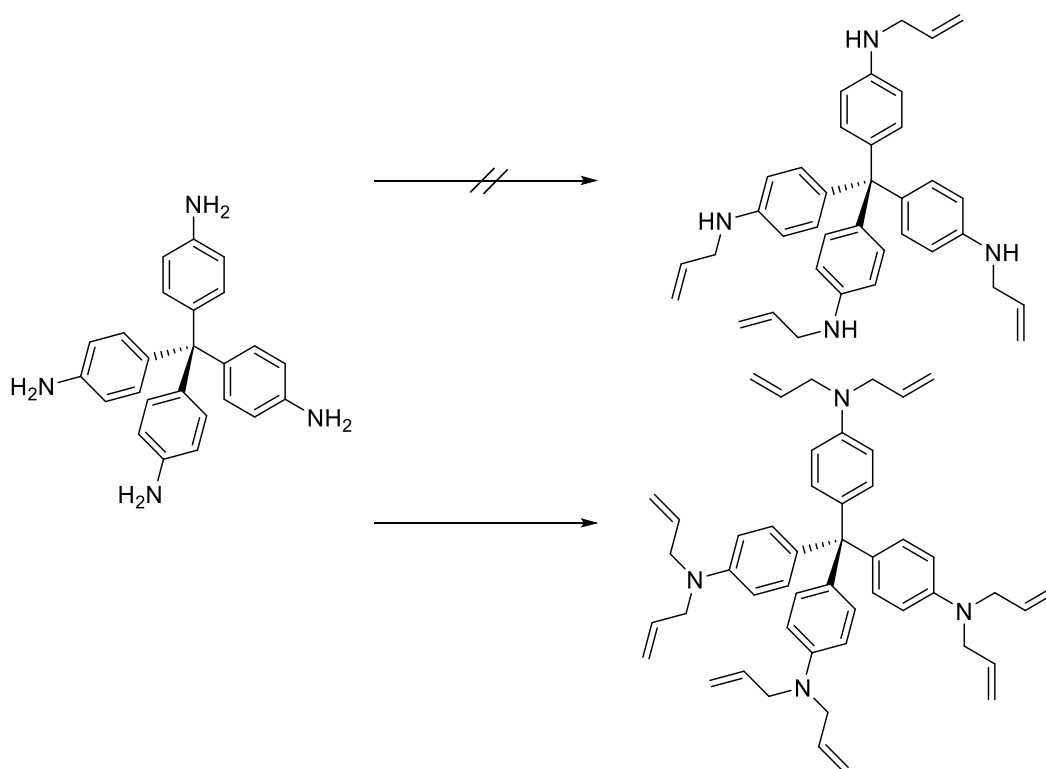
Scheme 44: Allylation of TPM-NH$_2$/Br and the resulting product (TPM-diallylamine).

In the Bachelor thesis "Bausteinsynthese für Amino-In Synthesen auf Oberflächen", synthesis protocols like the Steglich esterification and the coupling *via* 1,1'-carbonyldiimidazole (CDI) of benzyl alcohol and propiolic acid and acid catalysed esterification of diethyleneglycol and propiolic acid were compared for the synthesis of propiolic ester compounds (*199*) The esterifications *via* activated transition states

(Steglich, CDI) led to high amounts of side products, which might be explained by the oligomerisation of propiolic acid or by hydroamination reactions of the reactant and the coupling reagent. In acidic media, the hydroamination reaction is suppressed because of the faster acid-base hydrogen exchange and thus, 2-propynoic acid, 1,1'-(oxydi-2,1-ethanediyl) ester was synthesised. The synthesis procedure was adapted from Long and co-workers (*207, 71, 208*). Following this procedure, diethylene glycol was dissolved in dry toluene and *p*-toluene sulfonic acid was added as catalyst. The mixture was stirred under reflux conditions using a dean stark apparatus for 18 hours obtaining a colourless liquid in 59% yield (Scheme 45). This product was then used as activated alkyne building block for surface modifications and POP synthesis via hydroamination.
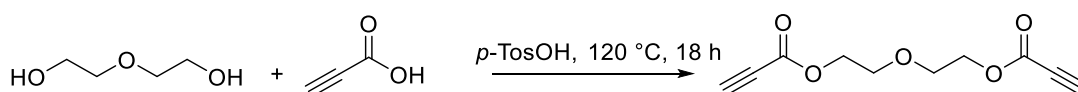
Scheme 45: General procedure for the esterification of diethylene glycol with propiolic acid under acid catalysis (71, 208, 207).

For the synthesis of more rigid propiolic ester building blocks, TPM was chosen as core unit. As a first step, a "spacer" was introduced to enhance the stability of the ester and avoid an active ester (phenylester). Therefore, Ullmann-like coupling reactions were chosen to generate aliphatic hydroxy groups for further modifications by coupling TPM-Br with ethylene glycol or 1,3-propanediol (Scheme 46).

= ethyl, propyl
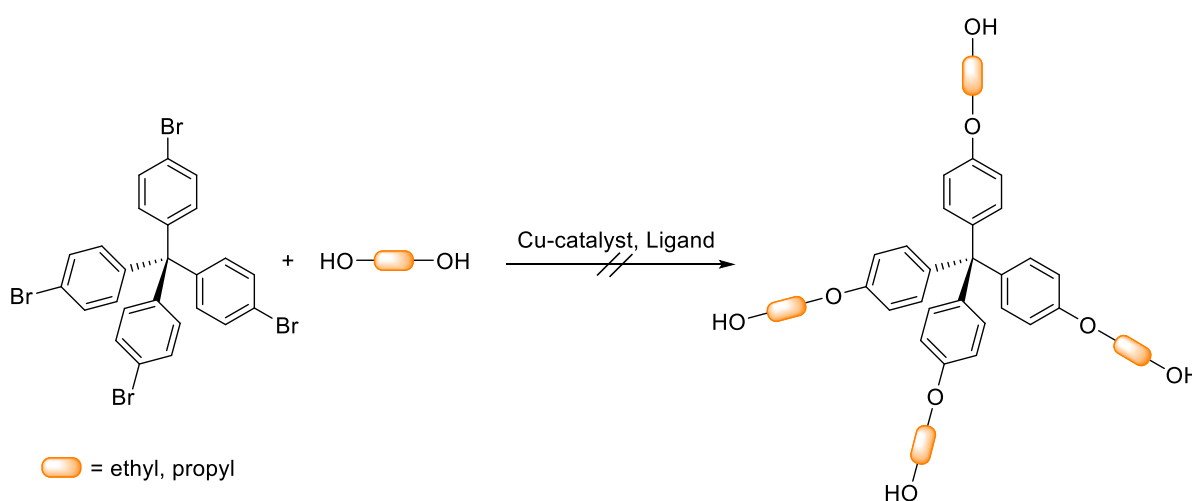
Scheme 46: General modification of TPM-Br via Ullmann-like coupling (209, 210).

Table 3: Reaction conditions tested for the Ullman-like coupling of TPM-Br and ethylene glycol/1,3-propanediol (209, 210).

Base	Catalyst	Diol	Ligand	Solvent
K_2CO_3	CuBr2	ethylene glycol	-	ethylene glycol
K_2CO_3	CuBr2	ethylene glycol	-	-
DBU	CuI	1,3 propanediol	-	xylene
DBU	CuI	1,3 propanediol	phenanthroline	toluene

All reactions were performed in an argon flooded crimp vial and stirred at 130 °C (except for the reaction in toluene, which was performed at 110 °C) (Table 3). Unfortunately, none of these reactions yielded detectable conversion by SEC or TLC because of bad solubility (entry 1 and 2) or water contaminated reactants.

methyl propiolate, DCM, r.t., 24 h.
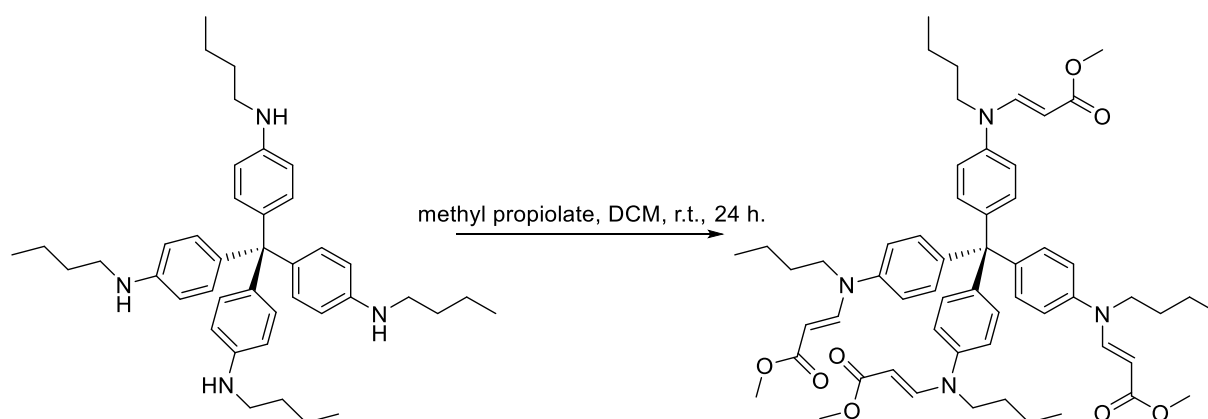
Scheme 47: Hydroamination of TPM-sec. butylamine and TPM-sec. methoxypropylamine with propiolic acid methyl ester.

The synthesis of tetrakis(*p*-*N*-butyl-*N*-2-methylmethacryl-aminophenyl)methane was realised by stirring TPM-*sec* butylamine in DCM with 4.8 equivalents of methylpropiolate for 24 hours at room temperature, leading to full conversion. The introduction of a carbonyl group was confirmed by IR spectroscopy (Figure 29) by the newly appearing C=O signal at 1690 cm^{-1}. Additionally, two new duplets at 7.8 ppm and 4.9 ppm were observed in the ^{1}H-NMR (Figure 30) compared to the ^{1}H-NMR of TPM-*sec.* butylamine (Figure 28).

4. Results
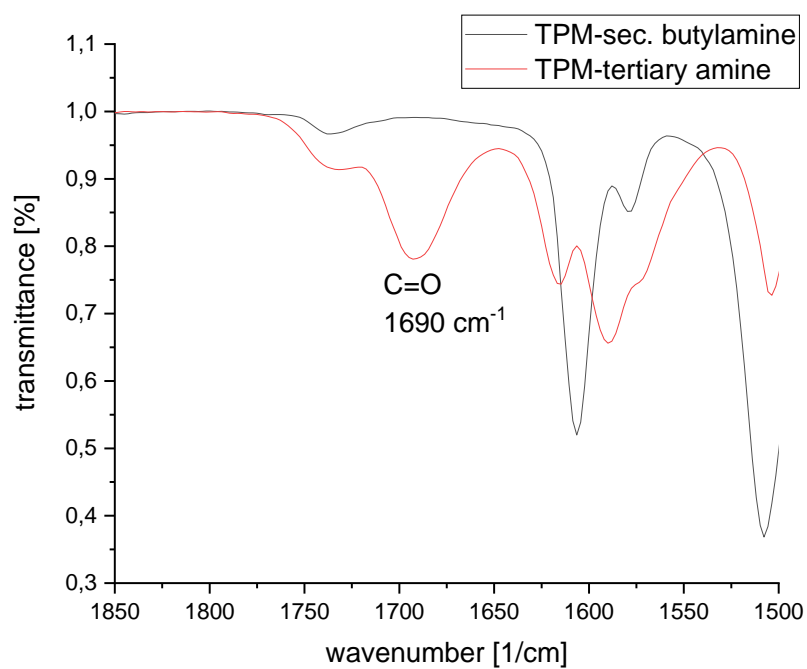
Figure 29: Infrared spectrum before (black) and after (red) reaction of TPM-sec. butylamine and propiolic acid methyl ester.
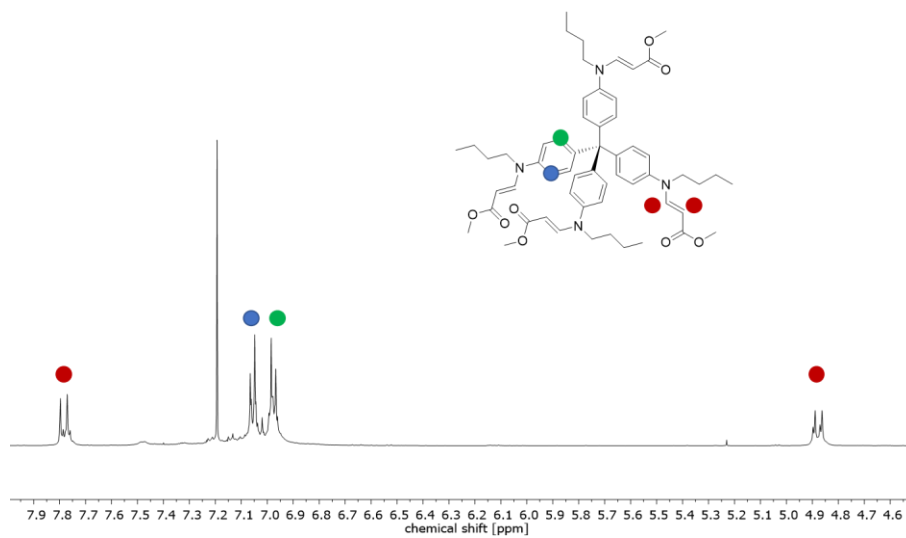
Figure 30: ^{1}H-sepctrum of the hydroaminated TPM-sec. butylamine with methyl propiolate in CDCl$_3$ as solvent.

4.2 Preparation of porous organic polymers (POPs)

In order to synthesise networks *via* amino-yne chemistry, TPM-*sec* butylamine was stirred in a solution of dichloromethane and 2-propynoic acid, 1,1'-(oxydi-2,1-ethanediyl) (PEG-dialkyne) ester at different ratios (TPM-*sec* butylamine / PEG-dialkyne: 1/4.8, 1/2.5 and 1/2) at room temperature. This serves as a model reaction for the synthesis of individual layers on surfaces (see chapter **4.3.6**). In each case, after three days, a gel was formed, which was subsequently washed with methanol and ethanol to eliminate remaining starting materials.
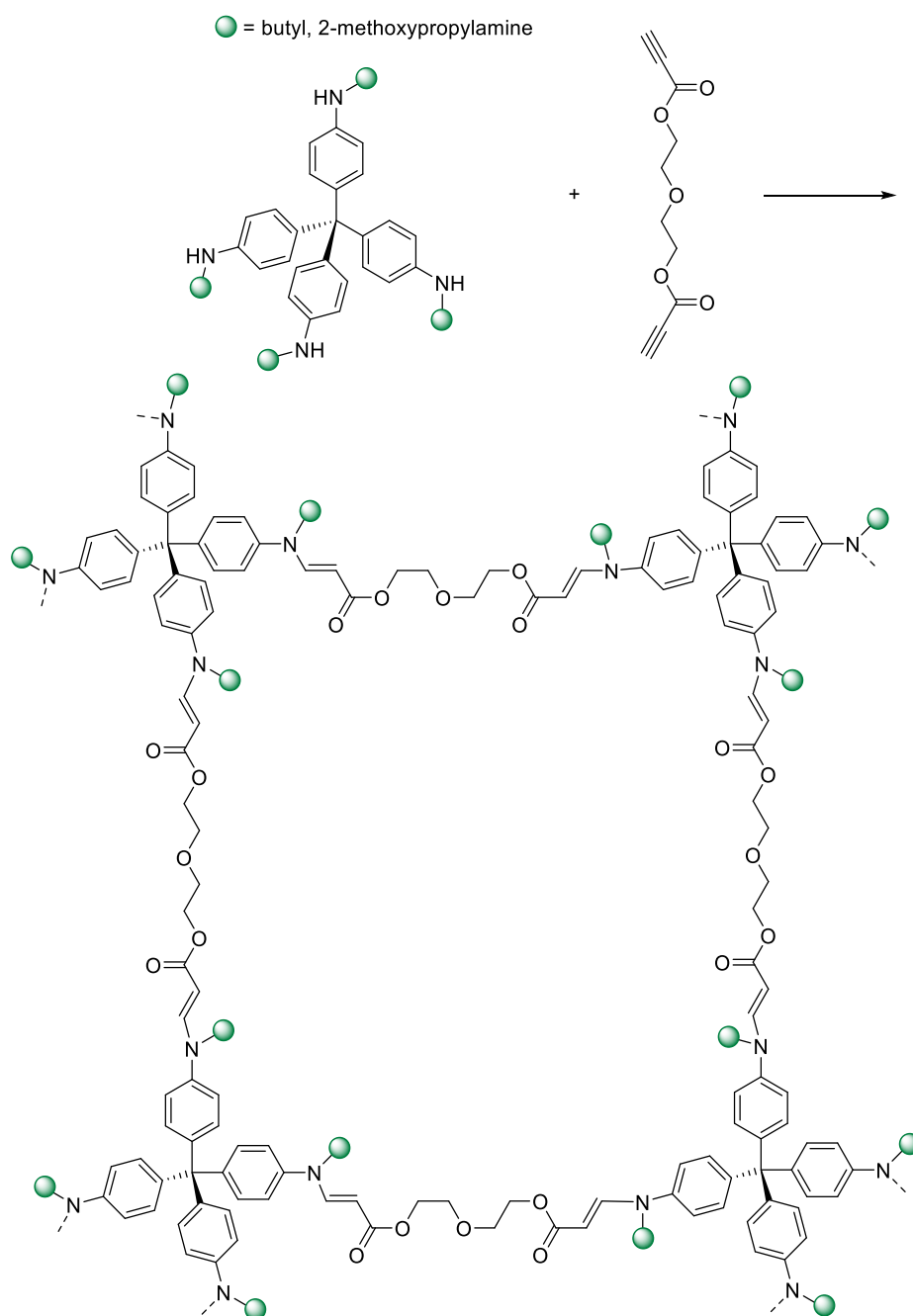
Scheme 48: General synthesis of a POP via amino yne "click" reaction.

4. Results

The porous organic framework with the highest equivalent of dialkyne exhibited a sponge-like behaviour during the workup, whereas the others precipitated as red solid. An additional POP with TPM-*sec* methoxypropylamine was synthesised in a 1:2 ratio using the same procedure. The difference in electronegativity and the sterically more demanding arm increased the reaction time to more than one week, which was reduced to two days by heating the reaction mixture to 80 °C (Scheme 48).

Due to its insolubility in every solvent, the butylamine network was not analysed *via* NMR spectroscopy but *via* IR spectroscopy, DSC, and BET measurements. DSC measurements indicated in a T_g of 113 °C and at 95.67 °C for the methoxypropylamine network. According to BET measurements, surface areas of 2.06 m^2/g (1/4.8 amine/alkyne), 4.51 m^2/g (1/2.5 amine/alkyne) and 1.82 m^2/g (1/2. amine/alkyne) were determined, which were not found to fit a trend. It was hypothesised that the linker is too flexible resulting in a collapsed structure and reduced surface areas. Figure 31 and Figure 32 show the corresponding IR spectra of the TPM-building blocks and the synthesised networks. In both spectra, the peak at 3400 cm^{-1} that corresponds to secondary amines vanishes, while a band corresponding to C-N vibrations appears at 1100 cm^{-1} as well as a band corresponding to carboxyl signals at 1700 cm^{-1}, thus confirming the crosslinking reaction.
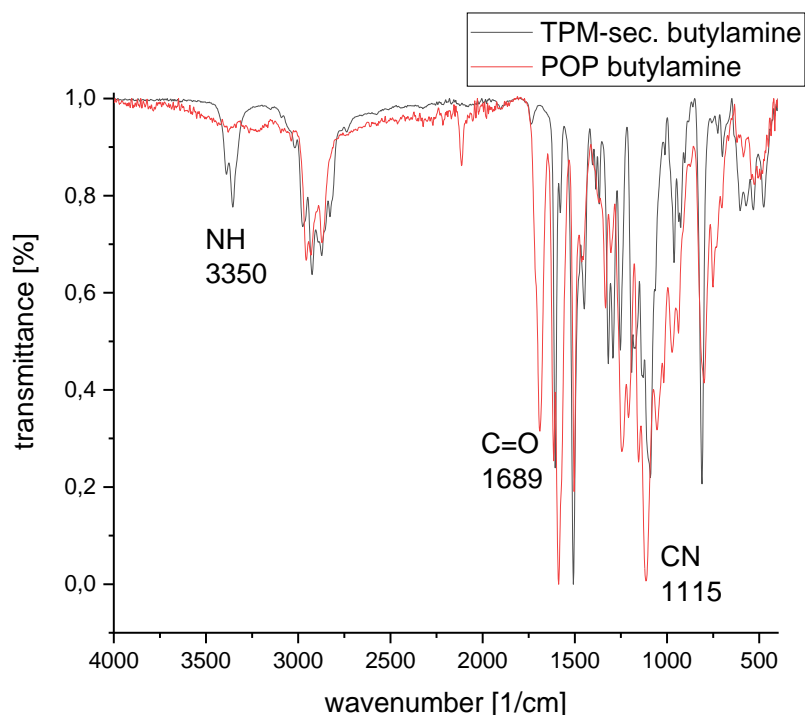
Figure 31: IR spectra of TPM-sec. butylamine and the corresponding POP.
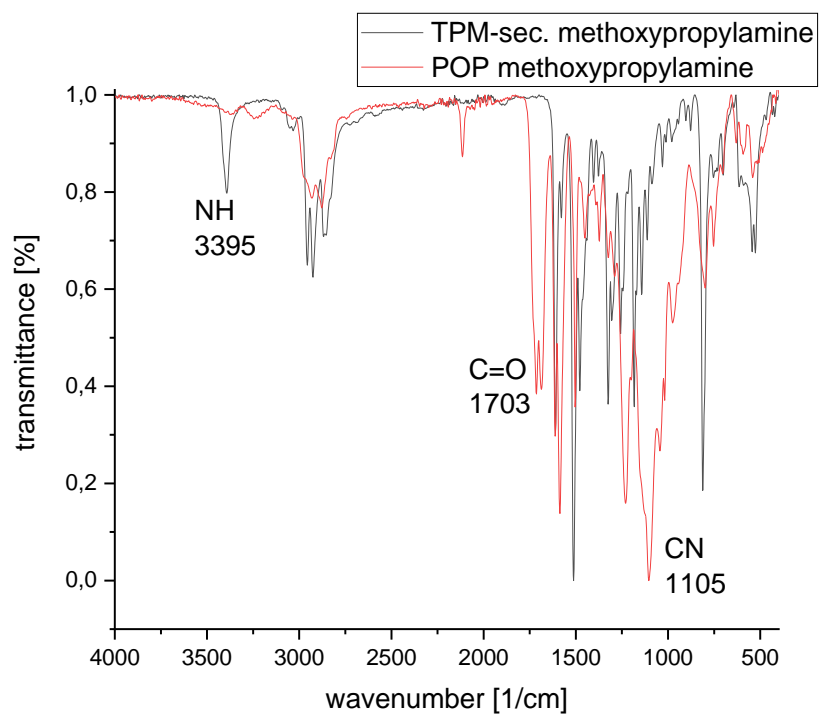
Figure 32: IR spectra of TPM-sec. methoxypropylamine and the corresponding POP.

4. Results

4.3 Layer-by-layer grafting on silicon wafers

4.3.1 Analysis of dropcasts

For the evaluation of surface attached layers, it is first necessary to fully characterise the building blocks with the available surface characterization techniques. Therefore, dropcasts (DC) of TPM-acetylene, TPM-SH and TPM-Br were made (Scheme 49) and analysed by ToF-SIMS and XPS. For the DCs, 20 mg of each building block was solubilised in 200 µl chloroform, one or two droplets were put on a freshly cleaned silicon wafer and the solvent was evaporated on air.
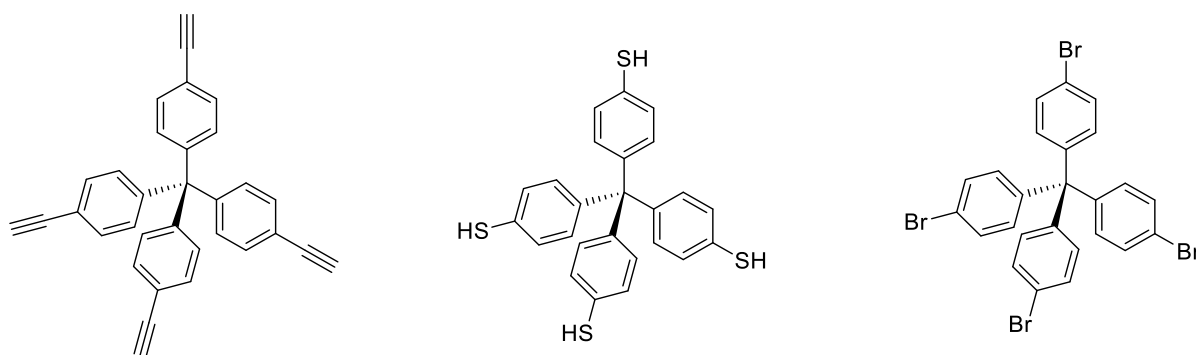
Scheme 49: Structures of molecules drop-casted for XPS and ToF-SIMS analysis.

Figure 33 shows the XPS peaks of DCs, aromatic C-C/C-H bonds at 285.0 eV and the pi-pi* transition at 291.4 eV and 291.1 eV is found, respectively, for TPM-Br and TPM-acetylene. The ratio of C-C/pi-pi* is 0.06 for both samples. For TPM-SH mainly a C-C/C-H peak at 285.0 eV was observed. The SiOx species measured by XPS could originate from substrate. Br$^-$ ions with a binding energy of 70.5 eV for Br $3d_{5/2}$ are assigned to C-Br bonding (*211*). S$^-$ ions with the binding energy of 164.0 and 228.3 eV for S $2p_{3/2}$ and S 2s, respectively, are assigned to thiol R-SH bonding (*16*). Furthermore, in the O 1s spectra, oxygen ions of SiOx at 532.5 eV and water molecules at 534.0 eV could be identified (*212, 213*). In TPM-acetylene, a peak at 285.7 eV was found, which is not successfully assigned and might originate from acetylene triple bond. Concerning the molecular structure, the ratio of triple bond carbon to others is 8 to 25 (i.e. 1 to 3), however the peak ratio of 285 eV to 285 7 eV is around 1 to 5.3 meaning there was more C-C/C-H bonding as expected. Although some of it could

originate from carbon contamination. Table 4 shows the atomic percentage of the different chemical states on the DCs.
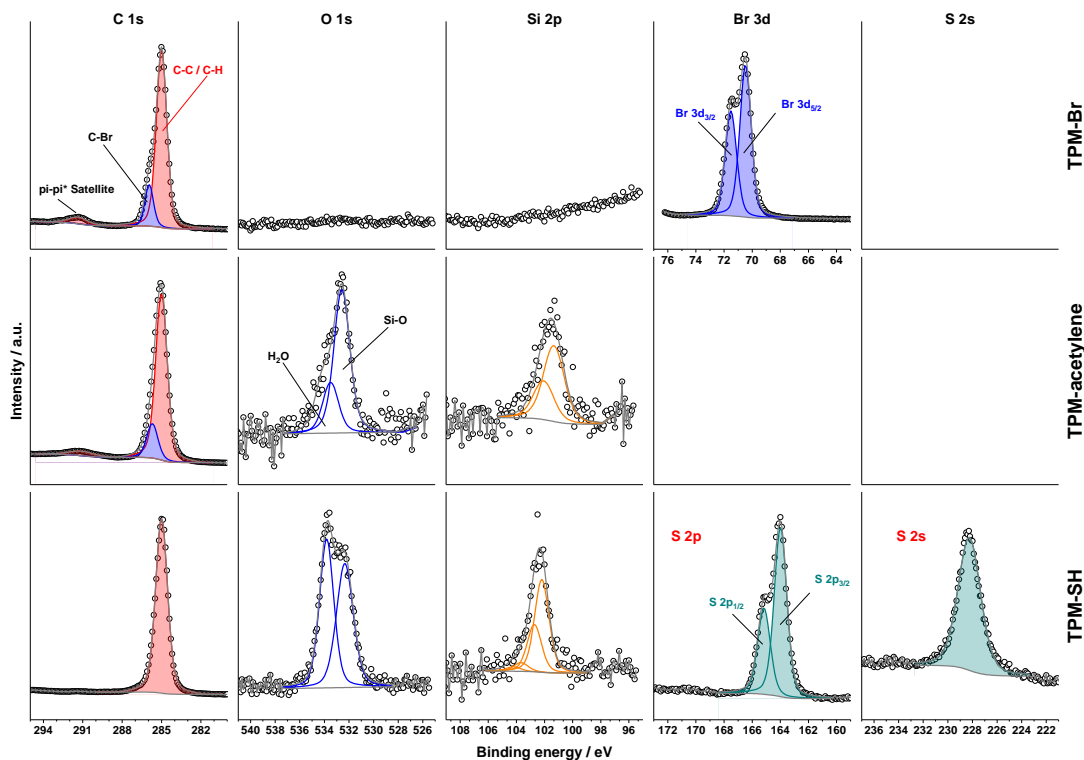
Figure 33: XPS-spectra of the DCs of various signals (carbon, oxygen, silicon, bromine and sulfur) of TPM-acetylene, TPM-SH and TPM-Br.

Table 4: Atomic% of three building blocks and their atomic composition measured via XPS.

peak position	TPM-acetylene		TPM-SH		TPM-Br	
	meas.	theor.	meas.	theor.	meas.	theor.
C 1s (285.0 eV)	79.0%	72.7%	94.9%	86.2%	69.5%	70.0%
C 1s (286.6 eV)	15.7%	24.2%	-	-	13.2%	13.8%
C 1s (288.5 eV)	4.5%	3.0%	-	-	4.3%	3.5%
S 2s (228.0 eV)	-	-	2.7%	13.8%	-	-
Br 3d$_{5/2}$ (70.5 eV)	-	-			13.1%	13.8%

ToF-SIMS analysis enabled the identification of specific masses referring to the respective molecular fragments. Figure 34 shows two exemplary fragments for each

4. Results

building block. The acetylene-group and the aromatic ring could nicely be observed, compared to the excerpt of the same mass (m/z) of the blank, etched surface. In case of the TPM-SH it was possible to detect a large fragment representing half of the building block ($C_{13}H_9S_2^-$) besides a fragment representing one arm ($C_7H_4S^-$). For TPM-Br, the bromine ion and, inter alia, the fragment of one arm without bromine could be detected. In following discussions related to ToF-SIMS, other fragments had to be used due to low und insignificant intensities.
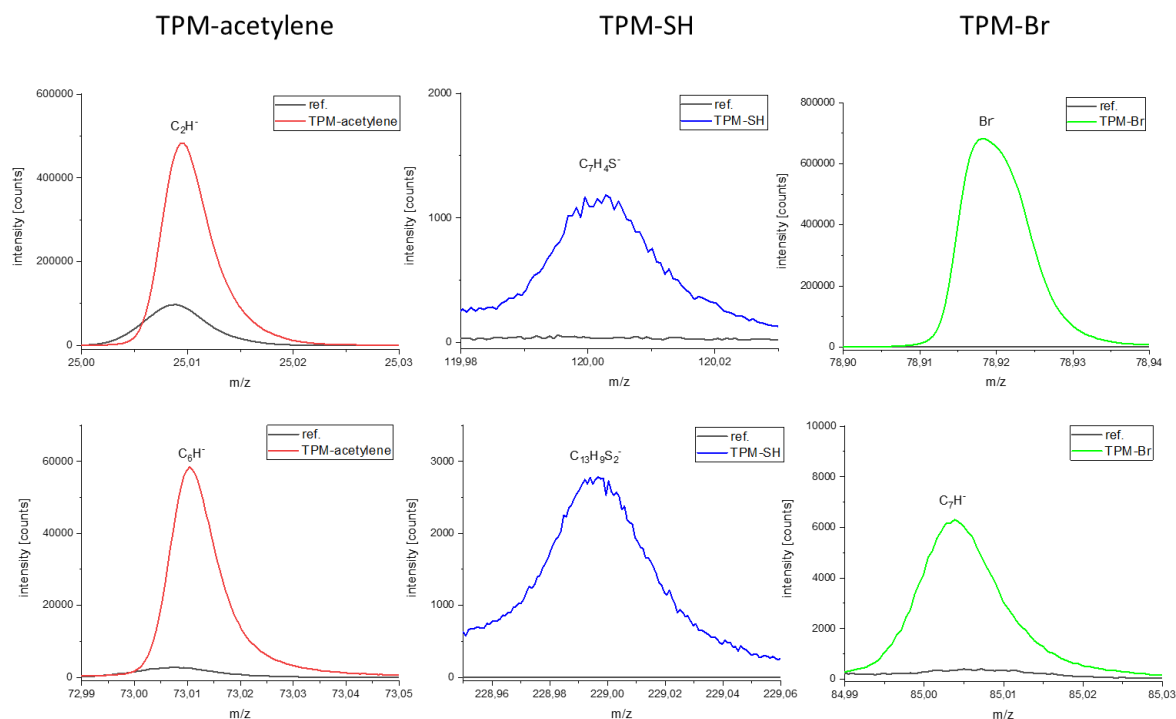
Figure 34: ToF-SIMS analysis of TPM-acetylene, TPM-SH, and TPM-Br. For each substrate, two specific negative fragments are shown allowing a clear detection of these compounds on the silicon wafer.

4.3.2 Silanisation processing

In general, silicon wafers were cut and then cleaned by placing them consecutively in chloroform, acetone, and ethanol in an ultrasonic bath. The substrates were then dried under the flow of argon stream. Treatment with piranha solution (H_2SO_4/H_2O_2, 70:30 v/v) at 80 °C for 30 min activated the surface and removed organic residues. This treatment was followed by two rinses with distilled water and isopropanol and subsequent drying under argon stream. The freshly edged samples are immediately modificated to avoid oxidation.

Initially, cleaned wafers were exposed to monolayer deposition solutions with a concentration of 8.4 mM of alkene-terminated silanes, namely trihydroxy(10-undecen-1-yl) silane (**Sil1**), trichloro(10-undecen-1-yl) silane (**Sil2**), or trimethoxy(7-octadecen-1-yl) silane (**Sil3**), in dry toluene at room temperature for 1.5 hours (Scheme 50). The procedure was carried out in an argon purged glove bag and the relative humidity was 28-33%. Samples were withdrawn from the silane solutions after the indicated deposition time and washed with chloroform, toluene, and acetone in an ultrasonic bath to remove adsorbed/non-covalently edposited siloxane oligomers formed by oligomerisation of the silanes in the solution.
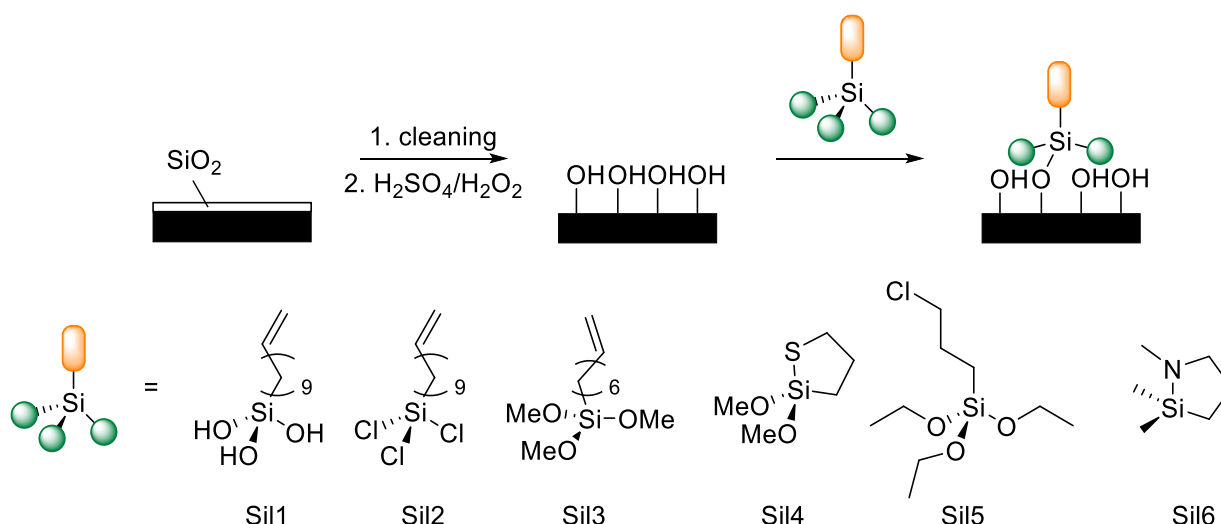
Scheme 50: Schematic display of the silanisation procedure with cleaning/etching and silansiation itself.

The modified silicon wafers were then analysed by XPS and ToF-SIMS. shows the development of carbon and silicon atomic percentages before (blank cleaned silicon wafer = ref) and after the silanisation. **Sil1** and **Sil3** showed a slight increase of carbon signal, however the decrease of the silicon percentage was either very low (Sil3,

4. Results

1.25%) or not detectable. **Sil2,** on the other hand, showed high oligomerisation resulting in a significant change of carbon and silicon percentage due to the formed multilayers.

Table 5 shows the development of carbon and silicon atomic percentages before (blank cleaned silicon wafer = ref) and after the silanisation. **Sil1** and **Sil3** showed a slight increase of carbon signal, however the decrease of the silicon percentage was either very low (Sil3, 1.25%) or not detectable. **Sil2**, on the other hand, showed high oligomerisation resulting in a significant change of carbon and silicon percentage due to the formed multilayers.

Table 5: Atomic% measured by XPS of a blank, cleaned silicon wafer as reference and the silanes Sil1, Sil2 and Sil3 after silanisation.

peak position	Sil1		Sil2		Sil3	
	ref.	silane	ref.	silane	ref.	silane
C 1s (285.0 eV)	8.8%	10.5%	9.0%	28.2%	3.6%	5.8%
Si 2p$_{3/2}$ (99.5 eV)	43.2%	43.4%	44.7%	34,4%	48.7%	47.5%

ToF-SIMS analytical data further explained the low variation of the atomic percentage detected *via* XPS (Figure 35). Since the brightness of the signal increases the more an ionic species of a selected fragment is present, a change of brightness was expected if the wafers treated with **Sil1-3** were compared with the references. However, compared to the relatively clean silicon wafer (Figure 35, **Sil1** ref., (a)), the surface after the treatment with Sil1 is not homogeneous, as visualized by the dark red spots on the bright yellow background. During the silanisation step, some contamination occurred, based on the appearance of darker spots in the Si$^+$ and darker spots in the $C_2H_5^+$ signal (Figure 35, **Sil1**, silane (b)). respectively. This inhomogeneity is herein considered the reason for the divergent results of the change of carbon percentage, while the silicon percentage remains nearly constant in XPS. High resolution ToF-SIMS results showed a significant increase for the $C_{11}H_{21}^-$ fragment, which is an indication that **Sil1** was attached onto the surface. In the case of the surface modification with **Sil3**, no major difference between the blank silicon and the modified one was observed (Figure 35, (d) and (e)). Due to the indication of oligomerisation of Sil2 *via* XPS, no further analysis with ToF-SIMS was conducted. As shown in chapter **2.3.2**, chlorosilanes are more reactive than their methoxy or ethoxy counterparts. It is

hypothesised that the modification in the glove bag under argon atmosphere could not prevent small amounts of physisorbed water and thus led to this oligomerisation.
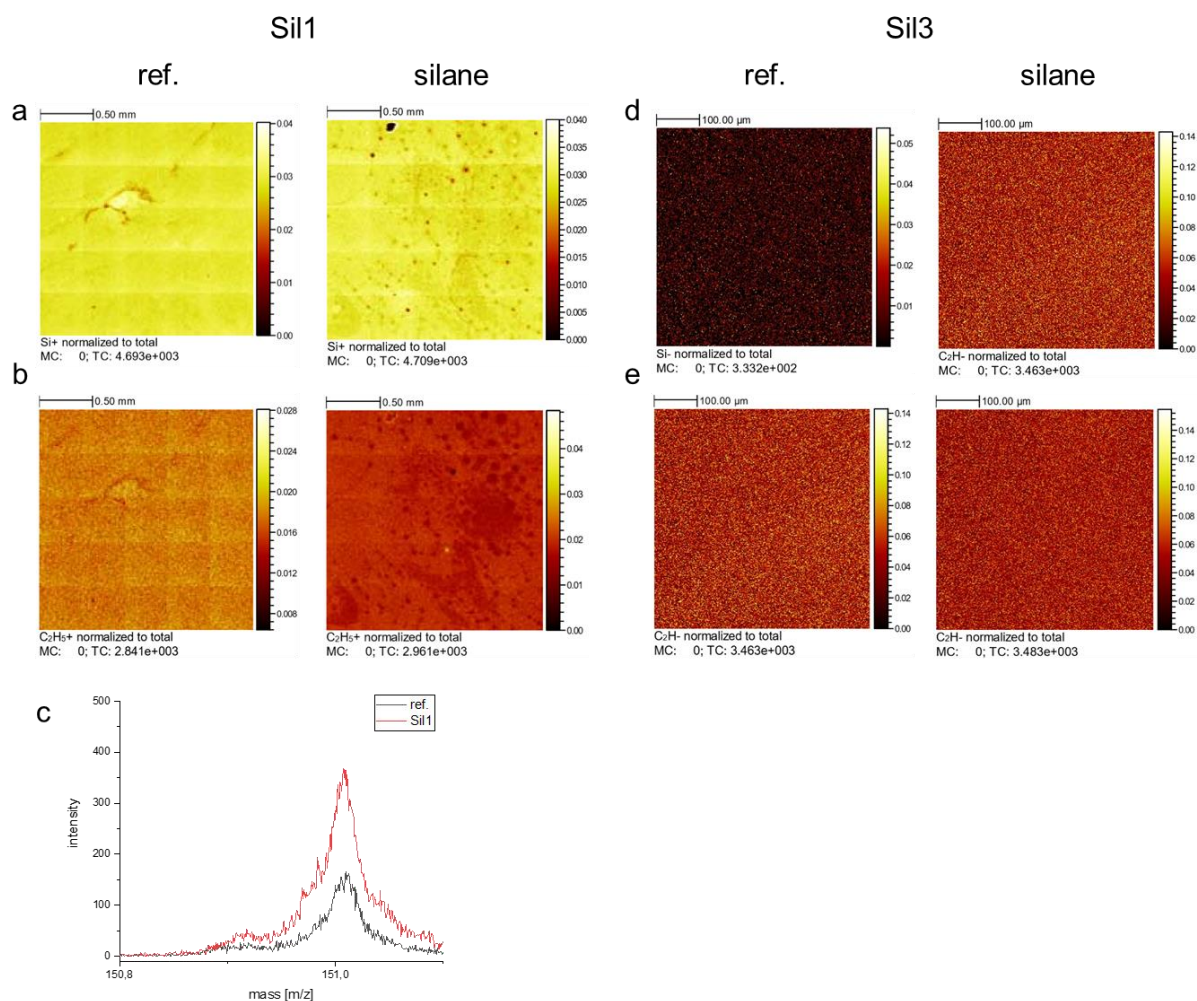
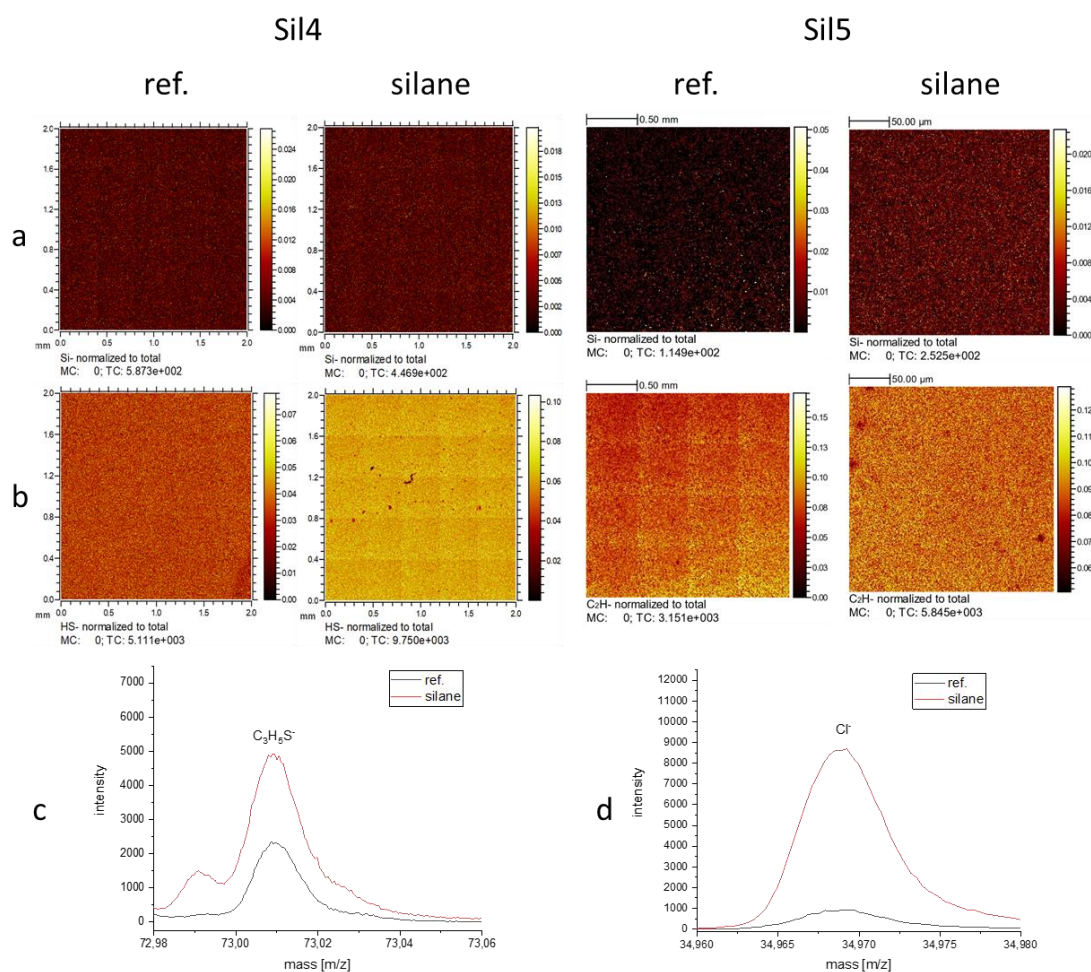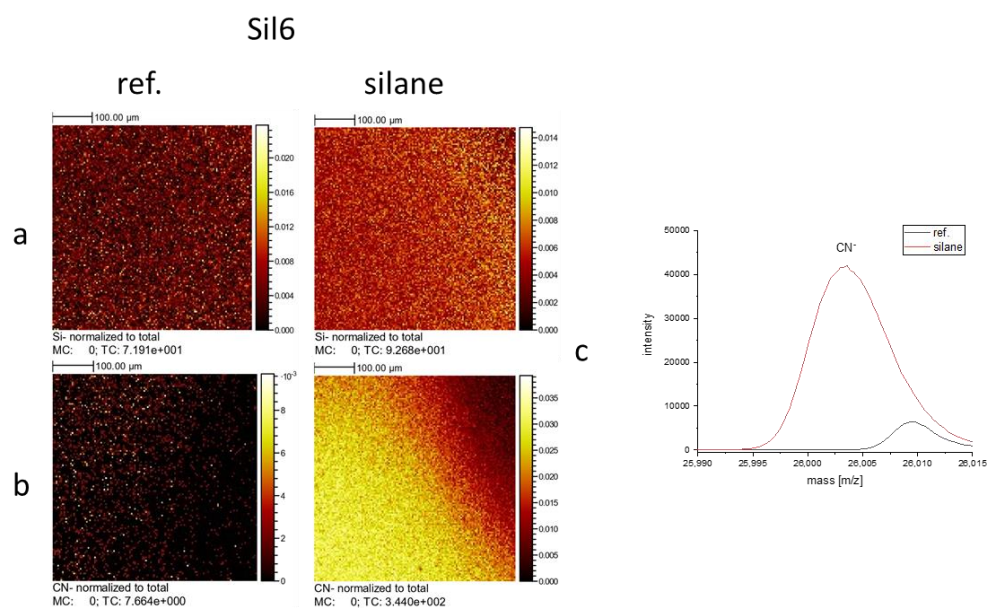Figure 35: ToF-SIMS analysis of the references as well as the silanisation with **Sil1** and **Sil3**; (a) spectra of the wafer treated with Sil1 in which mass of Si^+ was found, (b) spectra of $C_2H_5^+$ fragment c) high resolution mass ToF-SIMS of the $C_{11}H_{21}$ fragment for the wafer treated with Sil1, (d) spectra of Si^- fragment of the blank silicon wafer and Sil3, (e) spectra of C_2H^- fragment

Thiol-terminated surfaces were coated with 2,2-dimethoxy-1-thia-2-silacyclopentane (**Sil4**), chlorine-terminated surfaces with triethoxy(3-chloropropyl) silane (**Sil5**), and amine-terminated surfaces with *N*-methyl-aza-2,2,4-trimethylsilacyclopentane (**Sil6**). The synthesis of the cyclic silanes **Sil4** and **Sil6** were performed by covering silicon wafer with a solution of chloroform and silane in a ratio of 6/4 for 2 hours und argon atmosphere. **Sil5** was introduced following the same procedure as **Sil1-3**. Treatment of the silicon wafers with **Sil4-6** was successful, as revealed by the XPS results listed in Table 6. The increase of atomic percentage of the carbon ($\approx$ 3%) and thiol signal ($\approx$ 1%) by silanisation with the cyclic **Sil4** shows a ratio of 3/1 (excluding the methoxy

groups), which matches the ratio of the elements in **SiI4** and thus, verifies the attachment of the compound on the surface. Figure 36 additionally shows the C 1s, Si 2p, and S 2s XPS-spectrum. The arising S 2s signal proves the successful siilanisation. On silicon substrates, the Si 2p provides unreliable results because of overlap with a silicon *plasmon loss feature.*
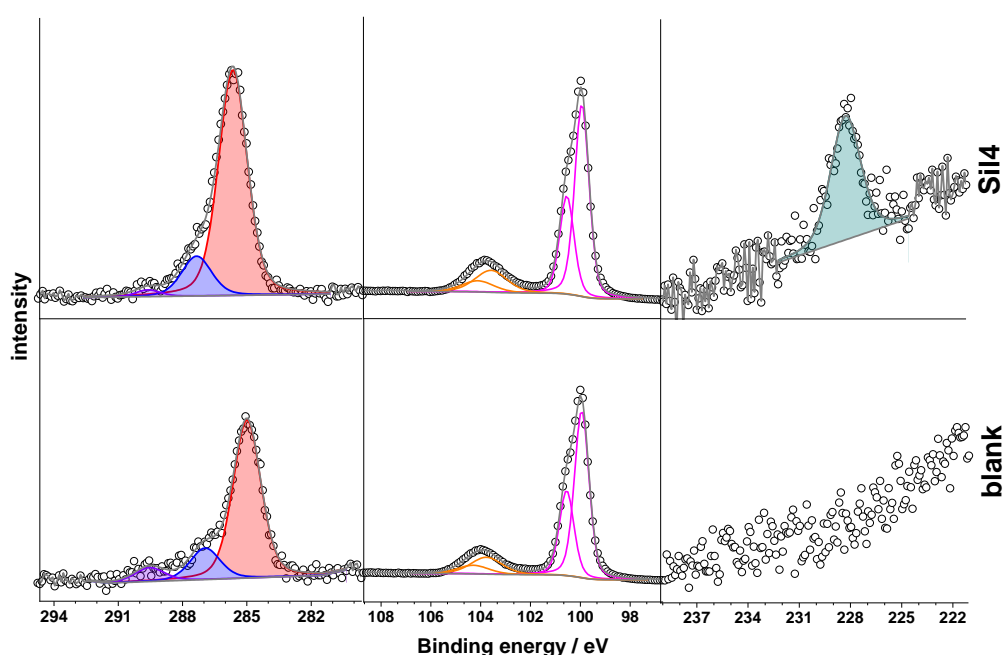
*Figure 36: XPS-spectra of the C1s, Si 2p and S 2s signal for the silanisation with **SiI4**.*

SiI5 shows an increase in chloride and carbon signals, while the ratio of the elements matches the compound, assuming an average of two ethoxy groups of the compound was substituted and attached to the surface (ratio of carbon and chlorine 6/1). The cyclic amino silane (**SiI6**) also shows a significant increase in the amine atomic percentage, but due to the appearance of a second nitrogen binding energy at 403.0 eV, it is reasonable that either some multilayers have been formed (N-Si bond formation of **SiI6** attached to the surface and another **SiI6**) or the ring has not been opened and attached.

*Table 6: Atomic% measured by XPS of a blank, cleaned silicon wafer as reference and the silanes **Sil4**, **Sil5** and **Sil6** after silanisation.*

peak position	Sil4		Sil5		Sil6	
	ref.	silane	ref.	silane	ref.	silane
C 1s (285.0 eV)	4.4%	7.4%	2.9%	6.3%	3.9%	7.4%
Si 2p$_{3/2}$ (99.5 eV)	48.7%	44.2%	49.3%	43.4%	48.8%	45.3
S 2s (228.0 eV)	-	0.9%	-	-	-	-
Cl 2p$_3$ (200.0 eV)	-	-	-	0.5%	-	-
N 1s (400.1 eV)	-	-	-	-	-	1.0%

Additional ToF-SIMS analysis confirmed the modification steps of **Sil4**, **Sil5**, and **Sil6**. Figure 37 shows the comparison of the Si^- signal before and after the grafting of **Sil4** and **Sil5** (a). Furthermore, SH^- (**Sil4**) and C_2H^- (**Sil5**) are displayed (Figure 37 (b)), showing an increase in total counts. To further confirm the silanisation step, HRMS ToF-SIMS spectra of the $C_3H_5S^-$ fragment for **Sil4** (c) and the Cl^- fragment for **Sil5** (d) are shown. Both sections display a significant increase of intensity for the corresponding ionic species, compared to the blank silicon wafer as reference. The analysis of the modification of Sil6 is shown in Figure 38 including the comparison of Si^- (a) and CN^- (b) distribution on the surface as well as the CN^- fragment (c), supporting the trend shown in the XPS results.

4. Results

*Figure 37: ToF-SIMS analysis of the references as well as the silanisation with **Sil4** and **Sil5**; (a) spectra of the wafer blank and treated with **Sil4** or **Sil5** and the amount of Si^- found, (b) spectra of SH^- and C_2H^- fragment, (c) specific fragment from high resolution mass ToF-SIMS $C_3H_5S^-$ for Sil4, and (d) Cl for Sil5.*

*Figure 38: ToF-SIMS analysis of the reference as well as the silanisation with **Sil6**, (a) spectra of the wafer blank and treated with Sil6, (b) spectra of CN^-, and (c) specific fragment from high resolution mass ToF-SIMS CN^-.*

In conclusion, the processability of trihydroxy(10-undecen-1-yl) silane (**Sil1**), trichloro(10-undecen-1-yl) silane (**Sil2**), trimethoxy(7-octadecen-1-yl) silane (**Sil3**), and 2,2-dimethoxy-1-thia-2-silacyclopentane (**Sil4**) were tested as possible silanes for thiol-yne/ene "click" chemistry modifications on surfaces. **Sil1**, and **Sil4** were found to be promising candidates, whereas **Sil2** showed a high tendency to polymerisation and **Sil3** low conversion. Due to the more practical pathway, **Sil4** was chosen for further reactions. In case of functionalisations for amino-yne "click" chemistry, triethoxy(3-chloropropyl) silane (**Sil5**), and *N*-methyl-aza-2,2,4-trimethylsilacyclopentane (**Sil6**) were evaluated, both showing promising coating results.

4.3.3 Thiol-ene/yne based surface modification

4.3.3.1 Synthesis of the first layer

For the modification of a **Sil1** functionalised surface, a 0.3 M solution of TPM-SH in degassed *N,N*-dimethylformamide (DMF) and 5 mg of 2,2-dimethoxy-2-phenylacetophenone (DMPA) were added to the silicon wafer, which was placed in a petri dish. Surfaces with **Sil2** and **Sil3** functionalisation were covered with a 0.1 M solution of TPM-SH in the same solvent, while the amount of radical starter was always 5 mg. All samples were then irradiated with a UV-lamp emitting at 365 nm for 1.5 hours, in an argon-flushed glove bag (Scheme 51). Then, the samples were washed and sonicated subsequently with chloroform, toluene and acetone. This washing process was employed for every following modification.
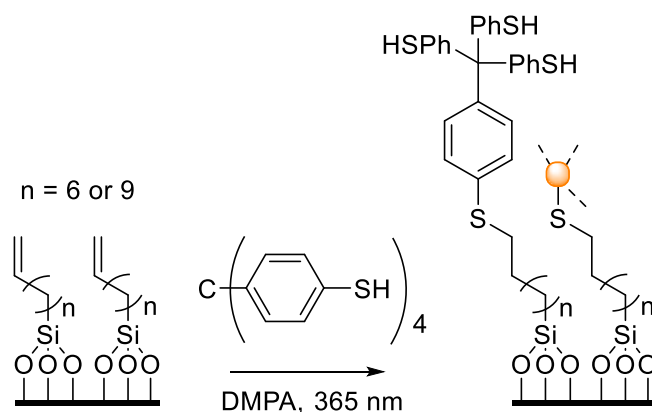
*Scheme 51: General procedure for the modification of **Sil1**, **Sil2**, and **Sil3** functionalised surfaces with TPM-SH via thiol-ene reaction.*

Table 7 shows the XPS results before and after the modification by comparing the signals of C 1s at 285.0 eV, Si $2p_{3/2}$ at 99.5 eV, and S 2s at 228.0 eV. The development of atomic percentage in the case of **Sil1** showed an increase of carbon by 6% and thiol by 0.6% and a corresponding decrease of silicon by 4%. The ratio of sulfur to carbon was *ca.* 1/10 and differed from the expected ratio of 4/25, which may be caused by organic contaminations on the surface and challenging detection of sulfur. Various settings have been tested to guarantee a detailed resolution of sulfur, but no improvement was achieved. The modification of **Sil2**-anchored surfaces showed no differences, caused by the polymer-like silane layer and the resulting deactivation due to the inaccessibility of the functional groups which was discussed in chapter **2.3.3.** The successful thiol-ene reaction of the **Sil3**-functionalised surface with TPM-SH was also verified, since the expected changes (increase of the carbon and thiol signals,

decrease of the silicon signal) in XPS were observed (comparable to the **SiI1** modified surface). The ratio of sulphur to carbon signals was again *ca.* 1/10 because of the challenging detectability of sulphur. Additionally, ToF-SIMS analysis supported the results obtained from XPS-analysis. As can be seen in Figure 39, the modification with a 0.3 M solution of TPM-SH resulted in an inhomogeneous surface displayed by the presence of scattered red and black spots. In contrast, the modification of **SiI3** with a 0.1 M solution resulted in a more homogeneous coverage. Furthermore, the successful reaction was confirmed by the increased intensity of several unique mass fragments ($C_6H_2S^-$ for **SiI1** and SH^- for **SiI3**).

*Table 7: Comparison of the atomic percentage of C 1s Si2P$_{3/2}$ and S 2s of **SiI1**, **SiI2** and **SiI3** functionalised surfaces before and after a thiol-ene reaction with TPM-SH measured by XPS*

peak position	Layer 1 (SiI1)		Layer 1 (SiI2)		Layer 1 (SiI3)	
	silane	TPM-SH	silane	TPM-SH	silane	TPM-SH
C 1s (285.0 eV)	10.45%	**16.44%**	28.2%	**28.45%**	5.75%	**9.90%**
Si 2p$_{3/2}$ (99.5 eV)	43.42%	**39.58%**	34,4%	35.05%	47.45%	**42.75%**
S 2s (228.0 eV)	-	**0.61%**	-	**0%**	-	0.45%
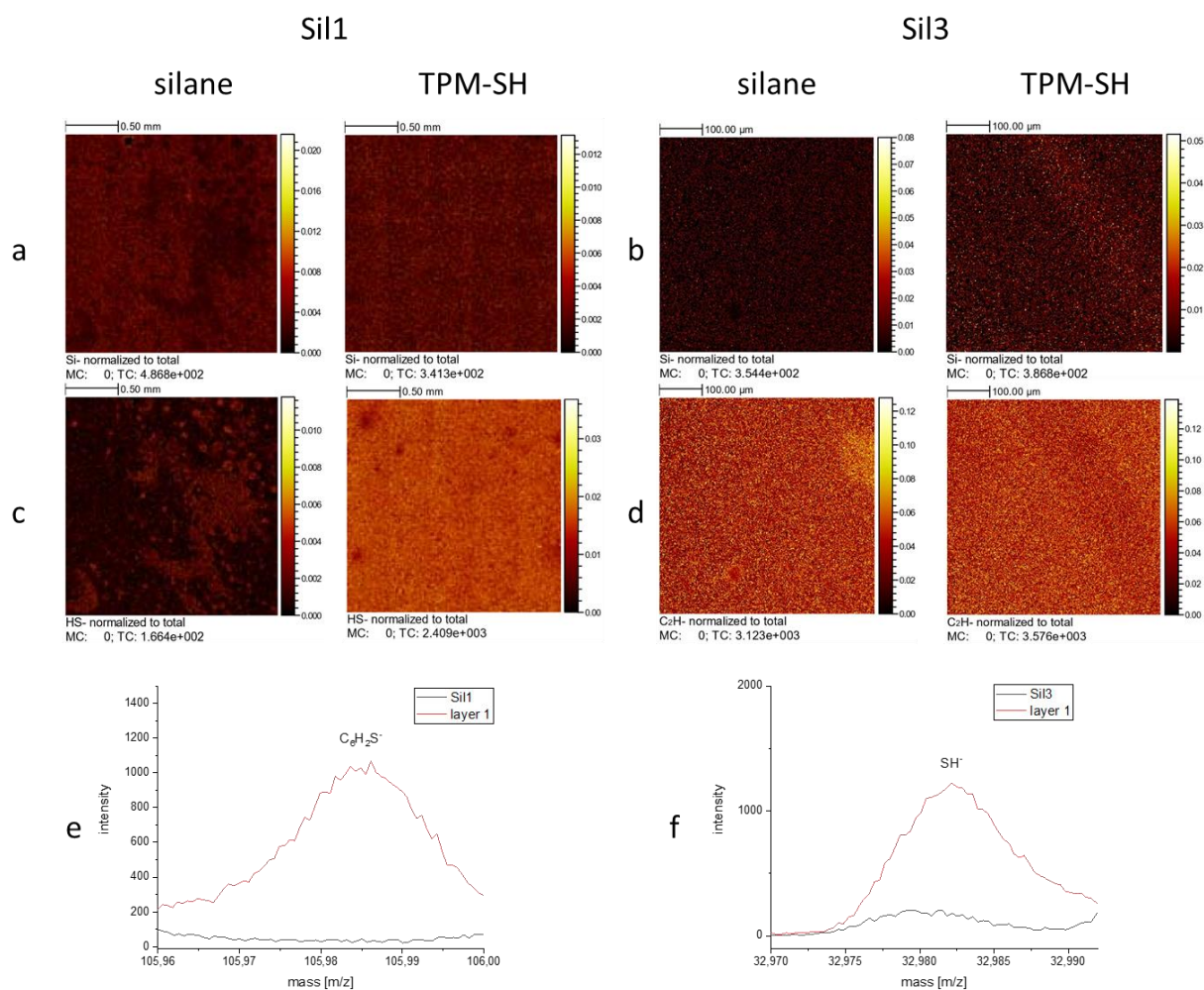
*Figure 39: ToF-SIMS analysis of the modified **Sil1** and **Sil3** surfaces via thiol-ene reaction with TPM-SH. (a) and (b) Si⁻ signals of the modified and unmodified sample, (c) HS- signal of the modified and unmodified sample functionalized with Sil1, (d) C2H- signal of the modified and unmodified sample functionalized with Sil1 (e) $C_6H_2S^-$ fragment and (f) SH⁻ fragment compared to the corresponding silanes.*

Thiol functionalised surfaces (**Sil4**) were modified with either TPM-acetylene (24 mM and 16 mM) or TPGe-acetylene. Therefore, the reaction conditions for TPM-acetylene were evaluated by using monomer solutions at different concentrations with the same amount of the UV-initiator, DMPA. TPGe-acetylene was introduced *via* a 0.21 mM solution in degassed DMF. All samples were then irradiated for 1.5 hours (Scheme 52).
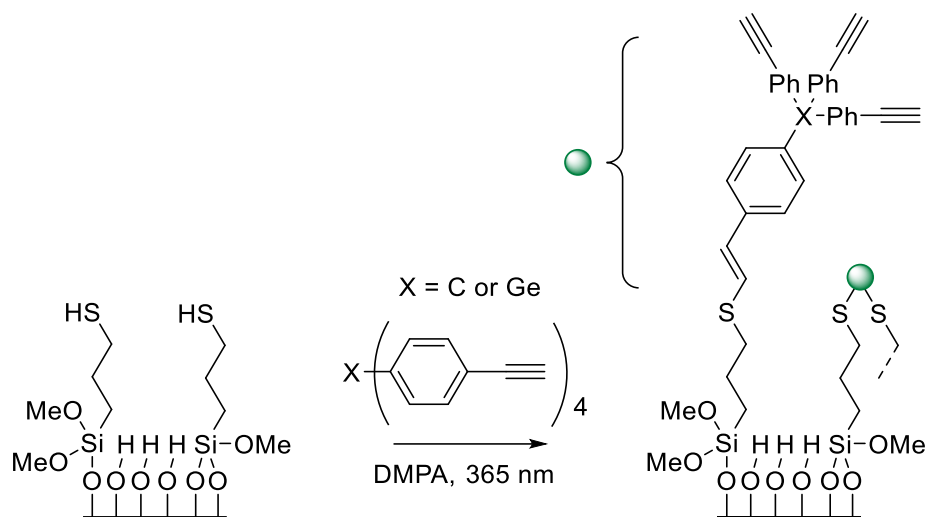
*Scheme 52: General procedure for the modification of **SiI4** functionalised surfaces with TPM-acetylene or TPGe-acetylene via thiol-yne and thiol-ene reaction.*

XPS-results showed that the modifications were successful (Table 8). However, further comparison of the obtained results of both entries (24 mM and 16 mM TPM-acetylene) with each other was not possible due to the high deviation of two measured **SiI4** references through XPS alone (two separate modification dates). Besides the increase in carbon and decrease in silicon atomic percentage, the appearance of a Ge $2p_{3/2}$ signal at 1218.9 eV confirmed the TPGe-acetylene layer in the third entry (Figure 40). Furthermore, a new S 2s signal at 232.4 eV appeared, typically representing an oxidised sulfur species, *i.e.* sulfoxide or sulfone. Regarding these procedures in this thesis, the newly formed signal could, on the one hand, describe the newly formed C-S-C bond or on the other hand the aforementioned oxididation. Additionally, all XPS results were further confirmed by ToF-SIMS analysis. As visible in Figure 41, all reactions led to homogeneous covalent modifications (comparison of silicon Si- and sulfur SH-) and additionally the intensity of the C_2H^- fragment significantly increased.

*Table 8: Comparison of the atomic percentage of characteristic signals of **SiI4** functionalised surfaces before and after a thiol-yne/ene reaction with TPM-acetylene and TPGe-acetylene measured by XPS*

peak position	SiI4		SiI4		SiI4	
	silane	TPM-acetylene (24 mM)	silane	TPM-acetylene (16 mM)	silane	TPGe-acetylene
C 1s (285.0 eV)	7.4%	16.7%	12.6%	17.5%	7.4%	12.4%
Si 2p$_{3/2}$ (99.5 eV)	44.2%	34.8%	40.3%	35.9%	44.2%	39.1%
S 2s (228.0 eV)	0.9%	0.6%	1.3	0.7%	0.9%	0.1%
S 2s (232.4 eV)	-	0.7%	-	0.5%-	-	0.6%
Ge 2p$_{3/2}$ (1218.9 eV)	-	-	-	-	-	0.5%
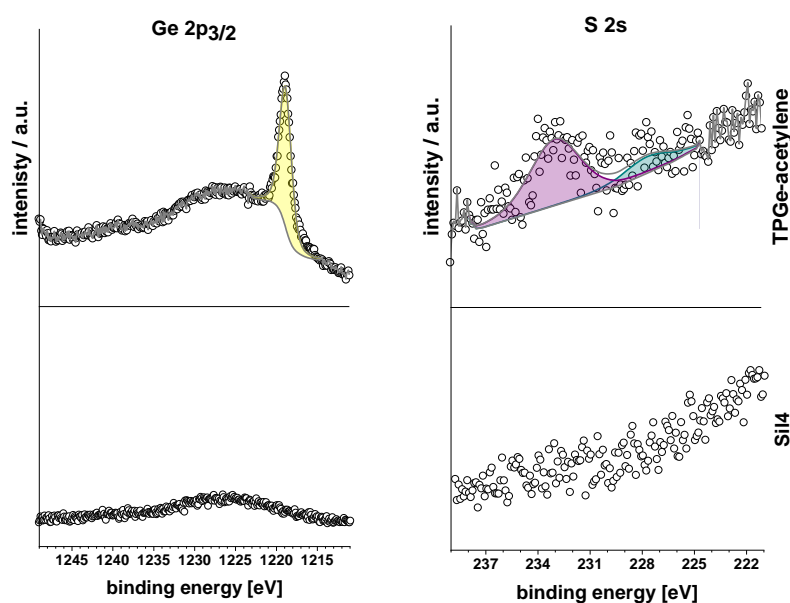
*Figure 40: Overlaid XPS-results of **SiI4** layer and after modification with TPGe-acetylene layer. The corresponding characteristic signals are coloured in yellow for germanium signal. The purple signal represent the oxidised sulphur species and the blue one.the C-S bond.*
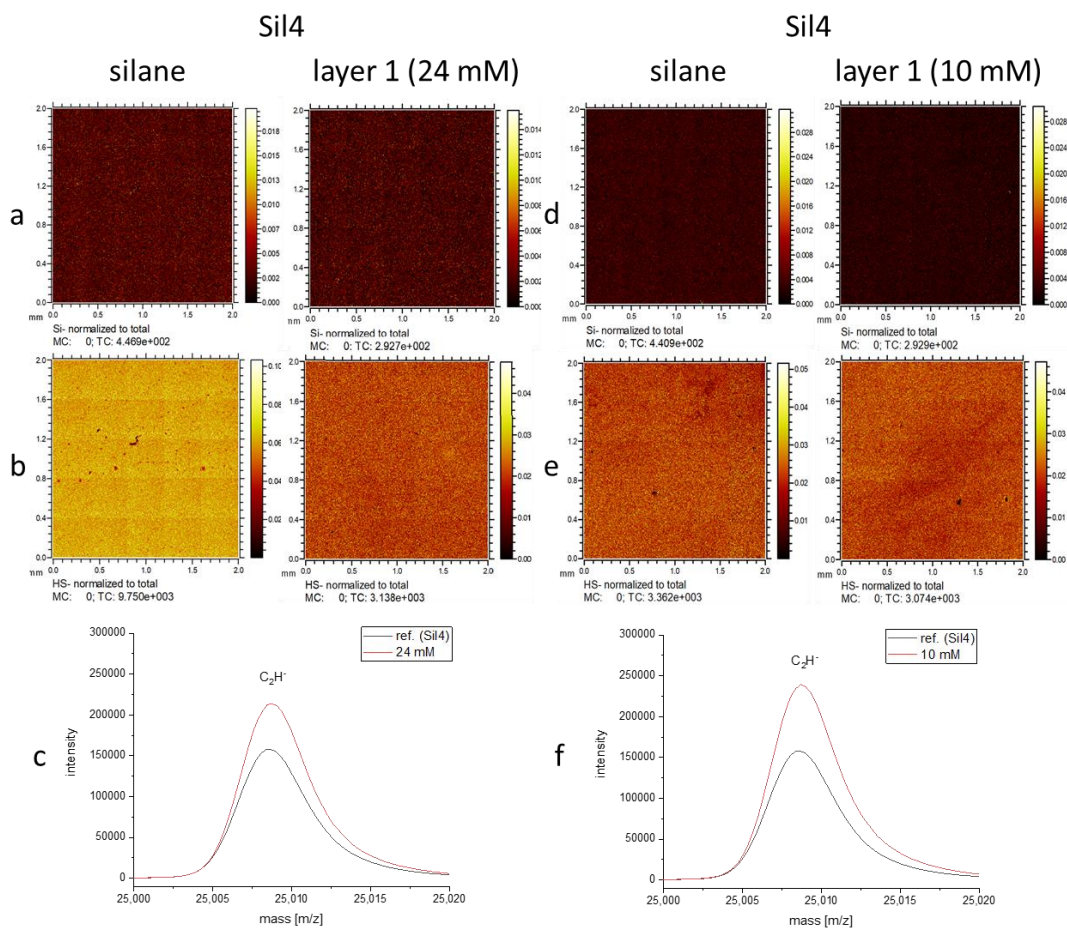
*Figure 41: ToF-SIMS analysis of the modified **Sil4** surfaces via thiol-yne/ene reaction with TPM-acetylene.(a) and (b) represent the corresponding Si⁻ signals of the modified and unmodified sample, (c) and (d) represent the corresponding Si⁻ signals of the modified and unmodified sample (e) and (f) show the increasing intensity of the C₂H⁻ fragment.*
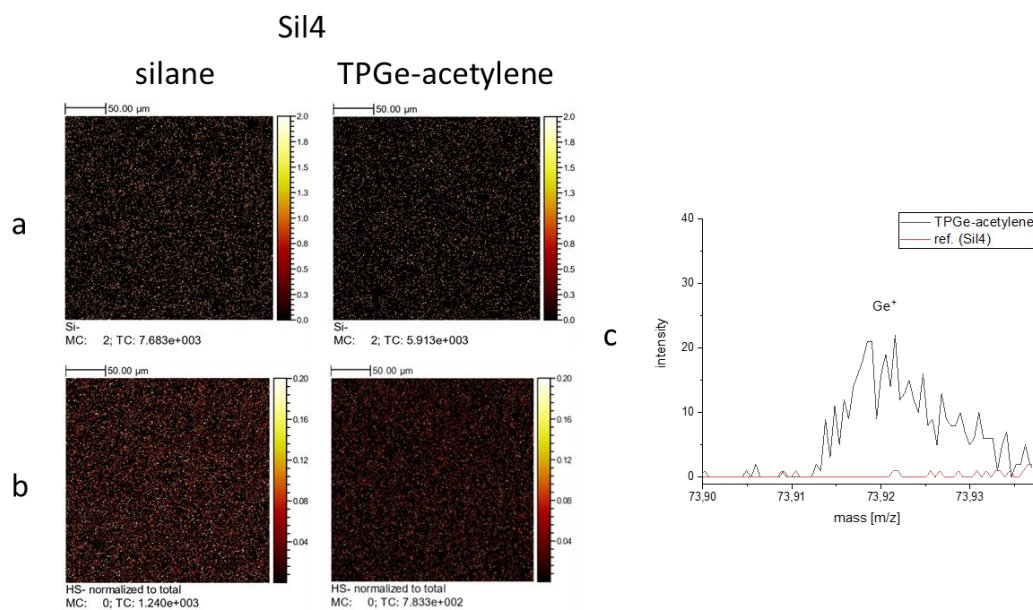
*Figure 42: ToF-SIMS analysis of the modified **Sil4** surfaces via thiol-yne/ene reaction with and TPGe-acetylene: (a) represents the corresponding Si⁻ si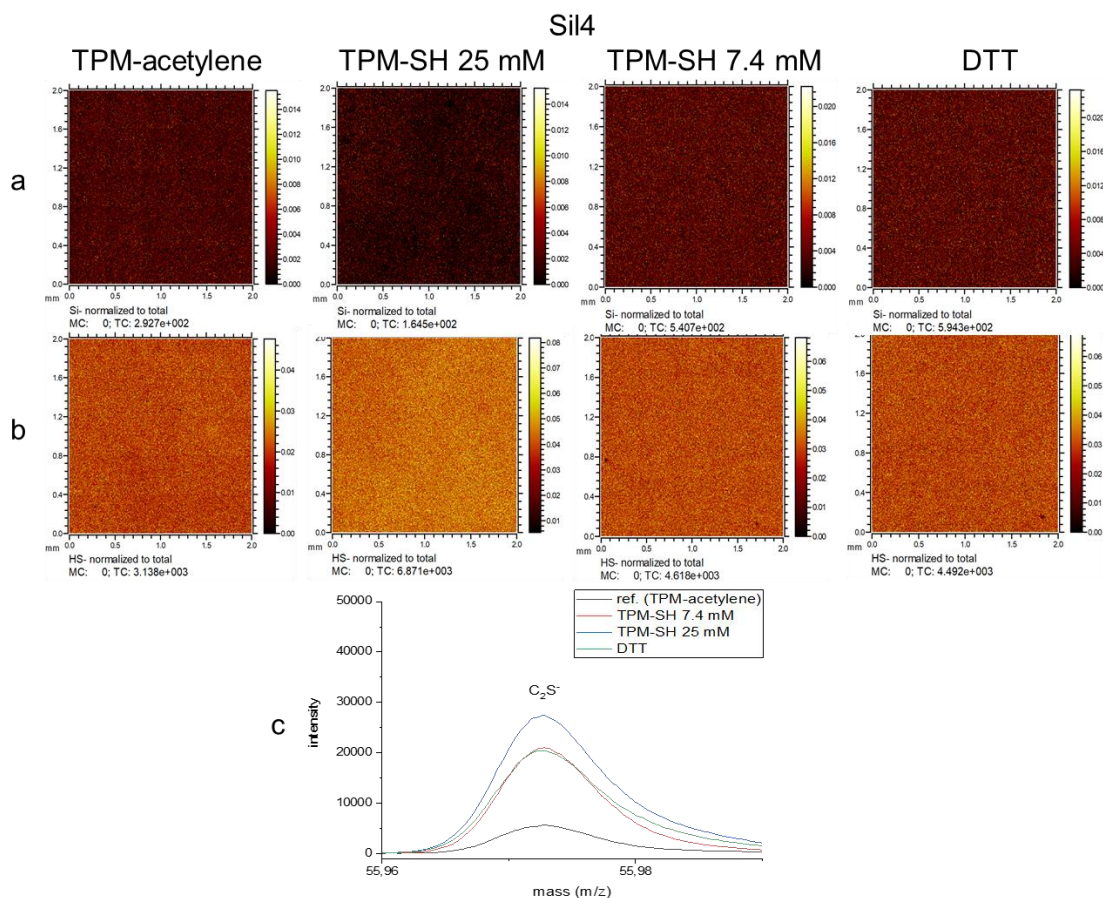gnals of the modified and unmodified sample, (b) represents the corresponding HS⁻ signals of the modified and unmodified sample. (c) shows the increasing intensity of Ge⁺ fragment.*

4. Results

Furthermore, modification of the thiol-terminated surface (**Sil4**) *via* base-catalysed nucleophilic addition of the thiolate onto the acetylene as shown by Oshima and co-workers was performed *(214).* Therefore, a 0.2 mM solution of TPM-acetylene containing 10 mol% Cs_2CO_3 was prepared and the functionalised silicon wafer was dipped into the solution with a dipping robot. After 4 hours, the samples were rinsed with chloroform and ethanol for 5 minutes each and dried under a nitrogen stream. XPS analysis showed no conversion to the desired first layer, but a decrease of carbon and sulfur signals was detected *(Table 9).* This can be explained by desilanisation (cleavage of attached **Sil4**) under basic conditions when water contaminated solvents are used.

*Table 9: Comparison of the atomic percentage of characteristic signals of **Sil4** functionalised surfaces before and after hydrothiolation by basic catalysis with TPM-acetylene measured by XPS*

Sil1	C 1s (285.0 eV)	Si 2p3/2 (99.5 eV)	S 2s (228.0 eV)	S 2s (232.4 eV)
silane	16.5%	36.6%	1.7%	0.3%
TPM-acetylene (robot)	13.9%	38.4%	0.9%	0.4%

In order to provide easier accessible functional groups per compound addressable by post-modification (compared to TPM-acetylene), TPM-diallylamine was coated onto a **Sil4**-functionalised silicon surface (Scheme 53 Due to the large size of the applied building blocks and the densely packed silane layer, not all functional groups can be addressed, leaving active functions inside the pores and surface. Therefore, the wafers were reacted with a 15 mM solution of TPM-diallylamine under UV radiation at 365 nm with DMPA as initiator. XPS results showed an increase of the carbon signal at 285.0 eV combined with a significant increase from 0% to 1.1% of the nitrogen signal at 400.3 eV binding energy (Table 10). ToF-SIMS analysis was inconclusive on account of significant errors in the measurement data.
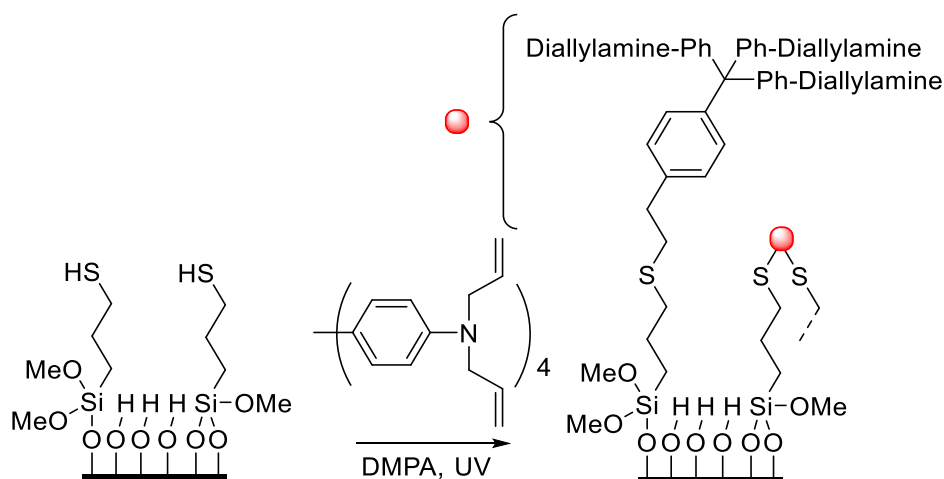
*Scheme 53: General procedure for the modification of **Sil4** functionalised surfaces with TPM-diallylamine via thiol-yne/ene reaction.*

*Table 10: Comparison of the atomic percentage of characteristic signals of **Sil4** functionalised surfaces before and after thio-yne/ene reaction with TPM-diallymin measured by XPS*

Sil1	C 1s (285.0 eV)	Si 2p3/2 (99.5 eV)	S 2s (228.0 eV)	S 2s (232.4 eV)	N 1s (400.3 eV)
silane	7.2	43.4%	0.6%	-	-
TPM-diallyl-amine	13.6%	36.0%	0.5%	-	1.1%

In conclusion, various functionalised silicon wafers were found to be suitable candidates for further modifications. The best results were obtained for **Sil1**,**Sil3**, and **Sil4** *via* modification reactions with TPM-SH, TPM/Ge-acetylene and TPM-diallylamine.

4.3.3.2 Synthesis of the second layer

Based on the established procedures for synthesis of a first layer onto **Sil1** and **Sil4** modified wafers, a second layer was subsequently synthesised using either TPM-acetylene for **Sil1** wafers or TPM-SH for **Sil4** wafers. Scheme 54 shows the procedure for the synthesis of the second layer onto a **Sil1** wafer with a 0.1 M and 0.3 M solution of TPM-acetylene.
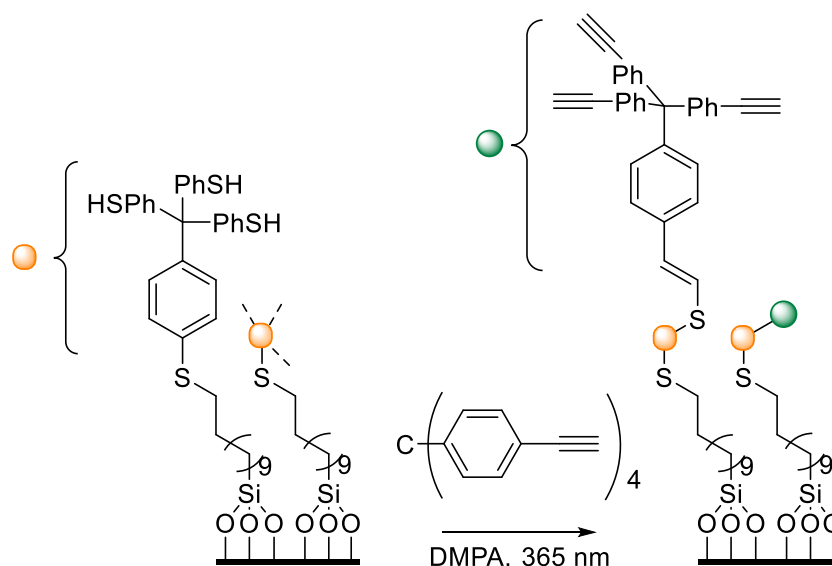
*Scheme 54: General procedure for the modification of **Sil1-TPM-SH** functionalised surfaces with TPM-acetylene via thiol-yne/ene reaction to form a second layer. The reaction was conducted with a 0.1 M and 0.3 M solution of TPM-acetylene.*

Formation of the desired second layer *via* thiol-yne/ene coupling was confirmed by XPS Table 11. However, conclusive proof of the presence of a clean monolayer was impossible due to deviation of values for the decrease of the silicon $2p_{3/2}$ signal at 99.5 eV and inconsistent values for the S 2s signal at 228.0 eV. To further examine if a clean and homogeneous monolayer was obtained, ToF-SIMS measurements were conducted, which showed that the underlying TPM-SH layer was rather inhomogeneous (scattered bright and dark spots, Figure 43 (a, TPM-SH)), thus also resulting in an inhomogeneous modification (Figure 43 a, TPM-acetylene). Besides surface inhomogeneity, a plausible explanation for the inconsistent XPS values is the formation of disulfide layers. Regarding the procedure with two different concentration of TPM-acetylene, the increase of the carbon signal at 285.0 eV and the increase in intensity of the C_2H^- fragment in ToF-SIMS for both concentrations led to the conclusion that lowering the concentration of the starting material from 0.3 M to 0.1 M does not significantly influence the formation of the new layer.

*Table 11: Comparison of the atomic percentage of C 1s, Si 2p$_{3/2}$ and S 2s of **SiI1-TPM-SH** functionalised surfaces before and after a thiol-yne reaction with TPM-acetylene measured by XPS*

peak position	**SiI1**		
	1. layer	0.3 M TPM-acetylene	0.1 M TPM-acetylene
C 1s (285.0 eV)	16.4%	32.0%	36.1
Si 2p$_{3/2}$ (99.5 eV)	39.6%	25.1%	18.3%
S 2s (228.0 eV)	0.6%	0.6%	0.8%
S 2s (232.4 eV)	-	0.3%	0.4%
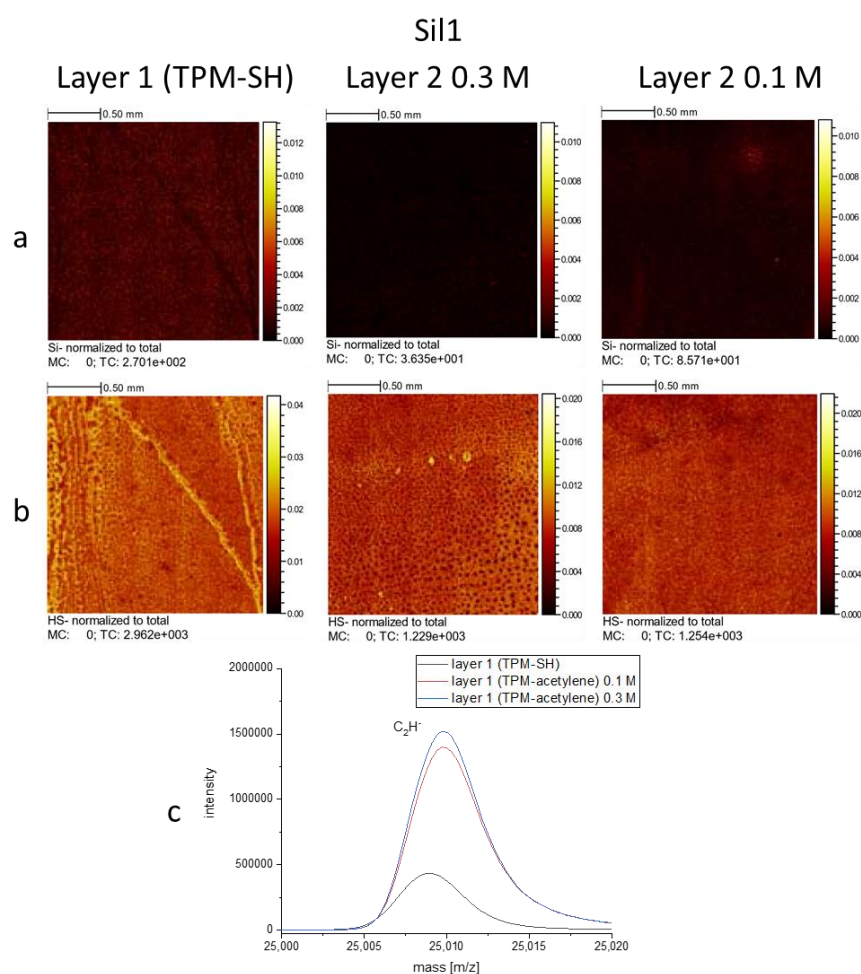
*Figure 43: ToF-SIMS analysis of the modified **SiI1-TPM-SH** surfaces via thiol-yne/ene reaction with TPM-acetylene: (a) represents the corresponding Si$^-$ signals of the modified and unmodified sample, (b) represents the corresponding HS$^-$ signals of the modified and unmodified sample. (c) shows the increasing intensity of C$_2$H$^-$ fragment.*

4. Results

As seen from the inhomogeneous modification of alkene-terminated silicon wafers with TPM-SH, further concentrations were evaluated to suppress the disulfide formation to obtain clean monomolecular layers. Therefore, different concentrations (25 mM, 15 mM, and 7.5 mM) and ratio of UV initiator were investigated. In addition, a possible *in situ* reduction of disulfide multilayers (based on the modification with a 25 mM solution) *via* dithiothreitol (DTT) and NaBH$_4$ were evaluated on a **SiI4-TPM-acetylene** functionalised wafer (Scheme 55).
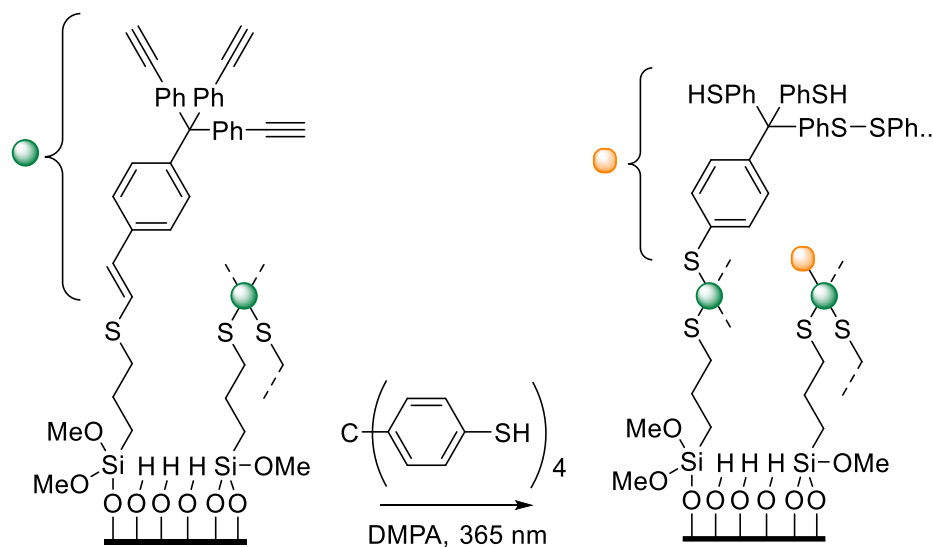
*Scheme 55: General procedure for the modification of **SiI4-TPM-acetylene** functionalised surfaces with TPM-SH via thiol-yne reaction.*

XPS- (Figure 44) and ToF-SIMS (Figure 45) analysis were performed to analyse the above mentioned test reactions. As suggested from the change of the carbon, silicon, and sulfur atomic percentages, the lower the concentration, the lower the carbon atomic percentage (46% using 25mM TPM-SH and 5 mg DMPA *vs.* 24% using 7.4 mM TPM-SH and 1 mg DMPA). In case of the 25 mM TPM-SH solution, the variation of UV-initiator (in.) also decreases the carbon atomic percentage (46% *vs.* 40%, respectively). Reduction of the formed multilayers *via* DTT led to a lower carbon and sulfur atomic percentage, whereas NaBH$_4$ only showed a minor effect (carbon: 46% *vs.* 39%, respectively), leading to the conclusion that these reagents do not foster the formation of monolayers (approximately 8% carbon increase). ToF-SIMS analysis showed relatively homogenous surfaces for all performed modifications (Figure 45) although the intensity of the C$_2$S$^-$ fragment was highest after reduction with DTT, concluding that either the disulfide multilayers do not fragment into this specific species, or DTT was attached to the remaining alkyne/alkene bonds of the previous layer and thus, increased the C$_2$S$^-$ signal.
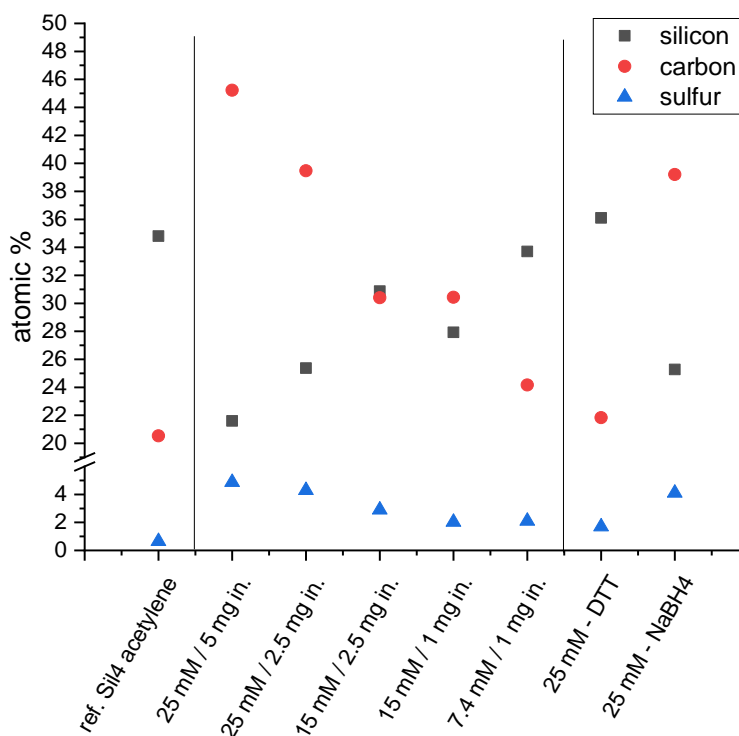
Figure 44: Comparison of atomic percentages of modification of **Sil1-TPM-SH** before and after modification with different concentrations of TPM-acetylene solution and ratios of initiator via thiol-yne/ene reaction.
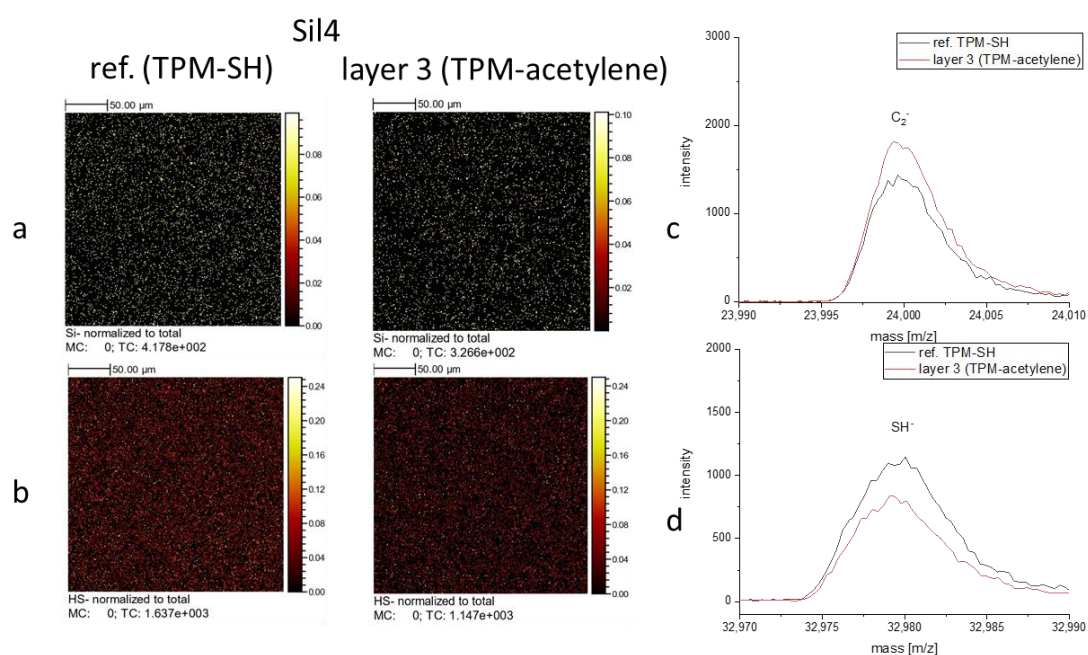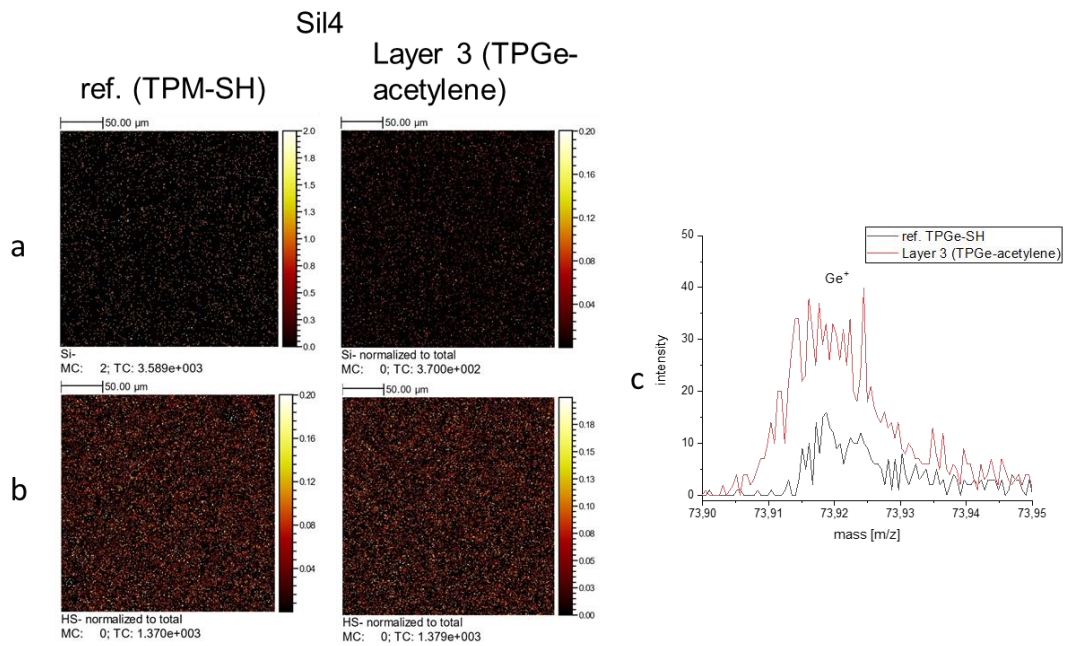

Figure 45: ToF-SIMS analysis of the modified **Sil1-TPM-SH** surfaces via thiol-yne reaction with and TPM-acetylene: (a) represents the corresponding Si^- signals of the modified and unmodified sample, (b) the SH^- signals, and (c) the C_2H^- fragment compared to the TPM-SH layer.

4. Results

Nevertheless, further investigations on the use of DTT as well as higher dilutions of TPM-SH were evaluated. The concentration of TPM-SH was further reduced from 7.5 mM to 3.75 mM and the ratio of UV initiator was adjusted. Furthermore, the reaction time was varied (7.5 mM/45 min, 3.75 mM/1.5 h (1), 3.75 mM/0.45 min (2)) and the reduction of formed disulfides was performed *via* the reaction procedure presented by Levkin and *co*-workers (*215*). Therefore, the TPM-SH modified surfaces were covered by a solution of DTT (22 mM) and Irgacure D-2595 (2.2 mM) in DMF and irradiated at 254 nm for 20 minutes before conducting typical purification steps, as mentioned in chapter **4.3.3.1**. As shown in Figure 46, modification with a 3.75 mM solution led to promising results with an increase of carbon atomic percentage from *ca.* 16% to ca. 27% (1,5 h) and 24% (45 min), indicating less disulphide formation and meeting the expected value of ca. 8%. This result could not be reproduced (no conversion in later entries even with longer reaction times) and further surface modifications were performed with 7.5 mM solutions of TPM-SH, 1 mg of initiator and 45 min irradiation time. Unexpectedly, the reduction of the formed layers did not take place. Instead, an increase of carbon and sulfur was observed, which was attributed to the thiol-yne/ene reaction of DTT with the previous TPM-acetylene layer.
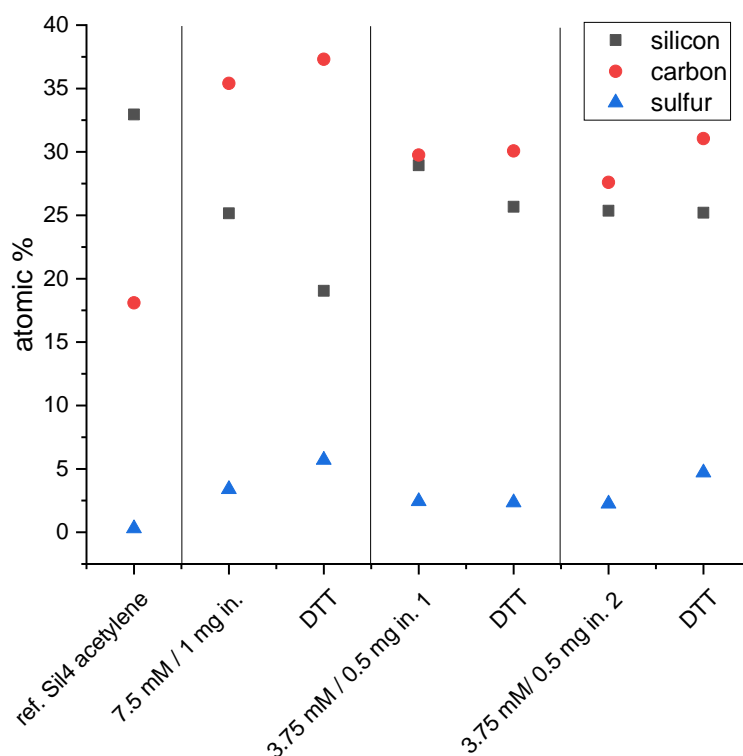
*Figure 46: Atomic% measured by XPS of **Sil1-TPM-acetylene** as reference and after modification with TPM-SH via thiol-yne reaction with different concentrations and reaction times plus the reduction of the formed layers with DTT.*

Based on these results, **Sil4-TPGe-acetylene** modified surfaces were further reacted with TPM-SH. XPS-analysis (Table 12) showed a significant increase of the carbon C 1s and sulfur S 2s (228.0 eV and 232.4 eV) signals and decrease of the Si $2p_{3/2}$ and Ge $2p_{3/2}$ signals. The successful modification was further confirmed by ToF-SIMS analysis (Figure 47). As depicted, the thiol signal increased in a homogeneous fashion (Figure 47, b) and the intensity of the Ge^+ fragment decreased (Figure 47, c).

*Table 12: Comparison of the atomic percentage of C 1s, Si $2p_{3/2}$, S 2s and Ge $2p_{3/2}$ of **Sil4-TPGe-acetylene** functionalised surfaces before and after a thiol-yne reaction with TPM-SH measured by XPS.*

Sil1	*C 1s* (285.0 eV)	*Si 2p3/2* (99.5 eV))	*S 2s* (228.0 eV)	*S 2s* (232.4 eV)	*Ge 2p3/2* (1218.9 eV)
1. layer (Ge)	12.4%	39.1%	0.1%	0.6%	0.5%
TPM-SH	17.2%	37.7%	0.9%	0.9%	0.3%
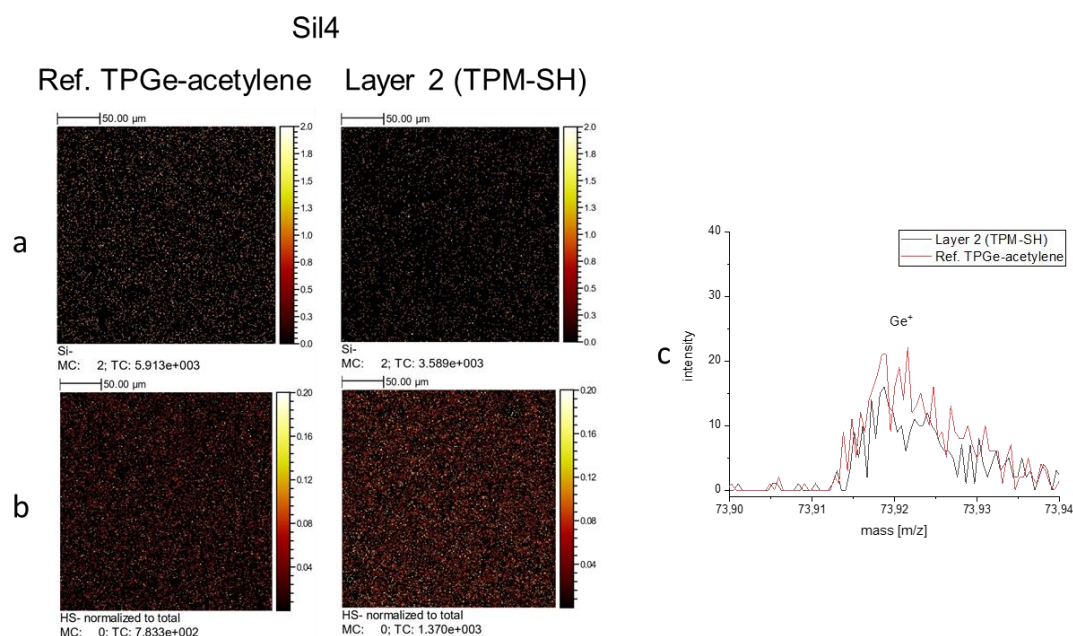
*Figure 47: ToF-SIMS analysis of the modified **Sil4-TPGe-acetylene** surfaces via thiol-yne reaction with and TPM-SH: (a) represents the corresponding Si⁻ signals of the modified and unmodified sample, (b) the SH⁻ signals, and (c) the Ge^+ fragment compared to the TPGe-acetylene layer.*

4. Results

The synthesis of the second layer on octafunctional TPM-diallylamine proceeded with the previous established procedure for TPM-SH (Scheme 56).
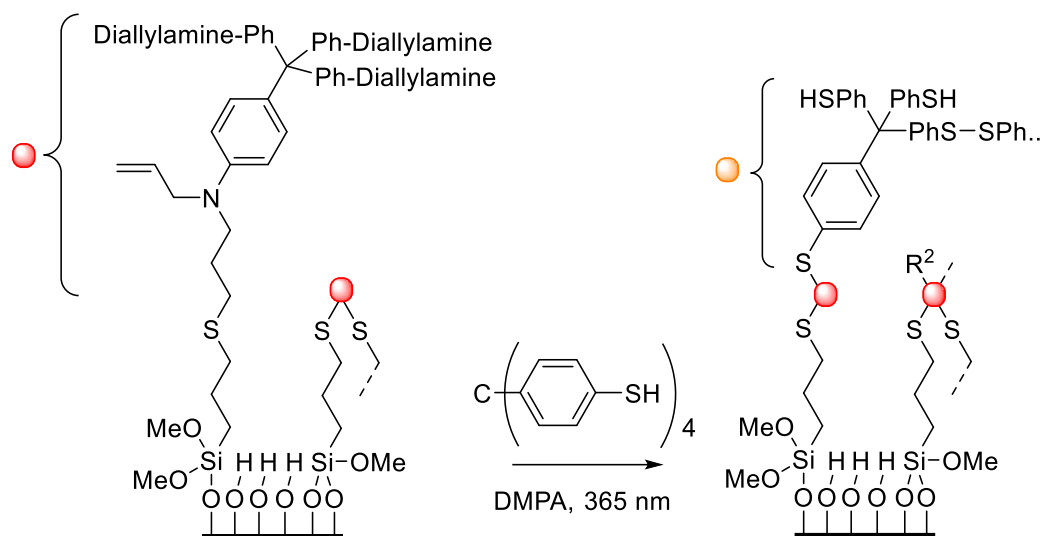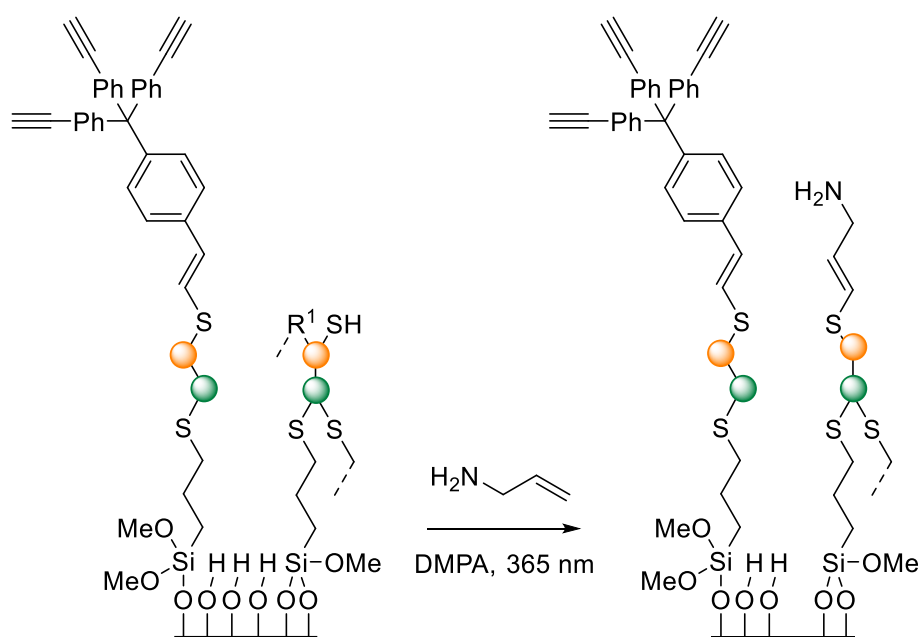

*Scheme 56: General procedure for the modification of **SiI4-TPM-diallylamine** functionalised surfaces with TPM-SH via thiol-yne reaction.*

Successful modification of the layer was confirmed by XPS- and ToF-SIMS analysis. XPS results showed a significant increase of the carbon C 1s and sulfur S 2s signal and a slight decrease of the nitrogen N 1s signal (Table 13 Although these results indicate the formation of TPM-SH multilayers *via* disulfide formation, the surfaces are homogeneously covered (Figure 48, a and b Additionally, the significant decrease of the CN⁻ fragment underpinned this conclusion (Figure 48, c), thus making further modifications not reasonable if monolayers are the goal.

*Table 13: Comparison of the atomic percentage of C 1s, Si 2p₃/₂, S 2s and N 1s of **SiI4-TPM-diallylamine** functionalised surfaces before and after a thiol-yne reaction with TPM-SH measured by XPS.*

Sil1	C 1s (285.0 eV)	Si 2p3/2 (99.5 eV)	S 2s (228.0 eV)	S 2s (232.4 eV)	N 1s (400.3 eV)
TPM-diallylamine	13.6%	36.0%	0.5%	-	1.1%
TPM-SH	45.0%	17.8%	5.5%	0.6%	0.9%

Sil4

ref. TPM-diallylamine   layer 2 (TPM-SH)
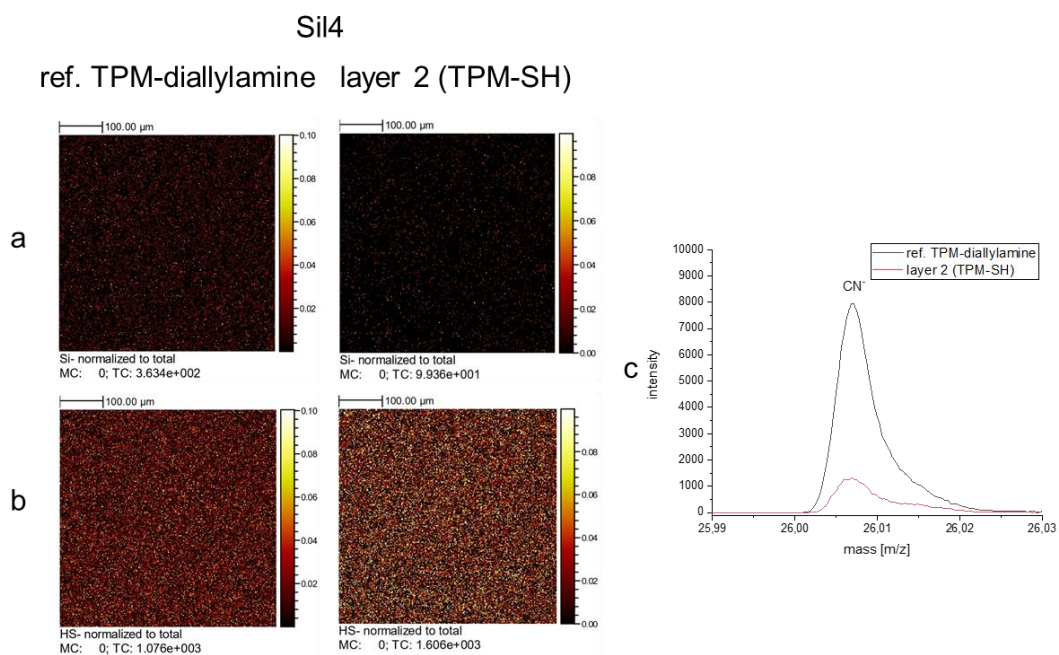
*Figure 48: ToF-SIMS analysis of the modified **Sil4-TPM-diallylamine** surfaces via thiol-yne reaction with and TPM-SH: (a) represents the corresponding Si⁻ signals of the modified and unmodified sample, (b) the SH⁻ signals, and (c) the CN⁻ fragment compared to the TPM-diallylamine layer.*

4. Results

4.3.3.3 Synthesis of the third layer

The synthesis of the third layer was only performed on **SiI4-TPM/TPGe-acetylene-TPM-SH** covered surfaces because of the development of the most practicable procedure over time. Therefore, the optimal reaction conditions evaluated in chapter **4.3.3.1** (Scheme 57) were applied.
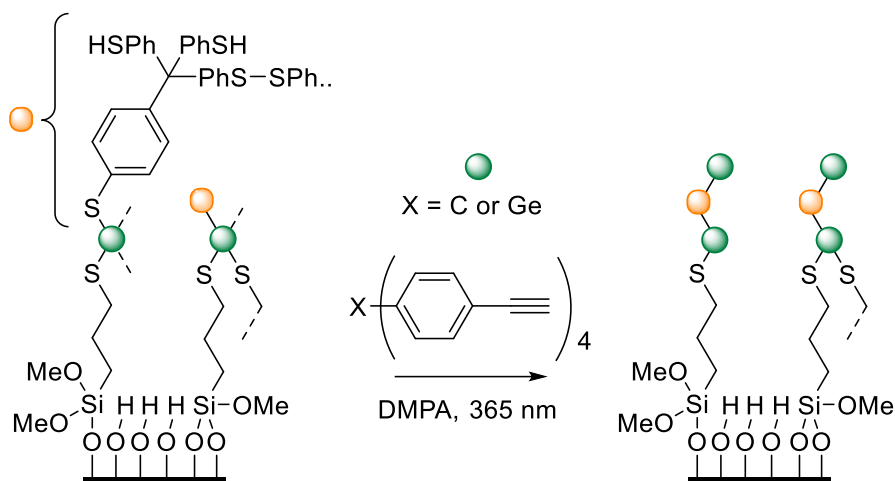
*Scheme 57: General procedure for the modification of **SiI4-TPM/Ge-acetylene-TPM-SH** functionalised surfaces with TPM/Ge-acetylene via thiol-yne reaction.*

Table 14 shows the XPS results before and after the introduction of the third layer on either **SiI4-TPM-acetylene-TPM-SH** with TPM-acetylene or on **SiI4-TPGe-acetylene-TPM-SH** with TPGe-acetylene. Both modifications showed increased atomic percentages for the carbon C 1s signal and decreased atomic percentage for the silicon Si $2p_{3/2}$ and the sulfur S 2s signal. Additionally, an increase in germanium Ge $2p_{3/2}$ signal was observed when TPGe-acetylene was used. ToF-SIMS analysis further confirmed these results as depicted in the comparison of the homogeneous surface before and after reaction for the TPM series (Figure 49, a and b) and for the TPGe series (Figure 50, a and b). Although the XPS data showed significant differences for modification with TPM-acetylene, two fragments (C_2^- and SH^-) had to be chosen to confirm the covalent coating by ToF-SIMS (Figure 49, c). An explanation for the divergent results may be that ToF-SIMS measurements were performed on a spot with low conversion. In addition, the modification with TPGe-acetylene showed a significant increase in the Ge^+ intensity (Figure 50, c). definitely confirming the formation of a third layer.

*Table 14: Comparison of the atomic percentage of C 1s, Si 2p$_{3/2}$, S 2s and Ge 2p$_{3/2}$ of **Sil4-TPM/Ge-acetylene-TPM-SH** functionalised surfaces before and after a thiol-yne reaction with TPM/Ge-acetylene measured by XPS.*

atom	Sil4			
	2.layer	TPM-acetylene	2. layer (Ge)	TPGe-acetylene
C 1s (285.0 eV)	16.6%	23.5%	17.2%	21.7%
Si 2p$_{3/2}$ (99.5 eV)	36.9%	32.9%	37.7%	32.9%
S 2s (228.0 eV)	0.9%	0.6%	0.9%	0.5%
S 2s (232.4 eV)	0.6%	1.3%	0.9%	1.3%
Ge 2p$_{3/2}$ (1218.9 eV)	-	-	0.3%	0.6%

*Figure 49: ToF-SIMS analysis of modified **Sil4-TPM-acetylene-TPM-SH** surfaces via thiol-yne/ene reaction with and TPM-acetylene: (a) represents the corresponding Si^{-} signals of the modified and unmodified sample, (b) represents the corresponding SH^{-} signals, (c) represents the corresponding C$_2^{-}$ fragment, and (d) represents the corresponding SH^{-} fragment compared to the TPM-SH layer.*

*Figure 50: ToF-SIMS analysis of the modified **Sil4-TPGe-acetylene-TPM-SH** surfaces via thiol-yne reaction with and TPGe-acetylene: (a) represents the corresponding Si⁻ signals of the modified and unmodified sample, (b) the SH⁻ signals, and (c) the Ge⁺ fragment.*

4.3.3.4 Synthesis of the fourth layer

Based on the previously built third layer, the introduction of a fourth layer was performed on the **Sil4-TPM-acetylene-TPM-SH-TPM-acetylene** and **Sil4-TPGe-acetylene-TPM-SH-TPGe-acetylene** samples with TPM-SH by applying the established synthesis protocol (Scheme 58).
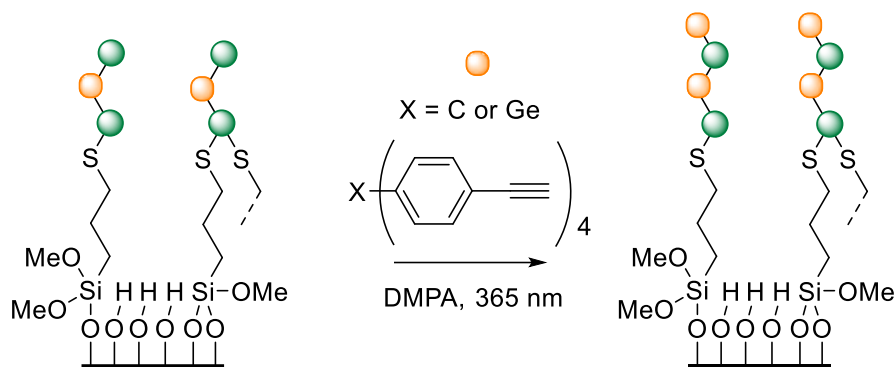
*Scheme 58: Synthesis protocolof modification of **Sil4-TPM/Ge-acetylene-TPM-SH-TPM/Ge-acetylene** functionalised surfaces with TPM-SH via thiol-yne/ene reaction.*

After modification, XPS analysis showed a decrease of the carbon C 1s as well as both sulfur signals, indicating no further layer growth (Table 15). This could be explained by an incomplete previous modification. Nevertheless, hints of modification for the Ge series were detected (based on the increased carbon C 1s and sulfur S 2s signals) although a difference, especially in the silicon Si $2p_{3/2}$ signal, was not detected. Furthermore, the germanium Ge $2p_{3/2}$ signal decreased, confirming the addition of the TPM-SH layer. Due to the lack of conversion, only the fourth layer of the TPGe series was further analysed by ToF-SIMS (Figure 51). Both the surface analysis and the fragment analysis showed slight decrease in the SH⁻ signal (Figure 51, a and b) and intensity of the Ge⁺ fragment (Figure 51, c) verifying a sporadic modification.

4. Results

*Table 15: Comparison of the atomic percentage of C 1s, Si 2p3/2, S 2s and Ge 2p3/2 of **SiI4-TPM/Ge-acetylene-TPM-SH-TPM/Ge-acetylene** functionalised surfaces before and after a thiol-yne reaction with TPM-SH measured by XPS.*

atom	SiI4			
	3.layer	TPM-SH	3. layer (Ge)	TPM-SH
C 1s (285.0 eV)	23.4%	16.3%	21.7%	23.4%
Si 2p3/2 (99.5 eV)	32.9%	36.8%	32.9%	32.8%
S 2s (228.0 eV)	0.6%	0.7%	0.5%	1.5%
S 2s (232.4 eV)	1.3%	1.0%	1.3%	1.4%
Ge 2p3/2 (1218.9 eV)	-	-	0.6%	0.4%
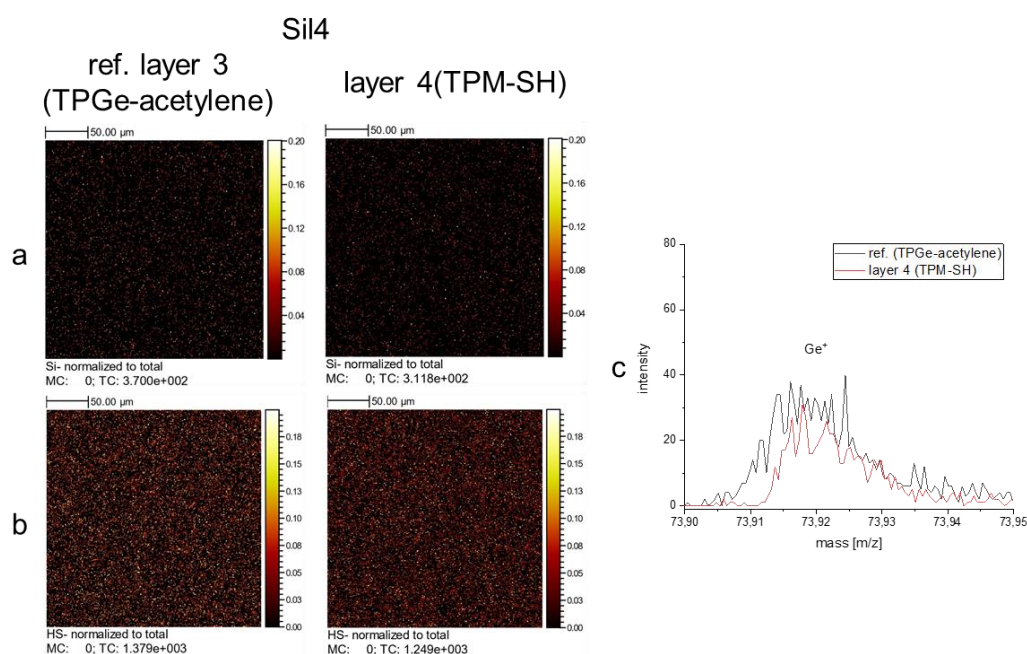
*Figure 51: ToF-SIMS analysis of the modified **SiI4-TPGe-acetylene-TPM-SH-TPGe-acetylene** surfaces via thiol-yne reaction with and TPM-SH: (a) represents the corresponding Si⁻ signals of the modified and unmodified sample, (b) the SH⁻ signals, and (c) the Ge⁺ fragment.*

In conclusion, wafer with up to three layers (TPM-series) and four layers (TPGe-series) were successfully synthesised and the presence as well as the homogeneity of each layer was confirmed by XPS- and ToF-SIMS measurements, which is further demonstrated by the summary of the XPS results in (Figure 52). In case of the TPM-series, the progress of sulfur percentage is not fully matching the progress of carbon percentage, displaying a linear increase and thus only indicating the formation of a third layer. Whereas the TPGe-series displays a linear increase of carbon up to

the third layer but weakening to the fourth. Sulfur and germanium signals show the expected zigzag progress up to the fourth layer, confirming its formation.
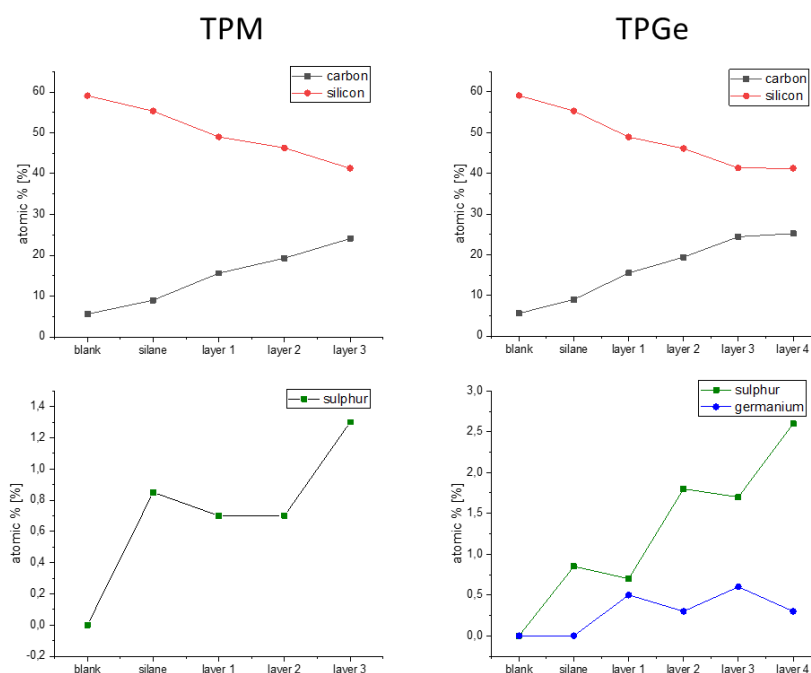
Figure 52: Development of the atomic percentage measured after each modification step for the TPM and TPGe series.

Therefore, the reaction conditions for the modification of silicon wafers with several distinct layers of thiol and acetylene compounds *via* thiol-yne/ene / MLD approach were successfully established. It was found that for the modification with TPM-acetylene, an irradiation time of 1.5 hours, a concentration of 0.16 mmol/L, 2.5 mg of 2,2-dimethoxy-2-phenylacetophenone (DMPA) per 1.5 mL, a wavelength of 365 nm, and argon atmosphere produced the best results. With regard to TPM-SH, the optimal reaction results were obtained when a monomer concentration of 7.5 mmol/L, 1 mg of DMPA per 1.5 mL DMF and an irradiation time 45 minutes were employed. The best results were achieved using a silicon wafer modified with **Sil4** as starting point for a stepwise layer formation. Furthermore, first modifications of *sec* amine-terminated surfaces *via* amino-yne "click" chemistry for the first and second layer were evaluated

4.3.3.5 Postmodification of thiol-yne network

Another goal of this thesis was the post-modification of previously formed networks on silicon surfaces with small molecules capable of permeating the pores of the top layer and thus being able to cap remaining free thiol groups. Therefore, a **Sil4-TPM-acetylene** functionalised surface was treated with 0.5 mL allylbromide in 1 mL DMF and 5 mg DMPA as radical starter and irradiated for 1.5 hours at 365 nm (Scheme 59). A possible side reaction is the nucleophilic substitution of the bromine by the thiol groups.
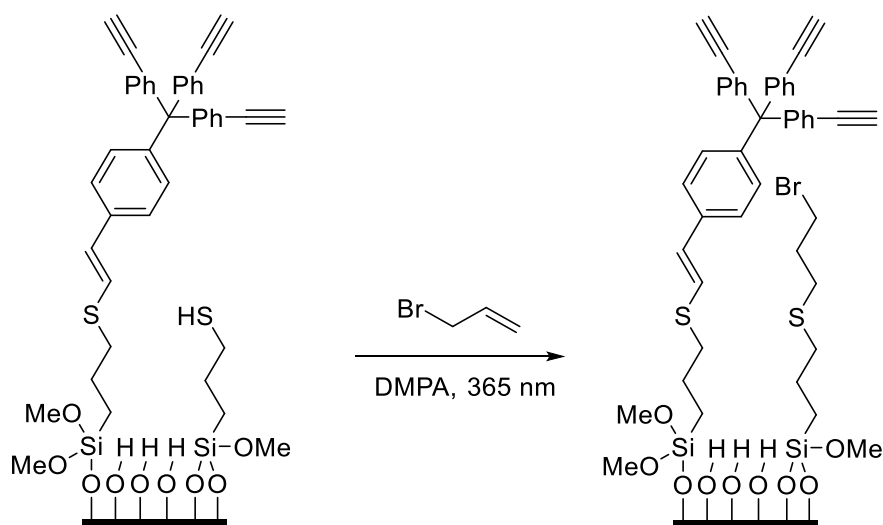
*Scheme 59: General procedure for the post-modification of **Sil4-TPM-acetylene** functionalised surfaces with allylbromide via thiol-ene reaction.*

Table 16 shows the XPS results after post-modification. Due to the small and inconsistent changes in atomic percentage, either degradation of the modified silicon wafers occurred, or the modification of the first layer was not homogeneous and thus the measured area shows low density of TPM-SH. Only a minor indication of modification was deduced by the appearance of the bromine Br $3d_5$ signal. ToF-SIMS analysis did not show any changes in the intensity of specific fragments like Br$^-$ or C_3H_x. No conversion was detected even after multiple attempts of conducting this procedure. However, since the reactive species, which starts the thiol-ene/yne reaction, is anchored on the surface and not onto the top layer, it was hypothesised that the characteristic signals are less abundant in an XPS measurement and thus this method cannot offer conclusive results for this setup.

*Table 16: Comparison of the atomic percentage of C 1s, Si 2p$_{3/2}$, S 2s and Br 3d$_{5/2}$ of **Sil4-TPM-acetylene** functionalised surfaces before and after a thiol-ene reaction with allylbromide measured by XPS.*

Sil4	C 1s (285.0 eV)	Si 2p$_{3/2}$ (99.5 eV)	S 2s (228.0 eV)	S 2s (232.4 eV)	Br 3d$_{5/2}$ (70.5 eV)
1. layer	19.53%	31.13%	0.93%	0.43%	-
Allyl-bromide	14.30%	38.30%	1.33%	0.43%	0.17%

Furthermore, the post-modification with small, double bond-containing molecules was investigated using allylamine on a **Sil4-TPM-acetylene-TPM-SH-TPM-acetylene** functionalised surface. Therefore, 0.5 mL of allylamine was dissolved in 1 mL of DMF, 5 mg DMPA was added, and the surface was irradiated for 1.5 hours at 365 nm (Scheme 60).

Scheme 60: General procedure for the post-modification of Sil4-TPM-acetylene-TPM-SH-TPM-acetylene

The depicted third layer was chosen for an appropriate sample, because there should be unreacted thiol groups accessible, which are covered with one TPM-acetylene. Furthermore, if there is a network like structure there is a possibility to even address the thiol groups of the silane layer, increasing the intensity when using the applied analysis methods. XPS analysis showed a slight decrease of the silicon Si 2p$_{3/2}$ and both sulfur signals, while a slight increase in the nitrogen N 1s signal was observed.

4. Results

This confirmed the successful post-modification of the available thiol groups of the previous TPM-SH layer. However, due to the small changes, ToF-SIMS analysis showed no clear results and is thus not discussed further.

*Table 17: Comparison of the atomic percentage of C 1s, Si 2p$_{3/2}$, S 2s and N 1s of of **SiI4-TPM-acetylene-TPM-SH-TPM-acetylene** functionalised surfaces before and after a thiol-ene reaction with allylamine measured by XPS.*

SiI4	C 1s (285.0 eV)	Si 2p$_{3/2}$ (99.5 eV)	S 2s (228.0 eV)	S 2s (232.4 eV)	N 1s (400.4 eV)I
3. layer	38.8%	22.7%	3.5%	1.3%	0.6%
allylamine	38.5%	19.4	3.3%	1.3%	1.1%

This detection problems consequently led to concerns regarding how to further proceed in changing the chemical environment *via* postmodification. As seen from the two previous examples, the post-modification of monomolecular layers only proceeded in small amounts, if at all, and were within a certain error of the modification density and measurement errors. To overcome this problem, the quantity of accessible functional groups could be increased as shown in chapter **4.3.3.1**, thus leading to better conversions and improved detection possibilities. Furthermore, increasing the size of building blocks is hypothesised to increase the permeability of both initiator and reactants.

To evaluate the influence of the reactant on post-modification of previously built surfaces, small thiol-functionalised molecules such as 1-propanethiol and 3-chloro-1-propanethiol were chosen. Therefore, 0.5 mL of the corresponding thiol were dissolved in 1 mL of DMF containing 5 mg DMPA and irradiated for 1.5 hours at 365 nm (Scheme 61).
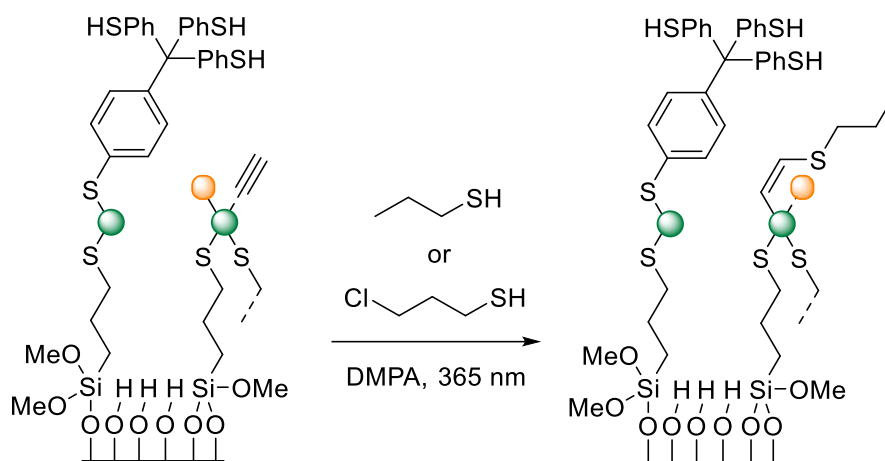
*Scheme 61: General procedure for the post-modification of **SiI4-TPM-acetylene-TPM-SH** functionalised surfaces with 1 propanethiol and 3 chloro 1 propanethiol via thiol-ene reaction.*

Both resulting surfaces showed a significant decrease in carbon C 1s and both sulfur signals, as derived from XPS analysis (Table 18). By comparing these values with the corresponding first layer (**SiI4-TPM-acetylene** = 1. layer), more reasonable values for the second layer were obtained. These results match with the aforementioned procedure published by Levkin and co-workers, reducing disulfides *via* a radical starter and a free thiol (*215*). This could thus be a possible pathway to eliminate the formed multilayers at the cost of eventually losing all accessible alkyne/ene functional groups of the previous layers(s).

*Table 18: Comparison of the atomic percentage of C 1s, Si 2p3/2, S 2s and Cl 2p3/2 of of **SiI4-TPM-acetylene-TPM-SH** functionalised surfaces before and after a thiol-ene reaction with 1-propanethiol and 3-chloro-1-propanethiol measured by XPS.*

SiI4	C 1s (285.0 eV)	Si 2p3/2 (99.5 eV)	S 2s (228.4 eV)	S 2s (232.4 eV)	Cl 2p3/2 (200.5 eV)l
2. layer	36.1%	22.3%	4.3%	1.1%	-
1-propane-thiol	18.7%	33.1%	1.9%	0.7%	-
2. layer	45.0%	17.8%	5.7%	0.6%	-
3-chloro-propane-1-thiol	28.4%	29.3%	4.1%	1.0%	-
1. layer	13.9	32.2%	2.3%	0.5%	-

4.3.4 Amino-yne surface modification

4.3.4.1 Synthesis of the first layer

In the course of the modification reactions on silicon substrates, more effort was devoted to an alternative, more selective modification method, finally leading to the evaluation of the hydroamination reaction. Especially the high atom economy as in thiol-yne/ene reactions and the catalyst free procedure at room temperature affirmed this choice as already mentioned in chapter **2.1.3**. At first, chlorine terminated surfaces (**Sil5**) needed to be further functionalised to bear the appropriate functional group. Therefore, the samples were modified with a 1 wt% piperazine solution in dry toluene for 6 hours in a petri-dish under argon atmosphere (Scheme 62), leading to terminal secondary amines. Afterwards, the samples were rinsed with chloroform, toluene and isopropanol and dried over an argon stream.
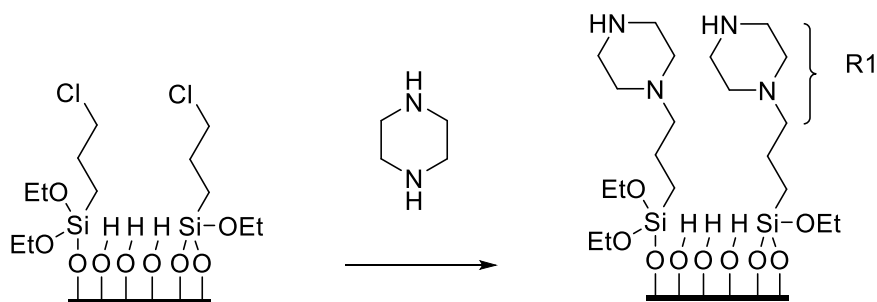
*Scheme 62: General procedure for the modification of **Sil5** functionalised surfaces with piperazine.*

After that, the sample was analysed *via* XPS and ToF-SIMS. The atomic percentages provided by XPS are inconsistent and there is no explicit prove of a successful modification (Table 19). Only by consideration of the ToF-SIMS results, an increase in C_2H^- and decrease in Si^- were observed (Figure 53) combined by an decrease of the unique Cl^- fragment, confirming at least a partial substitution of chlorine through piperazine.

*Table 19: Comparison of the atomic percentage of C 1s, Si 2p$_{3/2}$, Cl 2p$_{3/2}$ and N 1s of of **Sil5** functionalised surfaces before and after a thiol-ene reaction with piperazine measured by XPS.*

Sil5	**C 1s** (285.0 eV)	**Si 2p$_{3/2}$** (99.5 eV)	**Cl 2p$_{3/2}$** (200.5 eV)	**N 1s** (400.5 eVl
silane	6.3%	43.4%	0.50%	0.7%-
piperazine	6.4%	43.8%	0.4%	0.6%

Sil5

ref. silane   layer 1 (piperazine)
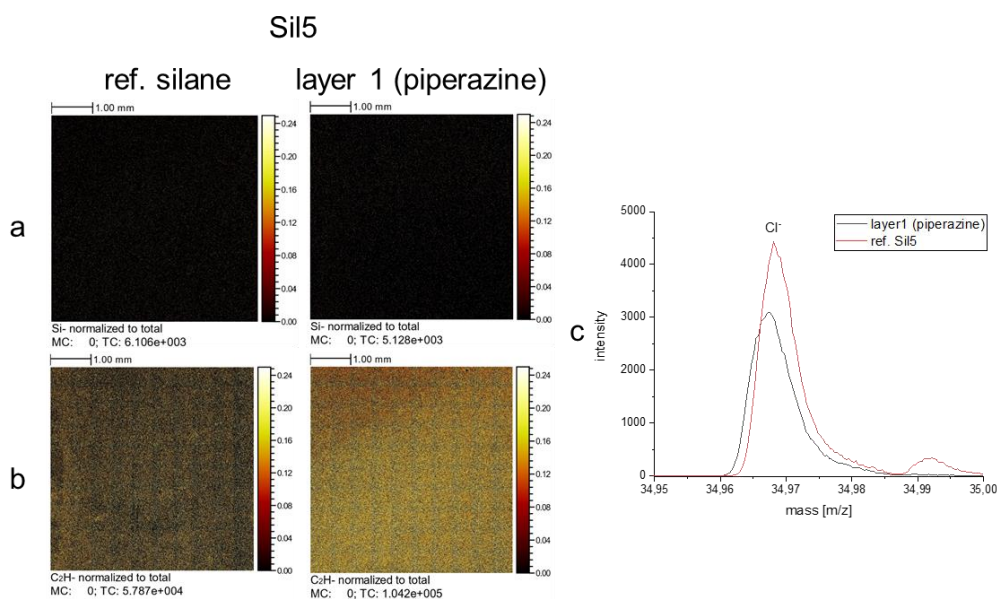
*Figure 53: ToF-SIMS analysis of the modified **Sil5** surfaces via nucleophilic substitution of chlorine with piperazine: (a) represents the corresponding Si⁻ signals of the modified and unmodified sample, (b) the C_2H^- signals, and (c) the Cl⁻ fragment.*

Due to these unsatisfying results, **Sil6** was introduced providing a secondary amine, as shown in chapter **4.3.2**. As first layer, 200 µl of 2-propiolic acid, 1,1'-(oxydi-2,1-ethanediyl) ester (PEG-A) was dissolved in 1.5 mL chloroform and poured over the amine modified silicon wafer inside a petri-dish under argon atmosphere for 4 hours (Scheme 63).
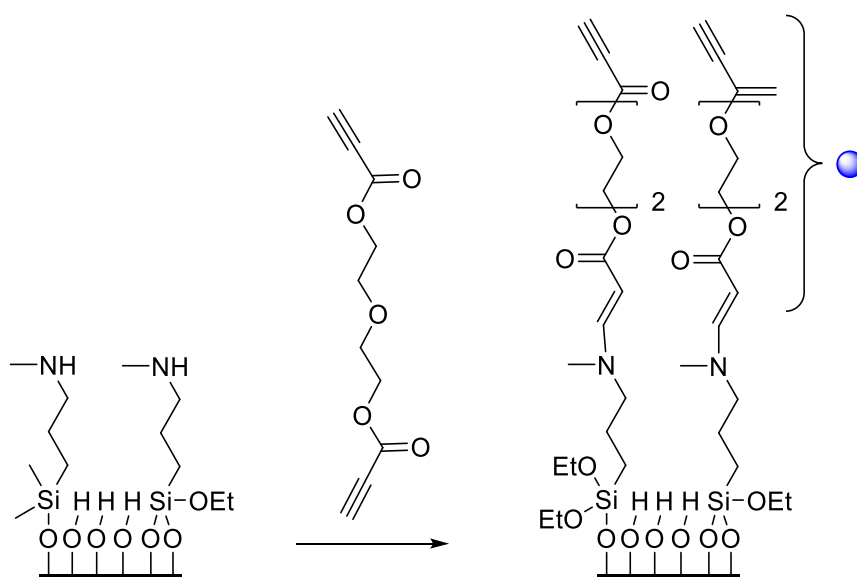
*Scheme 63: General procedure for the modification of **Sil6** functionalised surfaces with PEG-A.*

4. Results

As expected, XPS-analysis showed a significant increase in carbon C 1s signal, and decrease in silicon Si 2p$_{3/2}$ and nitrogen N 1s (402.7 eV) signals (Table 20). Analogously to the developed analytical protocol, ToF-SIMS measurements were performed identifying the typical fragment $C_2H_4O_2^-$ for the modified surfaces (Figure 54). However, compared to the silane layer **Sil6**, the total counts of CN$^-$ increased, which can be explained by a denser functionalisation of the silane **Sil6** onto the silicon wafer.

*Table 20: Comparison of the atomic percentage of C 1s, Si 2p$_{3/2}$, and N 1s of **Sil6** functionalised surfaces before and after an amino-yne reaction with PEG-A measured by XPS.*

Sil6	C 1s (285.0 eV)	Si 2p$_{3/2}$ (99.5 eV)	N 1s (400.5 eV)	N 1s (402.7 eV)
silane	7.9%	45.8%	0.8%	0.4%
PEG-A	10.5%	41.5%	0.8%	0.2%
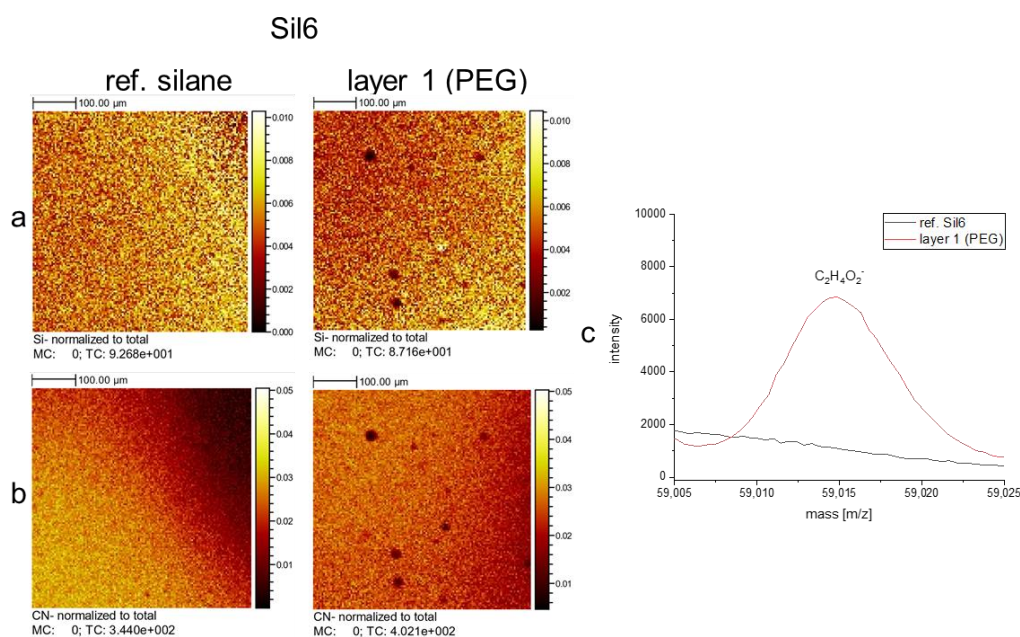
*Figure 54: ToF-SIMS analysis of the modified **Sil6** surfaces via hydroamination with PEG-A: (a) represents the corresponding Si$^-$ signals of the modified and unmodified sample, (b) the CN$^-$ signals, and (c) the C2H4O2- fragment.*

Concluding, amino-yne was shown to be a useful tool to graft layers onto a silicon wafer via the LBL approach. To enhance the process ability, higher temperatures or higher concentrations may be advantageous.

4.3.4.2 Synthesis of second layer

After the successful modification of **Sil6** functionalised surfaces with PEG-A, a second layer was introduced as proof of principle for hydroamination reactions. Therefore, samples with **Sil6-PEG-A** modification were covered with a solution of 0.2 mL diisopropylamine dissolved in 1 mL chloroform at room temperature for two hours (Scheme 64).
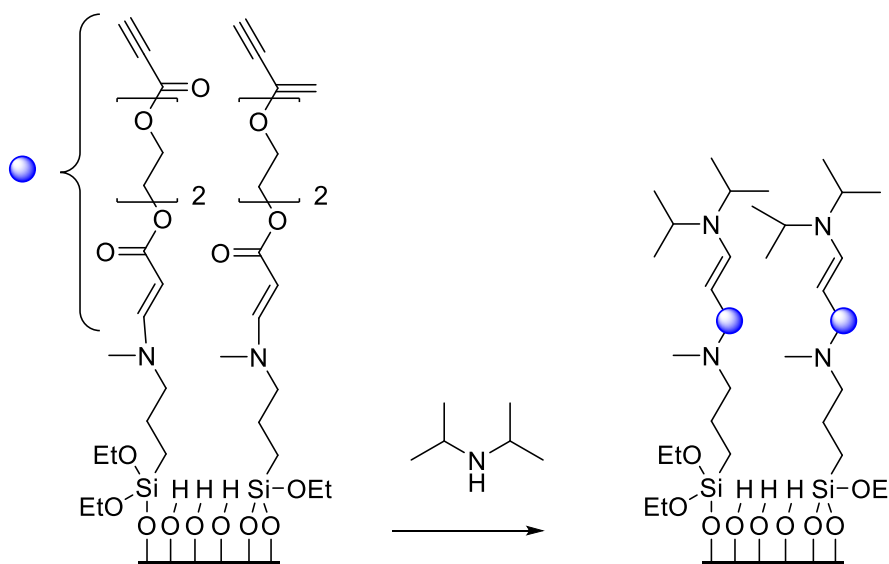
*Scheme 64: Synthesis protocol for the modification of **Sil6-PEG-A** functionalised surfaces with diisopropylamine.*

As with previous samples, analysis was performed by XPS and ToF-SIMS. By comparison of the carbon C 1s binding energies of the first and second layer, the atomic percentage was found to decrease followed by an overall increase in the nitrogen N 1s signal. It was hypothesised that cleavage of the ester group or the silanol groups took place due to the presence of water in diisopropylamine, thus decreasing the carbon percentage and concomitantly increasing the nitrogen ratio. This explanation was further supported by ToF-SIMS analysis, shown in Figure 55. The silicon Si$^-$ intensity significantly increased, as did the CN$^-$ intensity (Figure 55, a and b). Furthermore, the inhomogeneity of the surface was reduced (fewer black spots on the surface) and the intensity of characteristic fragment C$_2$HO$^-$ for PEG-A dramatically decreased.

4. Results

*Table 21: Comparison of the atomic percentage of C 1s, Si 2p$_{3/2}$, and N 1s of **Sil6-PEG-A** functionalised surfaces before and after a amino-yne reaction with diisopropylamine measured by XPS.*

Sil6	C 1s (285.0 eV)	Si 2p$_{3/2}$ (99.5 eV)	N 1s (400.5 eV)	N 1s (402.7 eV)
1. layer (PEG-A)	10.5%	41.5%	0.8%	0.4%
diisopropylamine	7.8%	44.4%	1.1%	0.2%
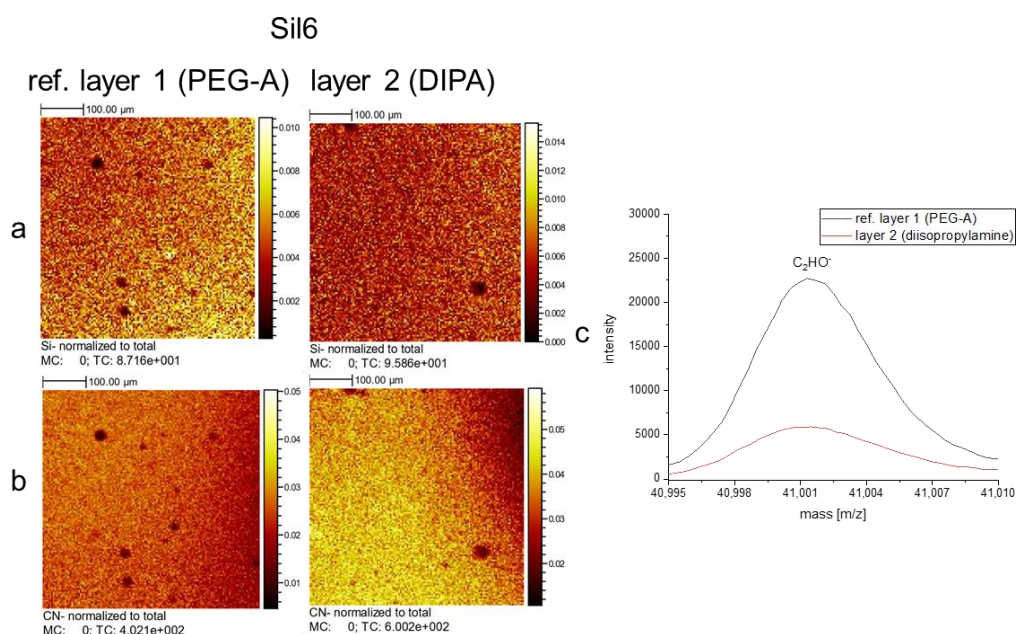
*Figure 55: ToF-SIMS analysis of the modified **Sil6-PEG-A** surfaces via hydroamination with diisopropylamine: (a) represents the corresponding Si$^-$ signals of the modified and unmodified sample, (b) the CN$^-$ signals, and (c) the C$_2$HO$^-$ fragment.*

In order to further confirm the PEG-A functionalisation of the surface *via* an amino-yne "click" reaction, **Sil6-PEG-A** was modified with in a thiol-yne/ene reaction with TPM-SH, targeting the free alkyne groups of the brush-like molecules. The procedure was adapted from previous optimised synthesis steps (chapter **4.3.3.2**) and is shown in Scheme 65.
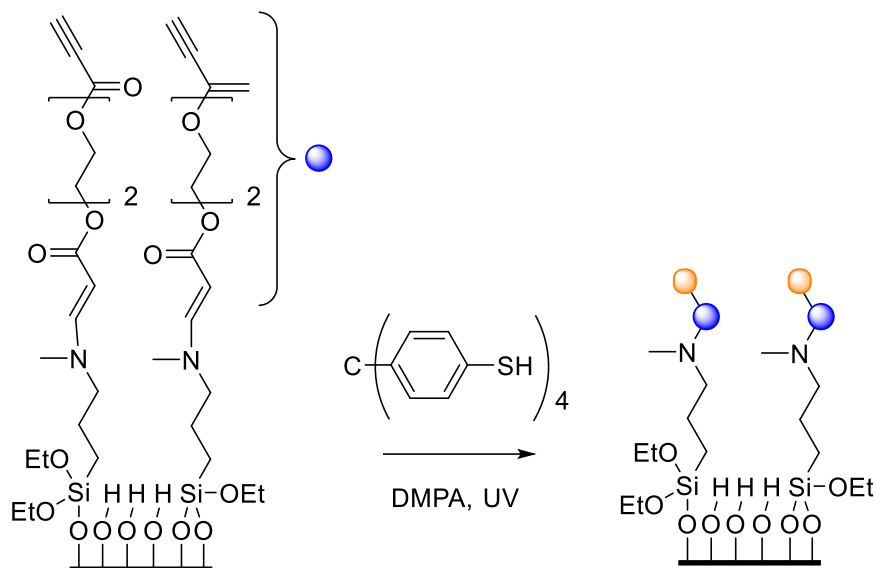
*Scheme 65: Synthesis protocol for the modification of **Sil6-PEG-A** functionalised surfaces with TPM-SH.*

XPS analysis indicated the successful modification of the alkyne-terminated **Sil6-PEG-A** (Table 22). The carbon C 1s and sulfur S 2s signals significantly increased while a second S 2s signal appeared indicating oxidation of the thiols to the corresponding disulfide network. According to XPS, ToF-SIMS analysis affirms these results by a decrease of the intensity of the Si⁻ fragment by a factor of 34 and an increase of the SH⁻ fragment by a factor of 13 (Figure 56).

*Table 22: Comparison of the atomic percentage of C 1s, Si 2p₃/₂, and N 1s of **Sil6-PEG-A** functionalised surfaces before and after a thiol-yne reaction with TPM-SH measured by XPS.*

Sil6	C 1s (285.0 eV)	Si 2p₃/₂ (99.5 eV)	S 2s (228.0 eV)	S 2s (232.4 eV)	N 1s (400.5 eV)l
1. layer (PEG-A)	10.5%	41.5%	-	-	0.8%
TPM-SH	72.3%	5.3%	9.4%	0.5%	0.3%
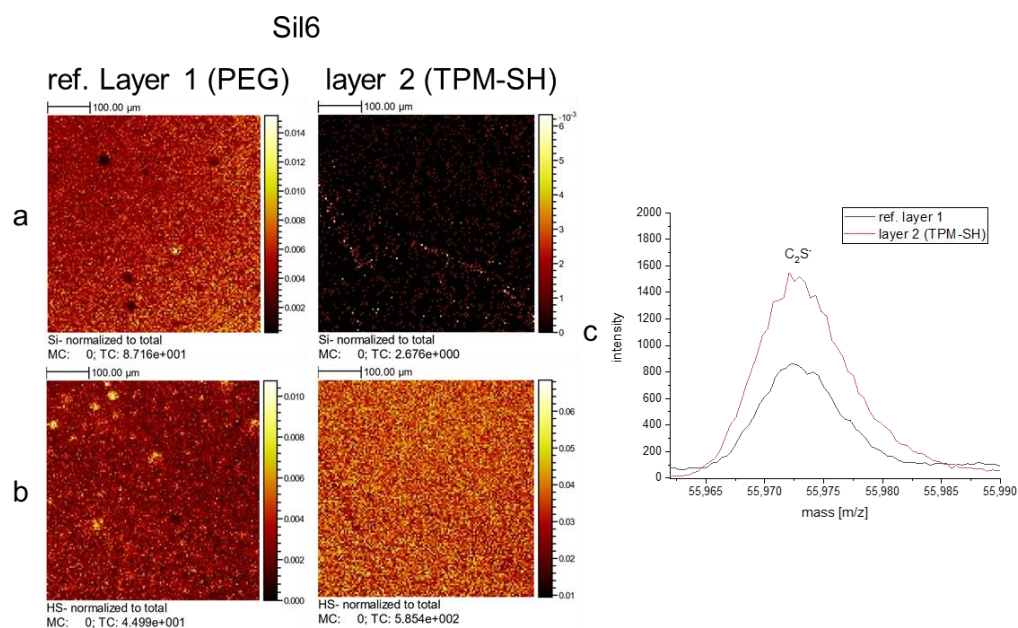
*Figure 56: ToF-SIMS analysis of the modified **Sil6-PEG-A** surfaces via thiol-yne raction with TPM-SH: (a) represents the corresponding Si⁻ signals of the modified and unmodified sample, (b) the SH⁻ signals, and (c) the C₂S- fragment.*

In conclusion one layer could be synthesised onto **Sil6** functionalised silicon surfaces *via* hydroamination. This was confirmed by XPS and ToF-SIMS measurements. Additionally, modification of the PEG-A layer *via* thiol-yne/ene "click"-chemistry was performed to combine both reaction types.

This can be seen as proof of principle for a LBL approach exploiting amino-yne instead of thiol-yne/ene reaction introducing a growing chain bearing γ-amino Michael systems. Applying this reaction some structure motifs or compounds can probably be easier introduced compared to the thiol-yne/ene reaction increasing the overall versatility of this approach. Furthermore, it has to be highlighted that in comparison to the thiol-yne reaction in which a follow-up thiol-ene reaction is an often-occurring side reaction no "amino-ene" reaction takes place due to a high energy barrier assuming the Michael system is an ester.

For further investigations several amines should be tested, for instance less sterically demanding ones like the used DIPA in low concentrations to examine the potential of this reaction. As already mentioned in chapter **6.3.6.1**, higher temperatures and concentrations may increase the conversion and reduce the time needed. However, as evident from modifications with diisopropylamine, too high concentrations led to degradation of previous PEG-A layer.

4.4 Theoretical calculations

4.4.1 Force-field calculations of tetrahedral building blocks

In order to better understand the "ideal" network formed by TPM-thiol and TPM-acetylene building blocks, quantum chemical calculations have been made by collaboration partners Y. Pramudya and M. Kozlowska. Calculations were performed by ReaxFF 6.0 developed by Goddard and co-workers (*216*) and further processed with the open source program Zeo++ (*217–219*). Figure 57 shows the optimised ideal structure of TPM-acetylene (a) and TPM-thiol (b) as perfect tetrahedra. This conformation forms a diamond-like network (c, d) with an exemplary composition of $H_{64}C_{116}S_8$ with initial diamond structures a = b = 21 Å, c = 37 Å and angles of 90 ° with a tetragonal lattice. The first shows the connection of four alternating building blocks in one dimension inside the network, whereas the second displays the network from a shifted angle to better visualise the pores. The blue (outside) and grey (inside) structure visualises the calculated volumetric surface of adsorbed nitrogen onto the specific surface. The theoretical calculated surface area is 7,444 m^2/g and the free accessible volume 4.09 cm^3/g.
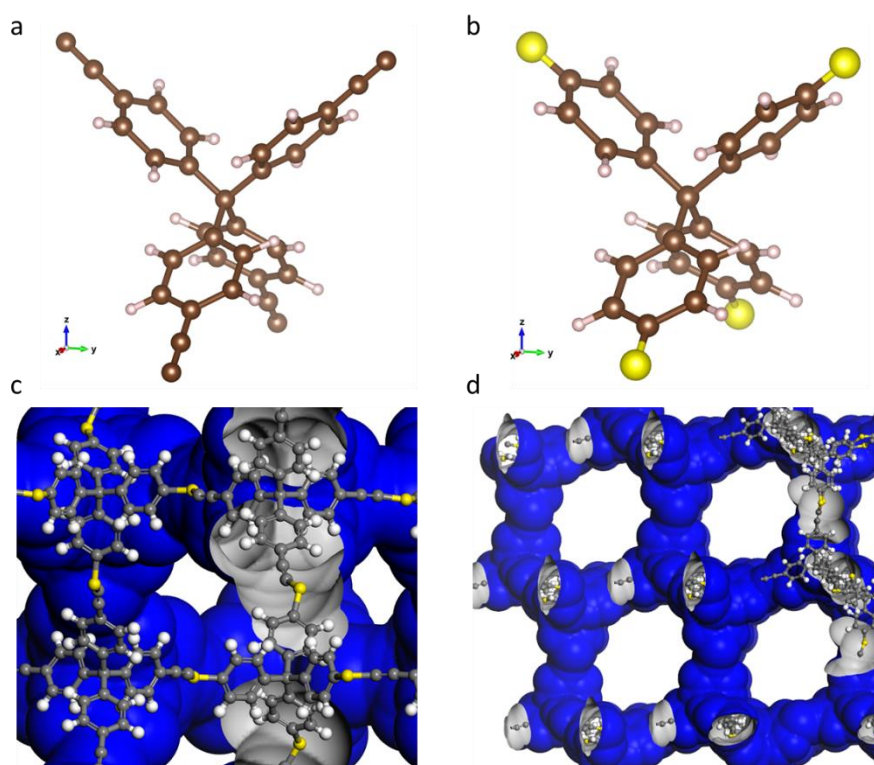
Figure 57: Quantum chemical calculations of the idealised network structure built from TPM-thiol and TPM-acetylene.

4. Results

Figure 58 shows the channels of the built diamond-like structure with an approximated window size of the channel straight direction (space diagonal) of 11.3 Å and a pore diameter (maximum ball diameter fit in the pore) of 13.1 Å. Therefore, the pores are large enough that a variety of ions, such as Li^+ (0.9 Å) and its counterions (e.g. PF_6^- = 5.1 Å) can easily pass through (*220*).
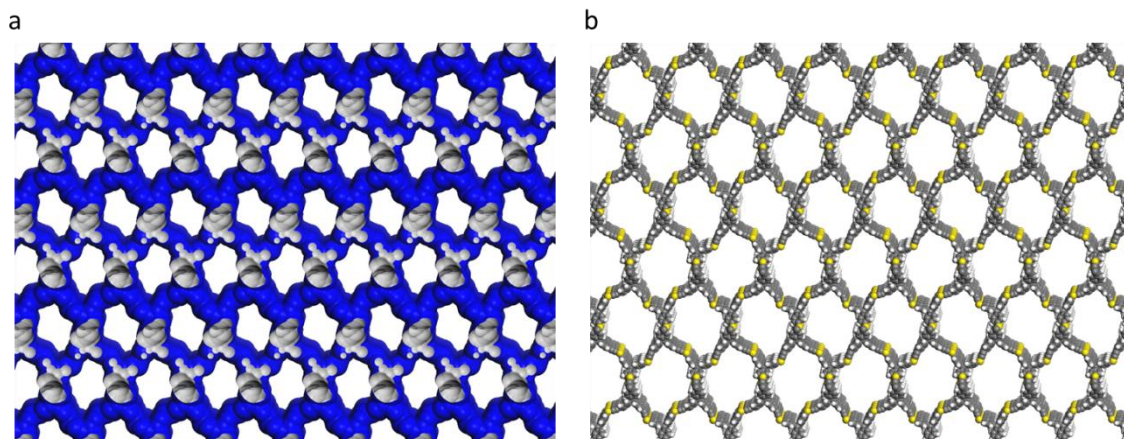
Figure 58: Quantum chemical calculations of the idealised network structure built from TPM-thiol and TPM-acetylene with view through the channels (a) with N_2 adsorption (b) without N_2 adsorption.

The ideal value of the specific surface area can be compared to already synthesised networks. Lang analysed the surface of the displayed network *via* BET measurements resulting in 180 m^2/g (*221*). This immense difference can be explained by the irreversible nature of the thiol-yne reaction and thus the lack of reorganisation to the thermodynamically more stable product. This generates defects and thus larger pores with less specific surface areas are present.

4.4.2 Quantum chemical calculations of Li-building block interactions

To calculate the influence of different groups on the lithium – building block interaction, a variety of secondary and tertiary amines and thio-ethers were theoretically investigated through quantum chemical calculations in close cooperation with Dr. K. Reiter. They were performed with the TURBOMOLE program package (*222, 223*) at the level of density functional theory (DFT) (*224*) employing the PBE0 hybrid exchange-correlation function with the basis sets of type def2-TZVPP (*225*). TURBOMOLE's grid 4 was used for the numerical quadrature and the self-consistent-field energy-convergence threshold was set to 10^{-8} E_h. Furthermore, the D3 dispersion correction in conjunction with Becke-Johnson damping was used (*226*). Geometries were optimised with geometry-convergence thresholds of 10^{-7} E_h for the energy and 10^{-5} E_h /a_0 for the Cartesian gradient. All following figures only show the interaction of one arm of the tetrahedral building blocks. Many simplifications to shorten the calculation time, such as focusing on only one arm, no interactions with other molecules and ideal surroundings, were made. All stated energy-differences are calculated regarding the neutral building block with a single lithium ion being infinitely far away. Figure 59 shows the one arm of the already introduced TPM-*sec* butylamine (a,b) and the lithium ion resting in the middle of the phenyl ring and on top of the nitrogen atom. As expected, the aromatic ring is more favoured (-223.6 KJ/mol vs. -203.0 KJ/mol).

a   b

c   d

-223.6 KJ/mol   -203.0 KJ/mol
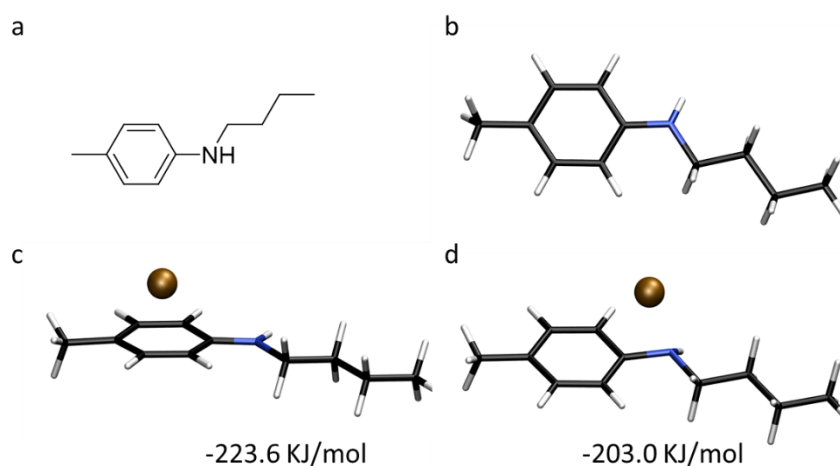
Figure 59: Calculated energy differences in comparison to one neutral arm of the TPM-sec. butylamine building block (a) or rather DFT calculated neutral fragment (b) by interaction with the aromatic ring (c) and the nitrogen (d).

4. Results

To further evaluate the influence of the sidearm on the system, another heteroatom (oxygen) has been introduced as ether function (Figure 60). In comparison, the alkyl chain sidearm has no influence on the energy gain of the aromatic and nitrogen position (-218.6 KJ/mol and -197.3 KJ/mol), but a chelating effect is observed, trapping the Li$^+$ ion (-275.5 KJ/mol). The position next to the oxygen is not favoured (-176.3 KJ/mol).
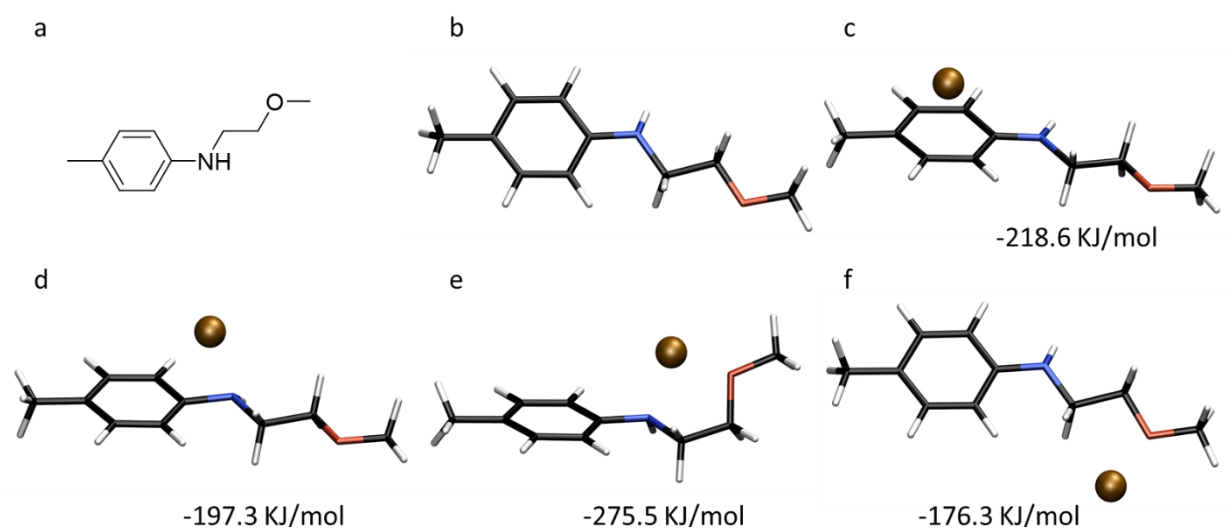
Figure 60: Calculated energy differences in comparison to one arm of the TPM-sec. methoxy ethylamine building block and (a) and (b) by interaction with the aromatic ring (c), nitrogen (d), chelate complex (e) and oxygen (f).
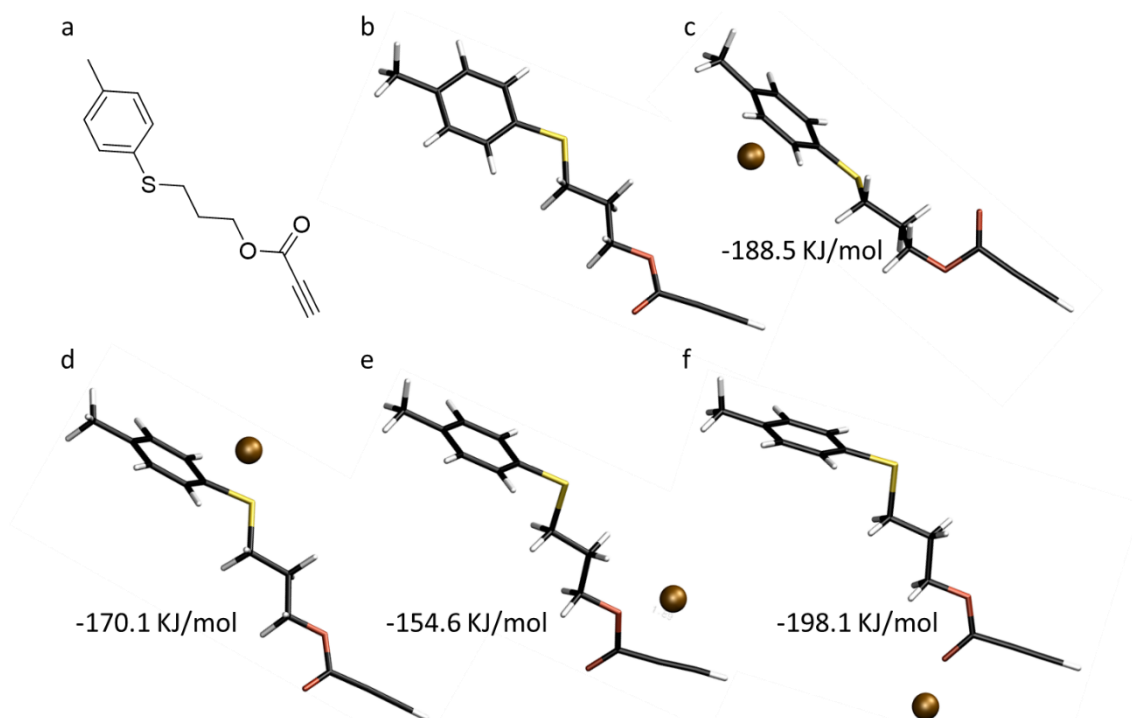
Figure 61: Calculated energy differences in comparison to one a combination of a thioether and an alkyne ester (a) and (b) by interaction with the aromatic ring (c), thiol (d), alkyne (e) and ester (f).

Figure 61 combines the connection of a thiol to an alkyl chain, such as in the thiol-yne reaction, and the necessary alkyne ester for the amino-yne "click" reaction. The thioether is destabilising the ring and therefore the gained energy of the Li-ring interaction is weakened to -188.5 KJ/mol and the interaction of the thiol itself is lower compared to that of nitrogen (170.1 KJ/mol vs. 197.3 KJ/mol). The bridging oxygen ester is less favoured than the ether and the double-bonded one (-154.6 KJ/mol *vs.* 176.3 KJ/mol *vs.* 198.1 KJ/mol).
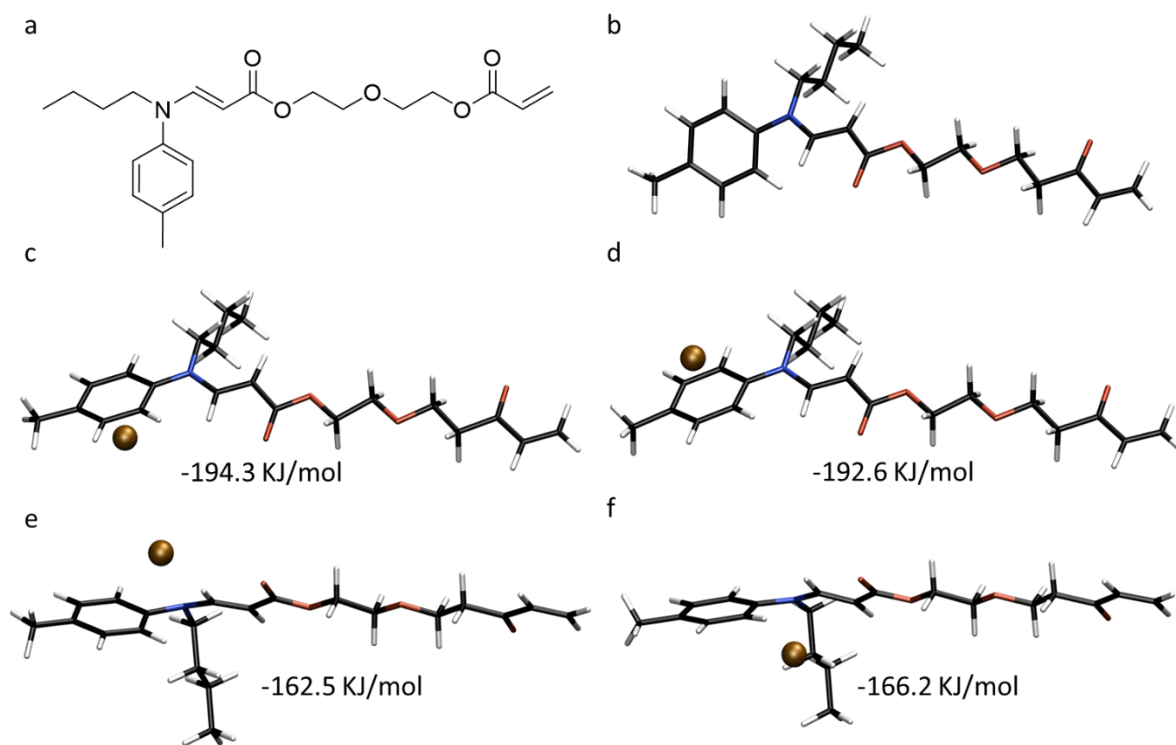
Figure 62: Calculated energy differences in comparison to one arm of the hydroaminated TPM-sec. butalamine building blick with 2-propynoic acid, 1,1´-(oxydi-2,1-ethanediyl) ester ester (a) and (b) by interaction with the aromatic ring (c), aromatic ring and butyl rest (d), tertiary nitrogen (e), butylrest only (f).

Finally, the fragments of hydroaminated secondary amines (TPM-*sec* butylamine and TPM-*sec* 2-furanamine) (→ tertiary amine) with a 2-propynoic acid, 1,1'-(oxydi-2,1-ethanediyl) ester was calculated (Figure 62, Figure 63). In both cases, the aromatic ring interactions are weakened because of the formation of a tertiary amine. Furthermore, the "sandwich" position of the aromatic ring and the sidearm is preferred, whereas the furanyl group is slightly more stable. If a poly(ethylene glycol) linker is used, chelation possibly traps the lithium ion.
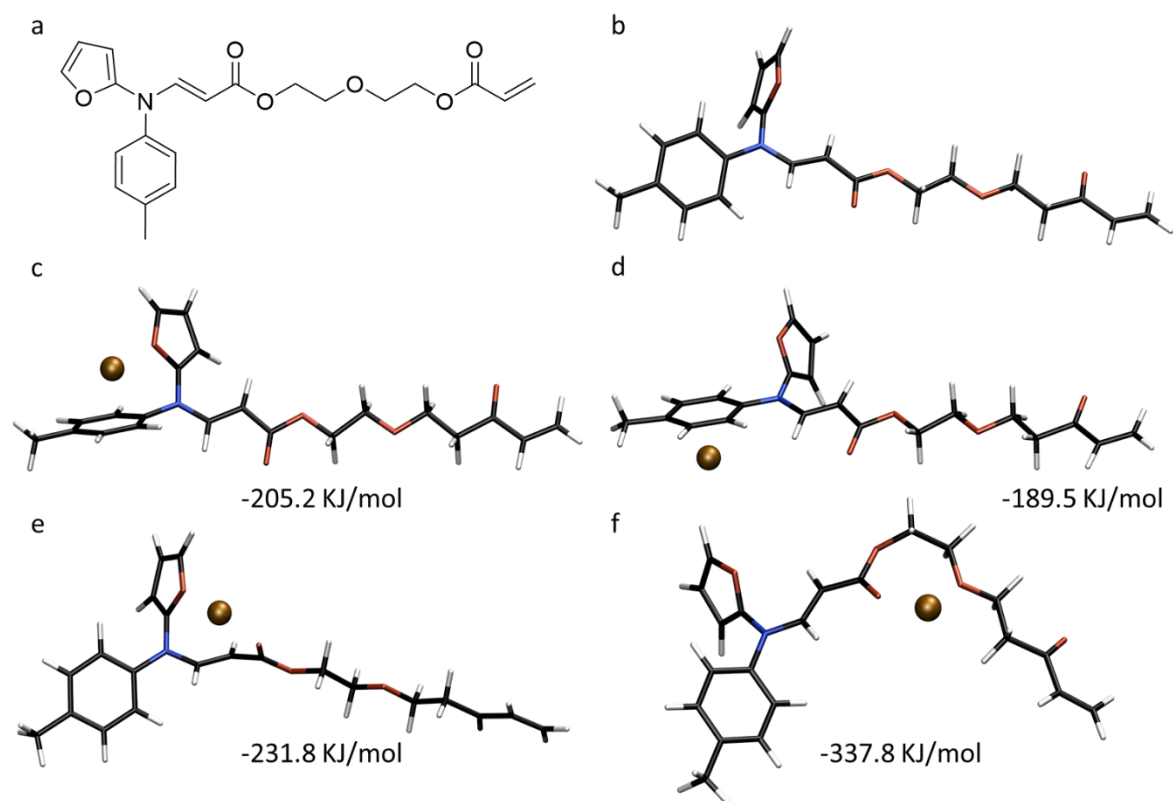
Figure 63: Calculated energy differences in comparison to one arm of the hydroaminated TPM-sec. 2-furanamine building blick with 2-propynoic acid, 1,1´-(oxydi-2,1-ethanediyl) ester ester (a) and (b), by interaction of the aromatic ring and furanyl rest (c), aromatic ring only (d), double bond and furanyl rest (e), chelation of the PEG unit (f).

Concluding, the variation of the linkage (amino-yne or thiol-yne) and sidearms (no or variation of heteroatoms) have a great impact on the stability of the lithium-network intermediates and therefore influence the transport of a lithium ion along an introduced gradient (synthesis of building blocks, chapter **4.1**). By using long PEG units, the possible chelation can immobilise the lithium ion and thus reduce the effectiveness of a lithium ion–based battery.

5. Conclusion

This thesis focused on the synthesis of rigid, multifunctional building blocks and the subsequent sequence-controlled modification of silicon wafers using these building blocks was shown. In a first step, a variety of tetrafunctional building blocks for thiol-ene/yne and amino-yne "click" reactions were synthesised and characterised *via* ^{1}H-, ^{13}C-NMR, COSY (correlated spectroscopy), HSQC (heteronuclear single quantum coherence spectroscopy), FT-IR (Fourier-transform infrared spectroscopy) and HRMS (Figure 64). Furthermore, the procedure for the synthesis of tetrakis(*p*-bromophenyl)methane (TPM) and tetrakis(*p*-bromophenyl)adamantane (TPA) were improved with regards to purity and yield by utilising less equivalents of elementary bromine. However, the sulfonation and nitration reaction for the synthesis of TPM molecules bearing functionalities that can work as easy detectable markers for XPS and ToF-SIMS led to no conversion.
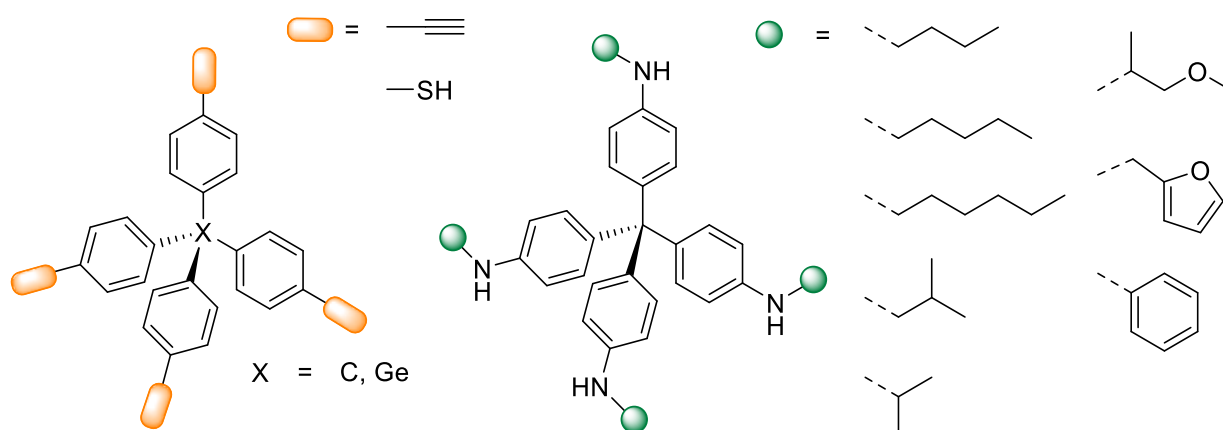
Figure 64: Successfully synthesised TPM-building blocks for thiol-yne or amino-yne "click" reactions.

On this basis, first studies for the formation of porous organic polymers (POPs) *via* amino-yne "click" reactions were performed. However, the obtained insoluble materials showed low surface areas (4.51 m^2/g). This finding was explained by the flexible structure of the linker, which is based on diethyleneglycol and the consequential collapse of the pores.

Furthermore, the silanisation process of different silanes (**Sil1**-**Sil6**) with different functional groups was evaluated. Hereby, the cyclic silanes **Sil4** and **Sil6** were found to be the most suitable ones, achieving homogeneous surface coverage in all

5. Conclusion

silanisation reactions. In various optimisation studies, it was found that, for the modification with TPM-acetylene, an irradiation time of 1.5 hours, a concentration of 0.16 mmol/L, 2.5 mg of 2,2-dimethoxy-2-phenylacetophenone (DMPA) per 1.5 mL, a wavelength of 365 nm and an argon atmosphere gave the best results. Regarding TPM-SH, this procedure was varied using a concentration of 7.5 mmol/L, 1 mg of DMPA per 1.5 mL DMF and an irradiation time 45 minutes. Applying these procedures, alternating layers up to the third layer of TPM-acetylene and TPM-SH were achieved. By changing the alkyne bearing building block to TPGe-acetylene, four monomolecular layers were obtained. All samples were carefully characterised by ToF-SIMS and XPS, confirming the deposition of molecular layers by the atomic percentage and significant fragments. Surface modifications *via* amino-yne "click" reactions were only performed as proof of concept studies up to the first layer.

Additionally, post-modification reactions of the formed TPM-acetylene/TPM-SH networks on the silicon surfaces were performed *via* thiol-ene/yne reactions using allylbromide, allylamine, 1-propanethiol and 3-chloro-1-propanethiol. Successful post-modification of the built networks were achieved for both allyl-reactants, but the reaction was not reproducible. The post-modification reaction applying the more active thiol-reactants led to the reduction of the formed disulphide. This finding is ibn agreement with the radical reduction of disulphide layers *via* a radical mechanism shown by Levkin and co-workers.

Finally, to get insight into the optimised structures of the formed porous organic frameworks, force field calculations of the TPM-thiol-yne network were performed, showing an approximated window size in the channel straight direction (space diagonal) about 11.3 Å. Based on the van-der Waals radius of the atom species in the channel and inside the pores, the calculated pore diameter is 13.1 Å. Those values prove the possible permeation of lithium and other ions as well as the corresponding counterions, for instance the ones mostly used in lithium-ion batteries. Additionally, quantum chemical calculations of Li-building block interactions with regards to various substituents of TPM provided information on how an electronical gradient can be introduced into a designed network consisting of tetrahedral building blocks.

6. Experimental Section

6.1 Equipment

6.1.1 ToF-SIMS (Time-of-Flight Secondary Ion Mass Spectrometry)

Tof-SIMS spectra were detected on a TOF-SIMS[5] spectrometer from ION-TOF GmbH Münster with $Cs/O_2/C_{60}$ and an Ar-Cluster gun with a sample size of 0.2 x 0.2 cm by either Dr. Sven Steinmüller, Dr. Raheleh Azmi or Vanessa Trouillet.

6.1.2 XPS (X-Ray Photoelectron Spectroscopy)

The XPS analyses was carried out in an ESCA/Alpha110 from Thermo Fisher Scientific, East Grinstead UK with a K-Alpha+ and an Ar-Ion Cluster Source in ultrahigh vacuum with spot sizes from 400 to 30 µm and a depth of 5 – 10 nm by either Dr. Sven Steinmüller, Dr. Raheleh Azmi or Vanessa Trouillet.

6.1.3 SEC (Size Exclusion Chromatography)

All measurements were performed on a Varian 390-LC SEC system equipped with a LC-290 pump (Varian), refractive index detector (24 °C), PL AS RT GPC autosampler (Polymer laboratories) and a Varian Pro Star column oven Model 510, operating at 40 °C. For separation, two SDV 5 µm linear S columns (8 × 300 mm) and a guard column (8 × 50 mm) supplied by PSS, Germany, were used. Tetrahydrofuran (THF) stabilised with butylated hydroxytoluene (BHT, HPLC-SEC grade) supplied by Sigma Aldrich was used at a flow rate 1.0 mL min-1. Calibration was carried out with linear poly(methyl methacrylate) standards (Agilent) ranging from 875 to 1 677 000 Da. Detection was done by a refractive index detector operating in THF (flow rate 1.0 mL min-1).

6.1.4 NMR (Nuclear Magnetic Resonance) – Spectroscopy

Two systems were used acquiring NMR spectra: WB Bruker AVANCE I spectrometer operating at 500 MHz for 1H- and 126 MHz for 13C-measurement or Bruker Aspect NMR spectrometer operating at 400 MHz for 1H- and 101 MHz for 13C-measurement.

CDCl3 or DMSO-d6 were used as solvents. Chemical shifts are presented in parts per million (δ) relative to the resonance signal at 7.26 ppm (1H, CDCl3) and 77.16ppm

(13C, CDCl3) or 2.50 ppm (1H, DMSO-d6) and 39.52 ppm (13C, DMSO-d6), respectively. Coupling constants (J) are reported in Hertz (Hz). All measurements were recorded in a standard fashion at 25 °C. Full assignment of structures was aided by 2D NMR analysis (COSY, HSQC). For the different splittings of the NMR-data following shortcuts were used: s = singlet, d = duplet, t = triplet, q = quartet, quint = quintet, m = multiplet.

6.1.5 IR (Infrared) – Spectroscopy

Infrared spectra (IR) were recorded on a BRUKER Alpha-p instrument in a frequency range from 3997 to 374 cm^{-1} applying ATR-technology. The signal shape and intensity were abbreviated in the following pattern: br = broad, s = strong, m = medium, w = weak.

6.1.6 UV-Lamps

Thiol-ene reactions utilising the photo initiator DMPA were irritated with a UV-Lamp from "Vilber" type VL-115.L with a wavelength of 365 nm and 15 W of Power.

6.1.7 Mass Spectrometry FAB-MS and EI-MS

Fast-atom-bombardment (FAB) and electron ionisation (EI) spectra were recorded utilising a Finnigan MAT 95 mass spectrometer. Molecule fragments were specified as mass / charge ratio m/z.

6.1.8 Computational details

Force-field calculations were performed by ReaxFF 6.0 developed by Goddard and co-workers (*216*) and further processed with the open source program Zeo++.

Quantum chemical calculations were performed with the TURBOMOLE program package (*222, 223*) at the level of density functional theory (DFT) employing the PBE0 hybrid exchange-correlation functional (*224*) with the basis sets of type def2-TZVPP (*225*). TURBOMOLE 's grid 4 was used for the numerical quadrature and the self-consistent-field energy-convergence threshold was set to 10^{-8} E_h. Furthermore, we used the D3

dispersion correction in conjunction with Becke-Johnson damping (*226*). Geometries were optimised with geometry-convergence thresholds of 10^{-7} E_h for the energy and 10^{-5} E_h /a_0 for the Cartesian gradient. Developer's version of TURBOMOLE V7.4 2019, a development of University of Karlsruhe and Forschungszentrum Karlsruhe GmbH, 1989–2007, TURBOMOLE GmbH, since 2007; available from http://www.turbomole.com.

6.1.9 Thin Layer Chromatography (TLC)

For the analysis aluminium foils with fluorescence indicator from MERCK (TLC Silica gel 60, F_{256}, layer thickness: 0.25 mm) were employed as stationary phase. The analyte substances were employed onto the TLC plates with a capillary, subsequently the plates were set into a TLC chamber filled with eluent solvent. The spots were firstly visualised by fluorescence quenching under UV-light (λ = 254 and 365 nm, Vetter Laborgeräte (Wiesloch) type UVKL4U) and secondly by staining with Seebach reagent (2.50 g cerium(IV) sulfate tetrahydrate ($Ce(SO_4)_2 \cdot 4H_2O$), 6.25 g ammonium heptamolybdate tetrahydrate (($NH_4)_6Mo_7O_{24} \cdot 4H_2O$), 225 ml H_2O and 25.0 ml concentrated sulfuric acid (H_2SO_4)).

6.1.10 Differential scanning calorimetry

Thermal properties of the prepared polymers were studied with a Mettler Toledo DSC stare system operating under nitrogen atmosphere. Therefore, about 5 mg of the POP was used for all analyses. The glass transitions were recorded on the second heating scan by using the following methods: Starting from = 25 °C – 200 °C (heating rate of 20 °C/min), cooling from 200 °C – 25 °C (cooling rate of 20 °C/min), isothermal segment at 0 °C for 10 min and heating from 0 °C – 200 °C (heating rate of 20 °C/min)

6.1.11 Chemicals

Cyclohexane (distilled), Dichloromethane (distilled), Tetrahydrofurane (distilled), Methanol (distilled), Aceton (99.5, Bernd Kraft), Dimethylformamid (distilled), tert-Butyl methyl ether (99.9%, TCI), Chlorosulfonic acid (99%, Institute), 2,2-dimethoxy-2-phenylacetophenone (99%, Aldrich), Vinyl acetate (> 99%, Acros), Potassium carbonate (Institute), caesium carbonate (Institute), Natriumcarbonate (Institute), H_2O_2

6. Experimental Section

(Merck), H_2SO_4 (98%, Institute), HSO_3Cl (Institute), (3-Chloropropyl)triethoxysilane (95%, Sigma-Aldrich), N-Methyl-aza-2,2,4-trimethylsilacyclopentane (95%, ChemPur), 2,2-Dimethoxy-1-thia-2-silacyclopentane (Gelest), trichloro(10-undecen-1-yl) silane (95%, Alfa), trimethoxy(7-octadecen-1-yl) silane (>90%, TCI), Chlorotriphenylmethane (Institute), Aniline (>99.5, Sigma-Aldricch), Hypophosphorous Acid, 50% w/w Aq.sol. (Fisher Scientific), Isopentyl nitrite (>95%, TCI), bromine (institute), 2-propanethiolate (>90%, Sigma-Aldrich), sodium (institute), trimthylsilylacetylene (98%, abcr), [Pd(PPh3)2Cl2] (98%, Sigma-Aldrich), copper(I) iodide (>99.9%, Sigma-Aldrich), diisopropylamine (99%, Fisher Scientific), 1,4'-dibromobenzene (99%, Alfa), diethyl ether (99.9%, Sigma-Aldrich), n-butyllithium 1.6M in hexane (Sigma-Aldrich), $GeCl_4$ (>99.9%, Sigma-Aldrich), 1-bromoadamantane (99%, Fisher Scientific), benzene (99.9%, Sigma-Aldrich), $AlCl_3$ (99%, Sigma-Aldrich), t-butylbromide (98%, Merck), Diethylene glycol (>99%, Sigma-Aldrich), propiolic acid (95%, Sigma-Aldrich), [Pd2dba3] (Sigma-Aldrich), SPhos (97%, Sigma-Aldrich), n-butylamine (99.5%, Sigma-Aldrich), n-pentylamine (99%, Sigma-Aldrich), n-hexylamine (99%, Sigma-Aldrich), isopropylamine (99%, Sigma-Aldrich), isobutylamine (99%, Sigma-Aldrich), furfurylamine (Sigma-Aldrich) 1-methoxy-2-propylamine (95%, Sigma-Aldrich)

6.2 Supplement

6.2.1 Reaction procedures for tetrafunctional building blocks

6.2.1.1 Synthesis of tetraphenylmethane
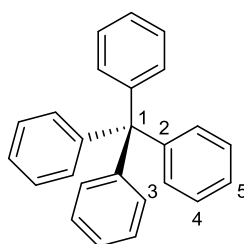
A mixture of 50 g tritylchloride (179 mmol, 1.0 eq.) and 42.6 mL aniline (466 mmol, 2.6 eq.) were heated at 220 °C for at least 15 minutes. Afterwards, the resulting solid was cooled to 90 °C and a mixture of 400 mL 2 M HCl and 600 mL ethanol was added and stirred for 30 minutes at 80 °C. After cooling to room temperature, a greyish precipitate occurred, which was thoroughly washed with deionised water. Then, 500 mL of dimethylformamide is added and the suspension is cooled to -15 °C, followed by stepwise addition of 54 mL conc. H_2SO_4 and 41 mL isoamylnitrite

(305 mmol, 1.7 eq.) *via* a dropping funnel. The mixture is stirred for1 hour. Afterwards, 100 mL of 50% H_3PO_2 are added and the solution is stirred at 50°C until no gas formation is visible. The resulting precipitate is thoroughly washed with DMF, deionised water and ethanol resulting in a white powder.

1H NMR (500 MHz, CDCl$_3$): δ [ppm] = 7.05 – 7.16 (m, 20 H, Ph-H); **13C NMR** (100 MHz, CDCl$_3$): δ [ppm] = 65.0 (C^1), 125.9 (C^5), 127.4 (C^4), 131.1 (C^3), 146.8 (C^2); **IR:** (ATR): n [cm-1] = 1569.9 (w), 1478.9 (m), 1396.6 (m), 1369.9 (w), 1184.8 (w), 1112.8 (w), 1077.8 (m), 1007.9 (s), 948.2 (w), 911.2 (w), 833.0 (m), 810.4 (s), 748.7 (w), 726.1 (w), 691.1 (w), 629.4 (w), 575.9 (w), 532.7 (m), 510,1 (s);**FAB – MS** [m/z] (relative intensity): 319.1 [M – H], 321.2 [M + H];**Yield:** 79%

6.1.2 Synthesis of tetrakis(*p*-bromophenyl)methane
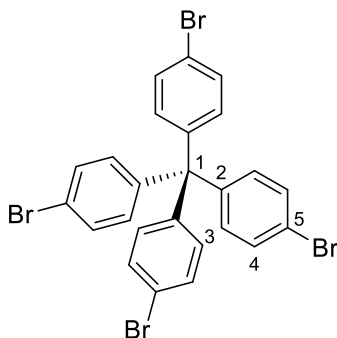
In a 500 mL flask, 10 g tetraphenylmethane (31.2 mmol, 1 eq.) were suspended in 50 mL chloroform and cooled to 0 °C. Bromine (79.8 g, 499.3 mmol, 16 eq.) were slowly under vigorous stirring added *via* a dropping funnel. Afterwards, the mixture is slowly heated to room temperature and stirred for 18 hours. After completion, 300 mL of cold ethanol are used to quench remaining bromine. The resulting yellowish precipitate is filtrated and thoroughly washed with 300 mL concentrated sodium hydrogen sulphite solution and cold ethanol. Drying results in a colourless powder.

1H NMR (500 MHz, CDCl$_3$): δ [ppm] = 7.39 (d, *J* = 8.7 Hz, 8H, CH^4), 7.01 (d, *J* = 8.7 Hz, 8H, CH^3); **13C NMR** (100 MHz, CDCl$_3$): δ [ppm] = 144.6 (C^2), 132.5 (C^3), 131.2 (C^4), 120.9 (C^5), 63.8 (C^1); **IR:** (ATR): n [cm-1] = 2942.9 (w), 2900.3 8 (w), 2852.9 (w), 1487.1 (s), 1448.1 (m), 1394.6 (m), 1355.5 (m), 1213.6 (w), 1180-7 (w), 1108.7 (w),

1075.8 (s), 1005.8 (vs), 888.6 (w), 822.8 (s), 777.5 (s), 748.7 (s), 717.9 (m), 670.6 (m), 559.5 (s), 528.6 (s), 485.4 (w), 450.5 (w); **FAB − MS** [m/z] (relative intensity): 636.0 [M], 558.1 [M − Br], 479.0 [M − C_6H_4Br], 401.0 [M − C_6H_4Br − Br], 321.1 [M − 2x C_6H_4Br], 239.1 [M − 2x C_6H_4Br - Br]; **HRMS − FAB** [m/z]: [M + H$^+$] calculated for $C_{25}H_{16}{}^{79}Br_2{}^{81}Br_2$, = 635.7945; found, 635.7945; Δ = 0.0481 mmu; **Yield:** 90%

6.1.3 Synthesis of tetrakis(*p*-isopropyl(phenyl)sulfane)methane
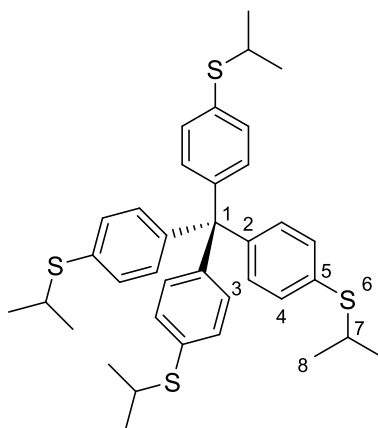
Under Schlenk-conditions, 2 g tetrakis(*p*-bromophenyl)methane (3.14 mmol, 1.0 eq.) and 3.09 g sodium 2-propanethiolate are dissolved in dry dimethylacetamide and stirred for 48 hours at 100 °C. After that, the product is precipitated by addition of water, filtered and thoroughly washed with water and ethanol and obtained as colourless solid.

^{1}H NMR (500 MHz, CDCl$_3$): δ [ppm] = 7.25 (d, *J* = 8.6 Hz, 8H, CH^4), 7.07 (d, *J* = 8.6 Hz, 8H, CH^3), 3.38 (h, *J* = 6.7, 4H, CH^7), 1.30 (d, *J* = 6.7, 24H, CH^8); **^{13}C NMR** (100 MHz, CDCl$_3$): δ [ppm] = 144.7 (C^2), 133.7 (C^5), 131.5 (C^3), 130.4 (C^4), 63.9 (C^1), 37.9 (C^7), 23.4 (C^8);**IR:** (ATR): n [cm-1] = 2957.8 (m), 2922.9 (m), 2861.2 (m), 1587.9 (w), 1557.1 (w), 1480.9 (s), 1448.1 (m), 1396.6 (m), 1382.2 (m), 1365.8 (m), 1310.2 (w), 1262.9 (m), 1240.3 (m), 1195.1 (m), 1153.9 (m), 1092.2 (s), 1049.0 (m), 1012.0 (s), 952.3 (w), 929.7 (w), 911.2 (w), 882.4 (w), 810.4 (vs), 734.3 (w), 697.3 (w), 652.0 (w), 631.5 (w), 549.2 (m), 528.6 (s), 485.4 (w), 419.6 (w); **FAB − MS** [m/z] (relative intensity): 616.3 [M], 573.2 [M − C_3H_7], 541.2 [M - C_3H_7S], 465.2 [M − $C_9H_{11}S$]; **HRMS − FAB** [m/z]: [M + H$^+$] calculated for $C_{37}H_{44}{}^{32}S_4$ = 616.2319, found 616-2320, Δ = 0.1149 mmu; **Yield:** 99%

6.2.1.4 Synthesis of tetrakis(*p*-mercaptophenyl)methane
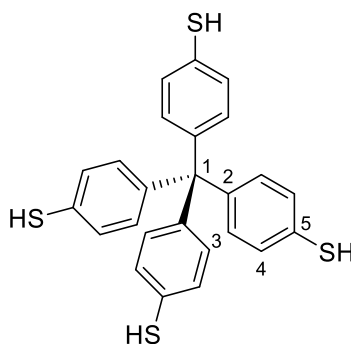
Under Schlenk-conditions, 1.41 g (3.14 mmol, 1 eq.) tetrakis(*p*-isopropyl(phenyl)sulfane)methane is dissolved in dry dimethylacetamide and 1.45 g sodium is added. The reaction mixture is stirred for 18 hours. After completion, it is quenched with 100 mL water and 80 mL *tert*-butylmethylether, acidified with hydrochloric acid to pH 1. The organic phase is separated and the aqueous phase is further extracted with *tert*-butylmethylether for at least 3 times. The combined organic phases are then washed with water and dried *via* addition of Na_2SO_4. After removing the solvent under reduced pressure, the crude product is separated *via* column chromatography (cyclohexane/*tert*-butylmethylether 85/15).

^{1}H NMR (500 MHz, $CDCl_3$): δ [ppm] = 7.14 (d, *J* = 8.5 Hz, 8H, CH^4), 7.01 (d, *J* = 8.5 Hz, 8H, CH^3), 3.41 (s, 1H, SH); **^{13}C NMR** (100 MHz, $CDCl_3$): δ [ppm] = 143.8 (C^2), 131.6 (C^3), 128.83 (C^5), 128.80 (C^4), 63.4 (C^1); **IR:** (ATR): n [cm-1] = 2920.8 (m), 2848.8 (m), 2558.8 (w), 1587.9 (w), 1563.5 (w), 1483.0 (s), 1400.8 (m), 1269.1 (w), 1190.9 (m), 1100.4 (s), 1014.1 (s), 948.2 (w), 900.9 (w), 837.2 (m), 806.3 (vs), 730.2 (m), 633.5 (w), 543.0 (s), 522.5 (s); **FAB – MS** [m/z] (relative intensity): 448.4 [M], 415.2 [M – SH], 339.2 [M – C_6H_5S], 307.2 [M – C_6H_5S – SH]; **HRMS – FAB** [m/z]: [M + H$^+$] calculated for $C_{25}H_{20}{}^{32}SH$ = 448.0448, found 448.0449, Δ = 0,0850 mmu; **Yield:** 60%

6.2.1.5 Synthesis of tetrakis(*p*-((trimethylsilyl)ethynyl)phenyl)methane
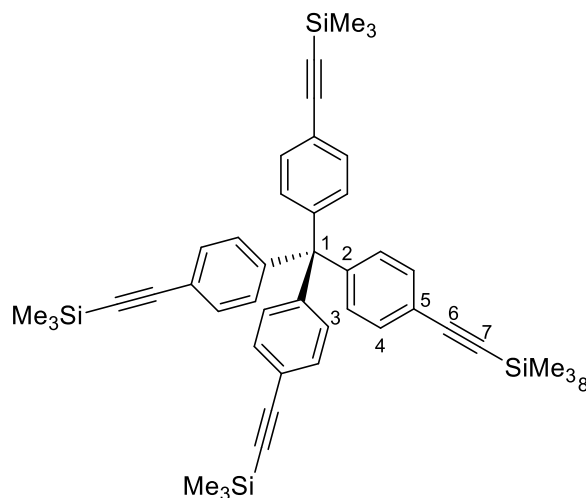
Under Schlenk-conditions, 6.0 g (9.44 mmol, 1.0 eq.) tetrakis(*p*-bromophenyl)-methane, 662 mg (0.94 mmol, 0.1 eq.) [Pd(PPh$_3$)$_2$Cl$_2$] and 161.4 mg (0.82 mmol, 0.09 eq.) copper(I) iodide are suspended in 80 mL degassed diisopropylamine. Furthermore, 18.8 mL (132.0 mmol, 14.0 eq.) trimethylsilylacetylene are slowly added *via* a dropping funnel, heated to 80 °C and stirred for 24 hours. After completion, the solvent was evaporated under reduced pressure and redissolved in 20 mL dichloromethane and separated *via* column chromatography (DCM 100%). Again, the resulting solid is dissolved in 80 mL ethanol and cooled to -18 °C for recrystallisation. The obtained colourless powder is thoroughly washed with ice-cold ethanol and the solvent evaporated under reduced pressure.

^{1}H NMR (500 MHz, CDCl$_3$): δ [ppm] = 7.33 (d, *J* = 8.6 Hz, 8H, CH^4), 7.04 (d, *J* = 8.6 Hz, 8H, CH^3), 0.23 (s, 36H, CH$_3^8$); **^{13}C NMR** (100 MHz, CDCl$_3$): δ [ppm] = 146.5 (C^2), 131.9 (C^3), 131.3 (C^5), 121.80 (C^4), 105.2 (C^6), 95.3 (C$_7$), 63.5 (C^1), 0.4 (C^8); **IR:** (ATR): n [cm-1] = 2959.9 (m), 2898.2 (w), 2157.7 (m) 1495.4 (m), 1406.9 (w), 1248.5 (s), 1186.8 (m), 1114.8 (w), 1020.2 (m), 861.8 (vs), 839.2 (vs), 812.5 (vs), 759.0 (s), 699.3 (m), 652.0 (s), 639.7 (s), 604.7 (m), 549.2 (m); **FAB – MS** [m/z] (relative intensity): 705.4 [M + H], 531.3 [M – C$_{11}$H$_{13}$Si]; **HRMS – FAB** [m/z]: [M + H$^+$] calculated for C$_{45}$H$_{53}$^{28}Si$_4$ = 705.3224, found 705.3224, Δ = 0.0418 mmu; **Yield:** 84%

6.2.1.6 Synthesis of tetrakis(*p*-acetylphenyl)methane
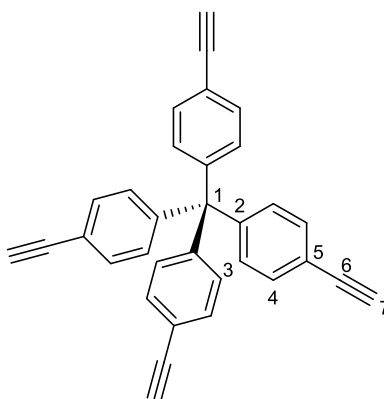
2.0 g (2.84 mmol, 1.0eq.) tetrakis(*p*-trimethylsilylacetylenephenyl)methane are dissolved in 25 mL dichloromethane and 70 mL methanol and 11.8 g potassium carbonate (85.1 mmol, 30.0 eq.) are added. The mixture is stirred for 18 hours. Afterwards, the solvent is evaporated under reduced pressure, again dissolved in dichloromethane and washed with water. The separated organic phase is then dried by addition of Na_2SO_4 and the solvent removed under reduced pressure leading to a beige solid.

^{1}H NMR (500 MHz, CDCl$_3$): δ [ppm] = 7.39 (d, J = 8.5 Hz, 8H, CH^4), 7.12 (d, J = 8.5 Hz, 8H, CH^3), 3.06 (s, 4H, CH^8); **^{13}C NMR** (100 MHz, CDCl$_3$): δ [ppm] = 146.3 (C^2), 131.8 (C^4), 130.9 (C^3), 123.5 (C^2), 120.4 (C^5), 83.3 (C^6), 77.8 (C^7), 64.9 (C^1); **IR:** (ATR): n [cm-1] = 3280.8 (s), 3029.8 (w), 2110.4 (w), 1602.3 (w), 1552.9 (w), 1497.4 (s), 1400.8 (m), 1250.6 (m), 1114.8 (m), 1018.2 (m), 958.5 (m), 826.9 (vs), 767.2 (w), 736.4 (m), 662.3 (vs), 629.4 (vs), 569.8 (s), 559.5 (vs), 518.3 (m), 501.9 (m), 438.1 (w), 413.4 (m); **FAB – MS** [m/z] (relative intensity): 417.2 [M + H], 391.3 [M – C$_2$H], 315.2 [M – C$_8$H$_5$]; **HRMS – FAB** [m/z]: [M + H$^+$] calculated for C$_{33}$H$_{20}$ = 417.1643, found 417.1645, Δ = 0.1693 mmu; **Yield: 98%**

6. Experimental Section

6.2.1.7 Synthesis of tetrakis(*p*-bromophenyl)germanium
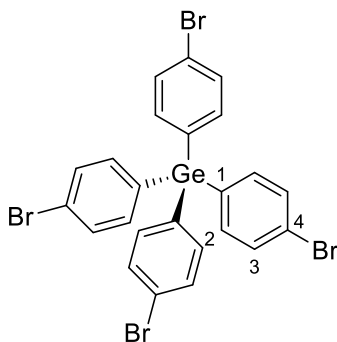
Under Schlenk-conditions, 23.6 g 4,4′-dibromobenzene (100 mmol, 4.2 eq.) is dissolved in 240 mL anhydrous diethyl ether and cooled *via* an ice/acetone bath. Then, 40 mL (100 mmol, 4.2 eq.) *n*-butyllithium in hexane is slowly added *via* a dropping funnel and stirred for 30 minutes. After that, 5.15 g (24 mmol, 1.0 eq.) GeCl$_4$ dissolved in 40 mL diethyl ether is added dropwise under vigorous cooling with an ice/acetone bath. Next, the cooling bath is removed, and the solution stirred for 8 hours at room temperature. After completion, 1 M hydrochloric acid is added, and the resulting mixture is extracted with diethylether. The combined extracts were washed with water and brine, dried over MgSO$_4$, and filtered. The solvent was removed under reduced pressure. Recrystallisation from 1,2-dichloroethane and benzene gave colourless needle-like crystals

^{1}H NMR (500 MHz, CDCl$_3$): δ [ppm] = 7.44 (d, *J* = 8.1 Hz, 8H, CH^4), 7.22 (d, *J* = 8.1 Hz, 8H, CH^3); **^{13}C NMR** (100 MHz, CDCl$_3$): δ [ppm] = 136.59 (C^1), 133.4 (C^3), 131.8 (C^2), 123.5 (C^4); **IR:** (ATR): n [cm-1] = 3048.3 (w), 3025.7 (w), 2953.7 (w), 2924.9 (w), 2854.9 (w), 1902.6 (w), 1779.2 (w), 1670.2 (w), 1637.3 (w), 1583.8 (m), 1567.4 (m), 1555.0 (m), 1468.6 (s), 1380.2 (s), 1299.6 (w), 1184.8 (m), 1100.4 (m), 1063.4 (s), 999.7 (s), 882.4 (w), 845.4 (m), 804.3 (s), 779.6 (s), 719.9 (m), 709.6 (m), 687.0 (m), 670.6 (m), 623.2 (w), 569.8 (w), 541.0 (m), 497.8 (s), 409.3 (s); **EI – MS** [m/z] (relative intensity): 698.0 [M + H], 618 [M – Br], 543.0 [M – C$_6$H$_4$Br], 461,0 [M - C$_6$H$_4$Br – Br], 388.0 [M – 2xC$_6$H$_4$Br], 386.0 [M - C$_6$H$_4$Br – 2xBr]; **HRMS – EI** [m/z]: [M + H$^+$] calculated for C$_{24}$H$_{16}$^{79}Br$_2$^{81}Br$_2$^{74}Ge = 697.7156, found 679.7156, Δ = 0.1006 mmu; **Yield: 40%**

6.2.1.8 Synthesis of tetrakis(*p*-((trimethylsilyl)ethynyl)phenyl)methane
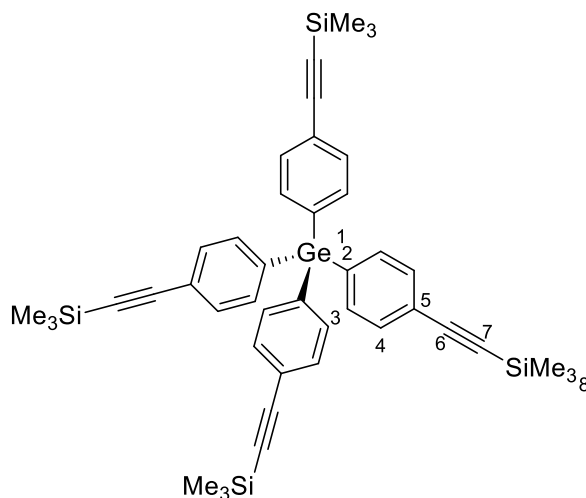
Under Schlenk-conditions, 0.750 g (1.08 mmol, 1.0 eq.) tetrakis(4-bromophenyl)germanium, 32 mg (0.017 mmol, 0.16 eq.) copper(I)iodide, 136.0 mg (0.19 mmol, 0.18 eq.) [Pd(PPh3)2Cl2], and 102 mg (0.39 mmol, 0.36 eq.) triphenylphosphine are dissolved in 25 mL degassed diisopropylamine and 2.3 mL (1.59 g, 16.15 mmol, 15.0 eq.) trimethylsilylacetylene was added subsequently. The yellow mixture turns rapidly into a dark solution after 30 minutes. The resulting suspension is stirred at 80°C for 24 hours, after which the reaction mixture was allowed to cool to room temperature. The solution was evaporated to dryness, then redissolved in a minimum amount of dichloromethane and purified by column chromatography (100% pentane) to afford tetrakis(*p*-((trimethylsilyl)ethynyl)phenyl)germanium as a brownish solid.

^{1}H NMR (500 MHz, CDCl3): δ [ppm] = 7.45 (d, J = 8.0 Hz, 8H, CH^4), 7.36 (d, J = 8.0 Hz, 8H, CH^3), 0.25 (s, 36H, CH^8); **^{13}C NMR** (100 MHz, CDCl3): δ [ppm] = 146.3 (C^2), 131.8 (C^4), 130.9 (C^3), 123.7 (C^2), 120.4 (C^5), 83.3 (C^6), 77.8 (C^7), 64.9 (C^1); **Yield:** 90%

6. Experimental Section

6.2.1.9 Synthesis of tetrakis(*p*-ethynylphenyl)methane
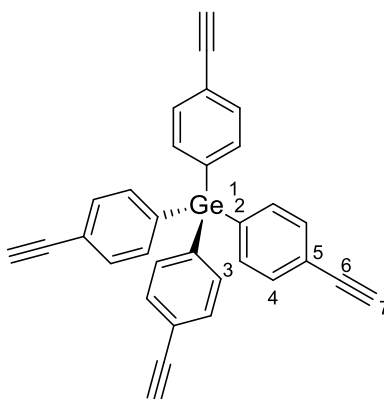
To a solution of 1.1 g (1.56 mmol, 1.0 eq.) tetrakis(*p*-((trimethylsilyl)ethynyl)phenyl)germanium in 50 mL tetrahydrofurane 10.4 g (74.9 mmol, 48 eq.) potassium carbonate, followed by 70 mL methanol is added. The resulting yellow suspension was stirred at room temperature for 48h. Solvents are removed in vacuo and the resulting solid is dissolved in a mixture of dichloromethane/water (1/1 v/v, 500 mL). The organic fraction was decantated and separated. The aqueous phase is extracted twice with CH2Cl2. The organic phase is united, washed with brine, dried over sodium sulfate and evaporated to dryness. The crude mixture was then passed through a plug of silica (100% pentane) eluting with 50/50 pentane/dichloromethane to afford the desired tetrakis(4-ethynylphenyl)germanium.

1H NMR (500 MHz, CDCl3): δ [ppm] = 7.44 (d, $J = 8.1$ Hz, 8H, CH^4), 7.22 (d, $J = 8.1$ Hz, 8H, CH^3); **13C NMR** (100 MHz, CDCl3): δ [ppm] = 136.1 (C^1), 135.2 (C^3), 132.1 (C^2), 123.5 (C^4), 83.4 (C^5), 78.5 (C^6); **Yield:** 99%

6.2.1.10 Synthesis of tetraphenyladmantane
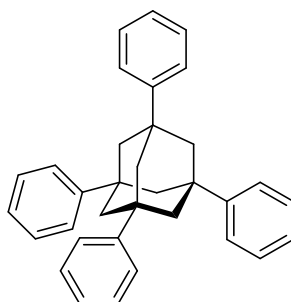
24.0 g (112 mmol, 1.0eq.) 1-bromoadamantane are dissolved in 240 mL benzene under argon atmosphere. Stepwise, 1.49 g (11.6 mmol, 0.1 eq.) $AlCl_3$ and 25 mL (224 mmol, 2.0 eq.) *t*-butylbromide are slowly added under vigorously stirring and further heated under reflux. The resulting yellowish powder is filtrated, thoroughly washed wit chloroform, water and again chloroform. A colourless powder is obtained after drying under reduced pressure.

IR: (ATR): n [cm^{-1}] = 3081.2 (w), 3056.6 (w), 3021.6 (w), 2941.4 (w), 2920.8 (m), 2898.2 (w), 2850.9 (w), 1598.2 (w), 1577.6 (w), 1493.3 (m), 1443.9 (m), 1355.5 (m), 1262.9 (w), 1079.9 (m), 1032.6 (m), 919.4 (w), 890.6 (w), 843.3 (w), 789.8 (w), 761.1 (s), 746.7 (s), 699.3 (vs), 631.5 (m), 617.1 (w), 569.8 (s), 528.6 (s), 499.8 (w), 477.2 (w), 434.0 (w); **FAB – MS** [m/z] (relative intensity): 440.4 [M+]; **HRMS – EI** [m/z]: [M+] calculated for $C_{34}H_{32}$ = 440.2504, found 440.2502, Δ = 0.2000 mmu; **Yield:** 74%

6.2.1.11 Synthesis of tetrakis(*p*-bromophenyl)adamantae
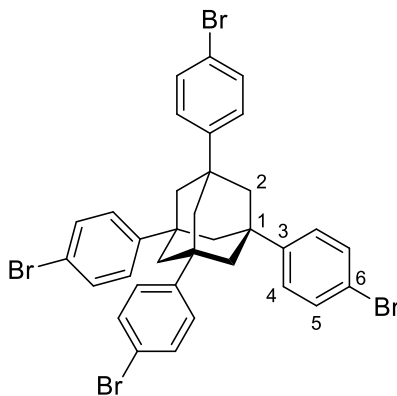
In a 500 mL flask, 5 g tetraphenyladamantane (11.3 mmol, 1 eq.) were suspended in 50 mL chloroform and cooled to 0 °C. 32.5 g Bromine (203 mmol, 18 eq.) are slowly added *via* a dropping funnel under vigorous stirring. Afterwards, the mixture is slowly heated to room temperature and stirred for 18 hours. After completion, 150 mL of cold ethanol are used to quench remaining bromine. The resulting yellowish precipitate is filtrated and thoroughly washed with 150 mL concentrated sodium hydrogen sulphite solution and cold ethanol. Drying results in a colourless powder.

¹H NMR (500 MHz, CDCl₃): δ [ppm] = 7.47 (d, *J* = 8.7 Hz, 8H, CH⁴), 7.32 (d, *J* = 8.7 Hz, 8H, CH³), 2.08 (s, 12H, CH₂²);**¹³C NMR** (100 MHz, CDCl₃): δ [ppm] = 147.8 (C³), 131.8 (C⁴), 126.9 (C⁵), 120.4 (C⁶), 46.9 (C¹), 39.2 (C²);**IR:** (ATR): n [cm⁻¹] = 2922.9 (m), 2898.2 (m), 2852.9 (m), 1902.6 (w), 1645.5 (w), 1585.9 (w), 1565.3 (w), 1487.1 (vs), 1448.1 (m), 1394.6 (s), 1355.5 (s), 1213.6 (m), 1180.7 (m), 1108.7 (m), 1075.8 (s), 1005.8 (vs), 960.6 (m), 944.1 (m), 890.6 (m), 822.8 (s), 777.5 (s), 748.7 (s), 717.9 (s), 670.6 (s), 559.5 (s), 528.6 (s), 485.4 (m), 454.6 (m); **FAB – MS** [m/z] (relative intensity): 756.0 [M + H], 596.2 [M – C₆H₄Br]; **HRMS – FAB** [m/z]: [M+] calculated for C₃₄H₂₈⁷⁹Br₂⁸¹Br₂ = 755.8884, found 755.8885, Δ = 0.1808 mmu; **Yield:** 76%

6.2.1.12 Synthesis of Diethylene glycol dipropiolate
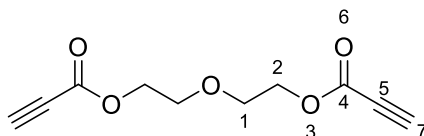
0.95 mL (1.62 g, 10.0 mmol, 1.0 eq.) diethyleneglycol, 6.2 mL (7.0 g, 100 mmol, 10.0 eq.), and 1.14 g (6.0 mmol, 0.6 eq.) *p*-toluene sulfonic acid are dissolved in anhydrous toluene and heated under reflux with a Dean-Stark apparatus for 18 hours. After completion, the solvent is removed under reduced pressure, dissolved in chloroform and washed with concentrated sodium hydrogen carbonate solution, water and concentrated sodium chloride solution. The organic phase is separated, dried over sodium sulphate and removed under reduced pressure. The crude mixture is separated *via* column chromatography (cyclohexane/ethyl acetate 8/2) and a yellowish oil is obtained.

¹H NMR (500 MHz, CDCl₃): δ [ppm] = 4.34 (m, 4H, CH₂²), 3.74 (m, 4H, CH₂¹), 2.92 (s, 2H, CH⁷); **¹³C NMR** (100 MHz, CDCl₃): δ [ppm] = 152.7 (C⁴), 75.4 (C²), 74.5 (C¹), 68.7 (C⁵) 65.2 (C⁷); **IR:** (ATR): n [cm⁻¹] = 3262.3 (m), 2959.9 (w), 2906.4 (w), 2881.7 (w), 2116.6 (s), 1705.2 (vs), 1450.1 (m), 1392.5 (w), 1374.0 (w), 1359.6 (w), 1213.6 (vs), 1127.2 (s), 1026.4 (s), 958.5 (m), 861.8 (m), 750.8 (s), 680.8 (s), 600.6 (m), 528.6 (w), 487.5 (m); **FAB – MS** [m/z] (relative intensity): 210.1 [M + H]; **HRMS – FAB** [m/z]: [M + H⁺] calculated for C₁₀H₁₁O₅ = 211.0606, found 211.0608, Δ = 0.1020 mmu; **Yield:** 59%

6.2.1.13 Synthesis of Tetrakis(*p-N,N'*-diallylaniline)methane
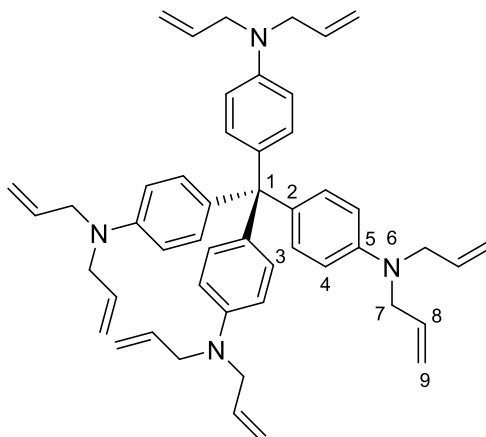
A mixture of 250 mg (393 mmol, 1 eq.) tetrakis(*p*-aminophenyl)methane and allyl bromide (3.1 mmol, 8 eq.) was refluxed overnight, in anhydrous DMF (5 mL) in the presence of 1.0 g Cs_2CO_3 (3.1 mmol, 8 eq.). The reaction mixture was then cooled to room temperature and filtered. The solvent was evaporated under reduced pressure and the crude product was purified using column chromatography (cyclohexane/ethyl acetate 8/2) to afford the desired product

^{1}H NMR (500 MHz, DMSO-*d_6*): δ [ppm] = 6.82 (d, *J* = 9.0 Hz, 8H, CH^4), 6.53 (d, *J* = 9.0 Hz, 8H, CH^3), 5.88 - 574 (m, 4H, CH^8), 5.28 – 5.03 (m, 8H, CH^7), 3.86 (d, *J* = 4.7 Hz, 8H, CH^9); **^{13}C NMR** (100 MHz, DMSO-*d_6*): δ [ppm] = 135.1 (C^8), 130.8 (C^4), 116.08 (C^7), 110.7 (C^3), 52.3 (C^9) (other signals not detectable); **IR:** (ATR): n [cm^{-1}] = 3336.3 (w, b), 3081.2 (w), 3042.2 (w), 3003.1 (w), 2974.3 (m), 2920.8 (m), 2852.9 (m), 1668.2 (s), 1643.5 (m), 1604.4 (s), 1507.7 (vs), 1435.7 (m), 1415.2 (m), 1388.4 (s), 1357.6 (s), 1332.9 (s), 1285.6 (m), 1232.1 (s), 1207.4 (s), 1180.7 (s), 1129.2 (m), 1079.9 (m), 1016.1 (m), 989.4 (m), 946.2 (s), 915.3 (s), 810.4 (s), 670.6 (w), 617.1 (w), 547.1 (s); **FAB – MS** [m/z] (relative intensity): 701.5 [M + H], 528.4 [M – $C_{12}H_{14}N$]; **HRMS – FAB** [m/z]: [M+] calculated for $C_{49}H_{56}N_4$ = 700.4499, found 700.4497, Δ = 0.2383 mmu; **Yield:** 72%

6.2.2 General procedure for the Hartwig-Buchwald crosscoupling.

All solids (TPM-Br: 0.4 mmol, 1.0 eq., Pd_2DBA_3: 0.064 mmol, 0.16 eq., SPhos: 0.192 mmol, 0.48 eq., Cs_2CO_3: 4 mmol, 10 eq.) and a stirring bar are put into a crimp

vial and sealed with a cap containing a septum. After that, it is evacuated three times and filled with argon. The solids are dissolved in anhydrous toluene and the amine is added (4.8 mmol, 12 eq.). The reaction mixture is heated in a metal block at 90 °C for 18 hours. Following, the mixture is quenched with water and dissolved in ethyl acetate. The organic phase is washed thoroughly with water and concentrated sodium chloride and dried over sodium sulphate. Afterwards, the solvent is removed under reduced pressure and the crude product is separated *via* column chromatography (cyclohexane/ethyl acetate 95/5) resulting in brownish solids.

6.2.2.1 Tetrakis(*p-N*-butylaniline)methane
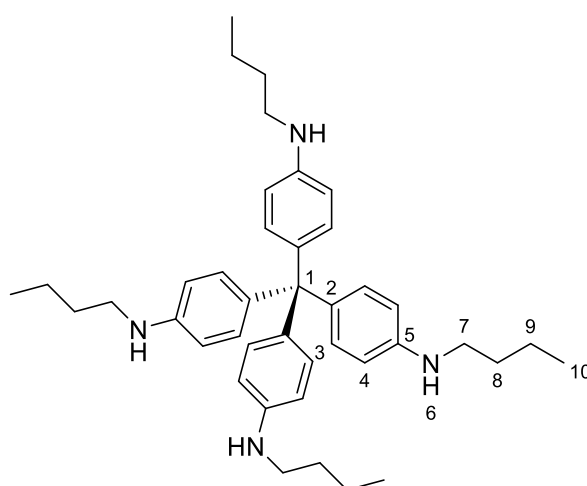
Chemical Formula: $C_{41}H_{56}N_4$
Exact Mass: 604,4505

^{1}H NMR (500 MHz, DMSO-d_6): δ [ppm] = 6.75 (d, J = 8.8 Hz, 8H, CH^4), 6.38 (d, J = 8.8 Hz, 8H, CH^3), 5.33 (t, J = 5.5 Hz, 4H, NH^6), 2.94 (q, J = 6.8 Hz, 8H, CH$_2$^{7}), 1.50 (p, J = 7.1 Hz, 8H, CH$_2$^{8}), 1.37 (dt, J = 14.7, 7.3 Hz, 8H, CH$_2$^{9}), 0.90 (t, J = 7.3 Hz, 12H, CH$_3$^{10}); **^{13}C NMR** (100 MHz, DMSO-d_6): δ [ppm] = 146.3 (C^2), 135.5 (C^5), 131.0 (C^4), 110.4 (C^3), 61.0 (C^1), 42.6 (C^7), 31.0 (C^8), 19.9 (C^9), 13.8 (C^{10}); **IR:** (ATR): n [cm^{-1}] = 3387.7(m), 3354.8 (m), 3017.5 (w), 2974.3 (m), 2924.9 (m), 2871.4 (m), 2828.2 (m), 1736.0 (w), 1606.4 (vs), 1579.7 (m), 1507.7 (vs), 1448.1 (s), 1402.8 (w), 1386.4 (w), 1367.8 (m), 1318.5 (s), 1293.8 (s), 1252.7 (s), 1190.9 (s), 1170.4 (s), 1129.2 (s), 1090.2 (vs), 962.6 (m), 933.8 (m), 902.9 (w), 810.4 (vs), 724.0 (w), 699.3 (w), 602.7 (m), 569.8 (m), 532.7 (m), 471.5 (m); **FAB – MS** [m/z] (relative intensity): 605.5 [M + H], 456.4 [M – C$_{10}$H$_{14}$N]; **HRMS – FAB** [m/z]: [M + H$^+$] calculated for C$_{41}$H$_{56}$N$_4$ = 604.4499, found 604.4499, Δ = 0.0852 mmu; **Yield:** 43%

6.2.2.2 Tetrakis(*p-N*-pentylaniline)methane
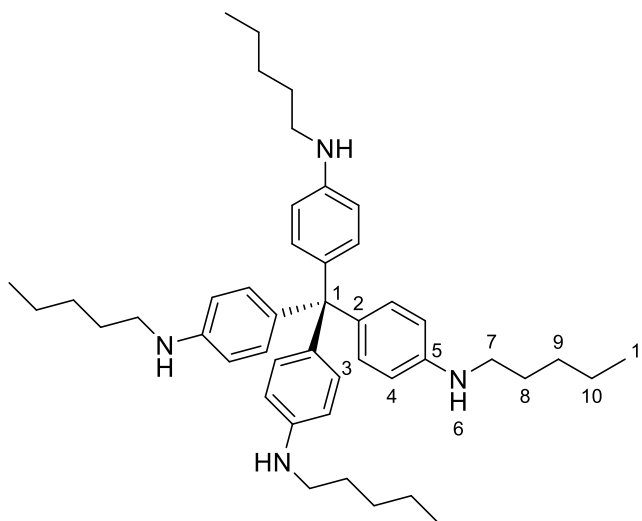
¹H NMR (500 MHz, DMSO-*d₆*): δ [ppm] = 6.75 (d, *J* = 8.7 Hz, 8H, CH^4), 6.39 (d, *J* = 8.7 Hz, 8H, CH^3), 5.41 (s, 4H, NH^6), 2.93 (t, *J* = 7.0 Hz, 8H, CH^7), 1.52 (p, *J* = 7.0 Hz, 8H, CH^8), 1.37 – 1.26 (m, 16H, CH$^{9.10}$), 0.88 (t, *J* = 7.0 Hz, 12H, CH^{11}); **¹³C NMR** (100 MHz, DMSO-*d₆*: δ [ppm] = 146.3 (C^2), 135.6 (C^5), 131.0 (C^4), 110.6 (C^3), 61.0 (C^1), 43.0 (C^7), 28.9 (C^9), 28.5 (C^8), 21.9 (C^{10}), 13.9 (C^{11}); **FAB – MS** [m/z] (relative intensity): 660.6 [M+], 498.4 [M – C$_{10}$H$_{16}$N]; **HRMS – FAB** [m/z]: [M + H$^+$] calculated for C$_{45}$H$_{65}$N$_4$ = 661.5204, found 661.5202, Δ = 0.1418 mmu; **Yield:** 39%

6.2.2.3 Tetrakis(*p-N*-hexylaniline)methane
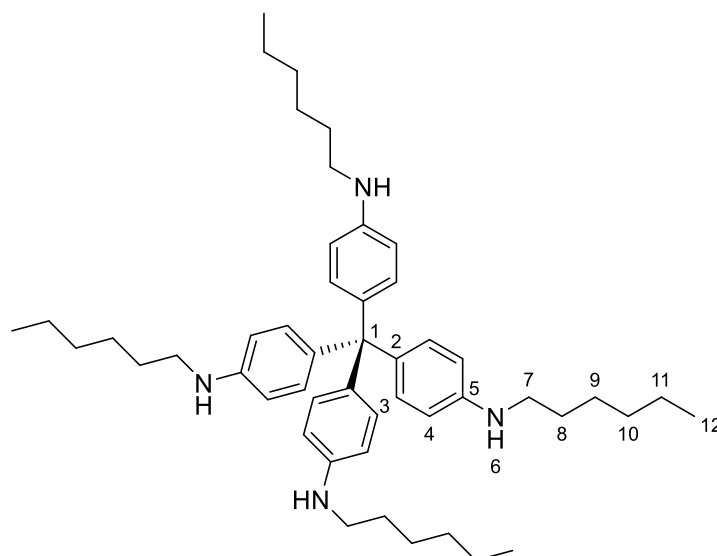
¹H NMR (500 MHz, CDCl₃): δ [ppm] = 6.99 (d, *J* = 8.7 Hz, 8H, CH^4), 6.48 (d, *J* = 8.7 Hz, 8H, CH^3), 3.55 (s, 4H, NH^6), 3.08 (t, *J* = 7.1 Hz, 8H, CH^7), 1.61 (p, *J* = 7.0 Hz, 8H, CH^8),

6. Experimental Section

1.55 – 1.15 (m, 16H, CH^{10,11}), 0.91 (t, J = 6.9 Hz, 12H, CH^{12}); **^{13}C NMR** (100 MHz, CDCl$_3$): δ [ppm] = 145.9 (C^2), 137.6 (C^5), 132.0 (C^4), 111.6 (C^3), 61.9 (C^1), 44.4 (C^7), 31.8 (C^8), 29.8 (C^9), 27.0 (C^{10}), 22.5 (C^{11}), 14.2 (C^{12}); **IR:** (ATR): n [cm^{-1}] = 3414.5 (m), 3054.5 (w), 3019.5 (w), 2951.7 (s), 2922.9 (s), 2852.9 (s), 1608.5 (s), 1575.6 (m), 1509.8 (vs), 1478.9 (s), 1406.9 (w), 1376.1 (w), 1316.4 (s), 1291.7 (s), 1252.7 (s), 1182.7 (s), 1139.5 (m), 1116.9 (m), 1088.1 (m), 1011.9 (w), 974.9 (w), 940.0 (w), 898.9 (w), 808.4 (s), 765.2 (m), 728.1 (m), 699.3 (m), 571.8 (m), 549.2 (m), 479.3 (w); **FAB – MS** [m/z] (relative intensity): 716.6 [M +], 540 [M – C$_{12}$H$_{14}$N]; **HRMS – FAB** [m/z]: [M+] calculated for C$_{49}$H$_{72}$N$_4$ = 716.5752, found 716.5751, Δ = 0.0675 mmu; **Yield:** 31%

6.2.2.4 Tetrakis(*p-N*-isopropylaniline)methane
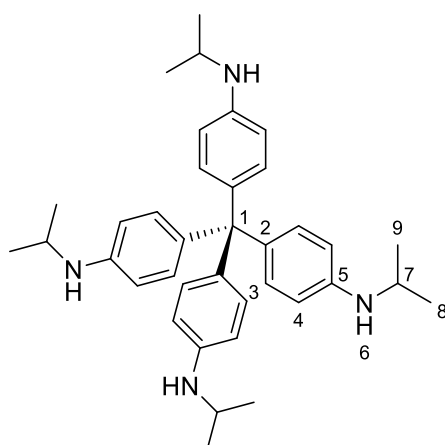
^{1}H NMR (500 MHz, CDCl$_3$): δ [ppm] = 6.97 (d, J = 8.7 Hz, 8H, CH^4), 6.46 (d, J = 8.7 Hz, 8H, CH^3), 3.59 (m, 4H, CH^7), 1.20 (d, J = 6.3 Hz, 24H, CH^{8,9}); **^{13}C NMR** (100 MHz, CDCl$_3$): δ [ppm] = 144.7 (C^2), 137.4 (C^5), 132.1 (C^4), 112.1 (C^3), 61.9 (C^1), 44.6 (C^7), 23.2 (C^{8,9}); **IR:** (ATR): n [cm^{-1}] = 3395.9 (m), 3050.4 (w), 3021.6 (w), 2964.0 (s), 2929.0 (m), 2869.4 (m), 1731.9 (m), 1608.5 (s), 1575.6 (m), 1507.7 (vs), 1462.5 (m), 1404.9 (w), 1382.2 (m), 1363.7 (m), 1320.5 (s), 1295.9 (s), 1248.5 (s), 1174.5 (s),1114.8 (s), 1042.9 (m), 808.4 (s), 734.3 (s), 701.4 (s), 606.8 (m), 534.8 (m), 475.1 (w); **FAB – MS** [m/z] (relative intensity): 549.5 [M + H], 414.3 [M – C$_9$H$_{12}$N]; **HRMS – FAB** [m/z]: [M+] calculated for C$_{37}$H$_{48}$N$_4$ = 548.3873, found 548.3873, Δ = 0.0966 mmu; **Yield:** 20%

6.2.2.5 Tetrakis(*p*-*N*-isobutylaniline)methane
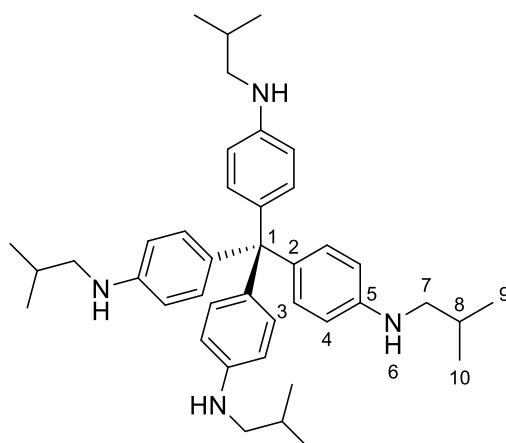
¹H NMR (500 MHz, CDCl$_3$): δ [ppm] = 6.99 (d, J = 8.8 Hz, 8H, CH^4), 6.48 (d, J = 8.8 Hz, 8H, CH^3), 3.64 (s, 4H, NH^6), 2.91 (d, J = 6.7, 8H, CH^7), 1.87 (m, 4H, CH^8), 0.98 (d, J = 6.7 Hz, 24H, CH^{9,10}); **¹³C NMR** (100 MHz, CDCl$_3$): δ [ppm] = 145.8 (C^2), 137.5 (C^5), 132.0 (C^4), 111.6 (C^3), 61.9 (C^1), 52.3 (C^7), 28.4 (C^8), 20.7 (C^{9,10}); **IR:** (ATR): n [cm^{-1}] = 3408.,3 (m), 3058.6 (w), 3025.7 (w), 2953.7 (s), 2924.9 (s), 2865.3 (s), 1733.9 (m), 1608.5 (s), 1575.6 (s), 1509.8 (vs), 1472.7 (s), 1404.9 (m), 1388.4 (m), 1369.9 (m), 1318.5 (s), 1246.5 (s), 1182.7 (s), 1172.4 (s), 1151.9 (s), 1116.9 (s), 1079.9 (m), 1030.5 (m), 968.8 (w), 940.0 (w), 900.9 (w), 808.4 (s), 765.2 (m), 699.3 (m), 608.8 (m), 536.9 (m); **FAB – MS** [m/z] (relative intensity): 605.5 [M + H], 456.4 [M – C$_{10}$H$_{14}$N]; **HRMS – FAB** [m/z]: [M+] calculated for C$_{41}$H$_{56}$N$_4$ = 604.4499, found 604.4500, Δ = 0.0310 mmu; **Yield:** 29%

6.2.2.6 Tetrakis(*p*-*N*-(1-methoxypropane-2-yl)aniline)methane
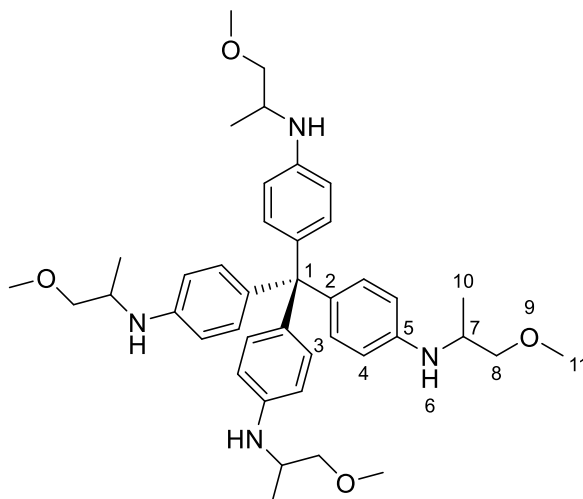
¹H NMR (500 MHz, DMSO-d_6): δ [ppm] = 6.74 (d, J = 8.7 Hz, 8H, CH⁴), 6.53 (d, J = 8.7 Hz, 8H, CH³), 5.19 (d, J = 8.0 Hz, 8H, NH⁶), 4.19 (s, 4H, NH⁶), 3.51 (dt, J = 12.9, 6.5 Hz, 4H, CH⁷), 3.26 (ddd, J = 91.5, 9.3, 6.6 Hz, 4H, CH⁸), 3.26 (s, 12H, CH¹¹), 1.09 (d, J = 6.4 Hz, 12H, CH¹⁰); **¹³C NMR** (100 MHz, DMSO-d_6): δ [ppm] = 145.2 (C²), 135.4 (C⁵), 131.1 (C⁴), 110.7 (C³), 75.7 (C⁸), 60.9 (C¹), 58.3 (C¹¹), 47.1 (C⁷), 18.1 (C¹⁰); **IR:** (ATR): n [cm⁻¹] = 3393.9 (m), 3050.4 (w), 3031.9 (w), 2955.8 (m), 2924.9 (m), 2863.2 (m), 1610.6 (s), 1577.6 (m), 1511.8 (vs), 1478.9 (s), 1404.9 (w), 1376.1 (w), 1324.6 (s), 1306.1 (m), 1256.8 (m), 1182.7 (s), 1143.6 (m), 1112.8 (m), 1086.0 (w), 1030.5 (w), 979.1 (w), 902.9 (w), 878.3 (w), 810.4 (s), 752.8 (m), 701.4 (m), 615.0 (m), 543.0 (m), 526.6 (m); **FAB – MS** [m/z] (relative intensity): 669.5 [M + H], 504.4 [M – C₁₀H₁₄NO]; **HRMS – FAB** [m/z]: [M+] calculated for C₄₁H₅₆N₄O = 668.4296, found 668.4297, Δ = 0.0515 mmu; **Yield:** 38%

6.2.2.7 Tetrakis(*p-N*-furfurylaniline)methane
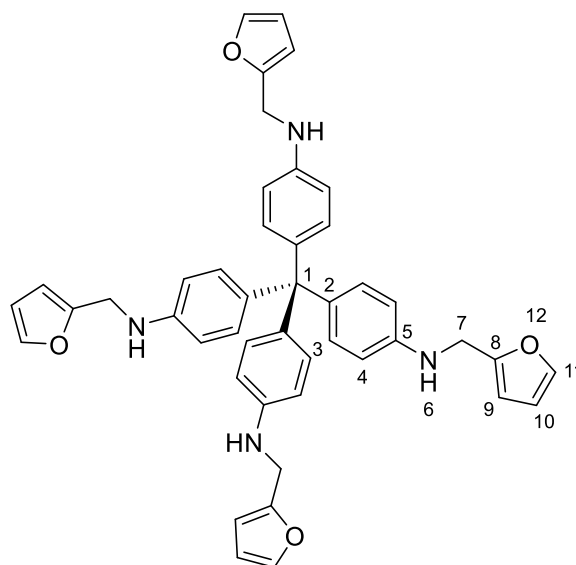
¹H NMR (500 MHz, DMSO-d_6): δ [ppm] = 7.56 (s, 4H, CH¹¹), 6.73 (d, J = 8.7 Hz, 8H, CH⁴), 6.48 (d, J = 8.7 Hz, 4H, CH³), 6.37 (m, 4H, CH¹⁰), 6.29 (d, J = 32. Hz, 4H, CH⁹), 5.92 (t, J = 5.8 Hz, 4H, NH⁶), 4.17 (d, 8H, CH⁷); **¹³C NMR** (100 MHz, DMSO-d_6): δ [ppm] = 153.5 (C⁸), 145.6 (C²), 141.9 (C¹¹), 135.9 (C⁵), 130.9 (C⁴), 110.9 (C³), 110.3 (C¹⁰), 106.8 (C⁹), 61.1 (C¹), 40.5 (C⁷); **IR:** (ATR): n [cm⁻¹] = 3393.9, (m), 3284.9 (w), 2980.5 (s), 2929.0 (m), 2852.9 (m), 1731.9 (s), 1610.6 (s), 1511.8 (s), 1470.7 (s), 1446.0 (m), 1371.9 (m), 1320.5 (m), 1297.9 (m), 1240.3 (vs), 1184.8 (s), 1145.7 (s),

1110.7 (s),   1073.7 (m), 1042.9 (s), 1009.9 (m), 917.4 (m), 884.5 (m), 814.5 (s), 730.2 (s), 664.4 (w), 633.5 (w), 598.6 (m), 563.6 (m), 536.9 (m), 506.0 (w), 458.7 (w); **FAB – MS** [m/z] (relative intensity): 701.4 [M + H], 528.2 [M – $C_{11}H_{10}NO$]; **HRMS – FAB** [m/z]: [M+] calculated for $C_{45}H_{10}O_4N_4 = 700.3044$, found 7003043, $\Delta = 0.1052$ mmu; **Yield:** 19%

6.2.2.8 Tetrakis(*p-N*-phenylaniline)methane
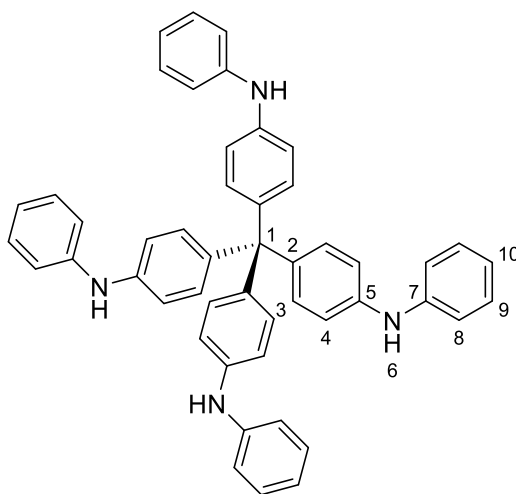
¹H NMR (500 MHz, CDCl₃): δ [ppm] = 8.36 (s, 4H, NH⁶), 7.20 (m, 20H, CH³,⁹), 7.09 (m, 16H, CH⁴,⁸), 6.79 (m, 4, CH¹⁰); **¹³C NMR** (100 MHz, CDCl₃): δ [ppm] = 143.4, 140.9, 138.6, 131.2, 129.1, 119.4, 116.5, 115.5, 61.9 (C¹); **IR:** (ATR): n [cm⁻¹] = 3404.2 (m), 3379.5 (m), 3021.6 (w), 1592.0 (s), 1503.6 (vs), 1493.3 (vs), 1439.8 (m), 1396.6 (m), 1314.4 (s), 1242.4 (m), 1172.4 (m), 1123.1 (w), 1071.6 (w), 1009.9 (w), 905.0 (w), 876.2 (w), 808.4 (s), 748.7 (s), 728.1 (s), 693.2 (s), 631.5 (w), 588.3 (m), 528.6 (m), 487.5 (m), 464.9 (m); **FAB – MS** [m/z] (relative intensity): 685.4 [M + H], 516.3 [M – $C_{12}H_{10}N$]; **HRMS – FAB** [m/z]: [M+] calculated for $C_{49}H_{40}N_4 = 684.3247$, found 684.3246, $\Delta = 0.1435$ mmu; **Yield:** 41%

6. Experimental Section

6.2.2.9 tetrakis(*p-(N-(3-methylacrylate)-N-butyl)aminophenyl)methane*
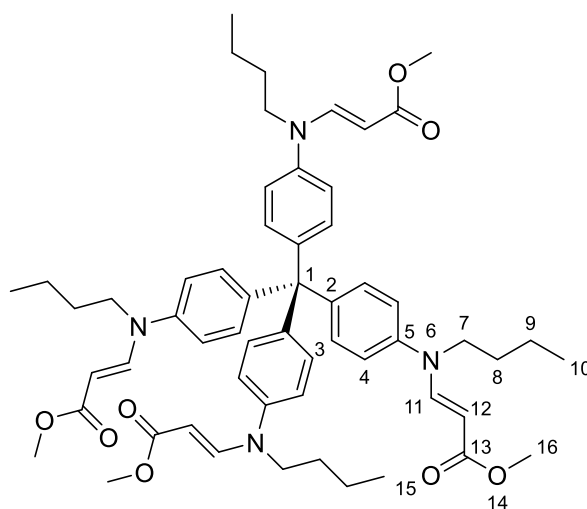
¹H NMR (500 MHz, CDCl₃): δ [ppm] = 7.85 (d, $J = 13.3$ Hz, 4H, C^{11}), 7.12 (d, $J = 8.9$ Hz, 8H, CH^4), 7.04 (d, $J = 8.9$ Hz, 8H, CH^3), 4.94 (d, $J = 13.3$ Hz, 4H, CH^{12}), 3.70 (s, 12H, CH^{16}), 3.60 (m, 8H, CH^7), 1.67 (m, 8H, CH^8), 1.36 (m, 8H, CH^9), 0.94 (m, 8H, CH^{10}); **¹³C NMR** (100 MHz, CDCl₃): δ [ppm] = 169.9 (C^{13}), 147.8 (C^2), 143.7 (C^4), 142.4 (C^3), 131.9 (C^{11,12}), 119.6 (C^5), 89.8 (C^{16}), 51.1 (C^7), 28.7 (C^8), 20.3 (C^9), 13.9 (C^{10}); **IR:** (ATR): n [cm^{-1}] = 2953.7 (m), 2869.4 (m), 1727.8 (m), 1692.8 (s), 1614.7 (s), 1589.9 (vs), 1503.6 (s), 1460.4 (m), 1433.7 (m), 1380.2 (m), 1332.9 (s), 1306.1 (m), 1248.5 (s), 1205-3 (s), 1153.9 (s), 1125.1 (vs), 1042.9 (s), 1016.1 (s), 974.9 (s), 925.6 (m), 800.1 (s), 730.2 (m), 705.5 (m), 619.1 (w), 577.9 (w), 534.8 (w), 493.7 (w); **FAB – MS** [m/z] (relative intensity): 941.7 [M + H], 856.6 [M – C₄H₅O₂], 708.4 [M – C₁₄H₁₈NO₂]; **HRMS – FAB** [m/z]: calculated for C₅₇H₇₂N₄O₈ = 940.5345, found 940.5346, Δ = 0.1618 mmu; **Yield: 99%**

6.2.3 Grafting procedure

6.2.3.1 Silanisation

In general, silicon wafers were cut in 1 cm x 1 cm squares and then cleaned by placing them consecutively in chloroform, acetone, and ethanol in an ultrasonic bath. The substrates were then dried under the flow of argon stream. Treatment with piranha solution (H_2SO_4/H_2O_2, 70:30 v/v) at 80 °C for 30 min activated the surface and removed organic residues. This treatment was followed by two rinses with distilled water and isopropanol and subsequent drying under argon stream. The freshly edged samples are immediately modified to avoid oxidation.

Linear silanes:

Cleaned wafers were exposed to monolayer deposition solutions with a concentration of 8.4 mM of alkene-terminated silanes, (trihydroxy(10-undecen-1-yl) silane (**Sil1**), trichloro(10-undecen-1-yl) silane (**Sil2**), and trimethoxy(7-octadecen-1-yl) silane (**Sil3)**, triethoxy(3-chloropropyl) silane (**Sil5**), in dry toluene at room temperature for 1.5 hours The procedure was carried out in an argon purged glove bag and the relative humidity was 28-33%. Samples were withdrawn from the silane solutions after the indicated deposition time and washed with chloroform, toluene, and acetone in an ultrasonic bath and dried under argon stream.

Cyclic silanes:

The wafers were immersed in a solution containing DCM and 2,2-dimethoxy-1-thia-2-silacyclopentane (**Sil4**) or N-methyl-aza-2,2,4-trimethylsilacyclopentane (**Sil6**) in a ratio six to four and the mixture was agitated for 2 h. The substrate was rinsed with chloroform, toluene, and acetone several times as well as subjected to an ultrasonic bath for each solvent.

6.2.3.2 Molecular layer deposition

Modification with tetrakis(*p*-mercaptophenyl)methane (TPM-SH):

5 mg of TPM-SH and 1 mg of 2,2-dimethoxy-2-phenylacetophenone (DMPA) were dissolved in 1.5 mL degassed dimethylformamide and added to silicon wafers inside a petri dish. The reaction was performed in an argon filled glove-bag under a UV-lamp

and irradiated at 365 nm for 45 minutes. Samples were withdrawn from the silane solutions after the indicated deposition time and washed with chloroform, toluene, and acetone in an ultrasonic bath and dried under argon stream.

Modification with tetrakis(*p*-acetylenephenyl)methane (TPM-acetylene):

10 mg of TPM-SH and 2.5 mg of DMPA were dissolved in 1.5 mL degassed dimethylformamide and added to silicon wafers inside a petri dish. The reaction was performed in an argon filled glove-bag under a UV-lamp and irradiated at 365 nm for 1.5 hours. Samples were withdrawn from the silane solutions after the indicated deposition time and washed with chloroform, toluene, and acetone in an ultrasonic bath and dried under argon stream.

7. Appendix

7.1 References

1. Choubey, P. K.; Kim, M.-s.; Srivastava, R. R.; Lee, J.-c.; Lee, J.-Y. Advance review on the exploitation of the prominent energy-storage element: Lithium. Part I: From mineral and brine resources. *Minerals Engineering [Online]* **2016,** *89*, 119–137.

2. Choubey, P. K.; Chung, K.-S.; Kim, M.-s.; Lee, J.-c.; Srivastava, R. R. Advance review on the exploitation of the prominent energy-storage element Lithium. Part II: From sea water and spent lithium ion batteries (LIBs). *Minerals Engineering [Online]* **2017,** *110*, 104–121.

3. Vetter, J.; Novák, P.; Wagner, M. R.; Veit, C.; Möller, K.-C.; Besenhard, J. O.; Winter, M.; Wohlfahrt-Mehrens, M.; Vogler, C.; Hammouche, A. Ageing mechanisms in lithium-ion batteries. *Journal of Power Sources [Online]* **2005,** *147* (1-2), 269–281.

4. Reinhardt Wagner. Battery Fuel Gauges: Accurately Measuring Charge Level. https://pdfserv.maximintegrated.com/en/an/AN3958.pdf (accessed February 20, 2020).

5. Dunn, B.; Kamath, H.; Tarascon, J.-M. Electrical energy storage for the grid: a battery of choices. *Science (New York, N.Y.) [Online]* **2011,** *334* (6058), 928–935.

6. https://www.tesla.com/de_DE/gigafactory?redirect=no.

7. Verma, P.; Maire, P.; Novák, P. A review of the features and analyses of the solid electrolyte interphase in Li-ion batteries. *Electrochimica Acta [Online]* **2010,** *55* (22), 6332–6341.

8. Spotnitz, R. Simulation of capacity fade in lithium-ion batteries. *Journal of Power Sources [Online]* **2003,** *113* (1), 72–80.

9. Arora, P. Capacity Fade Mechanisms and Side Reactions in Lithium-Ion Batteries. *J. Electrochem. Soc. [Online]* **1998,** *145* (10), 3647.

10. Peled, E.; Menkin, S. Review—SEI: Past, Present and Future. *J. Electrochem. Soc. [Online]* **2017,** *164* (7), A1703-A1719.

11. Sonderforschungsbereich 1176. Molekulare Strukturierung weicher Materie [Online] **2016**, 139–154.

12. Chang, Y.; Chen, S.; Zhang, Z.; Jiang, S. Highly protein-resistant coatings from well-defined diblock copolymers containing sulfobetaines. *Langmuir [Online]* **2006,** *22* (5), 2222–2226.

13. Bechler, S. L.; Lynn, D. M. Reactive polymer multilayers fabricated by covalent layer-by-layer assembly: 1,4-conjugate addition-based approaches to the design of functional biointerfaces. *Biomacromolecules [Online]* **2012,** *13* (5), 1523–1532.

14. Lee, D.-C.; Morales, G. M.; Lee, Y.; Yu, L. Cofacial porphyrin multilayers via layer-by-layer assembly. *Chemical communications (Cambridge, England) [Online]* **2006,** No. 1, 100–102.

15. Kim, A.; Filler, M. A.; Kim, S.; Bent, S. F. Layer-by-layer growth on Ge(100) via spontaneous urea coupling reactions. *J. Am. Chem. Soc. [Online]* **2005,** *127* (16), 6123–6132.

16. Llevot, A.; Steinmüller, S. O.; Bitterer, B.; Ridder, B.; Berson, J.; Walheim, S.; Schimmel, T.; Bräse, S.; Scheiba, F.; Meier, M. A. R. Sequence-controlled molecular layers on surfaces by thiol–ene chemistry: synthesis and multitechnique characterization. *Polym. Chem. [Online]* **2017,** *8* (38), 5824–5828.

17. Vilan, A.; Cahen, D. Chemical Modification of Semiconductor Surfaces for Molecular Electronics. *Chem. Rev. [Online]* **2017,** *117* (5), 4624–4666.

18. Kolb, H. C.; Finn, M. G.; Sharpless, K. B. Click Chemistry: Diverse Chemical Function from a Few Good Reactions. *Angewandte Chemie (International ed. in English) [Online]* **2001,** *40* (11), 2004–2021.

19. Benjamin Bitterer. Neue Methoden zur Oberflächenbeschichtung mittels Thiol-En Chemie. Masterthesis; KIT, Karlsruhe, 2016.

20. Bohacek, R. S.; McMartin, C.; Guida, W. C. The art and practice of structure-based drug design: A molecular modeling perspective. *Med. Res. Rev. [Online]* **1996,** *16* (1), 3–50.

21. Kolb, H. C.; Sharpless, K.B. The growing impact of click chemistry on drug discovery. *Drug Discovery Today [Online]* **2003,** *8* (24), 1128–1137.

22. Hein, C. D.; Liu, X.-M.; Wang, D. Click chemistry, a powerful tool for pharmaceutical sciences. *Pharmaceutical research [Online]* **2008,** *25* (10), 2216–2230.

23. Huisgen, R. 1,3-Dipolar Cycloadditions. Past and Future. *Angew. Chem. Int. Ed. Engl. [Online]* **1963,** *2* (10), 565–598.

24. Proceedings of the Chemical Society. October 1961. *Proc. Chem. Soc. [Online]* **1961,** October, 357.

25. Rostovtsev, V. V.; Green, L. G.; Fokin, V. V.; Sharpless, K. B. A Stepwise Huisgen Cycloaddition Process: Copper(I)-Catalyzed Regioselective "Ligation" of Azides and Terminal Alkynes. *Angew. Chem. Int. Ed. Engl. [Online]* **2002,** *41* (14), 2596–2599.

26. Bock, V. D.; Hiemstra, H.; van Maarseveen, J. H. CuI-Catalyzed Alkyne-Azide "Click" Cycloadditions from a Mechanistic and Synthetic Perspective. *Eur. J. Org. Chem. [Online]* **2006,** *2006* (1), 51–68.

27. Tornøe, C. W.; Christensen, C.; Meldal, M. Peptidotriazoles on solid phase: 1,2,3-triazoles by regiospecific copper(i)-catalyzed 1,3-dipolar cycloadditions of terminal alkynes to azides. *J. Org. Chem. [Online]* **2002,** *67* (9), 3057–3064.

28. Himo, F.; Lovell, T.; Hilgraf, R.; Rostovtsev, V. V.; Noodleman, L.; Sharpless, K. B.; Fokin, V. V. Copper(I)-catalyzed synthesis of azoles. DFT study predicts

unprecedented reactivity and intermediates. *J. Am. Chem. Soc. [Online]* **2005,** *127* (1), 210–216.

29. Pérez-Balderas, F.; Ortega-Muñoz, M.; Morales-Sanfrutos, J.; Hernández-Mateo, F.; Calvo-Flores, F. G.; Calvo-Asín, J. A.; Isac-García, J.; Santoyo-González, F. Multivalent neoglycoconjugates by regiospecific cycloaddition of alkynes and azides using organic-soluble copper catalysts. *Organic letters [Online]* **2003,** *5* (11), 1951–1954.

30. Díez-González, S.; Correa, A.; Cavallo, L.; Nolan, S. P. (NHC)Copper(I)-catalyzed 3+2 cycloaddition of azides and mono- or disubstituted alkynes. *Chemistry (Weinheim an der Bergstrasse, Germany) [Online]* **2006,** *12* (29), 7558–7564.

31. Wang, F.; Fu, H.; Jiang, Y.; Zhao, Y. Quick and highly efficient copper-catalyzed cycloaddition of aliphatic and aryl azides with terminal alkynes "on water". *Green Chem. [Online]* **2008,** *10* (4), 452.

32. Zhang, L.; Chen, X.; Xue, P.; Sun, H. H. Y.; Williams, I. D.; Sharpless, K. B.; Fokin, V. V.; Jia, G. Ruthenium-catalyzed cycloaddition of alkynes and organic azides. *J. Am. Chem. Soc. [Online]* **2005,** *127* (46), 15998–15999.

33. Boren, B. C.; Narayan, S.; Rasmussen, L. K.; Zhang, L.; Zhao, H.; Lin, Z.; Jia, G.; Fokin, V. V. *Ruthenium-catalyzed azide-alkyne cycloaddition: scope and mechanism* 130, 2008.

34. Boren, B. C.; Narayan, S.; Rasmussen, L. K.; Zhang, L.; Zhao, H.; Lin, Z.; Jia, G.; Fokin, V. V. Ruthenium-catalyzed azide-alkyne cycloaddition: scope and mechanism. *J. Am. Chem. Soc. [Online]* **2008,** *130* (28), 8923–8930.

35. Wittig, G.; Krebs, A. Zur Existenz niedergliedriger Cycloalkine, I. *Chem. Ber. [Online]* **1961,** *94* (12), 3260–3275.

36. Baskin, J. M.; Prescher, J. A.; Laughlin, S. T.; Agard, N. J.; Chang, P. V.; Miller, I. A.; Lo, A.; Codelli, J. A.; Bertozzi, C. R. Copper-free click chemistry for dynamic in vivo imaging. *Proceedings of the National Academy of Sciences of the United States of America [Online]* **2007,** *104* (43), 16793–16797.

37. Agard, N. J.; Prescher, J. A.; Bertozzi, C. R. A strain-promoted 3 + 2 azide-alkyne cycloaddition for covalent modification of biomolecules in living systems. *J. Am. Chem. Soc. [Online]* **2004,** *126* (46), 15046–15047.

38. Ramapanicker, R.; Chauhan, P. *Click Chemistry: Mechanistic and Synthetic Perspectives* 40.

39. Ess, D. H.; Jones, G. O.; Houk, K. N. *Transition states of strain-promoted metal-free click chemistry: 1,3-dipolar cycloadditions of phenyl azide and cyclooctynes* 10, 2008.

40. Hu, R.; Li, W.; Tang, B. Z. Recent Advances in Alkyne-Based Multicomponent Polymerizations. *Macromol. Chem. Phys. [Online]* **2016,** *217* (2), 213–224.

41. Bae, I.; Han, H.; Chang, S. Highly efficient one-pot synthesis of N-sulfonylamidines by Cu-catalyzed three-component coupling of sulfonyl azide, alkyne, and amine. *J. Am. Chem. Soc. [Online]* **2005,** *127* (7), 2038–2039.

42. Zhang, Z.; You, Y.-Z.; Wu, D.-C.; Hong, C.-Y. Syntheses of Sequence-Controlled Polymers via Consecutive Multicomponent Reactions. *Macromolecules [Online]* **2015,** *48* (11), 3414–3421.

43. Deng, H.; Zhao, E.; Li, H.; Lam, J. W. Y.; Tang, B. Z. Multifunctional Poly(N -sulfonylamidine)s Constructed by Cu-Catalyzed Three-Component Polycouplings of Diynes, Disulfonyl Azide, and Amino Esters. *Macromolecules [Online]* **2015,** *48* (10), 3180–3189.

44. Kim, H.; Choi, T.-L. Preparation of a Library of Poly(N -sulfonylimidates) by Cu-Catalyzed Multicomponent Polymerization. *ACS Macro Lett. [Online]* **2014,** *3* (8), 791–794.

45. Huang, D.; Liu, Y.; Qin, A.; Tang, B. Z. Recent advances in alkyne-based click polymerizations. *Polym. Chem. [Online]* **2018,** *9* (21), 2853–2867.

46. Labrunie, A.; Lebailly, T.; Habibi, A. H.; Dalinot, C.; Jiang, Y.; Dabos-Seignon, S.; Roncali, J.; Blanchard, P.; Cabanetos, C. CuAAC-Based Assembly and Characterization of a New Molecular Dyad for Single Material Organic Solar Cell. *Metals [Online]* **2019,** *9* (6), 618.

47. Labrunie, A.; Londi, G.; Dayneko, S. V.; Blais, M.; Dabos-Seignon, S.; Welch, G. C.; Beljonne, D.; Blanchard, P.; Cabanetos, C. A triazatruxene-based molecular dyad for single-component organic solar cells. *Chem.Sq. [Online]* **2018**.

48. Labrunie, A.; Gorenflot, J.; Babics, M.; Alévêque, O.; Dabos-Seignon, S.; Balawi, A. H.; Kan, Z.; Wohlfahrt, M.; Levillain, E.; Hudhomme, P.; Beaujuge, P. M.; Laquai, F.; Cabanetos, C.; Blanchard, P. Triphenylamine-Based Push–Pull σ–C 60 Dyad As Photoactive Molecular Material for Single-Component Organic Solar Cells: Synthesis, Characterizations, and Photophysical Properties. *Chem. Mater. [Online]* **2018,** *30* (10), 3474–3485.

49. Posner, T. Beiträge zur Kenntniss der ungesättigten Verbindungen. II. Ueber die Addition von Mercaptanen an ungesättigte Kohlenwasserstoffe. *Chem. Ber. [Online]* **1905,** *38* (1), 646–657.

50. Morgan, C. R.; Ketley, A. D. The effect of phosphines on thiol/ene curing systems. *J. Polym. Sci. B Polym. Lett. Ed. [Online]* **1978,** *16* (2), 75–79.

51. Morgan, C. R.; Magnotta, F.; Ketley, A. D. Thiol/ene photocurable polymers. *J. Polym. Sci. Polym. Chem. Ed. [Online]* **1977,** *15* (3), 627–645.

52. Kade, M. J.; Burke, D. J.; Hawker, C. J. The power of thiol-ene chemistry. *J. Polym. Sci. A Polym. Chem. [Online]* **2010,** *48* (4), 743–750.

53. Lowe, A. B. Thiol–ene "click" reactions and recent applications in polymer and materials synthesis: a first update. *Polym. Chem. [Online]* **2014,** *5* (17), 4820–4870.

54. Hoyle, C. E.; Lee, T. Y.; Roper, T. Thiol-enes: Chemistry of the past with promise for the future. *J. Polym. Sci. A Polym. Chem. [Online]* **2004,** *42* (21), 5301–5338.

55. Hoyle, C. E.; Bowman, C. N. Thiol-ene click chemistry. *Angewandte Chemie (International ed. in English) [Online]* **2010,** *49* (9), 1540–1573.

56. Cramer, N. B.; Reddy, S. K.; O'Brien, A. K.; Bowman, C. N. Thiol−Ene Photopolymerization Mechanism and Rate Limiting Step Changes for Various Vinyl Functional Group Chemistries. *Macromolecules [Online]* **2003,** *36* (21), 7964–7969.

57. Northrop, B. H.; Coffey, R. N. Thiol-ene click chemistry: computational and kinetic analysis of the influence of alkene functionality. *J. Am. Chem. Soc. [Online]* **2012,** *134* (33), 13804–13817.

58. Lee, T. Y.; Roper, T. M.; Jonsson, E. S.; Guymon, C. A.; Hoyle, C. E. Thiol−Ene Photopolymerization Kinetics of Vinyl Acrylate/Multifunctional Thiol Mixtures. *Macromolecules [Online]* **2004,** *37* (10), 3606–3613.

59. M. C. Cole. Dissertation; University of Southern Mississippi, Mississippi, 2001.

60. Fairbanks, B. D.; Scott, T. F.; Kloxin, C. J.; Anseth, K. S.; Bowman, C. N. Thiol-Yne Photopolymerizations: Novel Mechanism, Kinetics, and Step-Growth Formation of Highly Cross-Linked Networks. *Macromolecules [Online]* **2009,** *42* (1), 211–217.

61. Guo, J.; Filpponen, I.; Johansson, L.-S.; Heißler, S.; Li, L.; Levkin, P.; Rojas, O. J. Micro-patterns on nanocellulose films and paper by photo-induced thiol–yne click coupling: a facile method toward wetting with spatial resolution. *Cellulose [Online]* **2018,** *25* (1), 367–375.

62. Siegel, A. C.; Phillips, S. T.; Dickey, M. D.; Lu, N.; Suo, Z.; Whitesides, G. M. Foldable Printed Circuit Boards on Paper Substrates. *Adv. Funct. Mater. [Online]* **2010,** *20* (1), 28–35.

63. Teisala, H.; Tuominen, M.; Kuusipalo, J. Superhydrophobic Coatings on Cellulose-Based Materials: Fabrication, Properties, and Applications. *Adv. Mater. Interfaces [Online]* **2014,** *1* (1), 1300026.

64. Cui, Y.-Y.; Yang, C.-X.; Yan, X.-P. Thiol-yne Click Post-Modification for the Synthesis of Chiral Microporous Organic Networks for Chiral Gas Chromatography. *ACS applied materials & interfaces [Online]* **2020,** *12* (4), 4954–4961.

65. Truce, W. E.; Brady, D. G. Stereochemistry of Amine Additions to Acetylenic Sulfones and Carboxylic Esters 1. *J. Org. Chem. [Online]* **1966,** *31* (11), 3543–3550.

66. *Catalytic heterofunctionalization. From hydroamination to hydrozirconation;* Togni, A., Grützmacher, H., Eds., 1st ed.; Wiley-VCH: Weinheim, 2001.

67. Hong, S.; Marks, T. J. Organolanthanide-catalyzed hydroamination. *Accounts of chemical research [Online]* **2004,** *37* (9), 673–686.

68. Shi, F.; Cui, X. *Catalytic amination for N-alkyl amine synthesis;* Academic Press an imprint of Elsevier: London, San Diego, Cambridge, Oxford, 2018.

69. He, B.; Zhen, S.; Wu, Y.; Hu, R.; Zhao, Z.; Qin, A.; Tang, B. Z. Cu(i)-Catalyzed amino-yne click polymerization. *Polym. Chem. [Online]* **2016,** *7* (48), 7375–7382.

70. He, B.; Su, H.; Bai, T.; Wu, Y.; Li, S.; Gao, M.; Hu, R.; Zhao, Z.; Qin, A.; Ling, J.; Tang, B. Z. Spontaneous Amino-yne Click Polymerization: A Powerful Tool toward Regio- and Stereospecific Poly(β-aminoacrylate)s. *J. Am. Chem. Soc. [Online]* **2017,** *139* (15), 5437–5443.

71. Yu, L.; Zhang, Z.; You, Y.-Z.; Hong, C.-Y. Synthesis of sequence-controlled polymers via sequential thiol-ene and amino-yne click reactions in one pot. *European Polymer Journal [Online]* **2018,** *103*, 80–87.

72. Huang, J.; Jiang, X. Injectable and Degradable pH-Responsive Hydrogels via Spontaneous Amino-Yne Click Reaction. *ACS applied materials & interfaces [Online]* **2018,** *10* (1), 361–370.

73. *Wege des Wissens: Berliner Blau, 1706-1726;* Alexander Kraft, Ed., 22nd ed.; Mitteilungen; Gesellschaft deutscher Chemiker: Frankfurt/Main, 2012.

74. Kekulé, A. Ueber die s. g. gepaarten Verbindungen und die Theorie der mehratomigen Radicale. *Eur. J. Org. Chem. [Online]* **1857,** *104* (2), 129–150.

75. Kekulé, A. Ueber die Constitution und die Metamorphosen der chemischen Verbindungen und über die chemische Natur des Kohlenstoffs. *Eur. J. Org. Chem. [Online]* **1858,** *106* (2), 129–159.

76. Werner, A. Beitrag zur Konstitution anorganischer Verbindungen. *Z. Anorg. Chem. [Online]* **1893,** *3* (1), 267–330.

77. Rayner, J. H.; Powell, H. M. 67. Structure of molecular compounds. Part X. Crystal structure of the compound of benzene with an ammonia–nickel cyanide complex. *J. Chem. Soc. [Online]* **1952,** *0* (0), 319–328.

78. *Introduction to reticular chemistry. Metal-organic frameworks and covalent organic frameworks;* Yaghi, O. M., Kalmutzki, M. J., Diercks, C. S., Eds., 2019.

79. Eddaoudi, M.; Kim, J.; Rosi, N.; Vodak, D.; Wachter, J.; O'Keeffe, M.; Yaghi, O. M. Systematic design of pore size and functionality in isoreticular MOFs and their application in methane storage. *Science (New York, N.Y.) [Online]* **2002,** *295* (5554), 469–472.

80. *The chemistry of metal-organic frameworks. Synthesis, characterization, and applications;* Kaskel, S., Ed.; Wiley-VCH: Weinheim, 2016.

81. Sing, K. S. W. Reporting physisorption data for gas/solid systems with special reference to the determination of surface area and porosity (Recommendations 1984). *Pure and Applied Chemistry [Online]* **1985,** *57* (4), 603–619.

82. Reineke, T. M.; Eddaoudi, M.; Moler, D.; O'Keeffe, M.; Yaghi, O. M. Large Free Volume in Maximally Interpenetrating Networks: The Role of Secondary Building Units Exemplified by Tb 2 (ADB) 3 [(CH 3) 2 SO] 4 ·16[(CH 3) 2 SO] 1. *J. Am. Chem. Soc. [Online]* **2000,** *122* (19), 4843–4844.

83. Karagiaridi, O.; Bury, W.; Mondloch, J. E.; Hupp, J. T.; Farha, O. K. Solvent-assisted linker exchange: an alternative to the de novo synthesis of unattainable

metal-organic frameworks. *Angew. Chem. Int. Ed. Engl. [Online]* **2014,** *53* (18), 4530–4540.

84. Farha, O. K.; Eryazici, I.; Jeong, N. C.; Hauser, B. G.; Wilmer, C. E.; Sarjeant, A. A.; Snurr, R. Q.; Nguyen, S. T.; Yazaydın, A. Ö.; Hupp, J. T. Metal-organic framework materials with ultrahigh surface areas: is the sky the limit? *J. Am. Chem. Soc. [Online]* **2012,** *134* (36), 15016–15021.

85. Rosi, N. L.; Eckert, J.; Eddaoudi, M.; Vodak, D. T.; Kim, J.; O'Keeffe, M.; Yaghi, O. M. Hydrogen storage in microporous metal-organic frameworks. *Science (New York, N.Y.) [Online]* **2003,** *300* (5622), 1127–1129.

86. Yilmaz, G.; Peh, S. B.; Zhao, D.; Ho, G. W. Atomic- and Molecular-Level Design of Functional Metal-Organic Frameworks (MOFs) and Derivatives for Energy and Environmental Applications. *Advanced science (Weinheim, Baden-Wurttemberg, Germany) [Online]* **2019,** *6* (21), 1901129.

87. O'Keeffe, M.; Peskov, M. A.; Ramsden, S. J.; Yaghi, O. M. The Reticular Chemistry Structure Resource (RCSR) database of, and symbols for, crystal nets. *Acc. Chem. Res. [Online]* **2008,** *41* (12), 1782–1789.

88. Li, M.; Li, D.; O'Keeffe, M.; Yaghi, O. M. Topological analysis of metal-organic frameworks with polytopic linkers and/or multiple building units and the minimal transitivity principle. *Chem. Rev. [Online]* **2014,** *114* (2), 1343–1370.

89. Nelson, A. P.; Farha, O. K.; Mulfort, K. L.; Hupp, J. T. Supercritical processing as a route to high internal surface areas and permanent microporosity in metal-organic framework materials. *J. Am. Chem. Soc. [Online]* **2009,** *131* (2), 458–460.

90. *Porous Organic Frameworks. Design, Synthesis and Their Advanced Applications;* Zhu, G., Ren, H., Eds.; SpringerBriefs in Molecular Science; Springer Berlin Heidelberg: Berlin, Heidelberg, s.l., 2015.

91. *Submicron porous materials;* Bettotti, P., Ed.; Springer International Publishing AG: Cham, 2017.

92. Xu, S.; Luo, Y.; Tan, B. Recent development of hypercrosslinked microporous organic polymers. *Macromolecular rapid communications [Online]* **2013,** *34* (6), 471–484.

93. Li, B.; Gong, R.; Wang, W.; Huang, X.; Zhang, W.; Li, H.; Hu, C.; Tan, B. A New Strategy to Microporous Polymers: Knitting Rigid Aromatic Building Blocks by External Cross-Linker. *Macromolecules [Online]* **2011,** *44* (8), 2410–2414.

94. McKeown, N. B.; Budd, P. M.; Msayib, K. J.; Ghanem, B. S.; Kingston, H. J.; Tattershall, C. E.; Makhseed, S.; Reynolds, K. J.; Fritsch, D. Polymers of intrinsic microporosity (PIMs): bridging the void between microporous and polymeric materials. *Chemistry (Weinheim an der Bergstrasse, Germany) [Online]* **2005,** *11* (9), 2610–2620.

95. McKeown, N. B.; Hanif, S.; Msayib, K.; Tattershall, C. E.; Budd, P. M. Porphyrin-based nanoporous network polymers. *Chemical communications (Cambridge, England) [Online]* **2002,** No. 23, 2782–2783.

96.   McKeown, N. B.; Makhseed, S.; Budd, P. M. Phthalocyanine-based nanoporous network polymers. *Chemical communications (Cambridge, England) [Online]* **2002,** No. 23, 2780–2781.

97.   Ding, S.-Y.; Wang, W. Covalent organic frameworks (COFs): from design to applications. *Chemical Society reviews [Online]* **2013,** *42* (2), 548–568.

98.   Kuhn, P.; Antonietti, M.; Thomas, A. Porous, covalent triazine-based frameworks prepared by ionothermal synthesis. *Angew. Chem. Int. Ed. Engl. [Online]* **2008,** *47* (18), 3450–3453.

99.   Côté, A. P.; Benin, A. I.; Ockwig, N. W.; O'Keeffe, M.; Matzger, A. J.; Yaghi, O. M. Porous, crystalline, covalent organic frameworks. *Science (New York, N.Y.) [Online]* **2005,** *310* (5751), 1166–1170.

100.   Hassan, Z.; Matt, Y.; Begum, S.; Tsotsalas, M.; Bräse, S. Assembly of Molecular Building Blocks into Integrated Complex Functional Molecular Systems: Structuring Matter Made to Order. *Adv. Funct. Mater. [Online]* **2020,** *17*, 1907625.

101.   Zou, X.; Ren, H.; Zhu, G. Topology-directed design of porous organic frameworks and their advanced applications. *Chemical communications (Cambridge, England) [Online]* **2013,** *49* (38), 3925–3936.

102.   Dawson, R.; Cooper, A. I.; Adams, D. J. Nanoporous organic polymer networks. *Progress in Polymer Science [Online]* **2012,** *37* (4), 530–563.

103.   McKeown, N. B.; Budd, P. M. Exploitation of Intrinsic Microporosity in Polymer-Based Materials. *Macromolecules [Online]* **2010,** *43* (12), 5163–5176.

104.   Yan, Z.; Ren, H.; Ma, H.; Yuan, R.; Yuan, Y.; Zou, X.; Sun, F.; Zhu, G. Construction and sorption properties of pyrene-based porous aromatic frameworks. *Microporous and Mesoporous Materials [Online]* **2013,** *173*, 92–98.

105.   Zhang, L.; Lin, T.; Pan, X.; Wang, W.; Liu, T.-X. Morphology-controlled synthesis of porous polymer nanospheres for gas absorption and bioimaging applications. *J. Mater. Chem. [Online]* **2012,** *22* (19), 9861.

106.   Kuhn, P.; Thomas, A.; Antonietti, M. Toward Tailorable Porous Organic Polymer Networks: A High-Temperature Dynamic Polymerization Scheme Based on Aromatic Nitriles. *Macromolecules [Online]* **2009,** *42* (1), 319–326.

107.   Chaikittisilp, W.; Kubo, M.; Moteki, T.; Sugawara-Narutaki, A.; Shimojima, A.; Okubo, T. Porous siloxane-organic hybrid with ultrahigh surface area through simultaneous polymerization-destruction of functionalized cubic siloxane cages. *J. Am. Chem. Soc. [Online]* **2011,** *133* (35), 13832–13835.

108.   Monnereau, L.; Muller, T.; Lang, M.; Bräse, S. Tunable porosity of 3D-networks with germanium nodes. *Chemical communications (Cambridge, England) [Online]* **2016,** *52* (3), 571–574.

109.   Hassan, Z.; Matt, Y.; Begum, S.; Tsotsalas, M.; Bräse, S. Assembly of Molecular Building Blocks into Integrated Complex Functional Molecular Systems: Structuring Matter Made to Order. *Adv. Funct. Mater. [Online]* **2020,** *17*, 1907625.

110. Dawson, R.; Laybourn, A.; Khimyak, Y. Z.; Adams, D. J.; Cooper, A. I. High Surface Area Conjugated Microporous Polymers: The Importance of Reaction Solvent Choice. *Macromolecules [Online]* **2010,** *43* (20), 8524–8530.

111. Kuhn, P.; Antonietti, M.; Thomas, A. Porous, covalent triazine-based frameworks prepared by ionothermal synthesis. *Angew. Chem. Int. Ed. Engl. [Online]* **2008,** *47* (18), 3450–3453.

112. Wang, W.; Ren, H.; Sun, F.; Cai, K.; Ma, H.; Du, J.; Zhao, H.; Zhu, G. Synthesis of porous aromatic framework with tuning porosity via ionothermal reaction. *Dalton transactions (Cambridge, England : 2003) [Online]* **2012,** *41* (14), 3933–3936.

113. Segura, J. L.; Royuela, S.; Mar Ramos, M. Post-synthetic modification of covalent organic frameworks. *Chemical Society reviews [Online]* **2019,** *48* (14), 3903–3945.

114. Cohen, S. M. Postsynthetic methods for the functionalization of metal-organic frameworks. *Chem. Rev. [Online]* **2012,** *112* (2), 970–1000.

115. Zhang, Q.; Zhang, S.; Li, S. Novel Functional Organic Network Containing Quaternary Phosphonium and Tertiary Phosphorus. *Macromolecules [Online]* **2012,** *45* (7), 2981–2988.

116. Yuan, Y.; Sun, F.; Zhang, F.; Ren, H.; Guo, M.; Cai, K.; Jing, X.; Gao, X.; Zhu, G. Targeted synthesis of porous aromatic frameworks and their composites for versatile, facile, efficacious, and durable antibacterial polymer coatings. *Adv. Mater. [Online]* **2013,** *25* (45), 6619–6624.

117. Yuan, Y.; Sun, F.; Li, L.; Cui, P.; Zhu, G. Porous aromatic frameworks with anion-templated pore apertures serving as polymeric sieves. *Nature communications [Online]* **2014,** *5*, 4260.

118. Roberts, J. M.; Fini, B. M.; Sarjeant, A. A.; Farha, O. K.; Hupp, J. T.; Scheidt, K. A. Urea metal-organic frameworks as effective and size-selective hydrogen-bond catalysts. *J. Am. Chem. Soc. [Online]* **2012,** *134* (7), 3334–3337.

119. Pereira, C. F.; Simões, M. M. Q.; Tomé, J. P. C.; Almeida Paz, F. A. Porphyrin-Based Metal-Organic Frameworks as Heterogeneous Catalysts in Oxidation Reactions. *Molecules (Basel, Switzerland)* **2016,** *21* (10). DOI: 10.3390/molecules21101348.

120. Farha, O. K.; Shultz, A. M.; Sarjeant, A. A.; Nguyen, S. T.; Hupp, J. T. Active-site-accessible, porphyrinic metal-organic framework materials. *J. Am. Chem. Soc. [Online]* **2011,** *133* (15), 5652–5655.

121. Shultz, A. M.; Farha, O. K.; Hupp, J. T.; Nguyen, S. T. A catalytically active, permanently microporous MOF with metalloporphyrin struts. *J. Am. Chem. Soc. [Online]* **2009,** *131* (12), 4204–4205.

122. Takaishi, S.; DeMarco, E. J.; Pellin, M. J.; Farha, O. K.; Hupp, J. T. Solvent-assisted linker exchange (SALE) and post-assembly metallation in porphyrinic metal–organic framework materials. *Chem. Sci. [Online]* **2013,** *4* (4), 1509.

123. Cohen, S. M. Postsynthetic methods for the functionalization of metal-organic frameworks. *Chem. Rev. [Online]* **2012,** *112* (2), 970–1000.

124. Tanabe, K. K.; Cohen, S. M. Postsynthetic modification of metal-organic frameworks--a progress report. *Chemical Society reviews [Online]* **2011,** *40* (2), 498–519.

125. Wang, Z.; Cohen, S. M. Postsynthetic modification of metal-organic frameworks. *Chemical Society reviews [Online]* **2009,** *38* (5), 1315–1329.

126. Ma, H.; Ren, H.; Zou, X.; Meng, S.; Sun, F.; Zhu, G. Post-metalation of porous aromatic frameworks for highly efficient carbon capture from CO 2 + N 2 and CH 4 + N 2 mixtures. *Polym. Chem. [Online]* **2014,** *5* (1), 144–152.

127. Ma, H.; Ren, H.; Zou, X.; Sun, F.; Yan, Z.; Cai, K.; Wang, D.; Zhu, G. Novel lithium-loaded porous aromatic framework for efficient CO 2 and H 2 uptake. *J. Mater. Chem. A [Online]* **2013,** *1* (3), 752–758.

128. Nagai, A.; Guo, Z.; Feng, X.; Jin, S.; Chen, X.; Ding, X.; Jiang, D. Pore surface engineering in covalent organic frameworks. *Nature communications [Online]* **2011,** *2*, 536.

129. Xu, H.; Chen, X.; Gao, J.; Lin, J.; Addicoat, M.; Irle, S.; Jiang, D. Catalytic covalent organic frameworks via pore surface engineering. *Chemical communications (Cambridge, England) [Online]* **2014,** *50* (11), 1292–1294.

130. Babarao, R.; Hu, Z.; Jiang, J.; Chempath, S.; Sandler, S. I. Storage and separation of CO2 and CH4 in silicalite, C168 schwarzite, and IRMOF-1: a comparative study from Monte Carlo simulation. *Langmuir [Online]* **2007,** *23* (2), 659–666.

131. Kim, M.-B.; Bae, Y.-S.; Choi, D.-K.; Lee, C.-H. Kinetic Separation of Landfill Gas by a Two-Bed Pressure Swing Adsorption Process Packed with Carbon Molecular Sieve: Nonisothermal Operation. *Ind. Eng. Chem. Res. [Online]* **2006,** *45* (14), 5050–5058.

132. McKeown, N. B.; Budd, P. M. Exploitation of Intrinsic Microporosity in Polymer-Based Materials. *Macromolecules [Online]* **2010,** *43* (12), 5163–5176.

133. Kaur, P.; Hupp, J. T.; Nguyen, S. T. Porous Organic Polymers in Catalysis: Opportunities and Challenges. *ACS Catal. [Online]* **2011,** *1* (7), 819–835.

134. Feng, D.; Chung, W.-C.; Wei, Z.; Gu, Z.-Y.; Jiang, H.-L.; Chen, Y.-P.; Darensbourg, D. J.; Zhou, H.-C. Construction of ultrastable porphyrin Zr metal-organic frameworks through linker elimination. *J. Am. Chem. Soc. [Online]* **2013,** *135* (45), 17105–17110.

135. Li, J.-R.; Sculley, J.; Zhou, H.-C. Metal-organic frameworks for separations. *Chem. Rev. [Online]* **2012,** *112* (2), 869–932.

136. *Silane Coupling Agents;* Plueddemann, E. P., Ed., Second Edition; Springer US: Boston, MA, s.l., 1991.

137. Onclin, S.; Ravoo, B. J.; Reinhoudt, D. N. Gestaltung der Siliciumoxidoberfläche durch selbstorganisierte Monoschichten. *Angew. Chem. [Online]* **2005,** *117* (39), 6438–6462.

138. Neergaard Waltenburg, H.; Yates, J. T. Surface Chemistry of Silicon. *Chem. Rev. [Online]* **1995,** *95* (5), 1589–1673.

139. Haneman, D. Surfaces of silicon. *J. Electrochem. Soc. [Online]* **1987,** *50* (8), 1045–1086.

140. Walsh, R. Bond dissociation energy values in silicon-containing compounds and some of their implications. *Acc. Chem. Res. [Online]* **1981,** *14* (8), 246–252.

141. Schlier, R. E.; Farnsworth, H. E. Structure and Adsorption Characteristics of Clean Surfaces of Germanium and Silicon. *J. Am. Chem. Soc. [Online]* **1959,** *30* (4), 917–926.

142. Chadi. Stabilities of single-layer and bilayer steps on Si(001) surfaces. *Physical review letters [Online]* **1987,** *59* (15), 1691–1694.

143. Johnson, N. M.; Doland, C.; Ponce, F.; Walker, J.; Anderson, G. Hydrogen in crystalline semiconductors. *Physica B: Condensed Matter [Online]* **1991,** *170* (1-4), 3–20.

144. Abrefah, J.; Olander, D. R. Reaction of atomic hydrogen with crystalline silicon. *Surface Science [Online]* **1989,** *209* (3), 291–313.

145. Choi, C. H.; Liu, D.-J.; Evans, J. W.; Gordon, M. S. Passive and active oxidation of Si(100) by atomic oxygen: a theoretical study of possible reaction mechanisms. *J. Am. Chem. Soc. [Online]* **2002,** *124* (29), 8730–8740.

146. Holleman, A. F.; Wiberg, E.; Wiberg, N. *Lehrbuch der anorganischen Chemie*, 102., stark umgearb. u. verb. Aufl.; de Gruyter: Berlin, 2007.

147. Stevens, M. J. Thoughts on the Structure of Alkylsilane Monolayers. *Langmuir [Online]* **1999,** *15* (8), 2773–2778.

148. Fadeev, A. Y.; McCarthy, T. J. Self-Assembly Is Not the Only Reaction Possible between Alkyltrichlorosilanes and Surfaces: Monomolecular and Oligomeric Covalently Attached Layers of Dichloro- and Trichloroalkylsilanes on Silicon. *Langmuir [Online]* **2000,** *16* (18), 7268–7274.

149. Ulman, A. Formation and Structure of Self-Assembled Monolayers. *Chemical reviews [Online]* **1996,** *96* (4), 1533–1554.

150. Xia, Y.; Whitesides, G. M. SOFT LITHOGRAPHY. *Annu. Rev. Mater. Sci. [Online]* **1998,** *28* (1), 153–184.

151. Tada, H.; Nagayama, H. Chemical Vapor Surface Modification of Porous Glass with Fluoroalkyl-Functional Silanes. 1. Characterization of the Molecular Layer. *Langmuir [Online]* **1994,** *10* (5), 1472–1476.

152. Almeida, A. T.; Salvadori, M. C.; Petri, D. F. S. Enolase Adsorption onto Hydrophobic and Hydrophilic Solid Substrates. *Langmuir [Online]* **2002,** *18* (18), 6914–6920.

153. Han, Y.; Offenhäusser, A.; Ingebrandt, S. Detection of DNA hybridization by a field-effect transistor with covalently attached catcher molecules. *Surf. Interface Anal. [Online]* **2006,** *38* (4), 176–181.

154. Li, Y.-h.; Wang, D.; Buriak, J. M. Molecular layer deposition of thiol-ene multilayers on semiconductor surfaces. *Langmuir [Online]* **2010,** *26* (2), 1232–1238.

155. Zisman, W. A. Surface Chemistry of Plastics Reinforced by Strong Fibers. *Ind. Eng. Chem. Prod. Res. Dev. [Online]* **1969,** *8* (2), 98–111.

156. Finklea, H. O.; Robinson, L. R.; Blackburn, A.; Richter, B.; Allara, D.; Bright, T. Formation of an organized monolayer by solution adsorption of octadecyltrichlorosilane on gold: electrochemical properties and structural characterization. *Langmuir [Online]* **1986,** *2* (2), 239–244.

157. Le Grange, J. D.; Markham, J. L.; Kurkjian, C. R. Effects of surface hydration on the deposition of silane monolayers on silica. *Langmuir [Online]* **1993,** *9* (7), 1749–1753.

158. Allara, D. L.; Parikh, A. N.; Rondelez, F. Evidence for a Unique Chain Organization in Long Chain Silane Monolayers Deposited on Two Widely Different Solid Substrates. *Langmuir [Online]* **1995,** *11* (7), 2357–2360.

159. Brzoska, J. B.; Azouz, I. B.; Rondelez, F. Silanization of Solid Substrates: A Step Toward Reproducibility. *Langmuir [Online]* **1994,** *10* (11), 4367–4373.

160. Tripp, C. P.; Hair, M. L. An infrared study of the reaction of octadecyltrichlorosilane with silica. *Langmuir [Online]* **1992,** *8* (4), 1120–1126.

161. White; Tripp. Reaction of (3-Aminopropyl)dimethylethoxysilane with Amine Catalysts on Silica Surfaces. *Journal of colloid and interface science [Online]* **2000,** *232* (2), 400–407.

162. Wasserman, S. R.; Tao, Y. T.; Whitesides, G. M. Structure and reactivity of alkylsiloxane monolayers formed by reaction of alkyltrichlorosilanes on silicon substrates. *Langmuir [Online]* **1989,** *5* (4), 1074–1087.

163. Roscioni, O. M.; Muccioli, L.; Mityashin, A.; Cornil, J.; Zannoni, C. Structural Characterization of Alkylsilane and Fluoroalkylsilane Self-Assembled Monolayers on SiO 2 by Molecular Dynamics Simulations. *J. Phys. Chem. C [Online]* **2016,** *120* (27), 14652–14662.

164. Wikström, P.; Mandenius, C. F.; Larsson, P.-o. Gas phase silylation, a rapid method for preparation of high-performance liquid chromatography supports. *Journal of Chromatography A [Online]* **1988,** *455*, 105–117.

165. Mohammadi Sejoubsari, R.; Martinez, A. P.; Kutes, Y.; Wang, Z.; Dobrynin, A. V.; Adamson, D. H. "Grafting-Through": Growing Polymer Brushes by Supplying Monomers through the Surface. *Macromolecules [Online]* **2016,** *49* (7), 2477–2483.

166. Datta, P.; Genzer, J. "Grafting through" polymerization involving surface-bound monomers. *J. Polym. Sci. A Polym. Chem. [Online]* **2016,** *54* (2), 263–274.

167. Decher, G.; Schlenoff, J. *Multilayer Thin Films. Sequential Assembly of Nanocomposite Materials*, 2. ed.; John Wiley & Sons: Hoboken, 2012.

168. Decher, G. Fuzzy Nanoassemblies: Toward Layered Polymeric Multicomposites. *Science (New York, N.Y.) [Online]* **1997,** *277* (5330), 1232–1237.

169. Zhang, X.; Chen, H.; Zhang, H. Layer-by-layer assembly: from conventional to unconventional methods. *Chemical communications (Cambridge, England) [Online]* **2007,** No. 14, 1395–1405.

170. Bergbreiter, D. E.; Liao, K.-S. Covalent layer-by-layer assembly—an effective, forgiving way to construct functional robust ultrathin films and nanocomposites. *Soft Matter [Online]* **2009,** *5* (1), 23–28.

171. George, S. M.; Yoon, B.; Dameron, A. A. Surface chemistry for molecular layer deposition of organic and hybrid organic-inorganic polymers. *Accounts of chemical research [Online]* **2009,** *42* (4), 498–508.

172. Kohli, P.; Blanchard, G. J. Applying Polymer Chemistry to Interfaces: Layer-by-Layer and Spontaneous Growth of Covalently Bound Multilayers. *Langmuir [Online]* **2000,** *16* (10), 4655–4661.

173. Major, J. S.; Blanchard, G. J. Strategies for Covalent Multilayer Growth. 2. Interlayer Linking Chemistry. *Chem. Mater. [Online]* **2002,** *14* (6), 2574–2581.

174. Serizawa, T.; Matsukuma, D.; Nanameki, K.; Uemura, M.; Kurusu, F.; Akashi, M. Stepwise Preparation and Characterization of Ultrathin Hydrogels Composed of Thermoresponsive Polymers. *Macromolecules [Online]* **2004,** *37* (17), 6531–6536.

175. Puniredd, S. R.; Srinivasan, M. P. Covalent Molecular Assembly in a Supercritical Medium: Formation of Nanoparticles Encapsulated in Immobilized Dendrimers. *Ind. Eng. Chem. Res. [Online]* **2007,** *46* (2), 464–471.

176. Moock, D. S.; Steinmüller, S. O.; Wessely, I. D.; Llevot, A.; Bitterer, B.; Meier, M. A. R.; Bräse, S.; Ehrenberg, H.; Scheiba, F. Surface Functionalization of Silicon, HOPG, and Graphite Electrodes: Toward an Artificial Solid Electrolyte Interface. *ACS applied materials & interfaces [Online]* **2018,** *10* (28), 24172–24180.

177. Carlson, T. A. *X-ray photoelectron spectroscopy*; Benchmark papers in physical chemistry and chemical physics 2; Dowden Hutchinson & Ross: Stroudsburg, Pa., 1978.

178. Nefedov, V. I. *X-ray photoelectron spectroscopy of solid surfaces;* VSP: Utrecht, 1988.

179. Fearn, S. *An introduction to time-of-flight secondary ion mass spectrometry (ToF-SIMS) and its application to materials science*; IOP concise physics; IOP Publ; Morgan & Claypool: Bristol, San Rafael, Calif., 2015.

180. Sodhi, R. N. S. Time-of-flight secondary ion mass spectrometry (TOF-SIMS):--versatility in chemical and imaging surface analysis. *The Analyst*, 483–487.

181. Belu, A. M.; Graham, D. J.; Castner, D. G. Time-of-flight secondary ion mass spectrometry: techniques and applications for the characterization of biomaterial surfaces. *Biomaterials*, 3635–3653.

182. Pal, B. K.; Sahedur Rahman, M. *A Nonextractive Quenchofluorimetric Method for the Determination of Palladium(II) at ?g/L Levels Using Bathophenanthroline* 131, 1999.

183. Binnig; Quate; Gerber. Atomic force microscope. *Physical review letters [Online]* **1986,** *56* (9), 930–933.

184. Zhong, J.; Yan, J. Seeing is believing: atomic force microscopy imaging for nanomaterial research. *RSC Adv.*, 1103–1121.

185. Yang, H.; Xie, H.; Wu, H.; Rong, W.; Sun, L.; Guo, S.; Wang, H. Mechanism of force mode dip-pen nanolithography. *Journal of Applied Physics [Online]* **2014,** *115* (17), 174314.

186. Hudson, S. D.; Zhurov, V.; Grbić, V.; Grbić, M.; Hutter, J. L. Measurement of the elastic modulus of spider mite silk fibers using atomic force microscopy. *Journal of Applied Physics [Online]* **2013,** *113* (15), 154307.

187. Weiß, W. Surface Analysis with STM and AFM. VonS. N. Magonov undM.-H. Whangbo, VCH, Verlagsgesellschaft, Weinheim, 1996. 324 S., geb. 198.00 DM.—ISBN 3–527–29313–2. *Angew. Chem. [Online]* **1997,** *109* (12), 1415–1417.

188. Braga, P. C.; Ricci, D. *Atomic Force Microscopy. Biomedical Methods and Applications*; Methods in Molecular Biology™ 242; Humana Press: Totowa, NJ, 2004.

189. An, Q.; Hassan, Y.; Yan, X.; Krolla-Sidenstein, P.; Mohammed, T.; Lang, M.; Bräse, S.; Tsotsalas, M. Fast and efficient synthesis of microporous polymer nanomembranes via light-induced click reaction. *Beilstein journal of organic chemistry [Online]* **2017,** *13*, 558–563.

190. Lu, W.; Yuan, D.; Zhao, D.; Schilling, C. I.; Plietzsch, O.; Muller, T.; Bräse, S.; Guenther, J.; Blümel, J.; Krishna, R.; Li, Z.; Zhou, H.-C. Porous Polymer Networks: Synthesis, Porosity, and Applications in Gas Storage/Separation. *Chem. Mater. [Online]* **2010,** *22* (21), 5964–5972.

191. Su, D.; Menger, F. M. Tetrastyrylmethane. *Tetrahedron Letters [Online]* **1997,** *38* (9), 1485–1488.

192. Becker, H. G. O. *Organikum. Organisch-chemisches Grundpraktikum*, 21., neu bearb. und erw. Aufl.; Wiley-VCH: Weinheim, 2001.

193. Monnereau, L.; Nieger, M.; Muller, T.; Bräse, S. Tetrakis-(4-thiyphenyl)methane: Origin of a Reversible 3D-Homopolymer. *Adv. Funct. Mater. [Online]* **2014,** *24* (8), 1054–1058.

194. Pandey, P.; Farha, O. K.; Spokoyny, A. M.; Mirkin, C. A.; Kanatzidis, M. G.; Hupp, J. T.; Nguyen, S. T. A "click-based" porous organic polymer from tetrahedral building blocks. *J. Mater. Chem. [Online]* **2011,** *21* (6), 1700.

195. Lambert, J. B.; Liu, Z.; Liu, C. Metal−Organic Frameworks from Silicon- and Germanium-Centered Tetrahedral Ligands. *Organometallics [Online]* **2008,** *27* (7), 1464–1469.

196. Monnereau, L.; Muller, T.; Lang, M.; Bräse, S. Tunable porosity of 3D-networks with germanium nodes. *Chemical communications (Cambridge, England) [Online]* **2016,** *52* (3), 571–574.

197. Reichert, V. R.; Mathias, L. J. Expanded Tetrahedral Molecules from 1,3,5,7-Tetraphenyladamantane. *Macromolecules [Online]* **1994,** *27* (24), 7015–7023.

198. Zimmermann, T.; Müller, T. Convenient Syntheses of Tetraarylmethane Starting Materials. *Synthesis* **2002,** *2002* (09). DOI: 10.1055/s-2002-32526.

199. David Geiß. Bausteinsynthese für Amino-In Synthesen auf Oberflächen. Bachelor Thesis; Karlsruher Institut für technologie, Karlsruhe, 2019.

200. van Brabandt, W.; Vanwalleghem, M.; D'hooghe, M.; Kimpe, N. de. Asymmetric synthesis of 1-(2- and 3-haloalkyl)azetidin-2-ones as precursors for novel piperazine, morpholine, and 1,4-diazepane annulated beta-lactams. *J. Org. Chem. [Online]* **2006,** *71* (18), 7083–7086.

201. Anderson, K. W.; Tundel, R. E.; Ikawa, T.; Altman, R. A.; Buchwald, S. L. Monodentate phosphines provide highly active catalysts for Pd-catalyzed C-N bond-forming reactions of heteroaromatic halides/amines and (H)N-heterocycles. *Angewandte Chemie (International ed. in English) [Online]* **2006,** *45* (39), 6523–6527.

202. Fors, B. P.; Buchwald, S. L. A multiligand based Pd catalyst for C-N cross-coupling reactions. *J. Am. Chem. Soc. [Online]* **2010,** *132* (45), 15914–15917.

203. Anderson, K. W.; Ikawa, T.; Tundel, R. E.; Buchwald, S. L. The selective reaction of aryl halides with KOH: synthesis of phenols, aromatic ethers, and benzofurans. *J. Am. Chem. Soc. [Online]* **2006,** *128* (33), 10694–10695.

204. Jensen, T.; Pedersen, H.; Bang-Andersen, B.; Madsen, R.; Jørgensen, M. Palladium-catalyzed aryl amination-heck cyclization cascade: a one-flask approach to 3-substituted indoles. *Angew. Chem. Int. Ed. Engl. [Online]* **2008,** *47* (5), 888–890.

205. Brotzel, F.; Chu, Y. C.; Mayr, H. Nucleophilicities of primary and secondary amines in water. *J. Org. Chem. [Online]* **2007,** *72* (10), 3679–3688.

206. Kanzian, T.; Nigst, T. A.; Maier, A.; Pichl, S.; Mayr, H. Nucleophilic Reactivities of Primary and Secondary Amines in Acetonitrile. *Eur. J. Org. Chem. [Online]* **2009,** *2009* (36), 6379–6385.

207. June, S. M.; Bissel, P.; Long, T. E. Segmented block copolyesters using click chemistry. *J. Polym. Sci. A Polym. Chem. [Online]* **2012,** *50* (18), 3797–3805.

208. Jiang, R.; Liu, M.; Huang, H.; Mao, L.; Huang, Q.; Wen, Y.; Cao, Q.-y.; Tian, J.; Zhang, X.; Wei, Y. Fabrication of AIE-active fluorescent polymeric nanoparticles with red emission through a facile catalyst-free amino-yne click polymerization. *Dyes and Pigments [Online]* **2018,** *151*, 123–129.

209. Shafir, A.; Buchwald, S. L. Highly selective room-temperature copper-catalyzed C-N coupling reactions. *J. Am. Chem. Soc. [Online]* **2006,** *128* (27), 8742–8743.

210. Sambiagio, C.; Marsden, S. P.; Blacker, A. J.; McGowan, P. C. Copper catalysed Ullmann type chemistry: from mechanistic aspects to modern development. *Chemical Society reviews [Online]* **2014,** *43* (10), 3525–3550.

211. Nayab, S.; Trouillet, V.; Gliemann, H.; Hurrle, S.; Weidler, P. G.; Rashid Tariq, S.; Goldmann, A. S.; Barner-Kowollik, C.; Yameen, B. Chemically reprogrammable metal organic frameworks (MOFs) based on Diels-Alder chemistry. *Chemical communications (Cambridge, England) [Online]* **2017,** *53* (83), 11461–11464.

212. Wahlqvist, M.; Shchukarev, A. XPS spectra and electronic structure of Group IA sulfates. *Journal of Electron Spectroscopy and Related Phenomena [Online]* **2007,** *156-158*, 310–314.

213. Terry, J.; Linford, M. R.; Wigren, C.; Cao, R.; Pianetta, P.; Chidsey, C. E. D. Determination of the bonding of alkyl monolayers to the Si(111) surface using chemical-shift, scanned-energy photoelectron diffraction. *Appl. Phys. Lett.*, 1056–1058.

214. Kondoh, A.; Takami, K.; Yorimitsu, H.; Oshima, K. Stereoselective hydrothiolation of alkynes catalyzed by cesium base: facile access to (Z)-1-alkenyl sulfides. *J. Org. Chem. [Online]* **2005,** *70* (16), 6468–6473.

215. Li, L.; Feng, W.; Welle, A.; Levkin, P. A. UV-Induced Disulfide Formation and Reduction for Dynamic Photopatterning. *Angewandte Chemie (International ed. in English) [Online]* **2016,** *55* (44), 13765–13769.

216. van Duin, A. C. T.; Dasgupta, S.; Lorant, F.; Goddard, W. A. ReaxFF: A Reactive Force Field for Hydrocarbons. *J. Phys. Chem. A [Online]* **2001,** *105* (41), 9396–9409.

217. http://www.maciejharanczyk.info/Zeopp/about.html.

218. Martin, R. L.; Smit, B.; Haranczyk, M. Addressing challenges of identifying geometrically diverse sets of crystalline porous materials. *Journal of chemical information and modeling [Online]* **2012,** *52* (2), 308–318.

219. Willems, T. F.; Rycroft, C. H.; Kazi, M.; Meza, J. C.; Haranczyk, M. Algorithms and tools for high-throughput geometry-based analysis of crystalline porous materials. *Microporous and Mesoporous Materials [Online]* **2012,** *149* (1), 134–141.

220. Feng, G.; Qiao, R.; Huang, J.; Dai, S.; Sumpter, B. G.; Meunier, V. The importance of ion size and electrode curvature on electrical double layers in ionic liquids. *Physical chemistry chemical physics : PCCP [Online]* **2011,** *13* (3), 1152–1161.

221. Matthias Lang. Darstellung poröser organischer Netzwerke via Thiol-Click-Reaktionen sowie die festphasenbasierte Synthese von para-Oligo(phenylenethinyl)-Derivaten. Dissertation; Karlsruher Institut für technologie, Karlsruhe, 2018.

222. Ahlrichs, R.; Bär, M.; Häser, M.; Horn, H.; Kölmel, C. Electronic structure calculations on workstation computers: The program system turbomole. *Chemical Physics Letters [Online]* **1989,** *162* (3), 165–169.

223. Furche, F.; Ahlrichs, R.; Hättig, C.; Klopper, W.; Sierka, M.; Weigend, F. Turbomole. *WIREs Comput Mol Sci [Online]* **2014,** *4* (2), 91–100.

224. Perdew, J. P.; Ernzerhof, M.; Burke, K. Rationale for mixing exact exchange with density functional approximations. *The Journal of Chemical Physics [Online]* **1996,** *105* (22), 9982–9985.

225. Weigend, F.; Ahlrichs, R. Balanced basis sets of split valence, triple zeta valence and quadruple zeta valence quality for H to Rn: Design and assessment of accuracy. *Physical chemistry chemical physics : PCCP [Online]* **2005,** *7* (18), 3297–3305.

226. Grimme, S.; Antony, J.; Ehrlich, S.; Krieg, H. A consistent and accurate ab initio parametrization of density functional dispersion correction (DFT-D) for the 94 elements H-Pu. *The Journal of Chemical Physics [Online]* **2010,** *132* (15), 154104.

7.2 List of Figures

7. Appendix

7. Appendix

7.3 List of Schemes

7.4 List of Tables

7.5 List of Abbreviations

A	Ampere
AFM	Atomic force microscopy
BDT	benzo[1,2-*b*:4,5-*b'*]dithiophene
BET	Nitrogen physisorption
br (IR)	Broad
Cat.	Catalyst
Cat.	Catalyst
CC	Click chemistry
CDCl$_3$	Deuterated chloroform
CH	Cyclohexane
CMC	carboxymethyl chitosan
COF	Covalent-organic framework
Conc.	Concentration
COSY	Correlation spectroscopy
CTF	covalent triazine framework

CuAAC	Copper-catalysed azide-alkyne "click" reaction
d (NMR)	Doublet
DCM	Dichlormethane
DEC	Diethyl carbonate
DFT	Density functional Theory
DMC	Dimethyl Carbonate
DME	1,2-Dimethoxyehtane
DMPA	2,2-dimethoxy-2-phenylacetophenone
DMSO	Dimethyl sulfoxide
DSC	Differential scanning calorimetry
EA	Ethyl acetate
EI	Electron ionisation
EI-MS	Electron ion mass spectroscopy
eq.	Equivalent
ESCA	Electron spectroscopy for chemical analysis
FAB-MS	Fast bombardment mass spectroscopy
GC	Gas chromatograph
GPC	Gel permeation chromatography
H_2BDC	terephtalic acid
H_2EDBA	(*E*) 4,4'-(ethene-1,2-diyl)dibenzoic acid
H_3BBC	4,4',4''-(benzene-1,3,5-triyltris(benzene-4,1-diyl))tribenzoate
H_3BTC	trimesic acid
HCP	Hyper crosslinked polymer
HDC	Huisgen 1,3-dipolar cycloaddition
HRMS	High resolution mass spectrometry
HSQC	Heteronuclear single quantum coherence
Hz	Hertz
IR	Infrared
IRMOF	Isoreticular metal-organic framework
J (NMR)	Coupling constant
kJ	Kilojoule
LED	Light-emitting diode
LIB	Lithium-ion batterie

7. Appendix

LIMG	Liquid Ion Metal Gun
m (IR)	Medium
m (NMR)	Multiplet
M_n	Number-average molar mass